


UNIVERSITY OF
BIRMINGHAM

# DEVELOPMENT OF A DESICCANT SYSTEM FOR SPACE AIR CONDITIONING USING METAL-ORGANIC FRAMEWORK MATERIALS

by

Andrew Nabil Aziz Makar

A thesis submitted to the University of Birmingham for the degree of

DOCTOR OF PHILOSOPHY

Department

School of Engineering

College of Engineering and Physical Sciences

University of Birmingham

September 2024

UNIVERSITY OF
BIRMINGHAM

## University of Birmingham Research Archive

### e-theses repository

This unpublished thesis/dissertation is copyright of the author and/or third parties. The intellectual property rights of the author or third parties in respect of this work are as defined by The Copyright Designs and Patents Act 1988 or as modified by any successor legislation.

Any use made of information contained in this thesis/dissertation must be in accordance with that legislation and must be properly acknowledged. Further distribution or reproduction in any format is prohibited without the permission of the copyright holder.

# Abstract

Metal-Organic Frameworks (MOFs) are very promising materials for improving the effectiveness of desiccant air conditioning systems due to their outstanding ability to adsorb moisture, adjustable features, and potential for sustainable heating and cooling applications. This study examines the incorporation of Metal-Organic Frameworks (MOFs) into desiccant systems to achieve energy-efficient control of indoor humidity and temperature, thus positively impacting occupants' health and comfort. Through a comprehensive literature review, several MOFs were identified and numerically and experimentally investigated in terms of moisture removal rate from air. MOF-303/G was identified as the best candidate adsorbent for this application. Various heat exchangers were considered, and the wire-finned heat exchanger was identified as the most efficient for coating with the identified MOF-303/G. An advanced computational fluid dynamics model of MOF-303/G coated wire-finned tube was created using COMSOL Multiphysics software. This model accurately simulates the heat and mass transfer process between the MOF material and the air and the heat transfer between the MOF material and the metal heat exchanger under different operating scenarios. In addition, a novel heating process for the MOF-coated heat exchanger was developed utilising electrical DC to optimise the heat transfer and energy consumption.

The developed DCHE's experimental testing confirmed the dynamic of the adsorption-desorption processes and validated the CFD model. The model-predicted water uptake during the adsorption process with the experimental measurements with time, showing good agreement with a maximum deviation of ±6%

Use the developed MOF-303/G DCHE to construct the desiccant air conditioning system consisting of an array of DCHEs, a direct evaporative cooler, an air-to-water heat exchanger, ducting and an automatic control system. The system was tested to achieve the comfort conditions for a $2m^3$ room. Results showed that the developed system effectively attained the ASHRAE comfort standards by consistently maintaining a steady indoor environment with a temperature of 25-28°C and a relative humidity of 50-60% at air ambient conditions ranging from 10-35°C and 50-80% with system COP ranging 0.7-1.54. This performance illustrates the system's capability to achieve the target indoor comfort conditions with lower energy consumption. The desiccant air conditioning system significantly reduced power consumption for heating, with a decrease of 74%, and for cooling, with a decrease of 66%, compared to a 2 kW vapour compression air conditioner (split type). Such results highlight the potential of the developed system in terms of energy savings and independent control of indoor temperature and humidity for climate control in residential, commercial, and agricultural environments.

## Dedicated To

My parents for all their love and support, and for putting me through the best education possible. I appreciate their sacrifices, and I wouldn't have been able to have reached this stage without them.

**"The God of heaven will prosper us. Therefore, we, his servants, will arise and build." Nehemiah (2:20)**

# Acknowledgements

I would like to express my deepest appreciation and gratitude to my PhD supervisors Dr. Raya Al-Dadah, Dr. Saad Mahmoud (School of Mechanical Engineering). Their valuable guidance, ideas, and reviews are undeniable in both my scientific papers and thesis. Many thanks go to all the adsorption group members, late and present, for all the valuable discussions, laughs and support. Thanks to all my friends in Egypt and Birmingham for their continuous support.

# List of Publications

**Andrew N. Aziz**, Saad Mahmoud, Raya Al-Dadah, Ibrahim Albaik, " Numerical Investigation of Desiccant Cooling Using Aluminium Fumarate Metal-Organic Framework Material", Heat Powered Cycles Conference, **2021**.

**Andrew N. Aziz** , Saad Mahmoud, Raya Al-Dadah, Mohamed A Ismail and Mohammed K Almesfer" Numerical and Experimental Investigation of Desiccant Cooling System using Metal-Organic Framework materials ", Applied Thermal Engineering, 2022.

**Andrew N. Aziz** , Raya Al-Dadah , Saad Mahmoud, Mohamed A. Ismail, Mohammed K. Almesfer, Marwa F. El-Kady, and Hassan Shokry "MOF-801/Graphene Adsorbent Material for Greenhouse Climate Control System—Numerical Investigation", Energies, vol. 16, no. 9, 2023.

**Andrew N. Aziz**, Saad Mahmoud, Raya Al-Dadah, Anil Taskin, Mohamed A. Ismail, Y.M. Fahmy, Md Mamoon Rashid, "Novel MOF-303/G coated wire-finned heat exchanger for dehumidification applications–Experimental investigation", Energy, Volume 305, 2024.

# Table of Contents

**Abstract**.....i
**Dedicated To**.....ii
**Acknowledgements**.....iii
**List of Publications**.....iv
**Table of Contents**.....v
**List of Figures**.....vii
**Abbreviations**.....xviii
**Nomenclature**.....xviii
**Chapter 1 Introduction**.....1
**1.1. Background**.....1
**1.2. Aims and objectives**.....4
**1.3. Thesis outlines**.....5
**Chapter 2 Literature Review**.....7
**2.1. Conventional climate control methods**.....7
**2.2. Adsorption systems for climate control**.....9
**2.2.1. Principles of adsorption**.....10
**2.2.2. Adsorption materials**.....13
**2.2.3. Adsorption heat exchangers**.....18
**2.2.4. The heating and cooling source of the DCHE**.....21
**2.2.5. Performance progress in different DCHEs.**.....24
**2.3. Direct and indirect evaporative coolers**.....29
**2.4. Desiccant Systems Configurations**.....30
**2.5. Experimental parameters to improve DW/DCHE performance**.....36
**2.6. Modelling of desiccant systems**.....39
**2.7. Summary of Key Findings and Knowledge Gap**.....41
**Chapter 3 Modelling of desiccant-coated heat exchanger**.....43
**3.1. One-dimensional dynamic numerical model of mass and heat transfer for stationary desiccant-coated heat exchanger**.....43
**3.2. Experimental setup**.....51
**3.3. Modelling and experimental results**.....55
**3.4. Summary**.....59
**Chapter 4 Development of electrically heated desiccant coated heat exchanger**.....62
**4.1. Heating element configuration**.....62
**4.2. Examining additional MOF materials**.....67

**4.3. MOF-303/G characterisation** ..... 74
**4.4. MOF Coated Multi-Tube Heat Exchanger** ..... 78
**4.5. Summary** ..... 88
**Chapter 5 Case study for DCHEs to control the greenhouse's climate** ..... 89
**5.1. Computational Fluid Dynamic Modelling of MOF-303/G** ..... 89
**5.1.1. CFD Model Validation and Results** ..... 95
**5.2. Green House Climate Control System Air-to-Air heat exchanger** ..... 104
**5.3. Overall System Performance Results** ..... 111
**5.4. Summary** ..... 113
**Chapter 6 Experimental test facility** ..... 114
**6.1. Test facility description** ..... 114
**6.1.1. Adsorber bed** ..... 115
**6.1.2. Motorized damper** ..... 118
**6.1.3. Elbows** ..... 119
**6.1.4. Control circuit for the two adsorber beds** ..... 119
**6.1.5. Main Fan** ..... 121
**6.1.1. Evaporative cooler** ..... 122
**6.1.2. Air-to-water heat exchanger** ..... 125
**6.1.3. Room description and insulation** ..... 126
**6.1.4. Sensors and data loggers** ..... 127
**6.2. Test rig commissioning** ..... 128
**6.3. Testing procedure** ..... 129
**6.3.1. Initialization** ..... 129
**6.3.2. Cycling** ..... 129
**6.3.3. Data collection and switching off** ..... 130
**Chapter 7 System Experimental Results** ..... 131
**7.1. Performance of single adsorber bed** ..... 131
**7.2. Desiccant air conditioning system for heating** ..... 136
**7.2.1. Adsorber beds performance without evaporative cooler** ..... 137
**7.2.2. Impact of Evaporative Cooling on Humidity and Temperature Control** ..... 159
**7.2.3. Impact of Varying Water Flow Rates in the Evaporative Cooler Pump on System Performance** ..... 161
**7.3. Desiccant air conditioning system for cooling** ..... 175
**7.3.1. Effect of air to water HE inlet water temperature on controlling the air relative humidity and the temperature level** ..... 176
**7.3.2. Cooling/Heating Power Consumption:** ..... 191

**7.4. Summary** ..... 192
**Chapter 8 Conclusions and Future Work** ..... 194
**8.1. Conclusions** ..... 194
**8.2. Future work** ..... 196
References ..... 198
AppendixI: Matlab Greenhouse Code ..... 210
AppendixII: Arduino Code for Switching Scenarios and Controlling DCHEs ..... 220
Appendix III: Arduino Code for controlling Evaporative cooler ..... 225

# List of Figures

Figure 1-1: Energy use for space cooling [6]. ..... 1
Figure 1-2: How vapour compression works [9]. ..... 2
Figure 1-3: Energy use for space heating [6]. ..... 2
Figure 1-4: Schematic of a conventional double-bed adsorption desalination system [11]. ..... 3
Figure 1-5: How evaporative cooler works [18]. ..... 4
Figure 1-6: Thesis outline diagram ..... 6
Figure 2-1: Chapter 2 flow diagram. ..... 7
Figure 2-2: Operative temperature and humidity ratio of indoor comfort Condition [20]. ..... 8
Figure 2-4: Schematic diagram showing the difference between traditional and hybrid air-conditioning systems and their psychometric process: (a) Conventional HVAC system, (b) Conventional HVAC psychometric process, (c) Hybrid air-conditioning desiccant system and (d) Hybrid air-conditioning desiccant system psychometric process [28]. ..... 10
Figure 2-5: Types of adsorption isotherms [38] ..... 12
Figure 2-6: The equilibrium adsorption curves for composite desiccant and silica gel [52]. ..... 15
Figure 2-7: The water uptake of several MOFs with silica gel and zeolite [31]. ..... 16
Figure 2-8: Typical range of regeneration temperature for the commonly employed desiccant materials [61]. ..... 17
Figure 2-9: Operation of a desiccant wheel [68]. ..... 18
Figure 2-10: Fixed bed Solid desiccant dehumidification [70] ..... 19

Figure 2-11: Heat exchanger designs reviewed. a) Finless tube, b) wire finned tube, c) metal foam, d) graphite plate, e) microchannel, f) lattice [72]. ..... 19

Figure 2-12: Rectangular finned and wire finned heat exchangers for adsorption application [74]. ..... 20

Figure 2-13: Application of ultrasound for regeneration of silica gel [92]. ..... 22

Figure 2-14: Experimental setup investigating the impact of microwave heating on the process of regeneration [94]. ..... 23

Figure 2-15: Comparison between the conventional vapour-compression heat pump and the thermo-electric humidity pump [95]. ..... 24

Figure 2-16: Schematic diagram and photo of the experimental setup [101]. ..... 25

Figure 2-17: Experimental system [105]. ..... 26

Figure 2-18: Schematic diagram of a desiccant system using SCHE with HRD [97]. ..... 28

Figure 2-19: Two-stage indirect-direct evaporator system [121]..... 30

Figure 2-20 Systems configurations [125]. ..... 31

Figure 2-21: Schematic diagram of a desiccant system [126]. ..... 32

Figure 2-22: Psychrometric chart of one-stage solar desiccant cooling system in ventilation mode [127]..... 33

Figure 2-23: Psychrometric chart of a two-stage solar desiccant cooling system in ventilation mode [127]..... 34

Figure 2-24: Psychrometric chart of one-stage solar desiccant cooling system in recirculation mode [127]..... 35

Figure 2-25: Psychrometric chart of a two-stage solar desiccant cooling system in recirculation mode [127]..... 35

Figure 2-26: Scheme of the desiccant cooling system and its evolution in the psychrometric chart [128]..... 36

Figure 2-27: Desiccant-coated heat exchanger before evaporative cooler. ..... 38

Figure 2-28: DCHE air-conditioner integrated with solar collectors and Direct evaporative cooler [49], [102]. ..... 38

Figure 2-29: The schematic diagram of the desiccant cooling system [57]. ..... 39

Figure 3-1: side view/cross-sectional for one channel from the desiccant wheel. ..... 43

Figure 3-2: Isotherm curve for MOF materials. ..... 45

Figure 3-3: flow chart for the stationary desiccant system process. ..... 47

Figure 3-4: Wheel and air flow passage presentation. ..... 49

Figure 3-5: Inlet velocity change vs moisture removal. ..... 50

Figure 3-6: psychrometric representation for stationary model output. ..... 51

Figure 3-7: 3-D drawing for the test facility. ..... 51

Figure 3-8: Coated honeycomb structure integrated with the test facility. ..... 53

Figure 3-9: moisture removal versus time step measured values output compared with scaler measurements. ..... 55

Figure 3-10: Relative humidity change versus time when using a humidifier. ..... 55

Figure 3-11: Temperature change with a humidifier. ..... 56

Figure 3-12: Relative humidity change versus time without humidifier. ..... 56

Figure 3-13: Temperature change without a humidifier. ..... 57

Figure 3-14: Relative humidity change at the same conditions with and without a humidifier. ..... 58

Figure 3-15: moisture removal variation with time experimental versus model results. ..... 59

Figure 3-16: moisture removal versus time step at different airspeeds. ..... 59

Figure 4-1: the heating wiring diagram. ..... 63

Figure 4-2: heating control circuit. ..... 64

Figure 4-3: The heating control circuit to control the desorption/adsorption process for the DCHE. ..... 65

Figure 4-4: Thermal Imaging Camera ..... 65

Figure 4-5: Thermal image of the electrically heated wire finned tube with 28.8 W. ..... 66

Figure 4-6: Temperature sensors distribution along the tube before coating. ..... 66

Figure 4-7: Temperature distribution along the tube using input power of 20 W. ..... 67

Figure 4-8:The water adsorption isotherm of Aluminium Fumarate and MIL-100(Fe) [31], MOF-801 and MOF-801/G [162], MOF-303 and MOF-303/G. ..... 68

Figure 4-9: Thermal diffusivity of MOF-303 and MOF-303/G. ..... 69

Figure 4-10: Six electrically heated copper wire finned tubes each coated with 0.3mm thick of the relevant MOF material. ..... 70

Figure 4-11: Optical images for MOFs coating powder. (a) Aluminium fumarate, (b) MOF-303/G, (c) MOF-80, (d) MIL-100(Fe), (e) MOF-100(Fe)/G (f) MOF-801/G (g) binder. ..... 71

Figure 4-12: Optical images for MOFs/binder solution(a) binder solution, (b) MIL-100 (Fe) /binder, (c) MOF-303/G/binder, (d) Aluminium fumarate/binder. ..... 71

Figure 4-13: Small tube test setup at ambient conditions. ..... 71

Figure 4-14: Six wire-finned tube's water uptake at ambient conditions. ..... 73

Figure 4-15: Repeatability test for MOF-303/G. ..... 73

Figure 4-16: SEM image of MOF-303 nanoparticles. (b) SEM image of graphene nanoplatelets. (c,d) SEM images of MOF-303/G. ..... 74

Figure 4-17: PXRDs patterns for graphene nanoplatelets, neat MOF-303 nanoparticles, and MOF-303/G (10%) composite. ..... 75

Figure 4-18: TGA of MOF-303 and MOF-303/G [163]. ..... 75

Figure 4-19: Cyclic performance of MOF-303/G nanoparticles compared to neat MOF-303 at P/Po = 0.9 and Tdesorption of 90 °C [163]. ..... 76

Figure 4-20: Single wired-finned tube coated with MOF-303/G characterisation at different watts for the desorption process. ..... 77

Figure 4-21: Full-coated desiccant heat exchanger with wire connections and its Thermal image after applying power. ..... 78

Figure 4-22: Test facility to characterise the single tube and the complete heat exchanger. 79

Figure 4-23: Temperature, humidity sensors and weight scaler used to collect the data for the dehumidification test facility. ..... 80

Figure 4-24: desorption process at three different MOF-303/G surface temperatures: 45°C,60°C and 70°C. ..... 81

Figure 4-25: The water uptake of MOF-303/G versus time at MOF surface temperature of 45, 60, and 70°C ..... 83

Figure 4-26: Temperature before and after the heat exchanger at MOF surface temperature of 45°C, 60°C, 70°C ..... 83

Figure 4-27: Relative humidity before and after the heat exchanger at MOF surface temperature of 45°C, 60°C, 70°C. ..... 84

Figure 4-28: Temperature/humidity ratio before and after the heat exchanger at MOF surface temperature of 45°C,60°C, and 70°C after 10 mins on psychrometric chart. ..... 85

Figure 4-29: The COP of MOF-303/G versus time at MOF surface temperature of 45°C, 60°C, 70°C. ..... 87

Figure 5-1: MOF-303/G-coated wire finned tube and its 3D CAD model. ..... 90

Figure 5-2: Simulation results at ambient operating conditions. ..... 92

Figure 5-3: Shows the temperature and the water uptake variation during the desorption process for a 15cm wire-finned tube coated with 10 grams after 10, 34 mins. ..... 93

Figure 5-4: Shows the temperature and the water uptake variation during the adsorption process for a 15cm wire-finned tube coated with 10 grams after 40, 80 mins. ..... 93

Figure 5-6: Mesh sensitivity analysis. ..... 94

Figure 5-6: Validation test setup ..... 95

Figure 5-7: Comparison of the simulation results with experimental data. ..... 96

Figure 5-8: Repeatability test. ..... 97

Figure 5-9: Temperature and water uptake variation with time during desorption and adsorption processes at input power of 12.8W and adsorption time of 40 mins. ..... 99

Figure 5-10: Temperature and water uptake variation with time during desorption and adsorption processes at input power of 20W and adsorption time of 40 mins. ..... 101

Figure 5-11: Temperature and water uptake variation with time during desorption and adsorption processes at input power of 28.8W and adsorption time of 40 mins. ..... 103

Figure 5-12: Greenhouse climate control based on a desiccant cooling system using MOF-303/G material. ..... 105

Figure 5-13: Schematic diagram of direct evaporative cooler/model flow chart. ..... 108

Figure 5-14: The flow chart of the integrated cycle for the greenhouse climate control system. ..... 109

Figure 5-15: Air-to-air heat exchanger model validation. ..... 110

Figure 5-16: DCHE model validation. ..... 111

Figure 5-17: Psychrometric chart output. ..... 112

Figure 5-18: Relative humidity change for the greenhouse and studies its effect on the system behaviour on a psychrometric chart. ..... 112

Figure 6-1: 3D CAD model for the desiccant air conditioning system. ..... 114
Figure 6-2: Testing facility of the double-bed adsorption air conditioning system. ..... 115
Figure 6-3: Square to Round fitting for the adsorber bed. ..... 116
Figure 6-4: 6-14 AWG Waterproof Wire Connectors. ..... 116
Figure 6-5: High-Temperature Wire Cable ..... 116
Figure 6-6: Heat exchanger and wiring connections assembly. ..... 117
Figure 6-7: Adsorber bed 3D assembly. ..... 117
Figure 6-8: 220V electric motorized damper air duct. ..... 118
Figure 6-9: 220V Damper bypass motorized damper electric air duct vent fittings. ..... 118
Figure 6-10: 90° Elbow and plastic t connection. ..... 119
Figure 6-11: Inlet velocity change for the desiccant wheel and studies its effect on the system behaviour on a psychrometric chart. ..... 120
Figure 6-12: DCHE electric control circuit. ..... 120
Figure 6-13: DuctStore 150mm main fan. ..... 121
Figure 6-14: PWM speed control circuit. ..... 121
Figure 6-15: Honeywell evaporative cooler. ..... 123
Figure 6-16: High flow peristaltic pump 12V. ..... 123
Figure 6-17: Water flowrate control circuit for evaporative cooler. ..... 124
Figure 6-18: Water flow rate control vs PWM(Hz). ..... 125
Figure 6-19: Air-to-water heat exchanger configuration ..... 125
Figure 6-20: Air-to-water heat exchanger dimensions. ..... 126
Figure 6-21: 3D CAD drawing of the the room. ..... 126
Figure 6-22: Piping insulation and Aluminium foil ducting. ..... 127
Figure 6-23a: Temperature and humidity sensors positions for all the system. ..... 128
Figure 6-23b: Temperature and humidity Sensors used for all the system. ..... 128
Figure 7-1: Schematic diagram of single adsorber bed. ..... 131
Figure 7-2: Single-row DCHE moisture removal/uptake and MOF-surface temperature. ..... 132

Figure 7-3: Moisture content difference of single-row DCHE adsorber bed using MOF-303/G. ..... 133

Figure 7-4: Two-rows DCHEs adsorber bed moisture removal/uptake and MOF-surface temperature. ..... 134

Figure 7-5: Moisture content difference of two-rows of adsorber bed using MOF-303/G. . 134

Figure 7-6: Three-rows moisture removal rate and MOF-surface temperature. ..... 135

Figure 7-7: Moisture content difference of three DCHEs rows in adsorber bed using MOF-303/G. ..... 136

Figure 7-8: Desiccant heating system with temperature and humidity sensors positions. .. 137

Figure 7-9a: Room air temperature at different half-cycle times and 50% fresh air. ..... 138

Figure 7-9b: Room Relative humidity at different half-cycle time s and 50% fresh air..... 138

Figure 7-9c: Air temperature after DCHE at different half-cycle time s and 50% fresh air... 139

Figure 7-9d: Air relative humidity after DCHE at different half-cycle times and 50% fresh air. ..... 139

Figure 7-9e: Psychrometric at different half-cycle times and 50% fresh air at 13°C, 5.6 g/kg(d.a.) inlet Temperature and specific humidity. ..... 140

Figure 7-10a: Room air temperature at different half-cycle times and 100% fresh air. ..... 141

Figure 7-10b: Room air relative humidity at different half-cycle times and 100% fresh air. 141

Figure 6-10c: Air temperature change after DCHE at different half-cycle times and 100% fresh air. ..... 142

Figure 6-10d: Air relative humidity change after DCHE at different half-cycle times and 100% fresh air. ..... 142

Figure 7-10e: Psychrometric chart output at different half-cycle times and 100% fresh air at 13.4 °C, 5.01 g/kg(d.a.) inlet Temperature and specific humidity. ..... 143

Figure 7-11: Effect of half-cycle time and mixing ratio on the COP of the desiccant air conditioning system for heating. ..... 144

Figure 7-12a: Room air temperature at different half-cycle times and 50% fresh air. ..... 145

Figure 7-12b: Room air relative humidity at different half-cycle times and 50% fresh air. .. 145

Figure 7-12c: Air temperature after DCHE at different half-cycle times and 50% fresh air.. 146

Figure 7-12d: Air relative humidity after DCHE at different half-cycle times and 50% fresh air. .....146

Figure 7-12e: Psychrometric chart output at different half-cycle times and 50% fresh air at 11.2 °C, 4.16 g/kg(d.a.) inlet Temperature and specific humidity. .....147

Figure 7-13a: Room air temperature at different half-cycle times and 100% fresh air. .....148

Figure 7-13b: Room air relative humidity at different half-cycle times and 100% fresh air. 148

Figure 7-13c: Air temperature after DCHE at different half-cycle times and 100% fresh air. .....149

Figure 7-13d: Air relative humidity after DCHE at different half-cycle times and 100% fresh air. .....149

Figure 7-13e: Psychrometric chart output at different half-cycle times and 100% fresh air at 14.7 °C, 4.6 g/kg(d.a.) inlet Temperature and specific humidity. .....150

Figure 7-14: Effect of half-cycle time and mixing ratio on the COP of the desiccant air conditioning system. .....151

Figure 7-15a Room air temperature at different half-cycle times and 50% fresh air. .....152

Figure 7-15b: Room air relative humidity at different half-cycle times and 50% fresh air. ..152

Figure 7-15c: Temperature after DCHE at different half-cycle times and 50% fresh air.....153

Figure 7-15d: Air relative humidity after DCHE at different half-cycle times at 50% fresh air. .....153

Figure 7-15e: Psychrometric chart output at different half-cycle times and 50% fresh air at 10 °C, 5.06 g/kg(d.a.) inlet Temperature and specific humidity. .....154

Figure 7-16a: Room air temperature at different half-cycle times and 100% fresh air. .....155

Figure 7-16b: Room air relative humidity at different half-cycle times and 100% fresh air. 155

Figure 7-16c: Air temperature after DCHE at different half-cycle times and 100% fresh air. .....156

Figure 7-16d: Air relative humidity after DCHE at different half-cycle times and 100% fresh air. .....156

Figure 7-16e: Psychrometric chart output at different half-cycle times and 100% fresh air at 10 °C, 4.38 g/kg(d.a.) inlet Temperature and specific humidity. .....157

Figure 7-17: Effect of half-cycle time and mixing ratio on the COP of the desiccant air conditioning system. .....157

Figure 7-18: Coefficient of Performance (COP) versus airspeed for 2.5, 5, and 10-mins half-cycle times. ..... 158

Figure 7-19: Output air temperature vs. half-cycle time and output air specific humidity vs. half-cycle time. ..... 159

Figure 7-20: Air temperature change for a dynamic cycle for the desiccant air-conditioning system for heating. ..... 160

Figure 7-21: Air relative humidity change for a dynamic cycle for the desiccant air-conditioning system for heating. ..... 161

Figure 7-22: Air temperature variation with time in the desiccant air-conditioning system for heating at a water flow rate of 5ml/s. ..... 162

Figure 7-23: Air relative humidity variation with time in the desiccant air-conditioning system for heating at a water flow rate of 5ml/s. ..... 163

Figure 7-24: Psychrometric chart of the process in the desiccant air-conditioning system for heating at a water flow rate of 5ml/s at minute 40. ..... 163

Figure 7-25: Air temperature variation with time in the desiccant air-conditioning system for heating at a water flow rate of 10ml/s. ..... 164

Figure 7-26: Air relative humidity variation with time in the desiccant air-conditioning system for heating at a water flow rate of 10ml/s. ..... 165

Figure 7-27: Psychrometric chart of the process in the desiccant air-conditioning system for heating at a water flow rate of 10ml/s at minute 40. ..... 165

Figure 7-28: Air temperature variation with time in the desiccant air-conditioning system for heating at a water flow rate of 15ml/s. ..... 166

Figure 7-29: Air relative humidity variation with time in the desiccant air-conditioning system for heating at a water flow rate of 15ml/s. ..... 167

Figure 7-30: Psychrometric chart of the process in the desiccant air-conditioning system for heating at a water flow rate of 15ml/s at minute 40. ..... 167

Figure 7-31: Coefficient of Performance (COP) versus water flow rate for 5, 10, and 15ml/s. ..... 168

Figure 7-32: Air temperature variation with time in the desiccant air-conditioning system for heating at a water flow rate of 5ml/s. ..... 169

Figure 7-33: Air relative humidity variation with time in the desiccant air-conditioning system for heating at a water flow rate of 5ml/s. ..... 170

Figure 7-34: Psychrometric chart of the process in the desiccant air-conditioning system for heating at a water flow rate of 5ml/s at minute 40. .....170

Figure 7-35: Air temperature variation with time in the desiccant air-conditioning system for heating at a water flow rate of 10ml/s. .....171

Figure 7-36: Air relative humidity variation with time in the desiccant air-conditioning system for heating at a water flow rate of 10ml/s. .....172

Figure 7-37: Psychrometric chart of the process in the desiccant air-conditioning system for heating at a water flow rate of 10ml/s at minute 40. .....172

Figure 7-38: Air temperature variation with time in the desiccant air-conditioning system for heating at a water flow rate of 15ml/s. .....173

Figure 7-39: Air relative humidity variation with time in the desiccant air-conditioning system for heating at a water flow rate of 15ml/s. .....174

Figure 7-40: Psychrometric chart of the process in the desiccant air-conditioning system for heating at a water flow rate of 15ml/s at minute 40. .....174

Figure 7-41: Coefficient of Performance (COP) versus water flow rate for 5, 10, and 15ml/s. .....175

Figure 7-42: Desiccant cooling system with temperature and humidity Sensors positions. 176

Figure 7-43: Air temperature variation with time in the desiccant air-conditioning system for cooling at water inlet temperature of 18°C and half-cycle time 10mins. .....177

Figure 7-44: Air humidity variation with time in the desiccant air-conditioning system for cooling at water inlet temperature of 18°C and half-cycle time 10mins. .....178

Figure 7-45: Air temperature variation with time in the desiccant air-conditioning system for cooling at water inlet temperature of 18°C and half-cycle time 5mins. .....179

Figure 7-46: Air humidity variation with time in the desiccant air-conditioning system for cooling at water inlet temperature of 18°C and half-cycle time 5mins. .....180

Figure 7-47: Air temperature variation with time in the desiccant air-conditioning system for cooling at water inlet temperature of 18°C and half-cycle time 2.5mins. .....181

Figure 7-48: Air humidity variation with time in the desiccant air-conditioning system for cooling at water inlet temperature of 18°C and half-cycle time 2.5mins. .....182

Figure 7-49: Psychrometric chart for the room conditions change at a water inlet temperature for the heat exchanger of 18°C and different half-cycle time .....183

Figure 7-50: Air temperature variation with time in the desiccant air-conditioning system for cooling at water inlet temperature of 21°C and half-cycle time 10mins. .....184

Figure 7-51: Air humidity variation with time in the desiccant air-conditioning system for cooling at water inlet temperature of 21°C and half-cycle time 10mins. .....185

Figure 7-52: Air temperature variation with time in the desiccant air-conditioning system for cooling at water inlet temperature of 21°C and half-cycle time 5mins. .....186

Figure 7-53: Air humidity variation with time in the desiccant air-conditioning system for cooling at water inlet temperature of 21°C and half-cycle time 5mins. .....187

Figure 7-54: Air temperature variation with time in the desiccant air-conditioning system for cooling at water inlet temperature of 21°C and half-cycle time 2.5mins. .....188

Figure 7-55: Air humidity variation with time in the desiccant air-conditioning system for cooling at water inlet temperature of 21°C and half-cycle time 2.5mins. .....189

Figure 7-56: COP for the desiccant air-conditioning system for cooling at a water inlet temperature of 21°C and 18°C at different half-cycle time s 2.5, 5, and 10mins. .....190

Figure 7-57: Psychrometric chart of the room conditions at a water inlet temperature to the heat exchanger of 21°C at different half-cycle times. .....191

## List of tables

Table 3-1 Physical channel dimensions and operating conditions for process air. .....38

Table 3-2 Thermophysical properties of silica gel and Aluminium fumarate MOF material. .38

Table 3-3 Model results for both regeneration and dehumidification processes. .....40

Table 3-4 Weight of honeycomb structure before and after coating. .....42

Table 3-5 Accuracy, range, and standard uncertainty of measuring instruments. .....44

Table 4-1 The parameters of the used MOFs .....62

Table 4-2 The performance parameters of the MOF-303/G coated wire-finned tube. .....68

Table 4-3 Accuracy, range, and standard uncertainty of measuring instruments. .....70

Table 4-4 Summary of the effect of changing the DCHE surface temperature desorption/ adsorption process versus the water uptake. .....76

Table 4-5 intended design in comparison to previously published designs. .....77

Table 5-1 Thermophysical parameters [27-28]. .....81

Table 5-2 mesh sensitivity analysis. .....85

Table 5-3 Effect of Desorption time and power input on the daily water adsorbed and power consumption. ..... 94

Table 5-4 Input parameters to the greenhouse climate control system. ..... 99

Table 5-5 Evaporative cooler model validation. ..... 100

## Abbreviations

| | |
|---|---|
| Dehumidification coefficient of performance | DCOP |
| Desiccant-coated heat exchangers | DCHEs |
| Desiccant-coated fin tube heat exchanger | DCFTHX |
| Desiccant Wheel | DW |
| Dynamic vapour sorption | DVS |
| Evaporative Coolers | ECs |
| Heating, Ventilation, and Air Conditioning | HVAC |
| Heat recovery device | HRD |
| International Union of Pure and Applied Chemistry | IUPAC |
| Metal-organic frameworks | MOFs |
| Moisture removal capacity | MRC |
| Solar desiccant-enhanced radiative Cooling | SDERC |
| Thermal coefficient of performance | $COP_{th}$ |
| vapour-compression | VC |

## Nomenclature

$A_f$ frontal area of the DEP [$m^2$]

a channel height [m]

b channel pitch [m]

ap input width of plates for evaorator[m]

At total heat exchanger area [$m^2$]

$D_{va}$ diffusion coefficient of vapour in air [$m^2/s$]

$D_h$ hydraulic diameter [m]

D distance between plates[m]

$h_T$ heat transfer coefficients [$W\ m^{-1}\ K^{-1}$]

$h_m$ mass transfer coefficients [$W\ m^{-1}\ K^{-1}$]

$K_a$ thermal conductivity of air [$W\ m^{-1}\ K^{-1}$]

L input length of plates for evaporator [m]

Lw desiccant width. [m]

$\dot{m}_a$ air mass flow rate [kg/s]

$\dot{m}_w$ water evaporation rate[ kg/s]

Nu nusselt number

n input no. of plates for evaporator

U mean velocity [m/s]

u facial air velocity [m/s]

V velocity of primary air at inlet [m/s]

P Pressure [Pa]

$\dot{Q}_L$ latent heating rate [W]

$\dot{Q}_S$ sensible heating rate [W]

RHd relative humidity [%]

$C_{pv}$ specific heat of water vapours [$J\ kg^{-1}\ K^{-1}$]

$C_{pa}$ specific heat of air [$J\ kg^{-1}\ K^{-1}$]

Sh sherwood number

t input thickness of plates [mm]

## Greek Symbols

$\rho_a$ air density[$kg/m^2$]

$\beta$ density area

$\upsilon_a$ kinetic viscosity of air [$m^2\ s^{-1}$]

$\delta$ input channel width [m]

# Chapter 1 Introduction

## 1.1. Background

In an era of rising global temperatures and increasingly extreme weather events, the need for effective cooling/heating solutions for space climate control has never been more pressing [1]. As we approach 2024, the demand for cooling is projected to skyrocket, driven by several factors. The world's urban population is expected to reach 6.8 billion by 2025, with cities becoming increasingly dense and heat-trapped [2]. This urban heat island effect and rising ambient temperatures will create an unprecedented demand for cooling in urban areas [3]. Global warming leads to more frequent and intense heat waves, exacerbating the need for cooling systems to maintain thermal comfort and protect human health [4]. The proliferation of data centres, fuelled by the growth of cloud computing, artificial intelligence, and cryptocurrency mining, drives the demand for energy-efficient cooling solutions to manage the heat generated by these massive computing facilities [5]. The cooling demand has increased significantly and is expected to exceed the demand for heating in 2050. Energy use for space cooling, almost entirely in the form of electricity, is expanding rapidly in absolute terms and as a share of overall energy use in buildings, as shown in Figure 1-1.

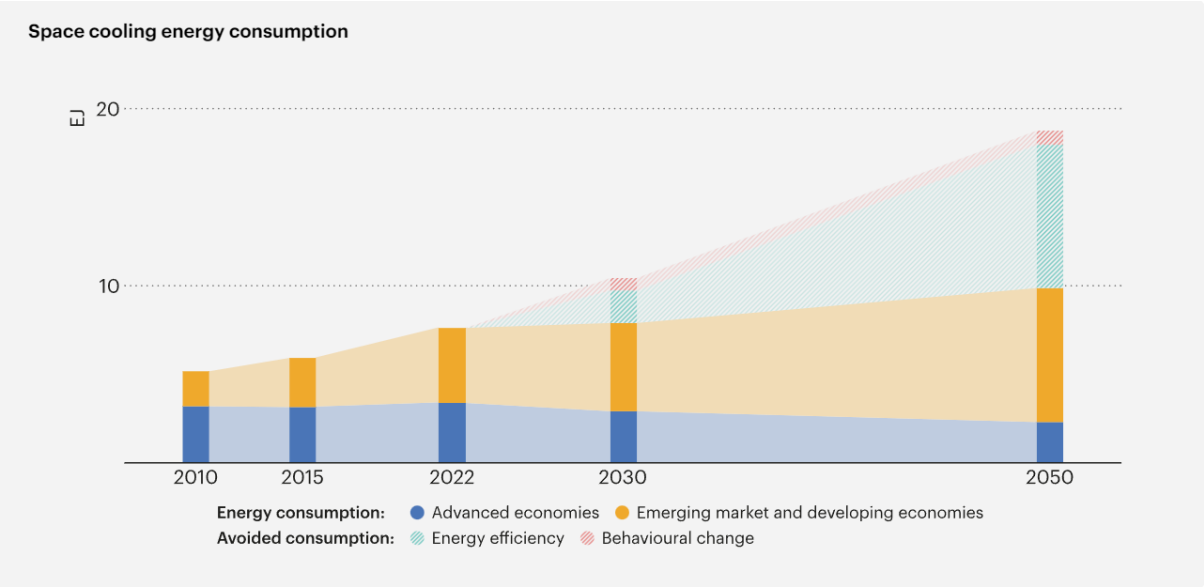



*Figure 1-1: Energy use for space cooling* [6].

Currently, most cooling systems are based on the electrically driven vapour compression refrigeration systems (see Figure 1-2), which utilises refrigerants with high global warming potential, suffer from high electricity consumption and are expensive. Air conditioners (AC) contribute to greenhouse gases emissions into the atmosphere, leading to climate change [7]. Also, AC systems can lead to health problems if not cleaned and maintained correctly [8].

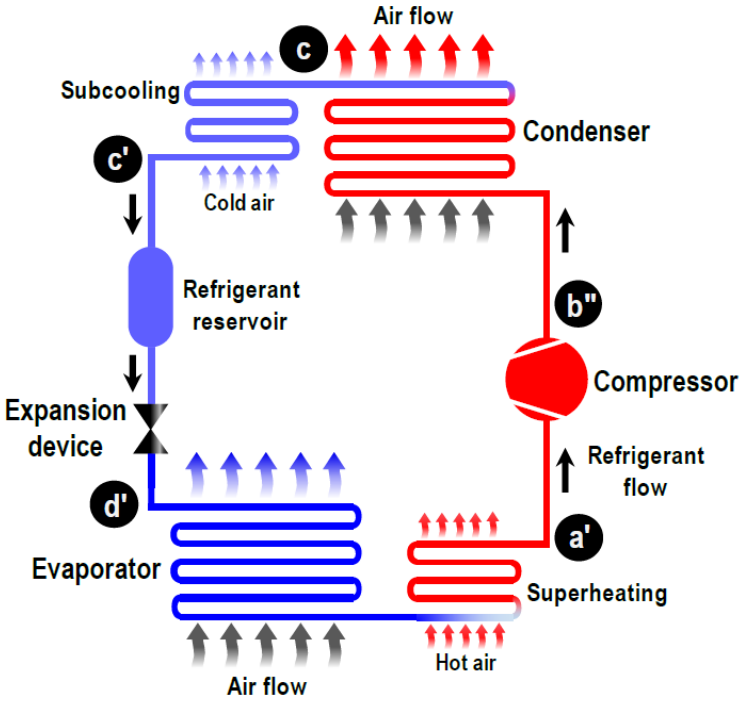



*Figure 1-2: How vapour compression works* [9].

Due to the implementation of zero-carbon-ready building energy codes and the development of more energy-efficient equipment, the energy consumption of space heating in buildings will decrease by nearly 70% by 2050, despite a 30% increase in the surface area of heated floors, as shown in Figure 1-3.

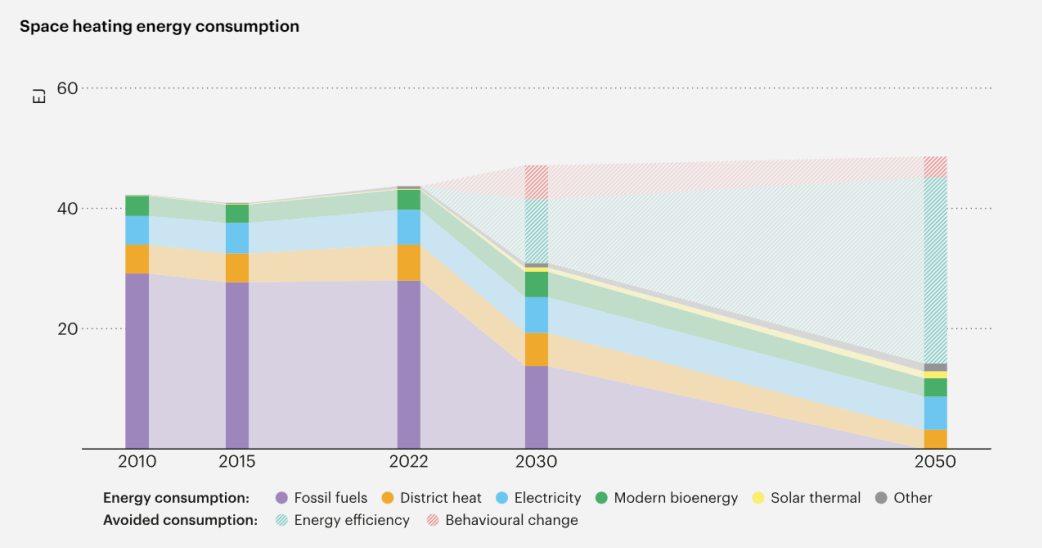



*Figure 1-3: Energy use for space heating* [6].

Adsorption is a surface phenomenon characterised by the physical adhesion of molecules to the surface of another phase, primarily through the Van der Waals force [10], [11], [12]. This adsorption phenomena is temperature dependent thus used in adsorption cooling and heat

pump systems. They have the advantage of using low-grade waste heat, solar, and geothermal energy, they are environmentally friendly, they use natural refrigerants like ammonia, water, and methanol, and they are noise and vibration-free [13]. Adsorption cooling systems can be classified as closed or open systems. The closed circuits include an evaporator, condenser, and thermal compressor (adsorber beds).

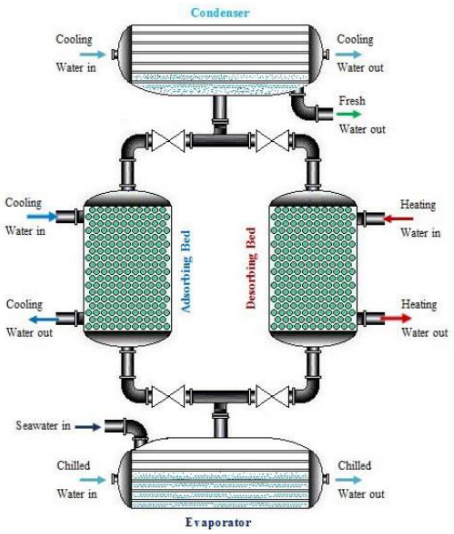



*Figure 1-4: Schematic of a conventional double-bed adsorption desalination system* [11].

In an open adsorption cycle, also known as a desiccant system, the working fluid is air, thus the system controls the exhaust air temperature and moisture content so the required comfort conditions in the living space can be achieved.

Desiccant systems are acknowledged for their energy efficiency and environmental advantages, especially in situations that independently require humidity control and cooling or heating. Solid desiccant systems are effective at dehumidifying air and releasing heat during adsorption, making them ideal for regions requiring moisture control and heating [14]. Moreover, these systems can use low-quality thermal energy sources for regeneration, including waste heat or solar thermal energy, leading to less dependence on fossil fuels and decrease greenhouse gas emissions. Research indicates that solid desiccant heating systems can lower energy usage by 20-50% in some scenarios [15]. When combined with renewable energy sources, they can also reduce the carbon footprint of heating and ventilation systems by 30-60% compared to traditional systems [16]. Solid desiccant systems' high efficiency and sustainability demonstrate their promise in promoting sustainable heating solutions, as evidenced by scientific publications [17].

Evaporative cooling is a cost-effective technology that can supply cold air and consumes much less power than the vapour compression refrigeration system. Evaporative cooling is a method of cooling air by spraying water into it, as seen in Figure 1-5. As the water evaporates,

it absorbs heat from the surrounding air, causing it to cool. Evaporative cooling is a more sustainable and energy-efficient way to cool buildings than traditional air conditioning, as it does not use environmentally harmful refrigerants.

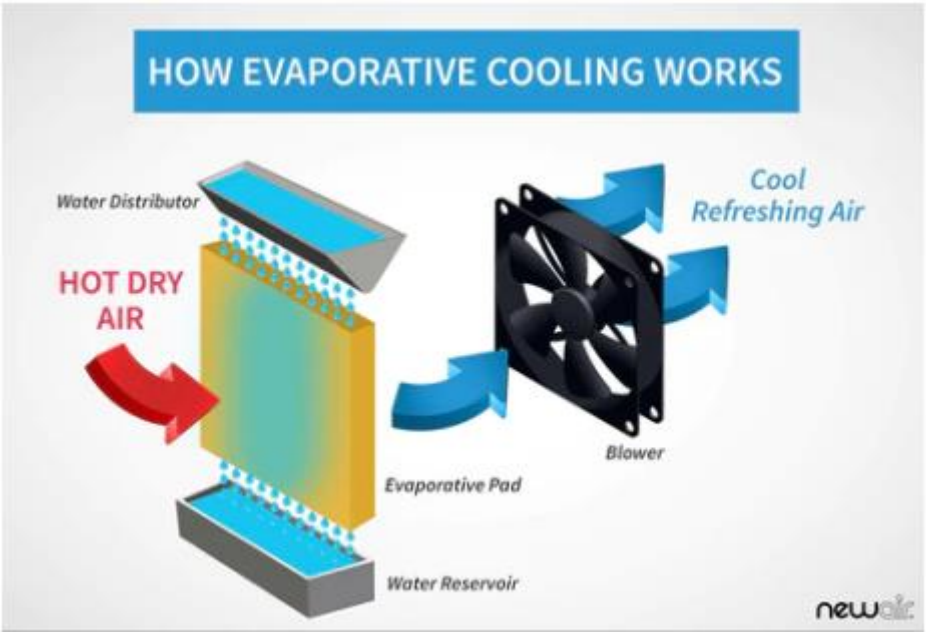



Figure 1-5: *How evaporative cooler works* [18].

Evaporative cooling has significant advantages; typically, it uses less than 25% of the electricity consumed by conventional air conditioning, uses no refrigerants, supplies 100% fresh cool air, has a low carbon dioxide footprint with simple engineering, and can significantly reduce the temperature on hot days [1]. However, the main disadvantage of evaporative cooling is that it is only applicable in dry atmospheres. It is ineffective in areas with high ambient humidity [2]. Integrating a desiccant-coated heat exchanger (DCHE) with the evaporative cooler is a promising method for reducing air humidity before entering the evaporative cooler. Currently, desiccant systems utilise silica gel as the adsorbent material on the desiccant heat exchanger, which has limited water uptake, thus reducing the system's performance. There is limited literature on using MOFs in desiccant cooling and heating systems. Therefore, the novelty of this investigation is experimental and theoretical. Metal-organic frameworks (MOFs) are mesoporous materials with exceptionally high porosity, large surface area (up to 5500$m^2$/g) and superior water uptake capacity compared to silica gel and other conventional materials [19].

## 1.2. Aims and objectives

This research aims to develop an efficient desiccant air conditioning system using advanced metal-organic framework (MOF) adsorbent materials while precisely controlling the air's

relative humidity and temperature independently. This aim will be achieved through the following objectives:

- Identify the best MOF materials suitable for this application through a comprehensive literature review and experimental investigation of available MOFs, their adsorption characteristics and thermophysical properties.
- Identify the best heat exchanger for holding the selected MOF material in terms of surface area, compactness, and thermal conductivity.
- Develop advanced computational fluid dynamics (CFD) model for identified MOF-coated heat exchangers. This model should simulate the heat and mass transfer process between the MOF material and the air and the heat transfer between the MOF material and the metal heat exchanger.
- Develop an energy-efficient MOF-303/G coated wire-finned heat exchanger and experimentally characterise its heating power and water removal rate performance.
- Develop an experimental test facility to evaluate the performance of the developed MOF-303/G desiccant-coated heat exchanger (DCHE) and validate its developed CFD model at various operating conditions.
- Use the developed MOF-303/G DCHE to construct the desiccant air conditioning system consisting of an array of DCHEs, a direct evaporative cooler, an air-to-water heat exchanger, ducting and an automatic control system. Carry out performance testing to prove the system capability to achieve the target temperature and humidity.

## 1.3. Thesis outlines

This thesis is provided in 8 chapters, Figure 1-6. The literature review of the adsorption systems, principles of adsorption, adsorption materials, adsorption heat exchangers, the heating and cooling sources of the DCHE, performance progress in different DCHEs, effect of evaporative cooler and their contribution to the desiccant systems, desiccant system configurations, experimental and numerical parameters to improve the DCHE performance were described in Chapter two. The modelling of DCHE for different MOF materials and its experimental validation are described in Chapter Three. The development of electrically heated DCHE coated with MOF-303/G was discussed in Chapter Four. Chapter Five includes a Case study for DCHE coated with MOF-303/G to control the greenhouse's climate using mathematical modelling and experimental validation (COMSOL and MATLAB). Based on Chapters Three, Four, and Five results, MOF-303/G was chosen and integrated with the developed DCHE and experimentally tested in two beds of desiccant air conditioning system in Chapter 6. The results are discussed in Chapter Seven. Finally, a summary of the main point

discussed in each chapter and recommendations for future work are presented in Chapter Eight.

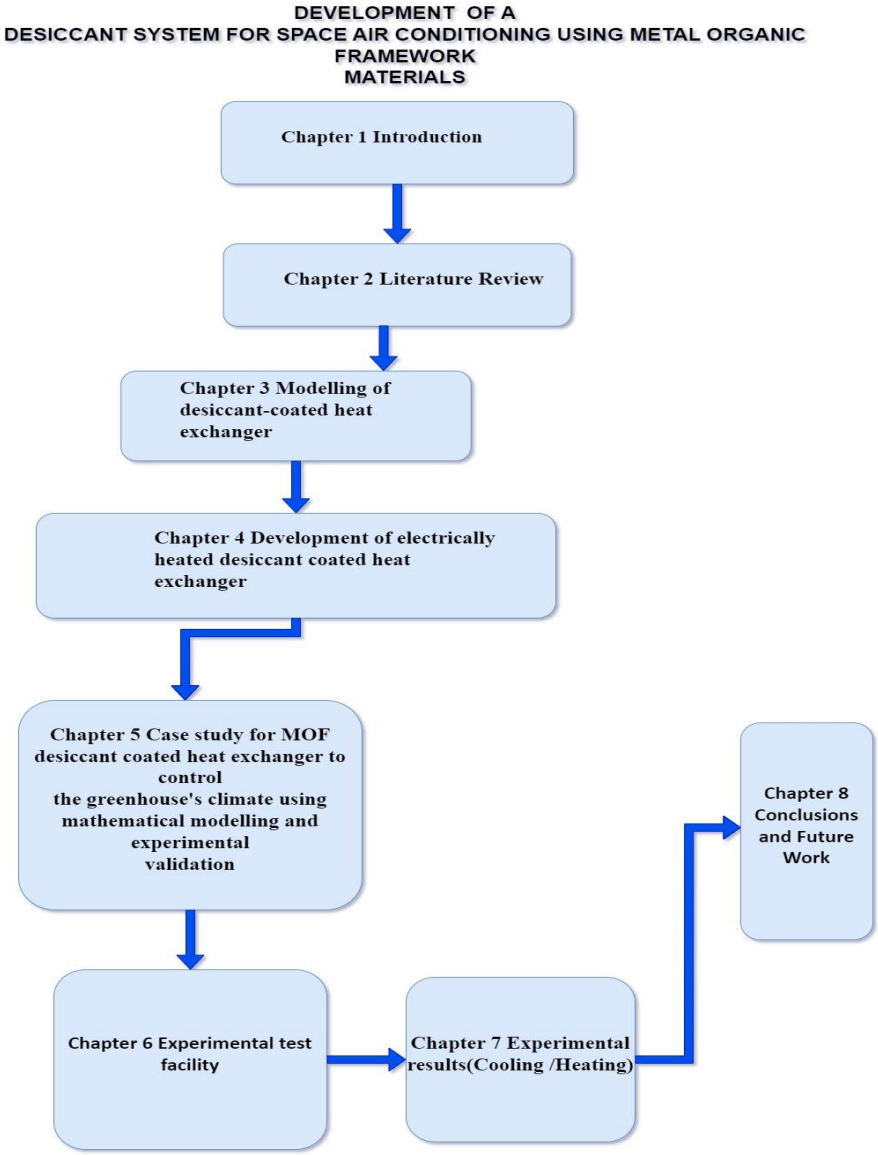



*Figure 1-6: Thesis outline diagram.*

# Chapter 2 Literature Review

This chapter reviews the conventional climate control methods highlighting their advantages and disadvantages. Then, the chapter reviews the literature on adsorption systems including, the principles of the adsorption process, and the most common adsorbents used for climate control. As the performance of the adsorption system depends mainly on the adsorbent material capacity, a new class of materials, known as metal-organic frameworks, that have significantly high adsorption capacity is comprehensively reviewed. The review also covers coating techniques that enhance the adsorption system heat and mass transfer rates and the methods of heating and cooling the adsorber bed. Different configurations for the desiccant system are also reviewed. Figure 2-1 illustrates the areas reviewed in this chapter.

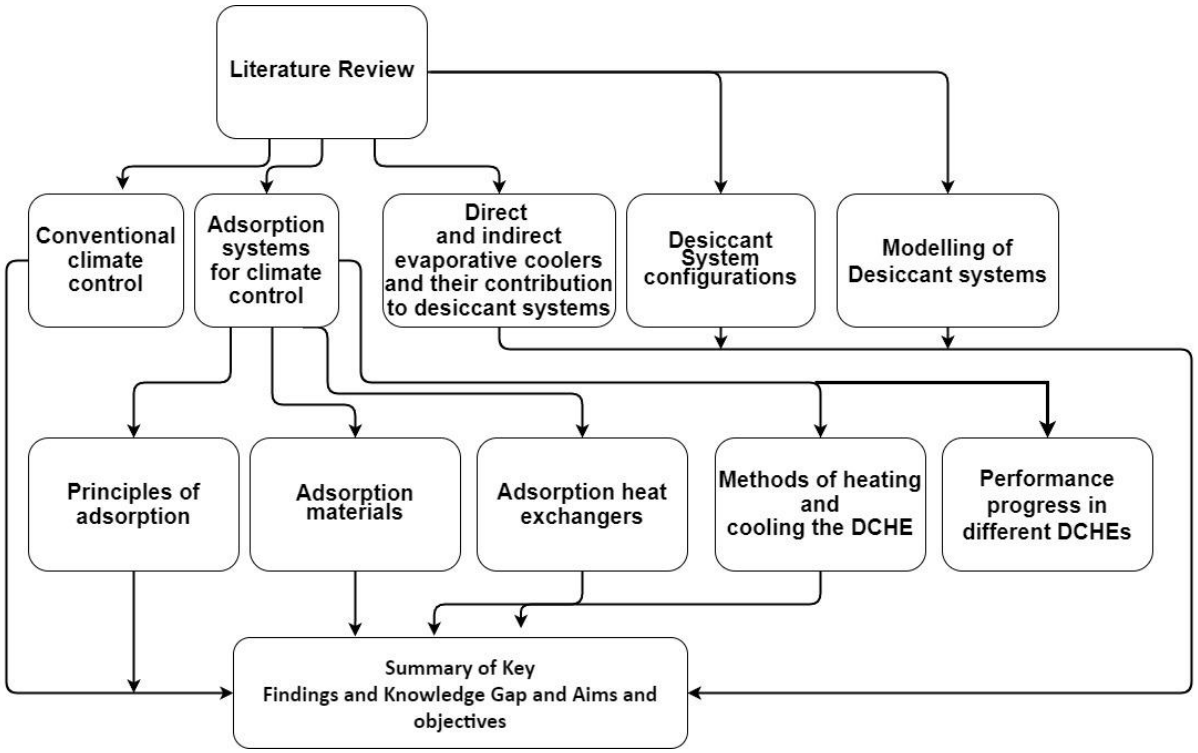



*Figure 2-1: Chapter 2 flow diagram.*

## 2.1.Conventional climate control methods

ASHRAE guidelines state that indoor comfort conditions are a temperature range of 25-28°C, relative humidity 50-60% and a humidity ratio of 0.012 kg/kg. These conditions may vary based on factors such as airspeed and the thermal insulation of clothing in the area. Nevertheless, a greater velocity can potentially elevate the indoor comfort temperature. Consequently, all air conditioning engineers are tasked with designing systems that meet these conditions [20], [21] as shown in Figure 2-2.

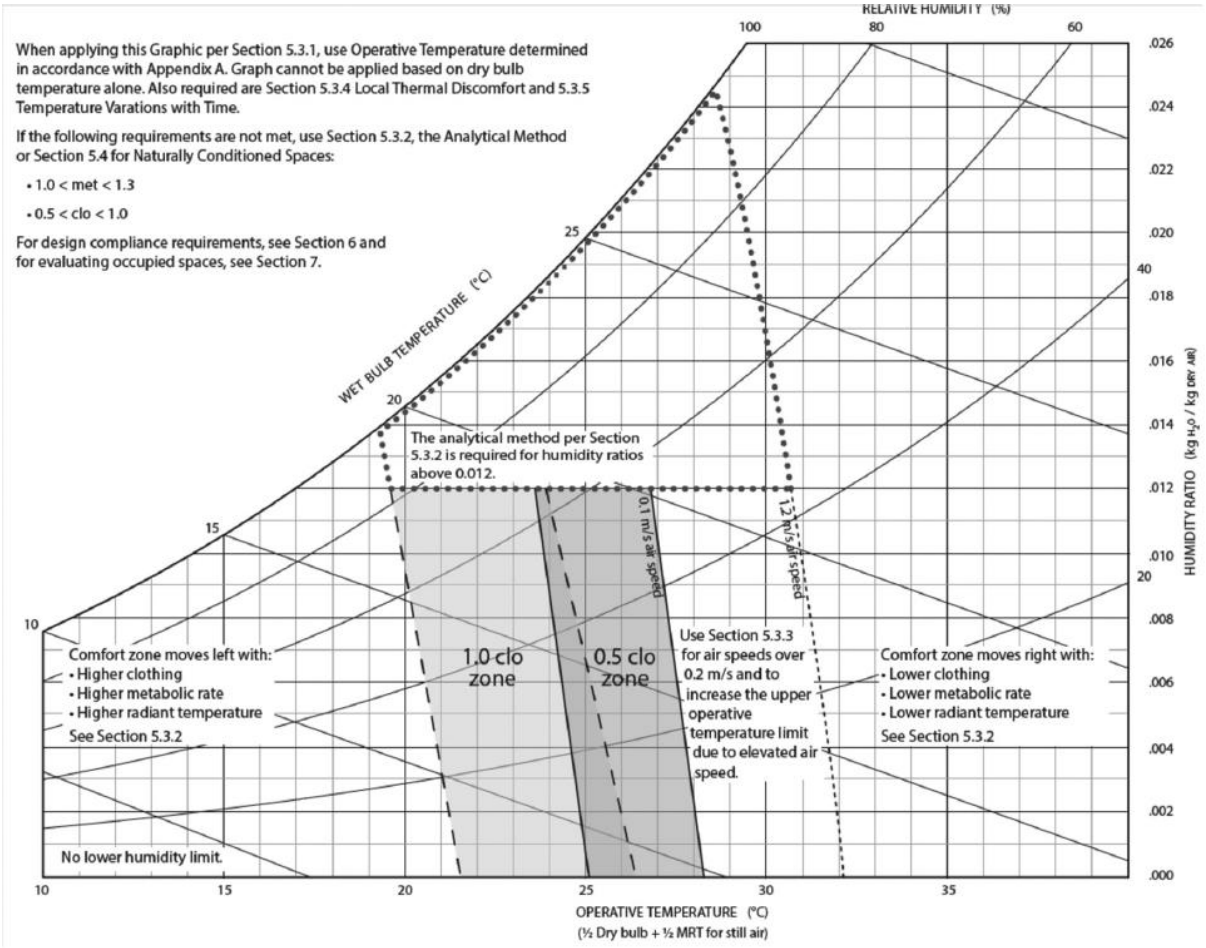



*Figure 2-2: Operative temperature and humidity ratio of indoor comfort Condition* [20].

In order to get optimal indoor comfort, it is necessary to implement climate control measures. Methods that regulate and maintain optimum temperatures, humidity levels, and indoor air quality, ensuring comfort, health, and productivity. **1.0 clo zone** is the thermal insulation value that maintains a person at a comfortable temperature in typical indoor conditions (around 21°C or 70°F), typically equivalent to wearing a business suit. **0.5 clo zone** would represent a lower level of insulation, indicating lighter clothing, which would be more suitable for warmer environments.

Traditional techniques for temperature regulation include Heating, Ventilation, and Air Conditioning (HVAC) Systems, which are frequently implemented to regulate indoor temperature and humidity. Typical heating systems consist of furnaces or boilers, while air conditioning uses refrigerants to cool the air. Ventilation maintains indoor air quality by facilitating the flow of fresh outdoor air [22]. Humidifiers and Dehumidifiers regulate humidity levels by adding moisture to the air when it is dry or removing extra moisture from the air when it is humid.

The research and development of adsorption systems for application in hot and humid climates have demonstrated promising outcomes compared to conventional climate control

systems. Adsorption systems utilizing solar energy of waste heat are an environmentally friendly alternative to traditional mechanical vapour compression (MVC) systems [23]. Unlike traditional MVC systems that condense moisture, the adsorption system uses sorbent to remove air moisture. Sensible cooling through the desiccant systems is achieved through cooling towers, evaporative coolers, and absorption chillers. Compared to MVC, desiccant air coolers are much better in cost, carbon emissions, and energy efficiency [24]. Baniyounes et al. [25] created solar rotary desiccant wheel air conditioners for educational buildings, showing 17.8% less annual power consumption than MVC refrigeration systems. Speerforck and Schmitz [26] created a desiccant air conditioner combined with solar collectors. Significantly reducing electricity consumption rates, with savings of up to 70% compared to traditional MVC systems.

## 2.2.Adsorption systems for climate control

The application of the adsorption process in air conditioning systems is usually performed using rotary desiccant, as illustrated in Figure 2-3. The desiccant wheel acts as a dehumidifier to reduce air moisture content.

In a dehumidifier, moisture is removed from airflow by transferring it to absorbent desiccants inside the unit. This process occurs because of differences in vapour pressure between the airstream and the surface of the desiccant. As water is absorbed, heat is released, causing an increase in the temperature of the material. Some of this heat is transferred to the passing air, leading to a rise in temperature at the dehumidifier outlet. When desiccant particles become fully saturated with water, they need to be regenerated. Typically, regeneration involves passing them through an airstream that absorbs heat from them, subsequently cooling down as it releases energy back into its surroundings.

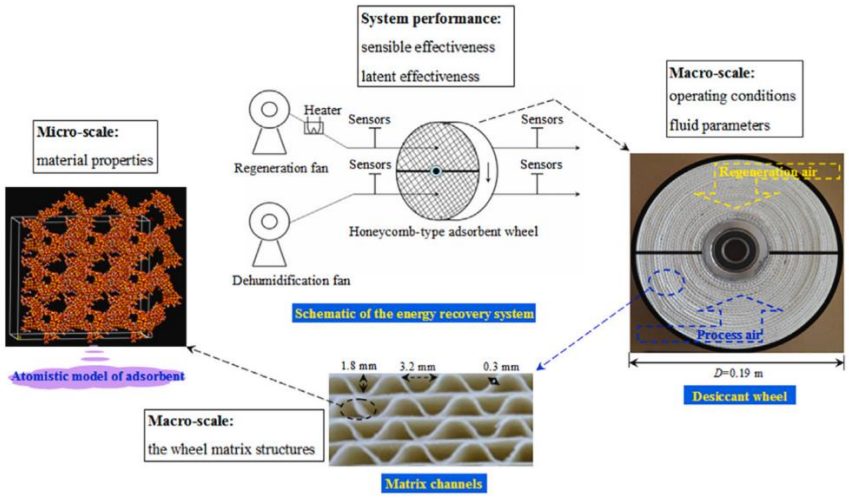



*Figure 2-3: A typical configuration of a rotary desiccant wheel, illustrating the small-scale adsorbents and large-scale system components* [27].

In Figure 2-4, The hybrid adsorption dehumidification system presents notable benefits compared to MVC systems. In an MVC system, dehumidifying air involves condensing water vapour into liquid form, necessitating multiple cycles of chilling and warming. Otherwise, a desiccant dehumidifier can be installed before the cooling coil to remove moisture at a higher temperature, thus preventing the temperature from dropping to the dew point. This technique only marginally elevates the air temperature but can be modified to get the desired temperature for a conditioned environment. In contrast to a standard MVC system, a hybrid system eliminates the requirement for repetitive chilling and reheating, enhancing the overall energy efficiency. Nevertheless, it is crucial to minimise the energy consumption during the regeneration process of wet desiccant particles to attain a high COP.

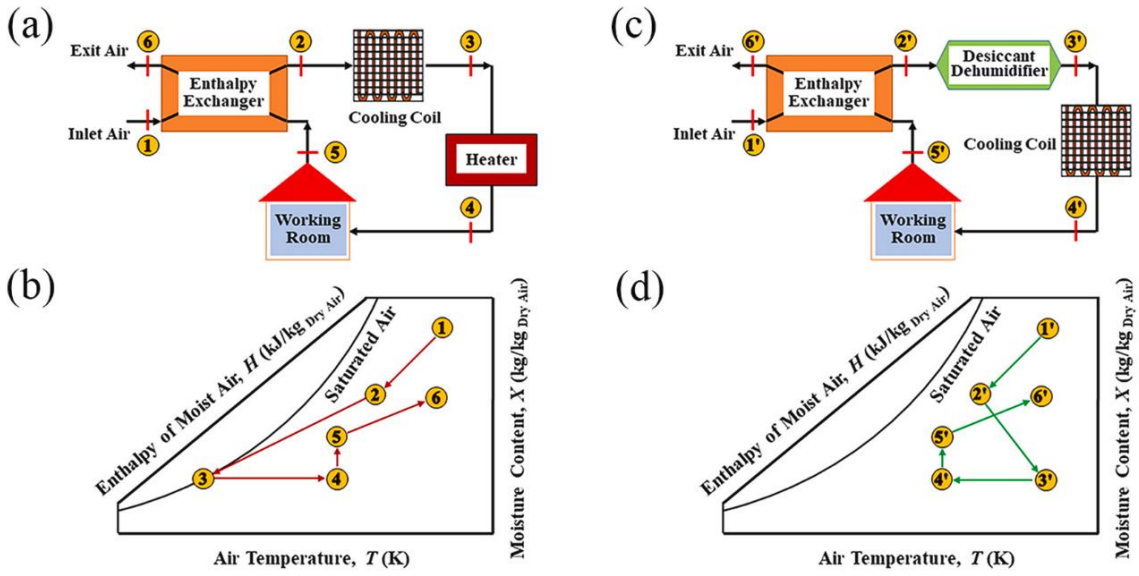



*Figure 2-4: Schematic diagram showing the difference between traditional and hybrid air-conditioning systems and their psychometric process: (a) Conventional HVAC system, (b) Conventional HVAC psychometric process, (c) Hybrid air-conditioning desiccant system and (d) Hybrid air-conditioning desiccant system psychometric process* [28].

### 2.2.1. Principles of adsorption

The origins of adsorption can be traced back to ancient civilisations, which employed substances such as charcoal to effectively cleanse and purify water by removing contaminants. Nonetheless, the theoretical examination of adsorption commenced during the latter part of the 19th century with groundbreaking research conducted by scientists like Ostwald (1891), Mühlfarth (1900) and Patten (1907) [29].

Adsorption is the process of accumulating a substance (adsorbate or sorbate) on the surface of a solid (adsorbent or sorbent). The adsorbate may exist in either a gaseous or liquid state.

The primary driving factor for adsorption is the presence of unsaturated forces on the solid surface, which can form bonds with the adsorbate. The forces involved in these interactions are usually electrostatic or van der Waals forces, which are reversible. More powerful interactions occur when there is a direct exchange of electrons between the substance being adsorbed and the substance adsorbing; this exchange is irreversible. The intensity of this interaction determines the degree of ease or difficulty in removing (desorbing) the adsorbate to regenerate the adsorbent and recover the adsorbate. The adsorbent's selectivity is mainly determined by the relative accessibility and strength of the surface contact for one component in a mixture of substances. The solid serves as the agent for separating masses, while the partitioning between the fluid and solid phases acts as the mechanism for separation. A sorbent is regenerated using an energy-separating agent, such as a change in pressure or temperature, to reverse the process [30].

Porous materials are categorised into macroporous, mesoporous, or microporous based on the International Union of Pure and Applied Chemistry (IUPAC) classification. Microporous materials have pores with an interior diameter smaller than 2 nm. A material with 2 to 50 nm pores would be classified as mesoporous. Macroporous materials are characterised by pores with a diameter greater than 50 nm. When gas molecules adhere to the surface, they transition from gaseous to liquid states. The time that the molecules remain in this adsorptive state, without being released, relies mainly on the contact forces between the surface of the material and the gas being adsorbed [31], [32].

Adsorption can be classified into two categories: physisorption, which refers to physical sorption, and chemisorption, which refers to chemical sorption. Physical adsorption involves bonding the adsorbate (gas being adsorbed) and the adsorbent (solid material with pores) through Van der Waals interactions, forming several adsorbate layers. Consequently, applying a specific quantity of energy can facilitate the conversion of the trapped molecules back into their initial gaseous state. In contrast, chemisorption is distinguished by the formation of significantly stronger chemical bonds between the adsorbed gas and the adsorbent material [33].

The IUPAC classifies adsorption isotherms presenting the water uptake versus relative pressures into six main types based on their shape see Figure 2-5, offering insights into the nature of the adsorption process and the adsorbent-adsorbate interaction [34]. Type I: The observed isotherm demonstrates a distinct increase in value at low pressures, followed by a plateau at high pressures. This characteristic suggests the presence of microporous adsorbents, which possess relatively small pores compared to the adsorbate molecules. Small-pored zeolites and activated carbon are two such examples [34], [35]. Type

II: Characterised by a smooth rise from low to high pressures without a plateau, this type signifies non-porous or macro-porous adsorbents with unrestricted monolayer-multilayer adsorption. Silica gel and alumina powders are common examples [36]. Type III: A continuous increase with a convex shape throughout the isotherm suggests non-porous or macroporous adsorbents with weak adsorbate-adsorbent interaction. Some polymers and oxides with low surface energy fall under this category [37]. Type IV: This isotherm displays a distinct hysteresis loop between adsorption and desorption branches, an S-shaped curve and a plateau at intermediate pressures. It is representative of mesoporous adsorbents where capillary condensation within pores occurs. Many mesoporous silicas, clays, and activated carbons exhibit this type [34], [35]. Type V: Similar to Type IV but with less pronounced hysteresis and no apparent plateau, this type implies mesoporous adsorbents with weak interaction and capillary condensation. Some silica gels and porous carbons show this behaviour [36]. Type VI: Rarely observed, this type features a stepwise increase with distinct plateaus, reflecting layer-by-layer adsorption on well-defined, uniform surfaces. Graphite is one example [34], [35].

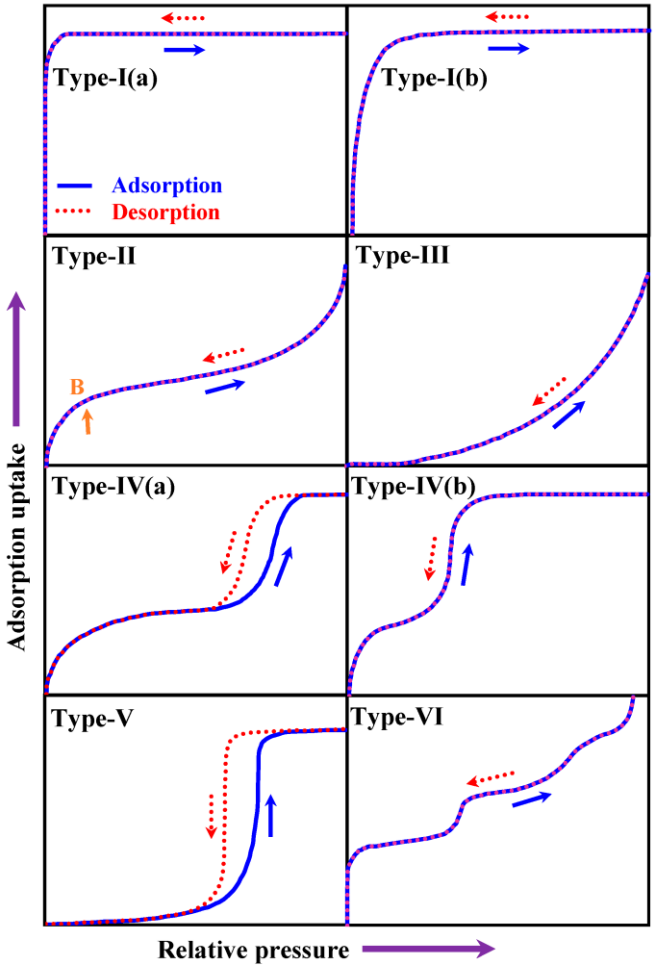



*Figure 2-5: Types of adsorption isotherms* [38].

### 2.2.2. Adsorption materials

A critical factor controlling the performance of the adsorption systems is selecting a desiccant material compatible with the application. Three primary considerations must be considered when choosing the desiccant material: (1) The capacity of desiccant materials to absorb water vapour. (2) The desiccant material needs to be regenerated at low temperatures. The kinetics of the chosen desiccant material influence the performance of the desiccant air conditioner [39].

Silica gel is the adsorbent material most frequently employed in various adsorption applications [31]. Silica gel possesses numerous benefits, including a broad temperature range for desorption, widespread availability, consistent performance, hydrophilic characteristics, and non-toxic nature [40]. However, Adsorption and desorption processes that are repeated continuously in adsorption refrigeration systems will significantly reduce the silica gel's capacity to adsorb water [41]. Silica gel is available in various pore diameters, with a corresponding drop in surface area per unit mass as the pore size increases. The surface area of 650 $m^2/g$ was achieved at a pore size of 2-3 nm (type A). For relative humidity above 50%, Silica gel type B with a pore size of 0.7 nm and adsorption heat of 2800 kJ/kg was utilised [42], [43].

Activated carbon is a highly porous carbon material with a significant adsorption capacity. It is commonly employed as an adsorbent to purify liquids and gases and as a catalyst and catalyst support. Various types of biomass, including coconut shells, walnut shells, almond shells, pistachio shells, oil palm shells, cherry stones, coffee endocarp, and chickpea husks, are utilised to manufacture activated carbon [44]. Activated carbon in powder form, with particles ranging from 15 to 25 mm, is utilised for liquid adsorption. Granulated activated carbon, consisting of sieved granules measuring 4 to 20 mesh or approximately 3 mm to 0.8 mm in diameter, and pellet forms, which are extruded pellets measuring 4 to 6 mm in length, are used for air purification and gas separation. Microporous activated carbon can selectively separate nitrogen and oxygen in air due to its molecular sieving properties. Activated carbon fibres, with a diameter ranging from 7 to 15 mm, are produced by carbonising synthetic fibres. These fibres are available in mats, cloths, and fibre chips and are utilised to purify air and water [42], [45]. The wasted impregnated carbon was catalytically regenerated by subjecting it to a temperature of 270°C in flowing air. This process restored nearly all of its original adsorption capacity [46]. Shimooka et al. [47] conducted experiments to enhance the adsorption capacity of activated carbon through various treatments. Their findings demonstrated that oxidised activated carbon exhibited an adsorption capacity ranging from 1.2 to 1.9 times that of silica gel.

Zeolites, which are aluminosilicate minerals, including crystalline zeolites and molecular sieves, occur naturally. A wide range of synthetic zeolites has been created for specific purposes. For instance, the Linde Co., U.S.A. has created molecular sieves of several varieties, including 4A, 5A, 10X, and 13X. The cavity volumes of these compounds range from 0.05 to 0.30 $cm^3\ g^{-1}$. Nevertheless, it is possible to subject them to temperatures of approximately 500°C without causing any damage to their adsorption and regeneration characteristics. Type 4A, also known as NaA by different producers, is utilised to dehydrate and isolate hydrocarbon mixtures. Type 5A (or $C_aA$) separates paraffin and certain cyclic hydrocarbons, while type 10X (or $C_aX$) and 13X (or $N_aX$) adsorb a wide spectrum of adsorbates due to their wider inlet necks [33], [42].

Activated (or porous) alumina is produced by removing the hydroxyl groups from aluminium hydroxide. It has a surface area that varies from 150 to 500 $m^2/g$, with pore diameters ranging from 1.5 to 6 nm. It also has an adsorption heat of 3000 kJ/kg, as reported by Srivastava and Eames [42] and Sultan et al. [43]. 110°C temperature is needed to regenerate the Activated alumina [48].

Extensive research has been conducted on composite desiccants due to their properties that closely resemble those of type I (b) material see Figure2-6, which exhibits optimal adsorption capacity and can be regenerated at low temperatures. Composite desiccant materials utilise porous matrix materials that incorporate a secondary element to enhance their water adsorption capabilities. An illustrative instance is using hygroscopic salts on silica gel or carbon matrices, such as lithium chloride (LiCl) and bromide (LiBr). During adsorption, salts with hygroscopic properties undergo a lyolysis process, and the air movement pulls salt particles into the airstream being supplied. By utilising a matrix material, the degraded salts are prevented from being carried away by the airflow and are contained within the host matrix. However, the intense attraction between the salts and the water vapour particles enhances moisture absorption [49]. Hu et al. [50] created desiccants using composite silica gel by saturating them with solutions of LiCl and $CaCl_2$. Their research showed that both composite desiccants exhibited a 30-45% improvement in sorption capacity. The LiCl-impregnated silica gels exhibited higher water absorption capacities than composite desiccants based on $CaCl_2$. Tu et al. [51] determined that salt in the porous matrix enhances both the capacity for absorption and the speed of sorption while facilitating capillary condensation. However, the overuse of highly absorbent materials leads to the spill-over issue. In order to avoid overflow and ensure a consistent application of desiccants on the metal surface, it is necessary to appropriately restrict the amount of salt present [51]. Jia et al. [52] conducted an empirical study comparing two types of desiccant wheels: one with silica gel and the other with a combination of lithium chloride (LiCl) and silica gel. The results demonstrated that the

composite material had an adsorption capacity one to two times higher than silica gel, as depicted in Figure 2-6. Additionally, the second wheel could be reactivated at a lower temperature while maintaining the same moisture level.

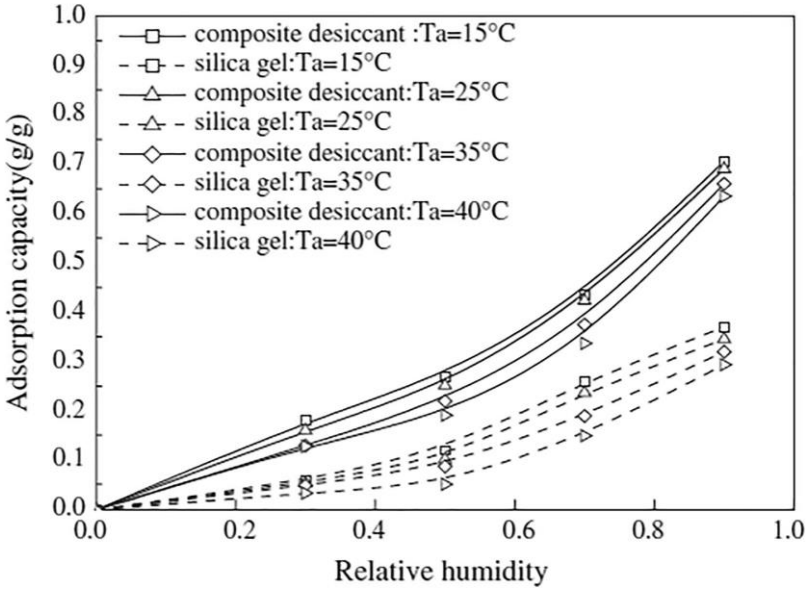



Figure 2-6: *The equilibrium adsorption curves for composite desiccant and silica gel* [52].

Liu et al. [53] performed an empirical study on the behaviour of a novel composite sorbent called $SiO_2.xH_2O.yCaCl_2$. This sorbent combines calcium chloride ($CaCl_2$) and silica gel. The researchers compared the outcomes of this sorbent with other commonly used desiccant materials. The researchers discovered that the temperature required to reactivate the composite desiccant was approximately 60-80°C. Additionally, they observed that the adsorption capacity of the desiccant reached 0.4 g $H_2O$/g dry adsorbent under ambient conditions, namely at 40% relative humidity and 25 °C. Despite the high water uptake capacity of inorganic composites, they are still severely limited in their dehumidification applications due to the high regeneration temperature requirement of over 70°C. The abundance of salt led to corrosion, spill-over and deliquescence, posing potential negative impacts on the effectiveness of desiccants in dehumidifiers and adsorption chillers [54].

Metal-organic frameworks (MOFs) are porous crystalline materials constructed from metal ions connected in three-dimensional structures by organic ligands. They have attracted significant interest due to their high porosity, structural versatility and high stability. MOFs have been widely investigated for water sorption-based applications [19], including seawater desalination [55], cooling [56], energy storage, humidity control in buildings [57] and water harvesting from air. Bozbiyik et al. [58] studied water vapour adsorption on Aluminium fumarate experimentally as a metal-organic framework (MOF) material in static and dynamic setups. Kapteijn et al. [59] reported that aluminium fumarate MOF material has higher water uptake than SAPO-34 and thus can be used for humidity control applications.

Hussein et al. [31] studied various MOF materials like MIL-101(Cr), CPO-27(Ni), MIL-100(Fe), and Aluminium fumarate and their composites, showing their high water adsorption capability and potential for heat pump applications.

Figure 2-7 compares the water uptake of several MOFs with silica gel and zeolite, highlighting significant improvements in their water uptake capabilities.

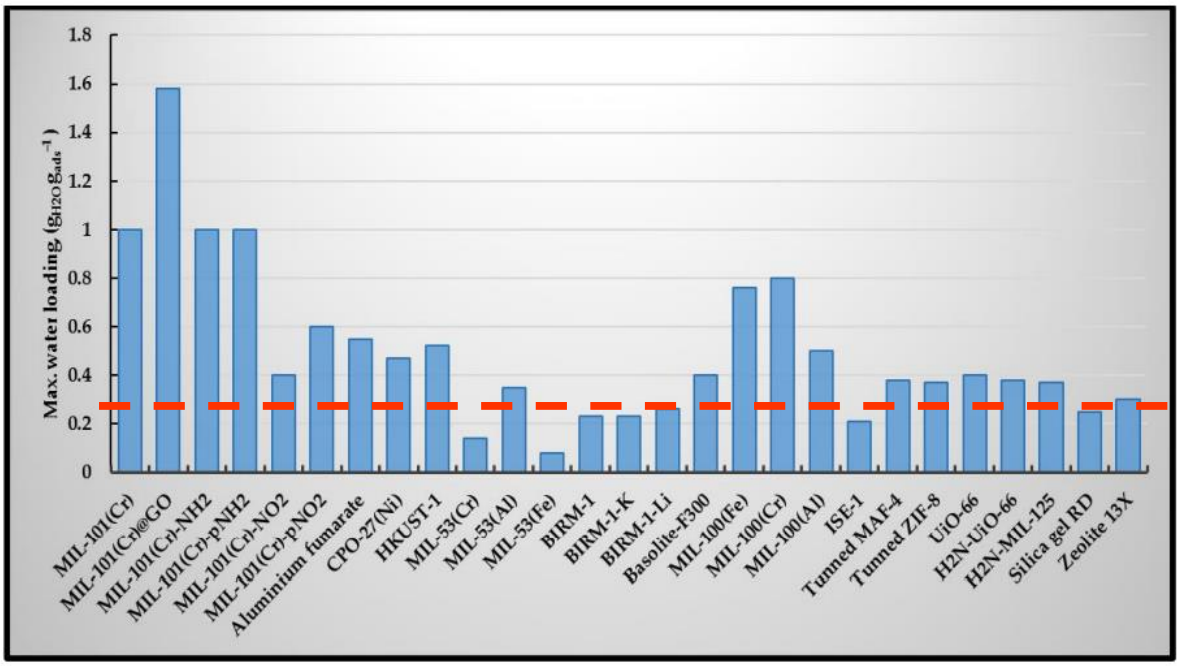



Figure 2-7: *The water uptake of several MOFs with silica gel and zeolite* [31].

Another advantage of MOFs is that they can be regenerated at low temperatures, 40-60°C, reducing the energy requirements of the dehumidification systems by 1/2 to 1/8 of the conventional adsorbents [60]. It has been reported [61] that the typical temperature range for regenerating commonly used desiccant materials is between 60 and 90°C as shown in Figure 2-8.

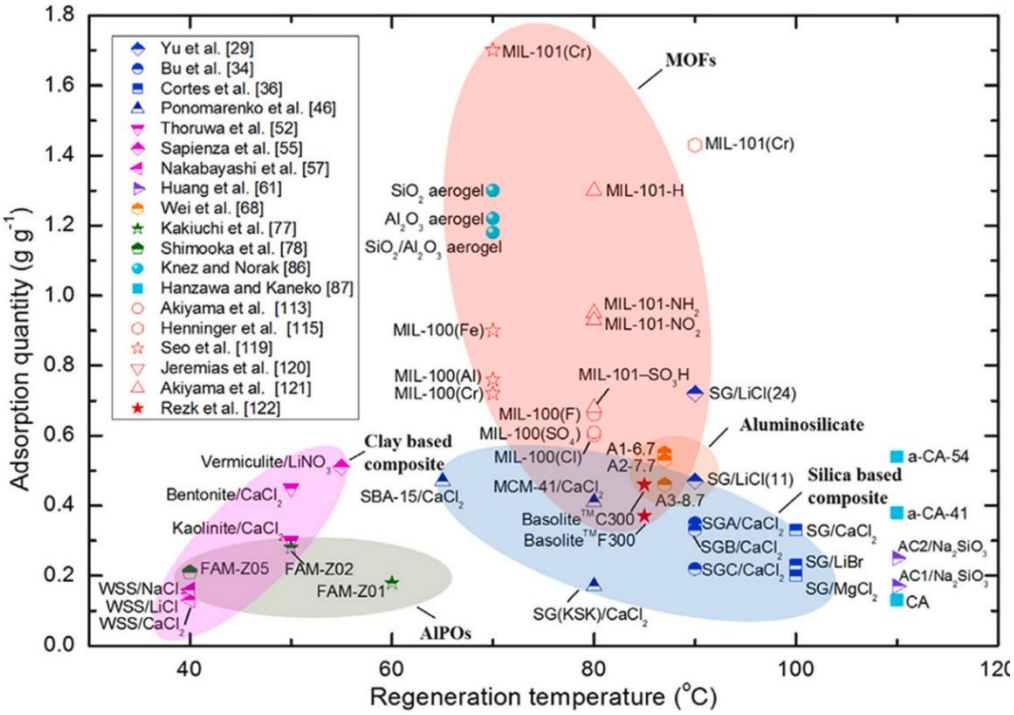



Figure 2-8: *Typical range of regeneration temperature for the commonly employed desiccant materials* [61].

Recently, Yaghi and co-workers reported the development of MOF-801 and MOF-303 for atmospheric water harvesting, showing their ability to be regenerated at low heating temperature (<90°C) and high water uptake at low RH (<0.2). Zirconium-based MOFs like MOF-801 are among the most investigated MOFs due to their exceptional stability and topological diversity [62]. Solovyeva et al. [63] studied MOF-801/water adsorption dynamics and equilibrium. They showed that the adsorption cycle's efficiency and cooling power, achievable with MOF-801/water working pair, are attractive for adsorption cooling.

Despite their advantages, MOF adsorbent materials suffer from poor thermal conductivity due to the free volume in their porous structure. This low conductivity can hinder the heat transfer process during the adsorption and desorption processes, causing longer cooling/heating times to reach the required operating temperatures [64]. In order to improve thermal conductivity, Wang et al. [65] synthesised a novel high thermal conductivity supporting material by heterogeneously modifying Cr-MIL-101-$NH_2$ on the surface of carbon nanotubes and then prepared PEG/CNT@Cr-MIL-101-$NH_2$ composite PCM. It was found that the thermal conductivity of the composite PCM was 100.9% higher than that of pure PEG. MOF-801/Graphene was synthesised by Diab et al. [66], where a mixture of ZrCl4 (1.16 g) and fumaric acid (0.55 g) was dissolved entirely in DMF (150 mL) dispersed with 0.1 g of graphene nanoplatelets. Then, 10.5 mL Acetic acid and 0.460 mL Triethylamine were added. The solution was transferred into a 100 mL capped bottle and kept in an oven overnight at 100°C. The resulting solution was allowed to cool down, and the precipitate was isolated by centrifugation and washed with Methanol. After that, the precipitate was immersed in

Methanol (80 mL) for 36 h, during which Methanol was refreshed every 12 h. Finally, the grey powder was collected by centrifugation and dried in an oven for 24 hours.

Diab et al. investigated MOF-801 with 10 %, 20 % and 30 % wt.% of graphene nanoplatelets. They concluded that 10 % graphene is the most appropriate ratio since increasing the graphene percentage by more than 10% will decrease the surface area to half (420 $m^2/g$ in the case of 20% graphene).

### 2.2.3. Adsorption heat exchangers

The desiccant air conditioning system for climate control consists of many thermal elements that can be integrated to achieve a specific output of the air conditions. One of the essential elements is the adsorber heat exchanger bed, which is classified as a rotational desiccant-coated heat exchanger (desiccant wheel), Fixed-bed dehumidifier and stationary desiccant-coated heat exchanger (DCHE).

Regarding the desiccant wheels, the desiccant material is infused into the wheel's structure, where during the wheel's rotation, a specific section removes moisture from the air involved in the process. While, another section of the wheel is simultaneously restored by applying hot air. Most of the reported literature have used a rotating desiccant wheel that alternates between the dehumidification and regeneration processes as it rotates, as depicted in Figure 2-9. This rotating process introduces mechanical complexities to the cooling system, thus increasing size and cost [67].

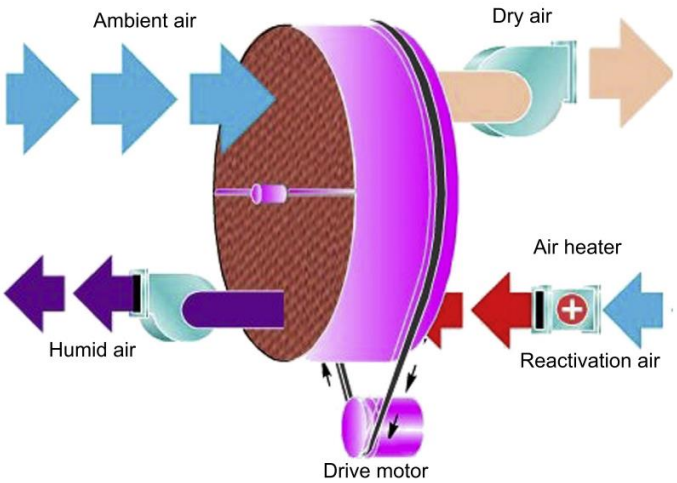



Figure 2-9: *Operation of a desiccant wheel* [68].

Fixed-bed dehumidifiers utilise stationary layers of desiccant materials in contact with humid air. They need lower maintenance levels than other alternatives or rotating dehumidification machines [69]. The fixed bed solid desiccant dehumidification schematic is represented in Figure 2-10.

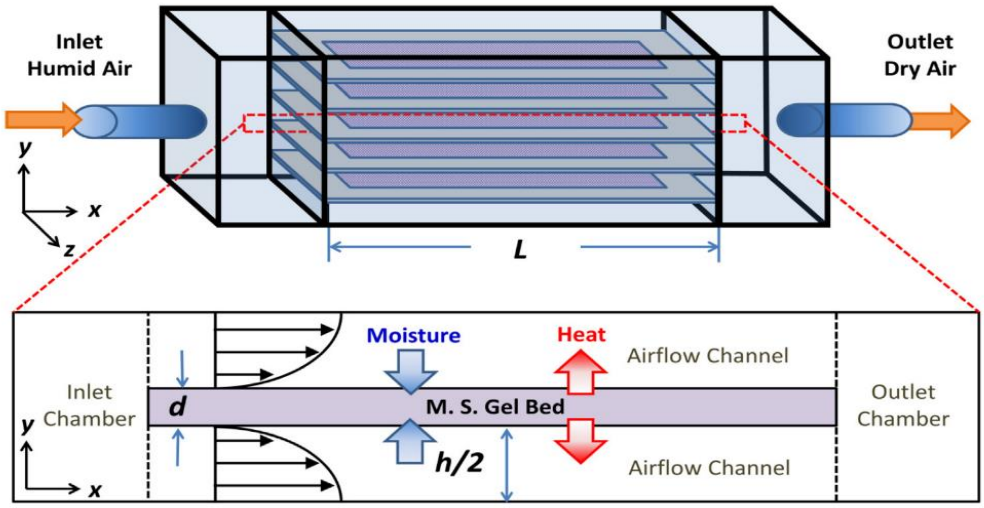



*Figure 2-10: Fixed bed Solid desiccant dehumidification* [70].

For the stationary desiccant-coated heat exchangers, the finless tube, metal foam, graphite plate, microchannel, lattice, finned-circular and finned-flat tube heat exchangers (HEs) were used [71], [72] as shown in figure 2-11. Finned tube heat exchangers are simple constructions based on straight tubes with perpendicular fins that may have circular or rectangular shapes. Finned tube HE was used in adsorption beds by filling the space between fins with loose grains of adsorbent and covering them with mesh to keep adsorbent grains in place. Also, it is possible to cover the heat exchanger surface with a coating made from adsorbent grains and binders. Various heat exchanger designs were developed from this finned tube concept [73].

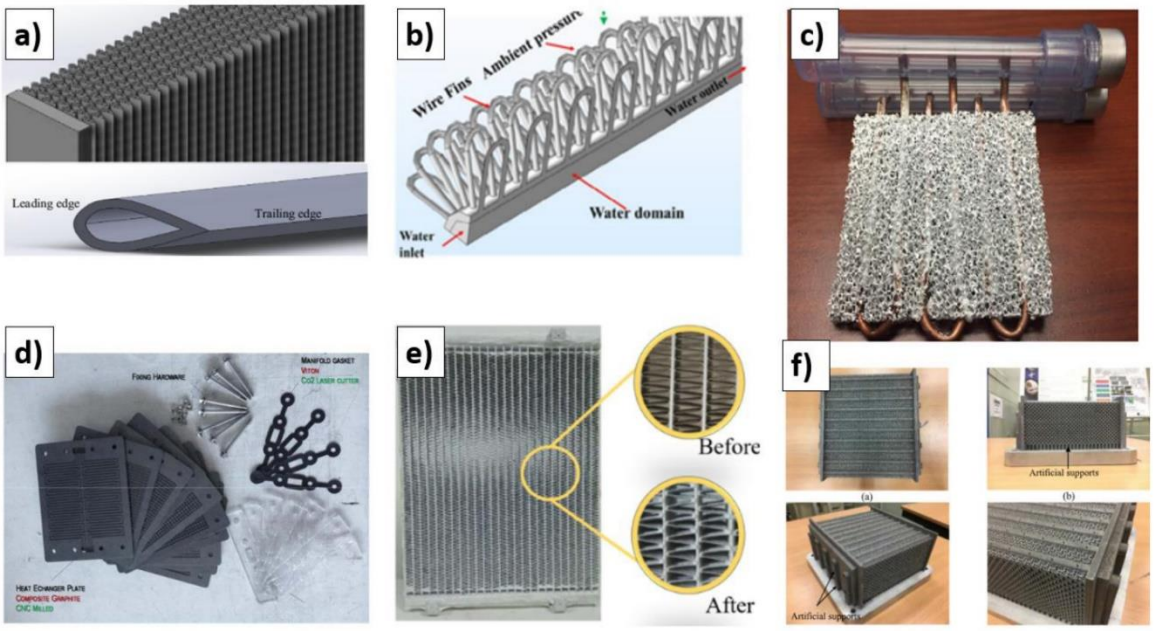



Figure 2-11: *Heat exchanger designs reviewed. a) Finless tube, b) wire finned tube, c) metal foam, d) graphite plate, e) microchannel, f) lattice* [72].

Majdi et al. [74] conducted experimental and numerical work to study microchannel, rectangular finned and wire-finned heat exchangers for adsorption application, as shown in Figure 2-12. Their results indicated that the wire-finned HE outperformed the other two heat exchangers in terms of high heat transfer performance and low-pressure drop.

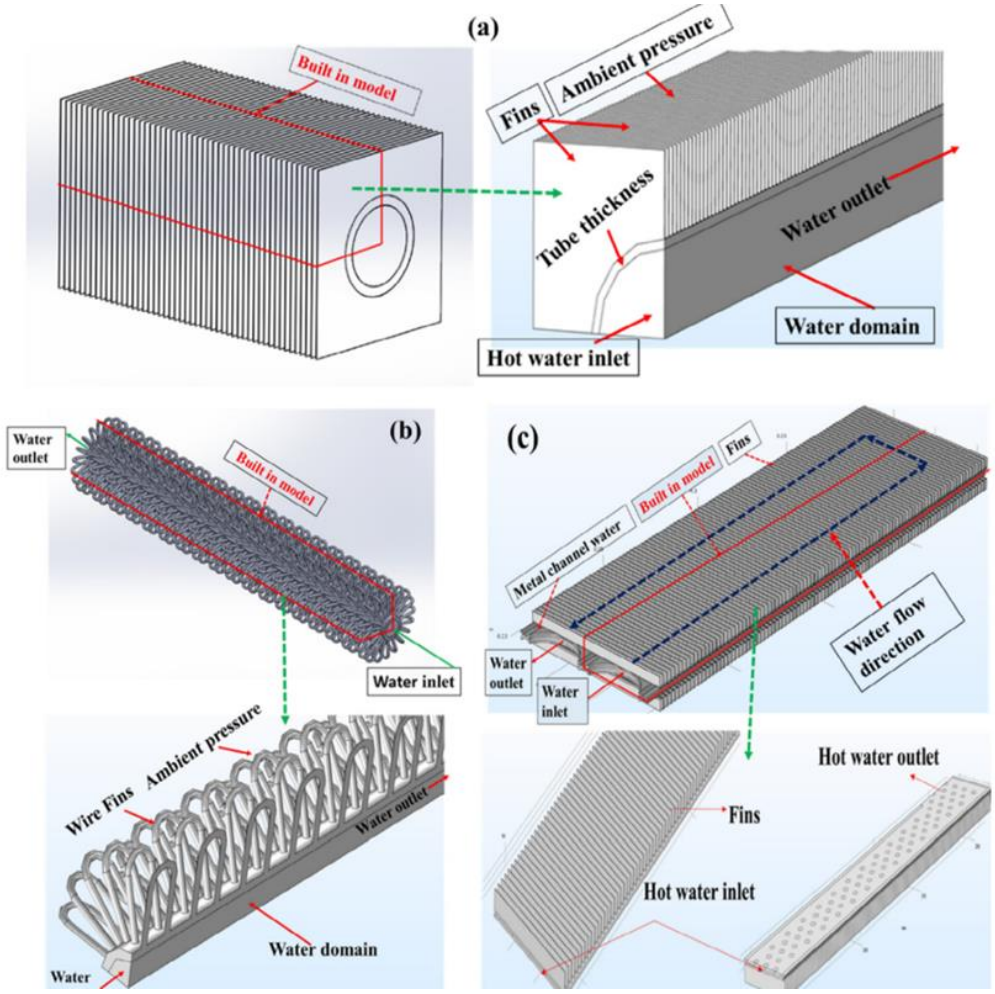



Figure 2-12: *Rectangular finned and wire finned heat exchangers for adsorption application* [74].

Also, various ways were used to integrate the MOF material into the adsorber beds. In order to maintain strong adhesion between the desiccant particles and the outside surface of the heat exchanger, an appropriate binder must be included. These will also help to provide good adhesion between the desiccant particles [71], impacting the efficiency of heat and mass transfer within the heat exchanger due to its physical and chemical properties [75]. Various techniques are available for attaching adsorbent substances to the heat exchanger's surface, each presenting distinct benefits and factors to consider. **Impregnation:** Involves the direct integration of the adsorbent into the porous structure of the heat exchanger, resulting in a firm binding. However, this method is susceptible to damage from moisture and temperature changes, cause cracking or delamination [76]. **Bonding:** Adhesives or binders offer versatility

in selecting materials and thickness, but their bond strength and endurance must be carefully chosen according to the specific requirements of the application [77]. **Coating:** The application methods of spraying, dipping, or painting allow for consistent coverage and the ability to manage the thickness. However, these coatings are vulnerable to mechanical damage and deterioration [78]. **Embedding:** Involves the combination of an adsorbent with a binder, which is then pressed or moulded onto the surface. This method provides excellent mechanical strength and stability. However, it necessitates intricate manufacturing procedures and specialised equipment [79]. Appropriate binders are essential in the coating process to maintain sustained contact between the fins and desiccant materials. [80], metallic foams [81], olyaniline [82], polyvinyl alcohol (PVA), Aluminium hydroxides (AlOH3), and polytetrafluoroethylene (PTFE) have been utilised to bind silica gel, zeolites onto metallic surfaces [78], and 2-hydroxyethyl cellulose for aluminium fumarate, MIL-100(Fe), MOF-801, and MOF-303 [83]. Albaik et al. [83] examined various coating thicknesses using Brunauer−Emmett−Teller (BET) and dynamic vapour sorption (DVS) equipment to compare them with the original MOFs without any coating. The adsorbent material mixed with 10% binder agent allows for multiple adsorption and desorption cycles in 75 mins, with coating thicknesses of 0.3 and 0.5 mm. However, coating thicknesses exceeding 0.85mm in aluminium fumarate and 1.1mm in MOF-801 become ineffective.

Although the coating improved heat transfer, their mass transfer characteristics remained insufficient, and their thickness continues to have an impact. Where coating the heat exchanger surfaces with the MOF adsorbent material has shown many advantages in terms of decreasing the contact resistance between adsorbent material and heat exchanger surfaces, providing good permeability and heat transfer rate through the coated layer leading to enhancing the performance of the adsorption system [84], [85].

### 2.2.4. The heating and cooling source of the DCHE

Desiccant air-conditioners can separate the sensible cooling load from the latent dehumidification load, resulting in significant energy savings. However, a drawback of these systems is the energy required to regenerate the desiccant materials after they get saturated with water vapour. Consequently, numerous studies have focused on lowering the regeneration temperature to improve the system's overall coefficient of performance (COP) [86].

Heating can be accomplished by several means: hot water [87], or hot air from electric heaters, or solar air heaters fitted in a compound parabolic concentrator [88], or microwave heating [89].

Lu and Yan [90] developed and tested the effectiveness of a Solar Desiccant Enhanced Radiative Cooling (SDERC) system, indicating its ability to save considerable amounts of energy. They found a significant reduction in energy costs, equivalent to around US $850, during one year in Taiwan throughout the 1990s. This study highlighted the SDERC system adsorption potential as a low-cost option for energy conservation in cooling applications. I. Albaik et al. [91] examined multiple heat exchangers numerically and experimentally to decrease their system energy consumption using a low desorption temperature (less than 90 ◦C). They were using the warm water to reactivate the material and their results revealed that connecting the modules in series will benefit from utilising a minimum thermal fluid flow rate and the effect of heat conduction in the metal tube along the thermal fluid direction, increasing the COP. In most of the reported work on adsorption systems, the adsorber beds were heated by water, which requires circulating pumps, hot water tanks and valves, which makes the system complex and costly [85].

Yao et al. [92] investigated silica gel's ultrasonic-assisted hot air drying process as presented in Figure 2-13. The ultrasonic method can improve drying kinetics and energy utilisation efficiency as a non-heating technique. Their findings demonstrated that ultrasonic could reduce regeneration time for certain regeneration temperatures below 45℃. The ultrasonic producer was configured with a power output of 40 watts. The electric heater has a maximum power input of 400 watts.

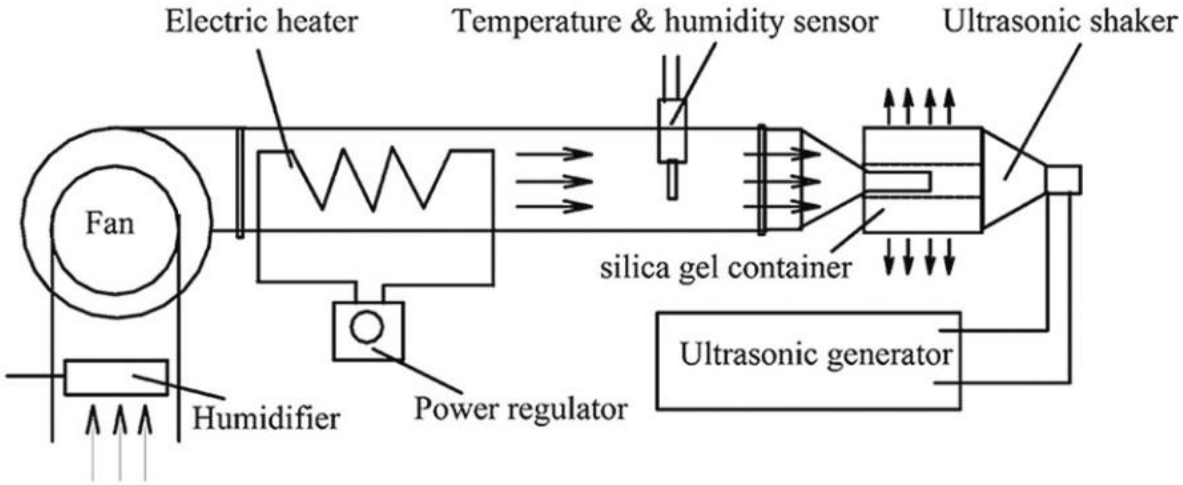



Figure 2-13: *Application of ultrasound for regeneration of silica gel* [92].

In addition, Ellison et al. [93] studied microwave irradiation as an alternative method to conventional heating for temperature swing adsorption. As a result, microwave regeneration raises adsorption/desorption cycling output and potentially reduces the energy penalty of temperature swing capture. The apparent activation energy for microwave-assisted

regeneration ranged from 15.8 to 18.1 kJ/mol, whereas traditional regeneration had an apparent activation energy of 41.5 kJ/mol.

Yang et al. [94] assessed the efficacy of a regeneration system that combines microwave and solar irradiation. They found that the combined method achieved a regeneration rate of 77.7%, which was 3.77 times higher than standalone solar regeneration and 1.05 times higher than microwave regeneration, as shown in Figure 2-14.

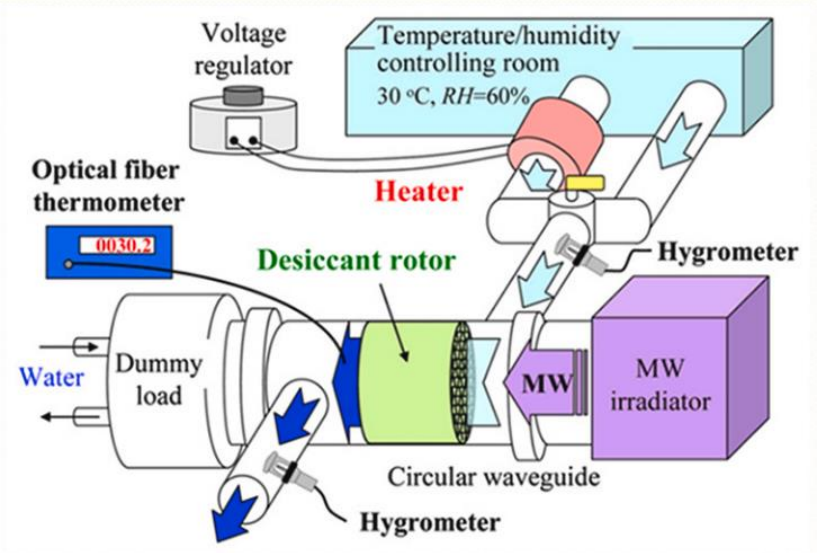



Figure 2-14: *Experimental setup investigating the impact of microwave heating on the process of regeneration* [94].

Furthermore, in Figure 2-15, a study by Li et al. [95] indicated that a desiccant-coated thermoelectric cooler can effectively function as a solid-state humidity pump for controlling humidity in a specific area. This technology does not require refrigerants or hot water to regenerate the desiccants. Based on the Peltier effect, it can be deduced that the hot side of thermoelectric materials is anticipated to supply thermal energy for desiccant regeneration in DCHE.

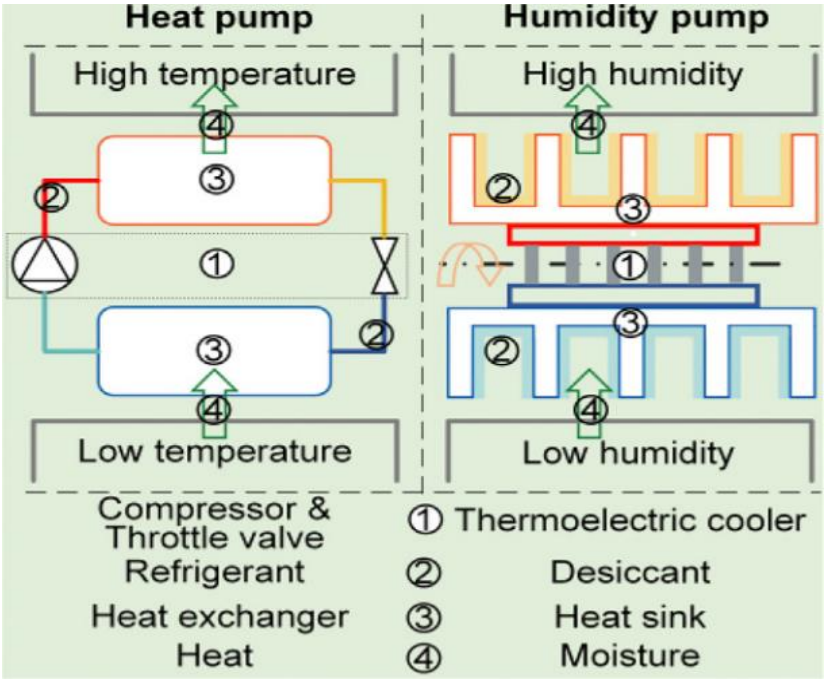



Figure 2-15: *Comparison between the conventional vapour-compression heat pump and the thermo-electric humidity pump* [95].

Cooling the desiccant material during adsorption is essential to maintain its capacity to absorb moisture and can even manage the sensible load carried by the process cooling fluid. Up to now, several cooling fluids have been used in DCHE, including cooling air [96], cooling water (cooling tower) [97], tap water [98], and refrigerant [99]; these systems are commonly defined by the use of cyclic switchover to ensure continuous operation. Water and refrigerants with high specific heat capacity are more suitable for cooling DCHE than air [99] with low thermal properties. Nevertheless, the studies indicated that DCHE, which utilises cooling water as a cooling fluid, demonstrated a significant capacity for dehumidification and enhancing its adsorption efficacy [97]. Using refrigeration sophisticated DCHE systems to chill the desiccant material can be incorporated into traditional air conditioning systems to improve dehumidification capability [99]; nevertheless, the combination of a high evaporation temperature, a low-pressure ratio of the compressor, and the control strategy for the expansion valve and compressor that can handle the switchover feature [100] are challenging issues.

### 2.2.5. Performance progress in different DCHEs.

Many researchers have examined the performance of desiccant-coated heat exchangers (DCHEs) coated with different solid desiccant materials and coating methods to develop DCHEs for air conditioning applications. An experimental arrangement was constructed using a single heat exchanger system that included a DCHE, heating and cooling water sources, and

air ducts. An axial flow fan was positioned at the heat exchanger's exit to move the air. Temperature-humidity sensors were employed to accurately measure the incoming air temperature and humidity conditions, as shown in Figure 2-16.

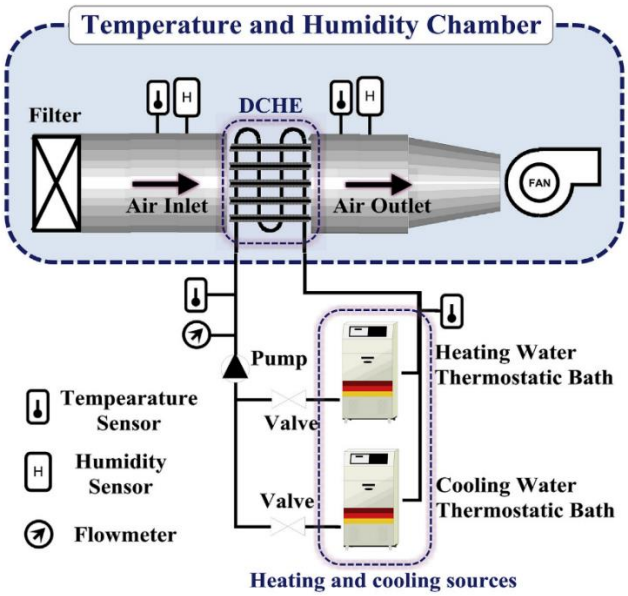



*Figure 2-16: Schematic diagram and photo of the experimental setup* [101].

The performance of DCHE is assessed using moisture removal capacity (MRC g/kg) and thermal coefficient of performance ($COP_{th}$) as the primary evaluation indices for dehumidification and cooling processes. The equations are provided in relative forms:

The moisture removal capacity can be expressed as [102]:

$$\mathrm{MRC} = \dot{m}\left(\omega_{a,in} - \omega_{a,out}\right) \tag{1}$$

The average thermal performance $COP_{th}$ which is computed as follows [103]:

$$COP_{th} = \frac{Q_{cooling}}{Q_{reg}} = \frac{\int_0^t \dot{m}_a(h_{a,out} - h_{a,in})dt}{\int_0^t \dot{m}_{water} \times C_{p,w}(T_{h,out} - T_{h,in})dt} \tag{2}$$

Ge et al. [104] examined silica gel desiccant with an emulsion binder (Polymer binder L267) applied via dip coating. The investigation obtained a maximum MRC of 5 g/kg and a maximum $COP_{th}$ of 0.48. Cooling was achieved using cooling water, while regeneration heating was supplied by electrically heated water and then pumped to a fin-tube heat exchanger coated with silica gel. The testing conditions consist of an air-specific humidity of 14.3 g/kg, an ambient temperature of 30°C, an air velocity of 1 m/s, and regeneration temperature ranging from 60°C to 80°C.

Ge et al. [105] used the dip-coating method to study the cooling system using silica gel as a desiccant material coated on a finned tube heat exchanger, as shown in Figure 2-17. Hot water was passed through the heat exchanger to regenerate the silica gel material, and the

air operating conditions were 60% RH and 30°C. For cooling water temperatures of 15°C and regeneration temperature of 40°C, a peak MRC of 1.8 g/kg was found for the silica gel. Moreover, when $SiO_2$ gel-LiCl was introduced into the system, $COP_{th}$ of 1.08 at a cooling temperature of 15 and, a regeneration temperature of 40 °C and cooling capacity ($Qc_{max}$) of 0.47 kW at cooling water temperatures of 15°C and a regeneration temperature of 50°C were recorded. It also increased its efficiency from 1.8 to 2.1 g/kg at cooling water temperatures of 15°C and regeneration temperature of 40°C. The range of regeneration temperature is from 40 °C to 60 °C while cooling temperature varies from 15 °C to 25 °C. Furthermore, they observed that at cooing and regeneration temperatures of 15°C,and 50°C respectively, and $COP_{th}$ of 1.02, $Qc_{max}$ of 0.6 kW and at cooing and regeneration temperatures of 15°C, 40°C respectively, $COP_{th}$ of 1.13 with $Qc_{max}$ of 0.6 kW

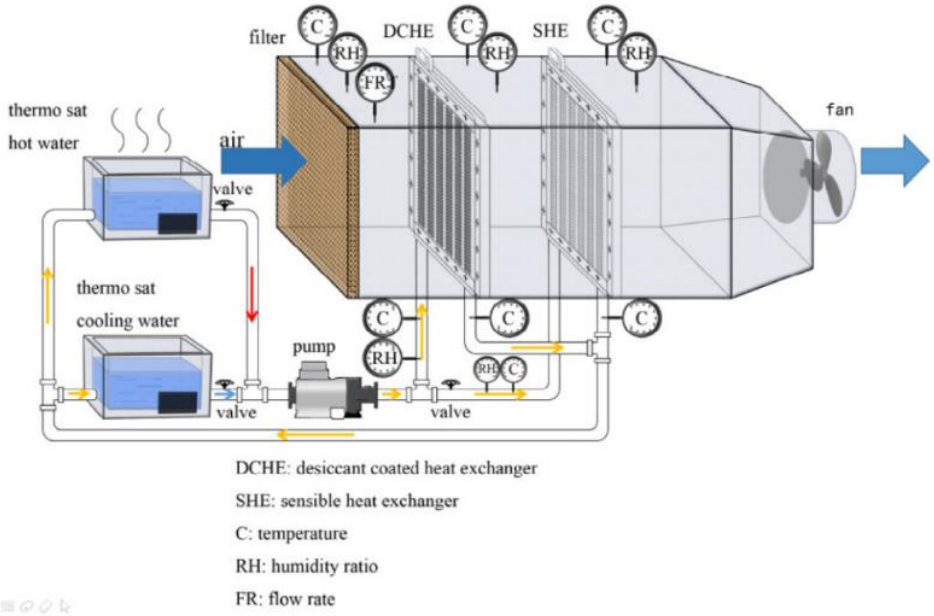



*Figure 2-17: Experimental system* [105].

Jiang et al. [101] studied silica gel and silica gel-LiCl as desiccants with emulsion binders. They achieved maximum MRC values ranging from 2.5 to 3.2 g/kg and maximum $COP_{th}$ values ranging from 0.81 to 1.7 under different conditions. These conditions included a relative humidity of 60%, a temperature of 30°C, an air velocity of 1.54 m/s, and a regeneration temperature of 40°C to 60°C. The cooling source used in the study was cooling water.

Hu et al. [106] and Oh et al. [107] studied the use of organic and hydroxyethyl cellulose binders in silica gel desiccants. They applied these binders by dip coating and achieved MRC values ranging from 1.26 to 6.1 g/kg and $COP_{th}$ values ranging from 0.32 to 0.49. Both investigations utilised cooling water as the cooling source, while electrically heated water passed through the fin-tube heat exchanger to regenerate the material.

Sun et al. [108], [109], [110] employed silica gel desiccants combined with liquid glue binders to achieve $MRC_{max}$ values ranging from 6.09 to 7.7 g/kg and $COP_{thmax}$ values from 0.78 to 0.92. Dip coating was used for the application, and cooling water was used as a cooling source. The primary heating source for regeneration was an electrically heated water tank, utilised through a Long-depth fin-tube and a Short-depth fin-tube heat exchanger.

Lertboonkankit et al. [111] found that the average $MRC_{max}$ was 3.2 g/kg for Silica-gel desiccant. They achieved this by using cooling water as the cooling source and hot water through a fin-tube heat exchanger as the regeneration heating source. Valarezo et al. [87] investigated the use of silica gel-sodium acetate desiccants. They achieved a maximum $COP_{th}$ of 0.83. The experiment involved using cooling water as the cooling source and electrically heated water pumped through the fin-tube heat exchanger as the regeneration heating source. Vivekh et al. [112] examined the performance of silica gel and polyvinyl alcohol-LiCl desiccants. They obtained MRC values ranging from 4.7 to 5.2 g/kg and $COP_{th}$ values from 0.18 to 0.58. A fin-tube heat exchanger was dip coated, cooling water was used as the cooling medium, while electrically heated hot water was used for regeneration.

Zhao et al. [97] conducted an experimental study on the performance of a desiccant-coated dehumidification system with and without a heat recovery device (HRD). The system consisted of two dehumidification and heat recovery subsystems, as shown in Figure 2-18. Solar evacuated tube collectors supplied hot water for regeneration, while a cooling tower supplied cooling water during dehumidification. The system's dehumidification performance improved slightly over 2% compared to the conventional system, but the regeneration energy requirement was significantly different. The standalone DCHE system used 4485 kJ of energy, but the system with HRD only required 2016 kJ of energy from solar collectors, yielding nearly double the $COP_{th}$.

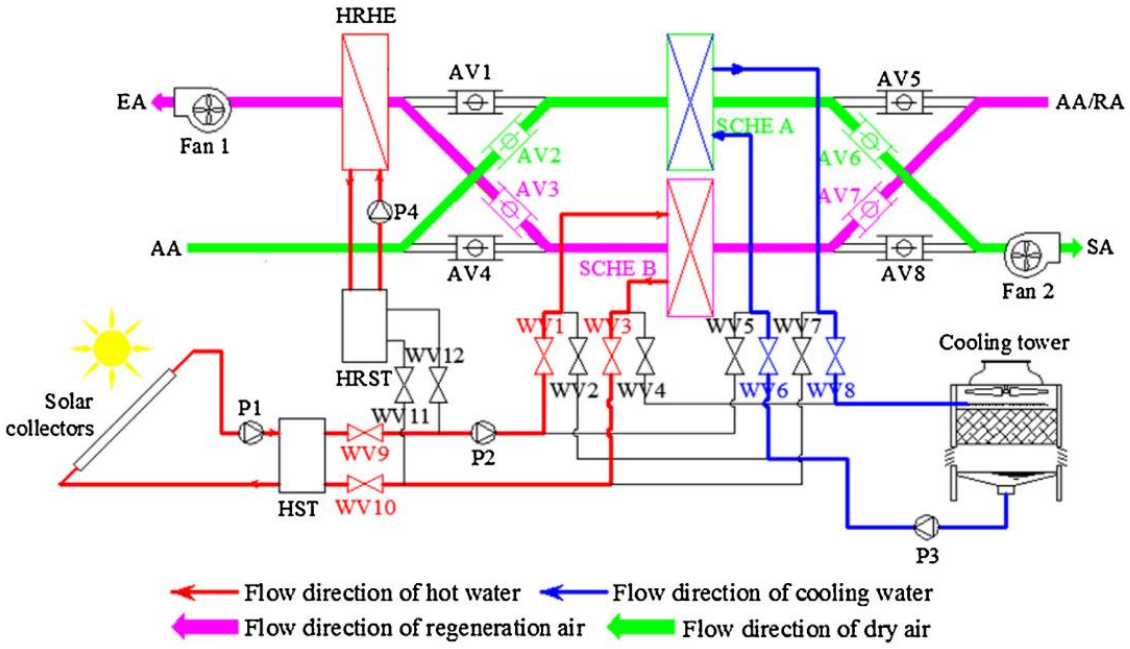



*Figure 2-18: Schematic diagram of a desiccant system using SCHE with HRD* [97].

Jiang et al. [101] studied the effect of varying inlet air velocity on heat exchangers using pure silica gel and composite silica gel with 38w% LiCl. They found that increased air velocity reduced the MRC and $COP_{th}$ of pure silica gel-coated heat exchangers, while composite desiccant improved the MRC and $COP_{th}$ by 18-40% and 20-25%, respectively. Ge et al. [113] studied the impact of air velocity on silica gel and T50 polymer-coated heat exchangers. They found that as air velocity increased from 0.5 m/s to 2 m/s, the MRC of the heat exchangers decreased from 3.75 to 1.8 for silica-gel and 1.8 to 0.9 for the polymer-coated heat exchanger.

A full cycle in the DCHE system comprises dehumidification and regeneration, where longer cycles enable more extensive dehumidification and regeneration. Zhao et al. [114] experimented on heat exchangers coated with silica gel. They extended the cycle duration from 300 s to 1200 s, keeping the air's dry bulb temperature, humidity ratio, $T_{cool}$, and Treg constant. Their results indicated that MRC and $COP_{th}$ had an upward trend until reaching a peak, after which they declined. An optimal performance was achieved by selecting a cycle time of 600 s.

Sun et al. [115] examined the dehumidification and thermal performance of DCHE by increasing the fin depth. The researchers discovered that doubling the depth of the fin resulted in a 40% rise in MRC, whereas the increase in $COP_{th}$ was just 10%. Nevertheless, the rise was offset by elevated flow resistance and energy demands.

A unique humidity pump has been developed by Menghao et al. [116], which utilises metal-organic frameworks (MOFs) as desiccant material. This pump efficiently transfers moisture from low-humidity areas to high-humidity areas. An investigation was conducted to assess

the dehumidification performance of the pump at a temperature of 22.8°C and a relative humidity of 60%. The pump demonstrated superior dehumidification rates and efficiency in removing moisture compared to conventional desiccant systems. The humidity pump has a maximum dehumidification coefficient of performance (DCOP) that may reach approximately 0.46, higher than typical desiccant dehumidification systems. The MOF humidity pump effectively achieved energy-efficient localised moisture control, regardless of cycle time, thermoelectric power, and air velocity variables.

Changes in DCHE system working conditions affect dehumidification and thermal performance, including inlet air dry bulb temperature and humidity content, incoming air velocity, cycle time, cooling water temperature, regeneration temperature, and fin-depth.

The temperature of the inlet air significantly impacts the dehumidification and thermal performance of DCHEs. At constant inlet air relative humidity, increased inlet air temperature increases moisture content, improving dehumidification performance and cooling capacity. Conversely, moisture content remains constant at a constant inlet air humidity ratio, negatively affecting the desiccant's sorption capacity and reducing its MRC. Despite these changes, increased cooling capacity improves the thermal performance of the DCHE [75].

## 2.3.Direct and indirect evaporative coolers

Direct and indirect evaporative coolers are essential in controlling the temperature and humidity in desiccant air conditioning systems. Direct evaporative coolers increase the air's humidity and reduce the temperature, especially in a dry environment [117]. This cooler can be used with other elements to give the best configuration to reach the required comfort conditions [118]. On the other hand, indirect evaporative coolers reduce the air temperature without affecting the air humidity [119]. Evaporative cooling happens when air and water interact at the water's surface, where heat from the air passes through the water interface, providing the necessary latent heat for evaporation and reducing the air temperature.

The fundamental disadvantage of evaporative cooling is that its performance is affected by ambient air conditions because it is driven by the temperature difference between the dry and wet-bulb temperatures of the ambient air, which decreases in humid climates [120]. Figure 2- 19(a) shows a two-stage indirect and direct evaporative cooler, as shown in the air conditioning process on a psychrometric chart. Figure 2-19(b) shows that from point 1 to point 2, the indirect evaporative cooler reduces the temperature at a constant specific humidity. On the other hand, from point 2 to point 3, the temperature is reduced, and the relative and specific humidity is reduced as air passes through the direct evaporative cooler [121]. Amer et al. [122] and Jain et al. [123] presented a review on direct evaporative cooling. They showed their effectiveness compared to other air conditioning systems, with $COP_{th}$

ranging from 15 to 20. An indirect evaporative cooler requires around 55% less power than a conventional air conditioner to achieve the same cooling effect [124].

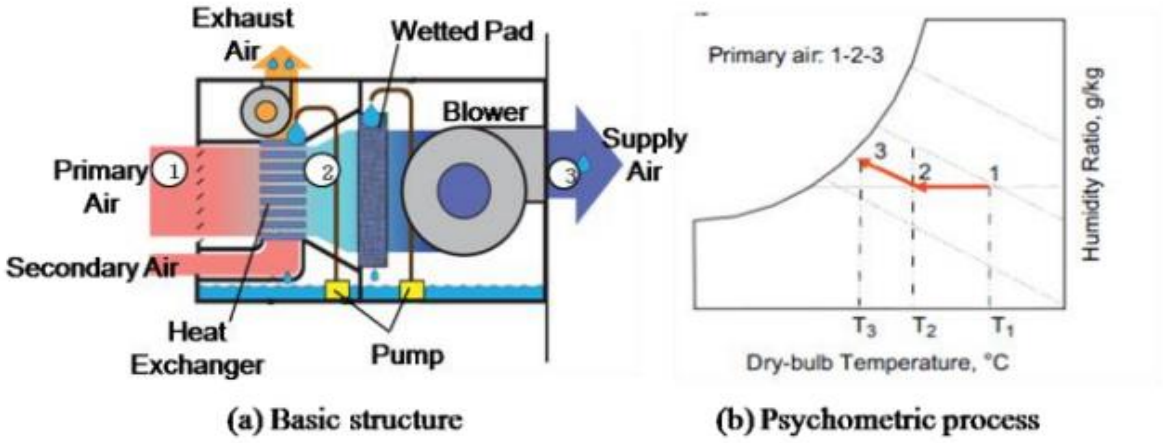



*Figure 2-19: Two-stage indirect-direct evaporator system* [121].

## 2.4. Desiccant Systems Configurations

The desiccant air conditioning system comprises multiple thermal components that can be combined to create a particular air condition output. The key components are a rotating desiccant-coated heat exchanger (desiccant wheel) or a stationary desiccant-coated heat exchanger, an evaporative cooler, an electric heater, a heat exchanger, and a cooling coil.

Ahlem Zouaoui et al. [125] reviewed open solid desiccant cooling air systems and showed six different configurations of open systems using different thermal elements, as shown in Figure 2-20, the red arrows for the regeneration and the blue arrows for the dehumidification process line. System 1's main elements are the desiccant wheel, humidifier, and heating coil. The outlet temperature is 38.82 °C, the absolute humidity is 0.02415 kg of water /kg of dry air, and the relative humidity of the air is 55.45%. This configuration's drawback is that the air temperature remains high with acceptable relative humidity. In system 2: a cooling coil is added to the previous configuration, which Lowed the air outlet temperature to a value ranging from 24.33 °C to 29.43 °C, but the humidity is increased to 100%. This system produced cool air more efficiently than system 1 but has a problem with high air humidity. In system 3, two extra parts are added, namely the heat recovery wheel and the humidifier at the inlet of the regeneration line. This system produces an air outlet temperature of 31.73 °C, and relative humidity of about 69.63%. For system 4, a cooling coil is added after the recovery wheel, thus, the average air outlet temperature is reduced to 19.07 °C, but the relative humidity is increased to 100%, which is too high for good building air conditioning. In system 5 the humidifier is removed from the regeneration line, producing an air outlet temperature of 28.69°C and an average relative humidity of 85%. In system 6 the humidifier is added to the regeneration line. This system produced a temperature of 28.33°C and a relative humidity

of 86.77%. Based on this analysis, it is vital to highlight that only systems 3, 5, and 6 are efficient. These desiccant cooling systems can efficiently extract both sensible and latent loads. The setups shown seemed good at cooling despite the high humidity levels. All the results were obtained for all systems using the same inlet condition for adsorption at an air temperature of 26°C and relative humidity of 50%. For desorption, the air temperature is 55°C, and the relative humidity is 11%.

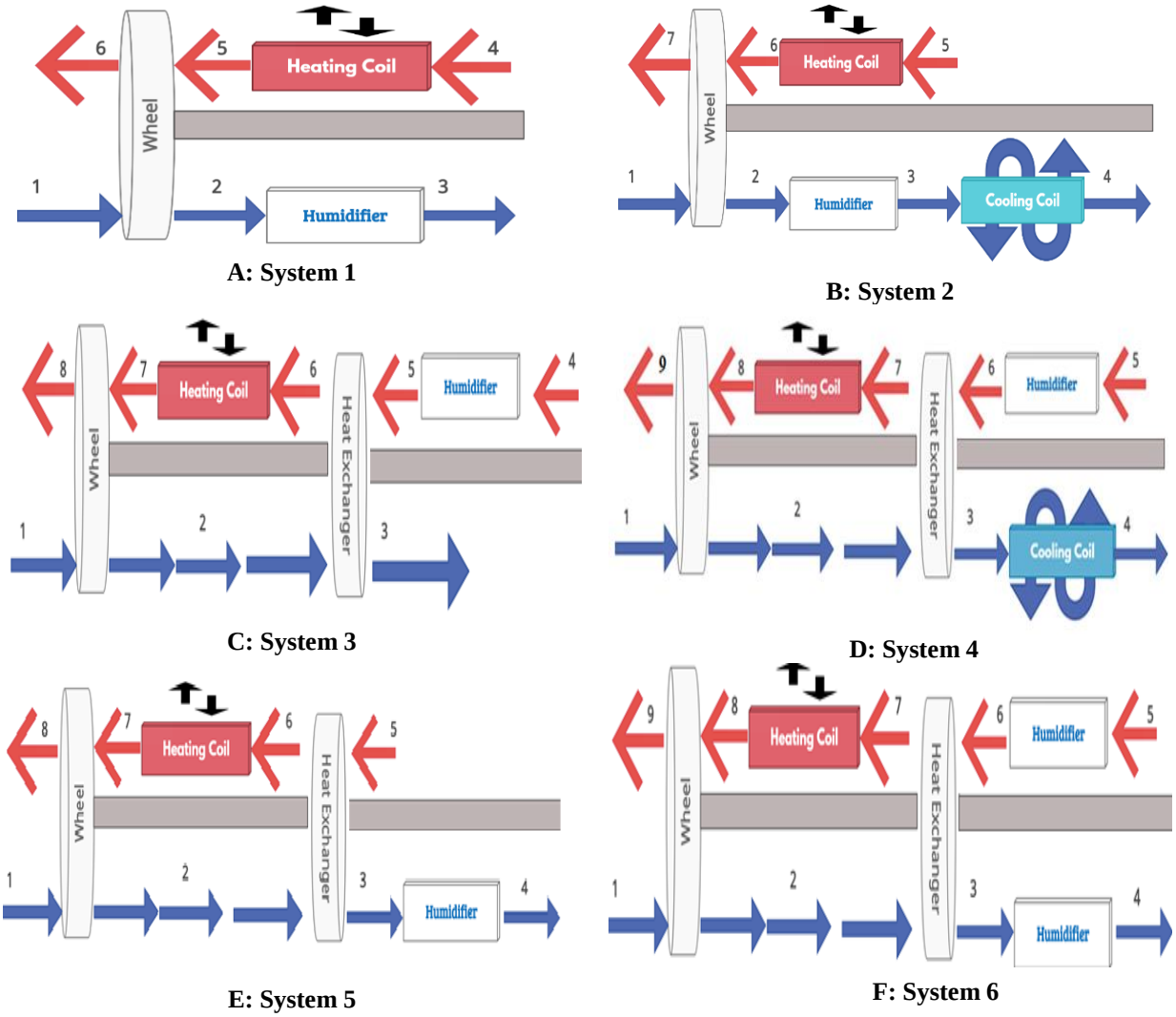



*Figure 2-20 Systems configurations* [125].

Rafique et al. [126] performed a performance analysis of a desiccant evaporative cooling system with hot and humid conditions using silica gel as an adsorbent material. Figure 2-21 shows the system consisting of a direct evaporative cooler, indirect evaporative cooler, heat recovery wheel, and heater powered by solar energy to heat the air and reduce its humidity levels. The results demonstrated that the proposed system is a reasonable and

practical option for meeting the high cooling demands in Dhahran, Saudi Arabia, with performance largely reliant on selecting optimum operating parameters. In July, the process air had a flow rate of 1.62 kg/s; the maximum moisture removal was 17 g/kg. The cooling impact reaches a maximum of 39 kilowatts when the process air flow rate is 1.62 kg/s (3000CFM). This value increases to 52 kilowatts when the process air flow rate is increased to 2.15 kg/s (4000CFM). The highest system $COP_{th}$ values of 0.41, 0.82, and 0.7 were observed on the 15th of April, July, and October, respectively, where the ambient average temperature and relative humidity values of 25°C and 35%, 25°C and 47.5%, and 30.8°C, and 27.8%, respectively These values were obtained at a process air flow rate of 1.62 kg/s (3000CFM) and a mass flow rate ratio of 0.33.

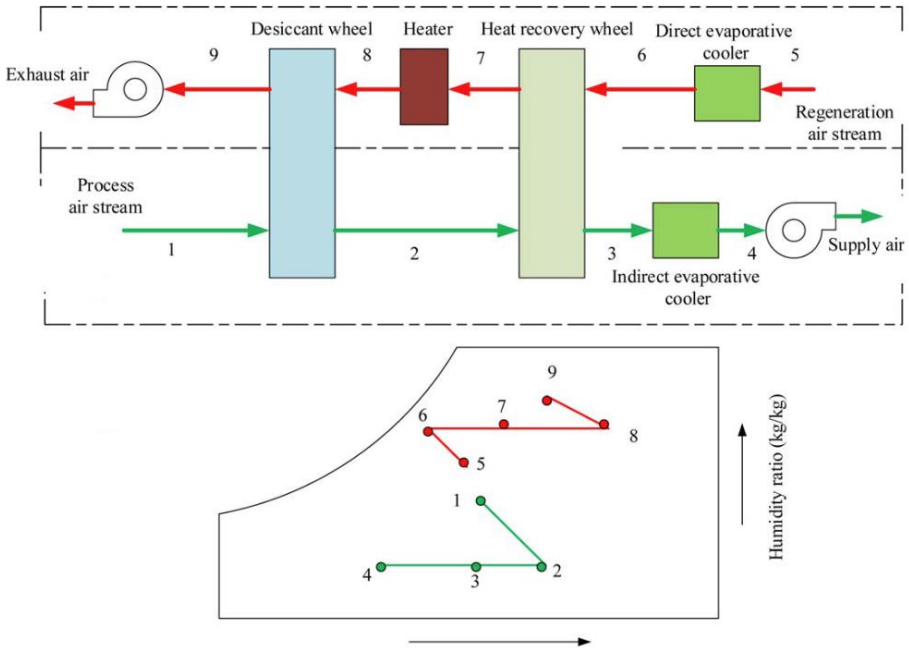
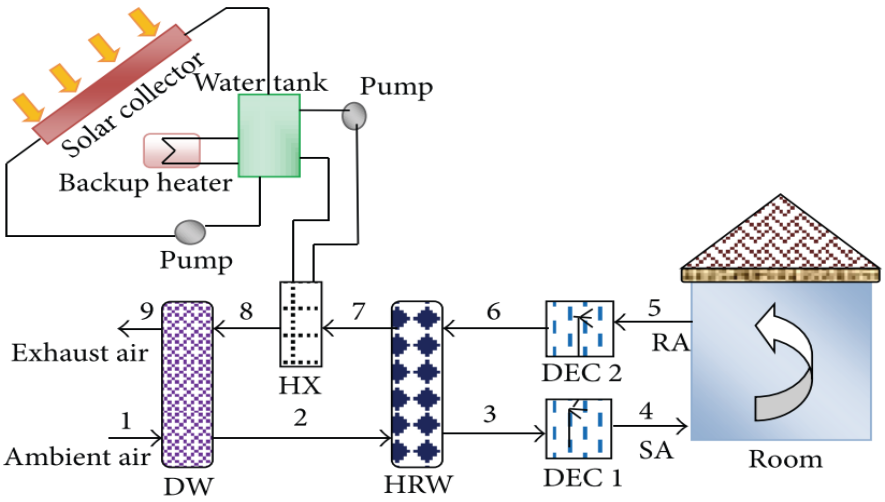



*Figure 2-21: Schematic diagram of a desiccant system* [126].

Dezfouli et al. [127] simulated four configurations of the solar desiccant cooling system using evaporative cooling under the tropical weather of Malaysia to achieve the (ASHRAE) comfort conditions, namely indoor temperature of 25°C and relative humidity of 50%. They used TRNSYS to simulate the operation of the four systems, namely one-stage ventilation, one-stage recirculation, two-stage ventilation, and two-stage recirculation, over 8,760 hours. Figure 2-22 denotes the schematic diagram for a single-stage solar desiccant cooling system operating in ventilation mode. It consists of one desiccant wheel, one recovery wheel, a solar heating panel with its heat exchanger and two direct evaporative coolers. All the process points were plotted on the psychrometric chart [127]. Figure 2-23 presents a two-stage cooling system using double the number of heat recovery wheels and desiccant wheels to be

more effective than the one stage. Point 6 on the psychrometric chart gives 76.1% relative humidity and a lower temperature of 18°C compared to the one-stage system [127]. Figure 2-24 depicts a one-stage solar desiccant cooling system operating in recirculation mode. The supply air from the room has a temperature of 31°C, a humidity ratio of 0.015 kg/kg, and a relative humidity of 52.8%. The output air condition is at point 4, with a temperature of 21.4°C and a relative humidity of 84.7%. Figure 2-25 shows a two-stage cooling system in recirculation mode. The input temperature is 27°C, and the relative humidity is 48.7%. The system output conditions at point 6 are as follows: the temperature is 18°C, the humidity ratio is 0.0096 kg/kg, and the relative humidity is 74.3%. The $COP_{th}$ of the two-stage ventilation mode was 1.06, which is better than that of the other configurations.



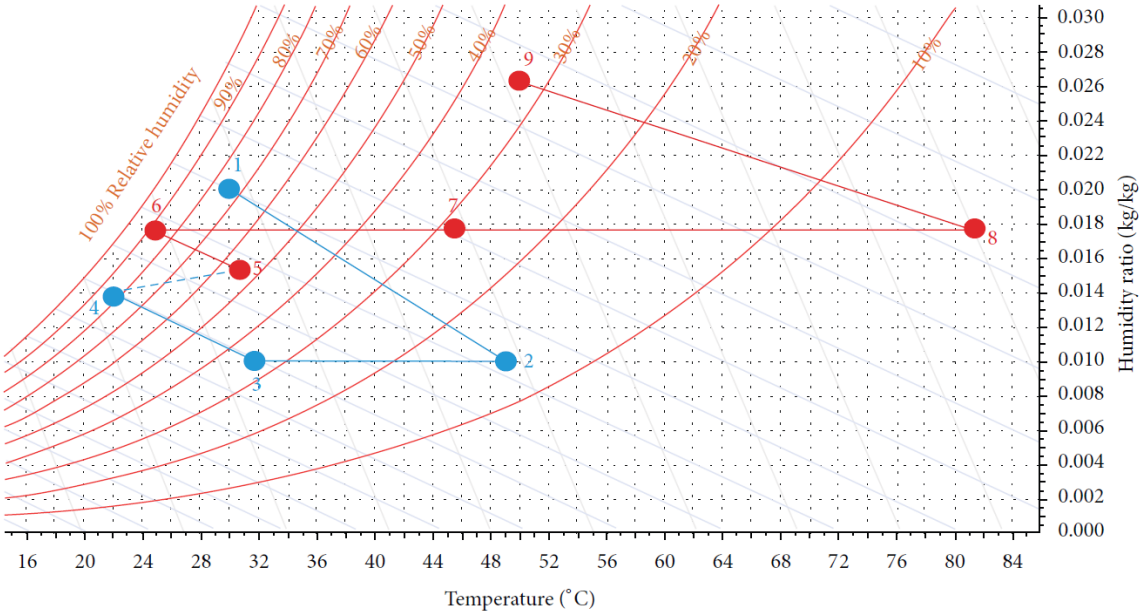




*Figure 2-22: Psychrometric chart of one-stage solar desiccant cooling system in ventilation mode* [127].

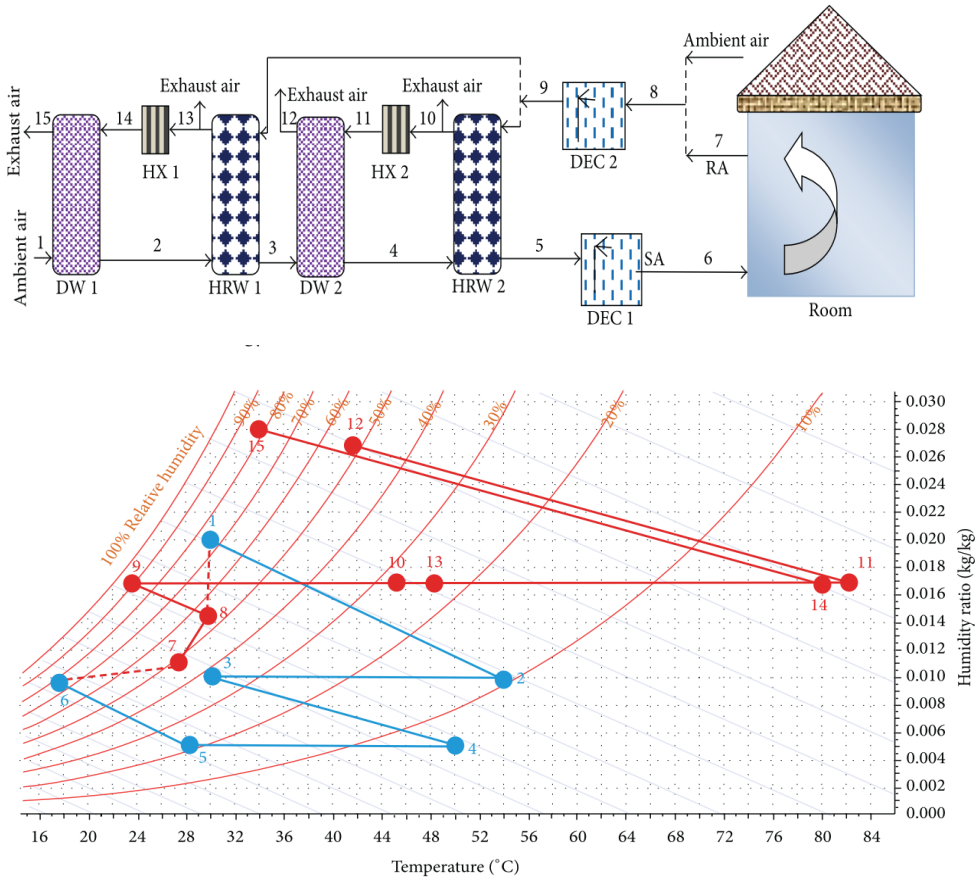
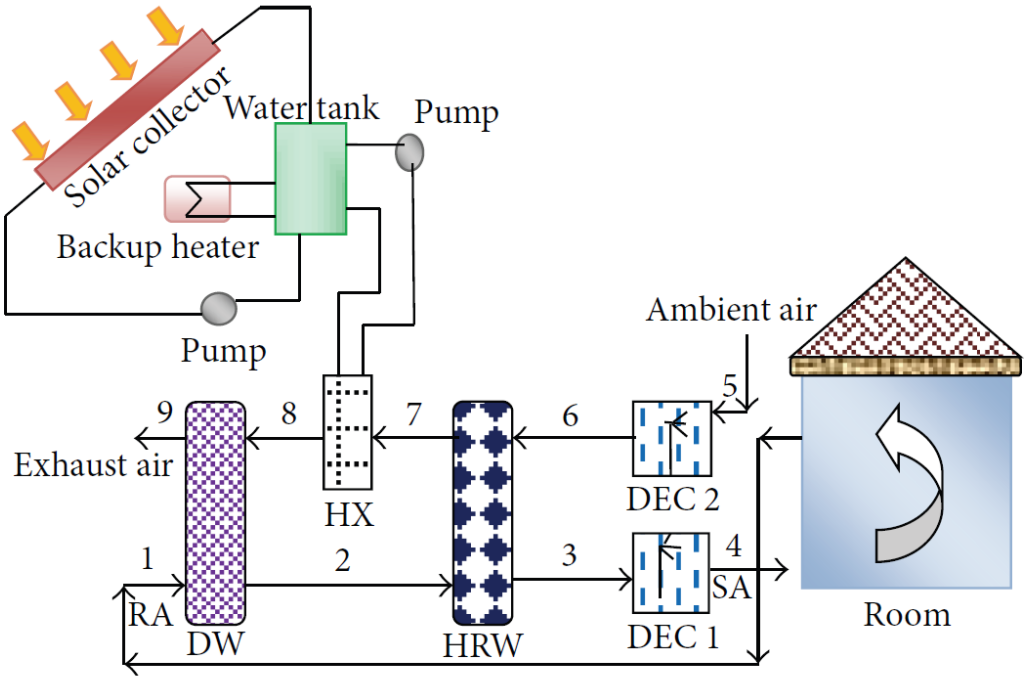



*Figure 2-23: Psychrometric chart of a two-stage solar desiccant cooling system in ventilation mode* [127].



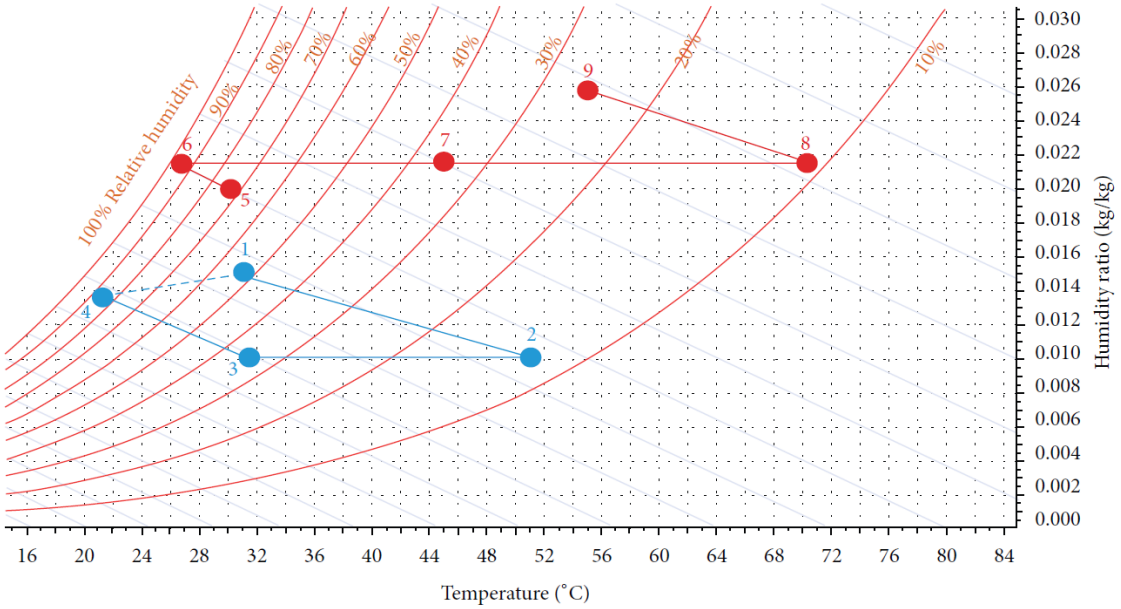
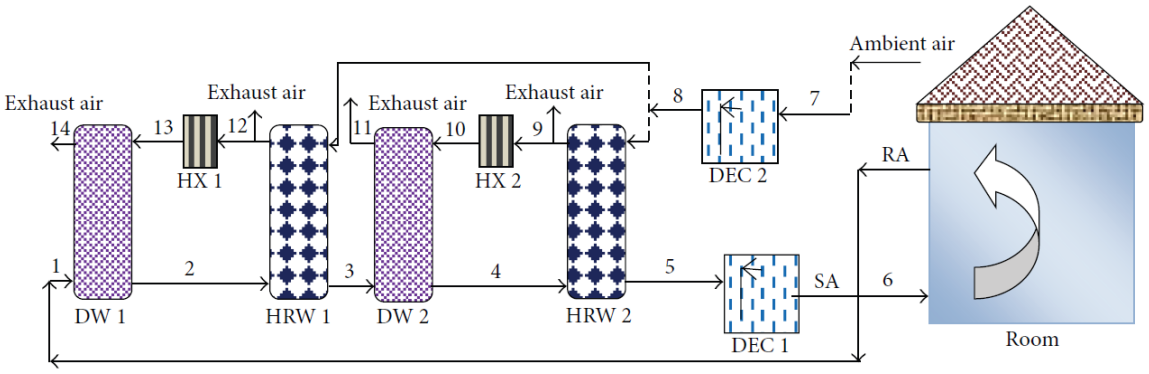



*Figure 2-24: Psychrometric chart of one-stage solar desiccant cooling system in recirculation mode* [127].



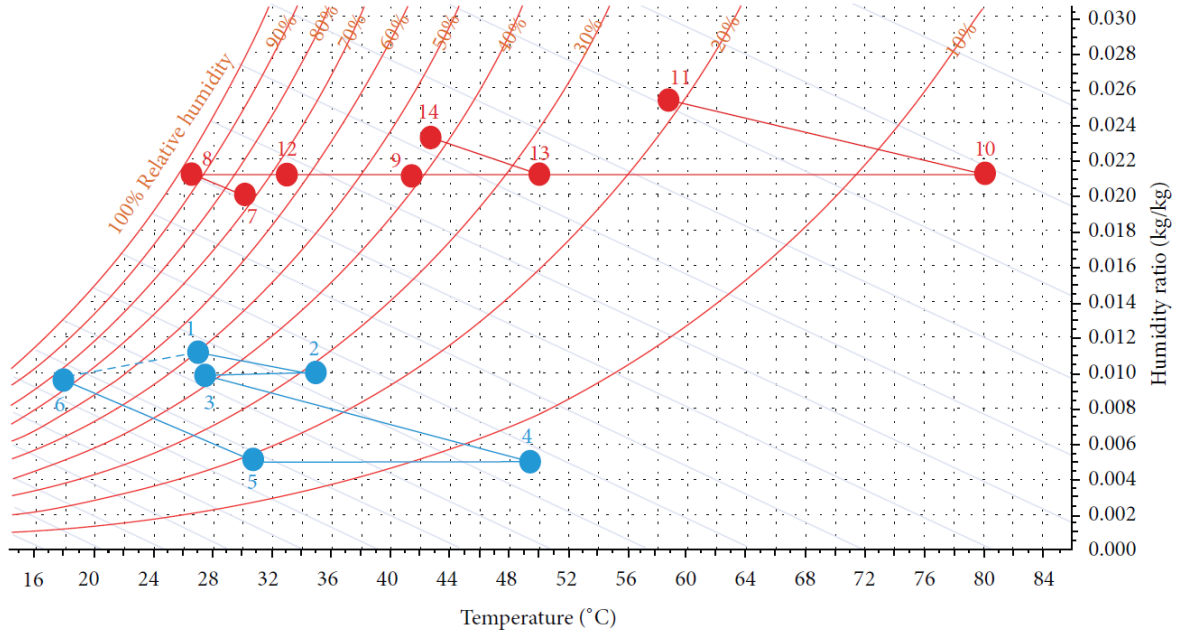




*Figure 2-25: Psychrometric chart of a two-stage solar desiccant cooling system in recirculation mode* [127].

Figure 2-26 shows another configuration for solar cooling systems developed by Merzouk et al. [128], who studied the performance of solar-driven solid desiccant cooling systems under the humid climate of the Algerian coast. The dehumidification process begins at Point 1, where the humid air is filtered. It then moves to Point 2, where the desiccant attracts moisture and leaves the air warm and dry. Point 3 cools the incoming air to dry exhaust air temperature. Point 4 rewets the air, restoring humidity. Point 5 ensures ventilation. Point 6 cools the exhaust air by humidification, and points 7 and 8 heat the air to absorb more moisture when passing through the desiccant wheel. Point 9 regenerates the desiccant wheel. Their results showed that moisture control related to the wet areas can be achieved.

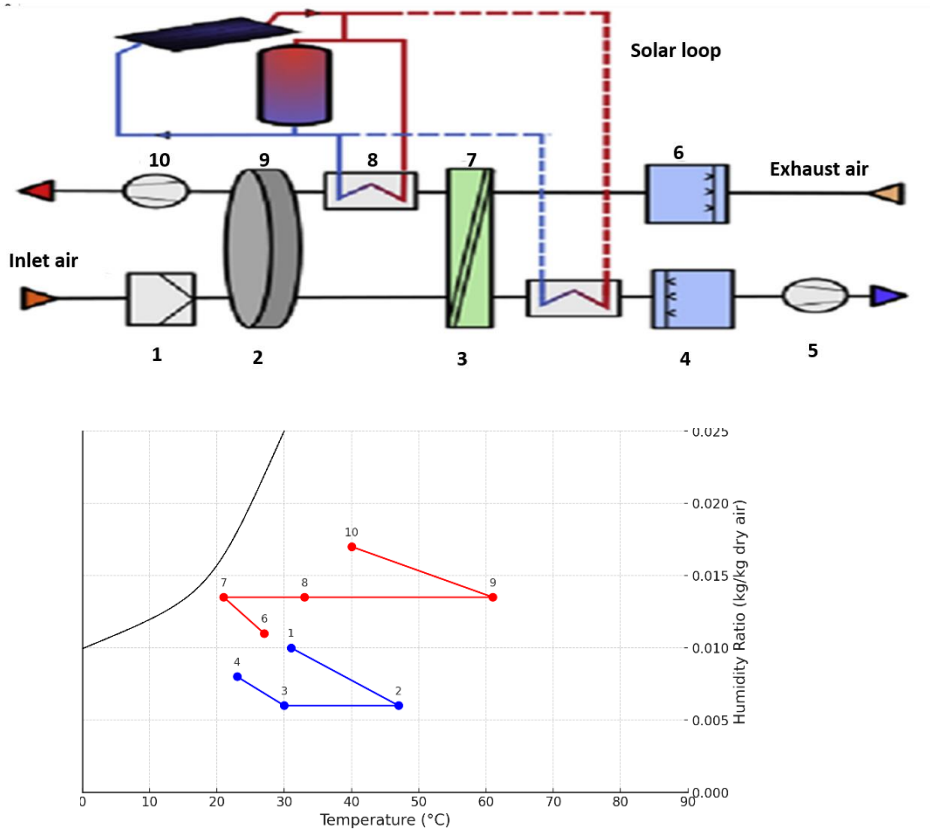



*Figure 2-26: Scheme of the desiccant cooling system and its evolution in the psychrometric chart* [128].

## 2.5.Experimental parameters to improve DW/DCHE performance

Ge et al. [129] built an experimental facility of a two-stage rotary desiccant cooling system to evaluate its performance. The material used as a desiccant is silica gel–haloids. The process involves the sequential passage of air through two desiccant wheels. After passing through each wheel, a sensible heat exchanger decreases its temperature. Their experimental results showed that lower inlet regeneration air temperature and humidity ratio led to better system performance, while increasing the inlet process air humidity led to a noticeable increase in

moisture removal. The system's coefficient of performance (COPth) is higher than 1 when the suggested regeneration temperatures are 60°C and 75°C.

Chung et al. [130] optimised a desiccant wheel speed and area ratio of regeneration to dehumidification as a function of regeneration temperature to improve the desiccant wheel's performance for cooling applications. The wheel's ability to remove moisture is critical to the system's overall performance. The wheel's performance is inversely affected by rising ambient temperatures and decreasing humidity levels.

Angrisani et al. [131] conducted an experimental study on desiccant-based air conditioning systems in southern Italy and showed that in the case of fixed regeneration temperature, as the ratio between the process and regeneration airflow rates increases, the effectiveness related to the dehumidification increases.

Tiwari [132] investigated several commercially available and newly fabricated desiccant wheels using lithium chloride and silica gel rotors. Their results showed that higher air temperature for the regeneration process leads to higher dehumidification potential. Antonellis et al. [133] established a numerical and experimental setup to study the desiccant wheel as a dehumidifier. The tested desiccant wheel is composed of a synthesised metal silicate material applied over an inorganic fibre substrate. Their studies found that the process airflow rate should be higher than that of regeneration.

Borowski et al. [134] investigated the impact of various operating parameters, such as inlet humidity ratio for process air, inlet volume flow rate, and Regeneration/Process (R/P) ratio. The adsorbent material was silica gel, and their results suggested that the desiccant cooling system could cool buildings under humid climatic conditions. Desiccant materials, such as silica gel and molecular sieve, have different moisture absorption capacities. Silica gel exhibits higher efficiency when used at a regeneration temperature of 80°C, but molecular sieve has a reduced capacity within the temperature range of 70°C to 140°C. With an increase in regeneration temperature, the capacity to remove moisture improved by 2.065 g/kg of dry air and 5.71 g/kg of dry air, respectively. Desiccant wheels have enhanced performance when subjected to a low process volume flow rate, and an increase in rotation speed results in a higher level of moisture removal, with optimal performance observed at 14 rpm.

Integrating a desiccant-coated heat exchanger (DCHE) with the evaporative cooler is a promising method for controlling air humidity [135]. This DCHE can adsorb water vapour from the coming humid air and deliver dry air to the evaporative cooler see Figure 2-22.

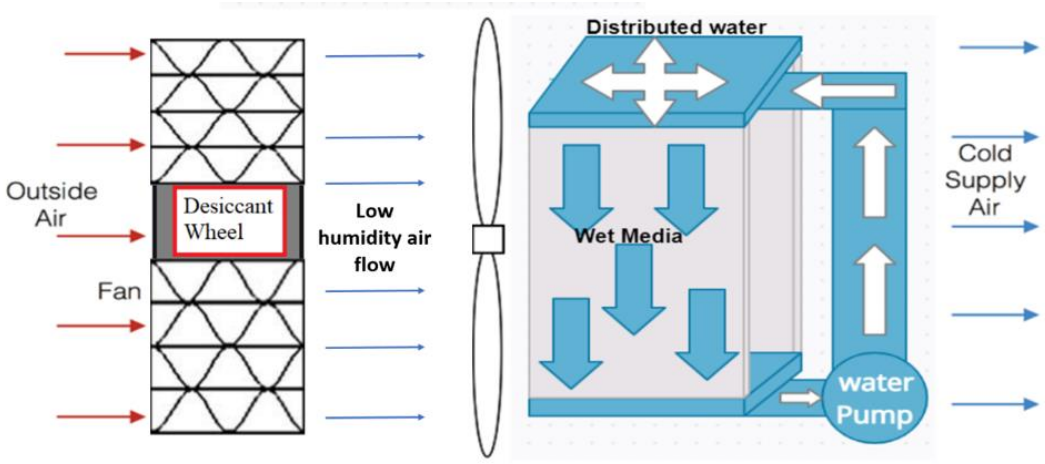



*Figure 2-27: Desiccant-coated heat exchanger before evaporative cooler.*

Kumar and Yadav [102] developed a solar energy-driven DCHE air-conditioning unit by integrating them with heat exchangers and direct evaporative coolers, as shown in Figure 2-23. Heat exchangers were used as pre-cooling devices to reduce process air temperature, while direct evaporative coolers were used as post-cooling devices. Solar evacuated tube collectors and cooling towers supplied the hot and cold water required to heat or cool the DCHE. Performance testing was conducted for cooling-dehumidification during summer and heating-humidification during winter conditions. Their results showed that the process air was pre-cooled by 4.1°C in the sensible heat exchanger, dehumidified and cooled by 1.5°C and MRC of 3.2 g/kg, and reduced by 3°C in the direct evaporative cooler. The system's average cooling capacity and $COP_{th}$ were 648 W and 0.45, respectively. The average dehumidification rate of the process air could be increased by 15.3% with pre-cooling. In winter, the DCHE was used without auxiliary units, and solar evacuated tube collectors provided hot water. Although the output did not meet the desired thermal comfort conditions, the authors concluded that with further developments, there is potential for using DCHE air conditioning systems as an alternative to conventional vapour compression systems.

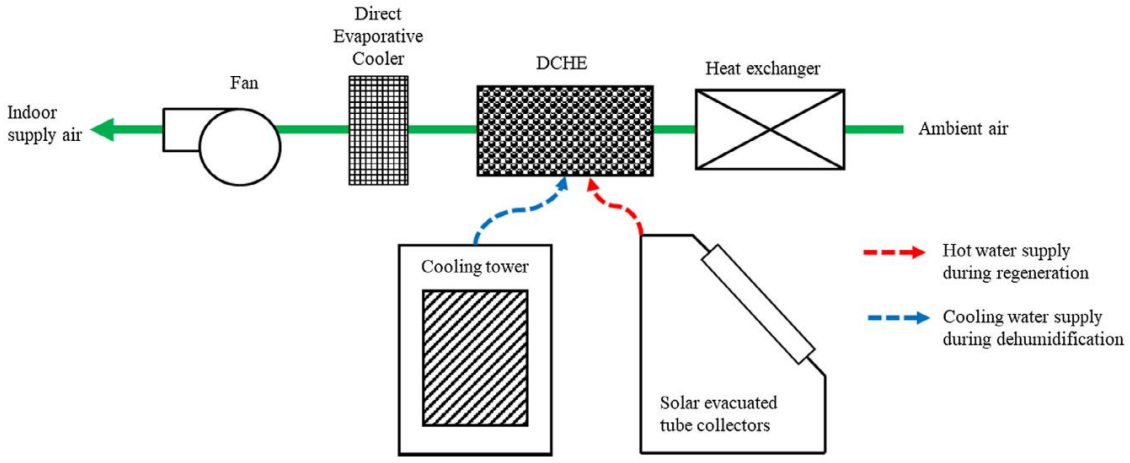



*Figure 2-28: DCHE air-conditioner integrated with solar collectors and Direct evaporative cooler* [49], [102].

Figure 2-29 shows a system that comprises two Dehumidification and Cooling (DCHEs) and two Evaporative Coolers (ECs). The DCHEs use water as an internal cooling fluid to drive desiccant adsorption and desiccant regeneration. The working mode of the DCHEs is periodically switched for continuous dehumidification and cooling. The outdoor air is dehumidified in DCHE A, then cooled in the regenerator and pumped into the evaporative cooler EC1. The process air is then supplied to the conditioned room. In the regeneration process, the return air is cooled in the evaporative cooler EC2, recovered heat in the regenerator, heated by a heater, reactivated by DCHE B, and discharged into the atmosphere. The DCHEs perform better in heat and moisture handling capacity than conventional dehumidification (desiccant wheel) [57].

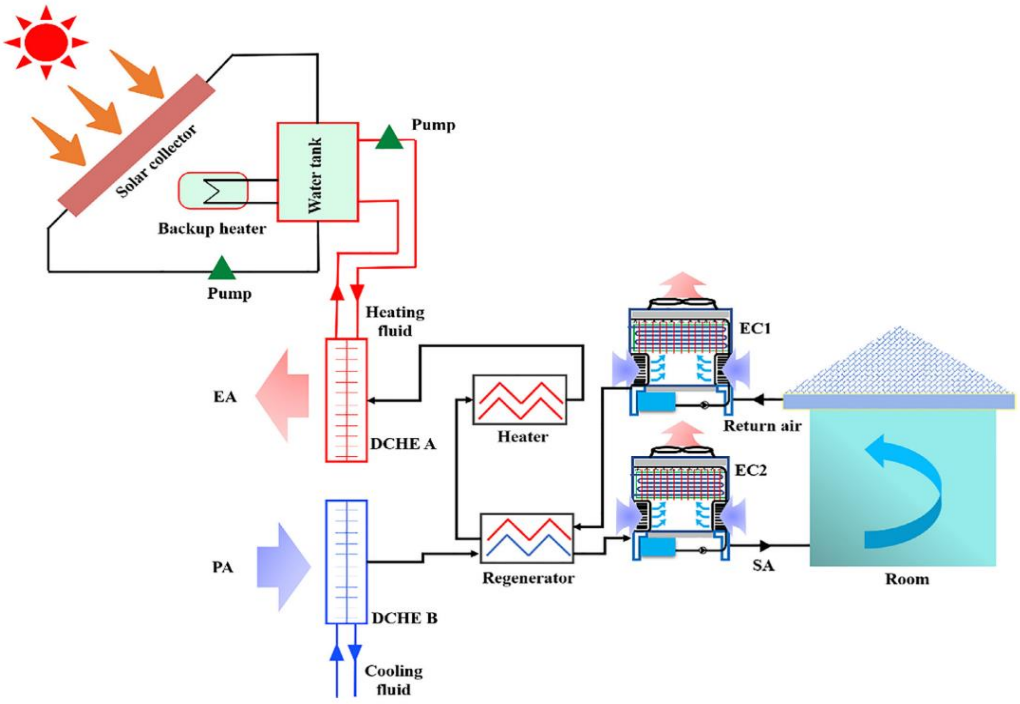



*Figure 2-29: The schematic diagram of the desiccant cooling system* [57].

## 2.6.Modelling of desiccant systems

Several studies were carried out to develop desiccant wheels for open cooling systems, and the designs of the desiccant wheels involve using solid adsorbent material like silica gel [136]. The operation of the desiccant wheel involves two processes, namely dehumidification and regeneration. In the dehumidification process, the moisture content of the process air is adsorbed by the adsorbent material, leading to process air leaving the desiccant wheel with lower humidity. In the regeneration process, the desiccant wheel is heated to remove the moisture adsorbed during dehumidification.

The mechanisms of mass and heat transfer in desiccant wheels are classified into two types: solid-side resistances (SSRs) and gas-side resistances (GSRs) [137]. SSRs consist of diffusion

and heat conduction within the air and convective heat and mass transfer between the air and the desiccant. They affect heat and mass transfer from the air stream to the desiccant wheel surface. GSRs neglect the solid resistance due to heat conduction and mass diffusion within the desiccant [138].

Beccali et al. [139] developed a simplified model to predict the performance of rotary desiccant wheels by fitting experimental data obtained from the industry to produce correlations for predicting the air outlet temperature and absolute humidity. This model is used to predict the performance of three different types of desiccant rotors made using various types of solid desiccants (Type I (silica gel), II (LiCl) and III (silica gel)). Zhang et al. [140] used heat and mass transfer equations to model a honeycombed rotary desiccant wheel. The numerical results were compared to experimental ones, showing good agreement with a maximum deviation of 3.5% and 6% for humidity and temperature, respectively.

Weixing et al. [141] created the first mathematical model for compact cross-flow desiccant-coated heat exchangers. They solved governing equations using a Newton iterative approach and discretized partial differential equations by the finite differential method. Critical assumptions were the adoption of the Lewis analogy for heat and mass transfer, neglecting the heat conduction and mass diffusion on the desiccant side, and a lumped parameter approach for thermodynamic properties.

A model for heat and mass transfer in fin-tube dehumidifiers (DCHEs) is presented in the studies by Ge et al. [104], [142] The model is discretized using a backward finite difference scheme, and the governing equations are solved using the Newton-Gauss method. Additional developments include incorporating solar evacuated tube collectors (DCHEs) into the model and utilising weather data to ascertain ambient conditions that satisfy air-conditioning demands. An aggregated parameter approach to thermodynamic properties, neglecting heat conduction and mass diffusion, uniformly coated desiccant molecules, and a one-dimensional system are among the assumptions used. Mrinal et al. [143] developed a 2D model that integrated fin-efficiency and desiccant-side mass diffusivity. They then performed a parametric study to investigate how changes in the geometric parameters of the heat exchangers affect dehumidification and thermal performance.

Lee et al. [143] presented a mathematical model to simulate heat and mass transport processes in a desiccant-coated fin tube heat exchanger (DCFTHX). The model incorporates apparent fin efficiency and solid side resistance due to the finite diffusivity of moisture and adsorbed water in the desiccant matrix. They conducted parametric analysis, assuming 50°C water for regeneration and plotted outlet-specific humidity and air temperature during dehumidification against varying geometrical and flow parameters. Cooling capacity, auxiliary

power consumption, system level $COP_{th}$, and energy savings were also plotted. Their results showed that a smaller fin pitch leads to more dehumidification and higher average outlet temperature, while thicker desiccant layers result in better performance but larger auxiliary power consumption. Dehumidification performance is insensitive to fin thickness and a larger mass flow rate of water results in better dehumidification. DCFTHX can be an excellent add-on component to conventional HVAC systems if low-grade waste heat (50°C) is available. Incorporating DCFTHX can help realize up to 31% energy savings for an existing high-efficiency HVAC system with a compressor $COP_{th}$ of 5.4. However, geometrical design and flow conditions are critical for maximizing benefits.

A new analytical model is developed by Bahrami et al. [144] to predict the performance of a dehumidification(DCHE) system, accurately predicting humidity ratio, temperature variations, MRC, and $COP_{th}$. The model considers linear and exponential air flow temperature and humidity ratio profiles. After comparing the experimental data, it was concluded that an exponential profile is more realistic and provides more accurate results.

Huang et al. [145] developed a transient numerical model to predict the dehumidification performance of an air-cooled desiccant-coated cross-flow heat exchanger (DCCFHE) system. The model considered the fin efficiency of DCCFHE and was verified by comparing it with experimental results. The authors carried out a parametric study to investigate the effects of several major operating and structural parameters on dehumidification performance. The main findings include that smaller process air velocity improved dehumidification performance as the minimum transient outlet humidity ratio decreases and the effective dehumidification time increases. The cooling air also improved dehumidification performance by reducing the minimum transient outlet humidity ratio and increasing the effective dehumidification time. Dehumidification performance increases nearly linearly with the increase in desiccant layer thickness but is sensitive to fin pitch.

## 2.7.Summary of Key Findings and Knowledge Gap

Using desiccant wheels/heat exchangers in air conditioning systems offers major advantages in lower energy consumption, $CO_2$ emissions, and costs.

From the above literature, the following key findings can be made:

- Several experimental and numerical works have used rotating desiccant wheels to investigate the different types of desiccant heat exchangers in open cooling systems. However, they are limited in using silica gel, zeolite, and activated carbon with limited water adsorption uptake.

- Different configurations for desiccant cooling systems were established using different thermal devices such as direct-indirect evaporative coolers, humidifiers, cooling coils, and heat recovery wheels to reach optimum output conditions but still limited to achieving higher humidity levels.
- The COP of the desiccant system is affected by the system operating conditions, such as the airspeed, operating temperature, and humidity, which are input parameters for regeneration and dehumidification.
- The design of the desiccant-coated heat exchanger significantly affects the open cycle performance in terms of COP and moisture removal during the dehumidification-regeneration processes. The type of fins, the geometry shape, and air direction play an important role in improving desiccant-coated heat exchanger behaviour. Also, the number of heat exchangers and the weight of the adsorbent material affect moisture adsorption in the cooling system.
- The configurations for heating applications using desiccant-coated heat exchangers are are still limited.

Therefore, the knowledge gap can be summarised as the following:

- Most studies are regarding rotating wheels, and research on stationary heat exchangers is still limited. The use of 3D CFD modelling to simulate the performance of desiccant-coated heat exchangers under various operating conditions is still limited.
- The numerical models developed to simulate the performance of the MOF materials are still limited and need to be investigated for different desiccant-coated heat exchangers.
- Using electrical heating to reactivate the desiccant material is still limited in both simulation and experimental studies.
- Integrating the stationary desiccant-coated heat exchanger with other thermal elements for space air conditioning is still limited.

# Chapter 3 Modelling of desiccant-coated heat exchanger

This chapter describes a one-dimensional dynamic model for a single channel in a stationary desiccant-coated heat exchanger (DCHE) based on a honeycomb structure coated with MOF materials. The honeycomb construction offers an increased surface area-to-volume ratio, enabling more desiccant material to be coated within a specific volume. This structure enhances the surface area of contact between the air and the desiccant, enhancing the efficacy of moisture adsorption. The model was developed using MATLAB software to predict the stationary DCHE based on the honeycomb structure performance in terms of moisture removal rate at various airflow input conditions and used to assess the effectiveness of four MOF adsorbent materials, compared to Silica Gel [146], namely Aluminium fumarate, Mill-100(Fe), CPO-27(Ni) and MIL-101(Cr).

(**This chapter is based on the previously published papers: Andrew N. Aziz, Saad Mahmoud, Raya Al-Dadah, Ibrahim Albaik, " Numerical Investigation of Desiccant Cooling Using Aluminium Fumarate Metal Organic Framework Material", Heat Powered Cycles Conference 2021. Andrew N Aziz, Saad Mahmoud, Raya Al-Dadah, Mohamed A Ismail, Mohammed K Al Mesfer" Numerical and experimental investigation of desiccant cooling system using metal organic framework materials", Applied Thermal Engineering, 2022**)

## 3.1. One-dimensional dynamic numerical model of mass and heat transfer for stationary desiccant-coated heat exchanger

Figure 3-1 shows a single channel's side view/cross-sectional area in a DCHE integrated with MOF material. Mass and heat transfer between the air and the adsorbent material are the dominant physical phenomena that affect the performance of the adsorbent material inside the channel.

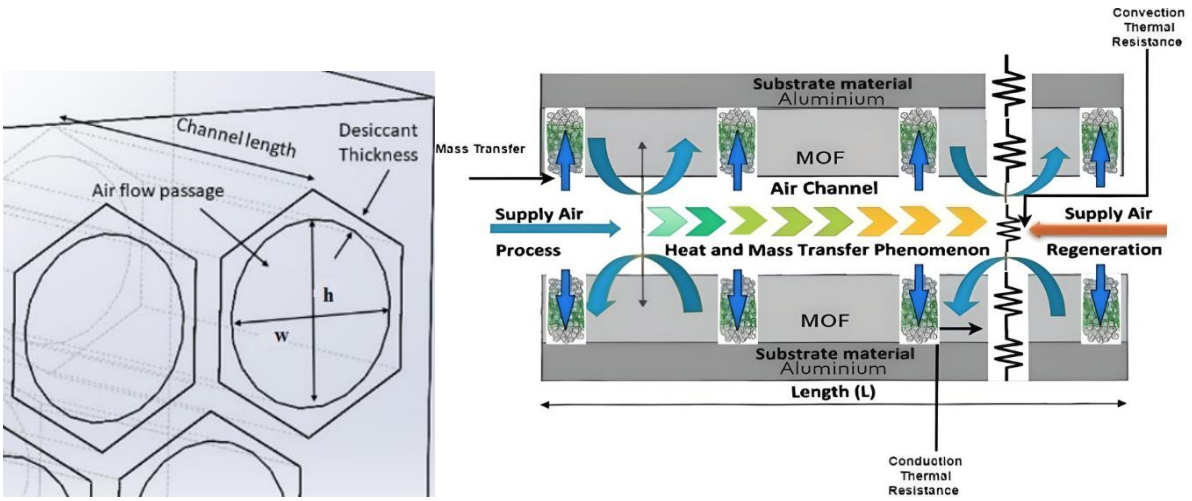



*Figure 3-1: side view/cross-sectional for one channel from the desiccant wheel.*

The mass conservation equation of moisture in the air is written as [147]:

$$\rho_a \, d_e \left(\frac{\partial W_p}{\partial t} + u \frac{\partial W_p}{\partial x}\right) = K_y \left(W_d - W_p\right) \quad (3\text{-}1)$$

The term on the equation's left-hand side (LHS) represents the amount of moisture stored within the desiccant material. The second phrase describes the process of mass diffusion occurring within the solid desiccant in the axial direction. The quantity on the right-hand side of Equation (3-1) represents the convective mass transfer between the air and desiccant. Where $\partial W_p$ is the water content in desiccant, $\rho_a$ is the air density, $u$ is the velocity, $K_y$ is coefficient of mass convection (kg/m2 s) and $d_e$ is the hydraulic diameter (m).

The energy conservation for the air is given as:

$$\rho_a C_{pa} d_e \left(\frac{\partial T_p}{\partial t} + u \frac{\partial T_p}{\partial x}\right) = h \left(T_d - T_p\right) + K_y \, C_{pv} \left(W_d - W_p\right)\left(T_d - T_p\right) \quad (3\text{-}2)$$

Where

The equation's left-hand side represents the energy storage components of the desiccant material and the heat conduction inside it. The right-hand side of the equation represents the convective heat transfer between the air and solid desiccant, the sensible heat transfer between the air and solid desiccant, and the heat released during the adsorption process in the desiccant layer. Where $C_{pa}$ is the air specific heat (kJ/kg K), $C_{pv}$ is specific heat of liquid vapour, $T_d$ is the desiccant temperature and $T_p$ is the air temperature.

Desiccant moisture mass conservation is determined by:

$$\delta d \, \rho_d \left(\frac{\partial W}{\partial t} - De \frac{\partial W}{\partial x^2}\right) = K_y \left(W_p - W_d\right) \quad (3\text{-}3)$$

where $\delta d$ is the thickness of the desiccant felt (m), and $\rho_d$ is the desiccant density.

Desiccant energy conservation can be written as follows:

$$\left(\frac{\partial T_d}{\partial t} - \frac{K_d}{C_{pd} \, \rho_d} \frac{\partial T_d}{\partial x^2}\right) \delta d . \rho_d . C_{pd} = h \left(T_p - T_d\right) + q_{st} . \, K_y \left(W_p - W_d\right) + C_{pv} \, K_y \left(T_p - T_d\right)\left(W_p - W_d\right) \quad (3\text{-}4)$$

Where $W_d$ is the adsorbent material equilibrium uptake expressed as a function of the desiccant relative humidity as [148]:

$$W_d = 0.62188 \frac{P_v}{P_{atm} - P_v} = 0.62188 \frac{RHd}{(P_{atm} - P_{vs}) - RHd} \quad (3\text{-}5)$$

The effective diffusivity (De) is determined as [149]:

$$De = D_s \frac{1.6\times 10^{-6}}{\tau} e^{(-0.974\times 10^{-6}\frac{q_{st}}{T_d})} \quad (3\text{-}6)$$

Where $q_{st}$ is the heat of adsorption given as [148]:

$$q_{st} = A = h_{fg}[1 + 0.2843e^{(-10.28W)}] \quad (3\text{-}7)$$

Where $h_{fg}$ is the latent heat of evaporation for water and is given by [148]:

$$h_{fg} = (2504.4 - 2.4425\ T_d)\ 1000 \quad (3\text{-}8)$$

The desiccant relative humidity equations for Silica Gel [146], Aluminium fumarate, Mill-100(Fe), CPO-27(Ni) and MIL-101(Cr) are given by equations 3-9 [148], 3-10, 3-11, 3-12, and 3-13 respectively:

$$RHd = 0.0078 - 0.0579*W + 24.16551*W^2 - 124.478*W^3 + 204.226*W^4 \quad (3\text{-}9)$$

$$RHd = -0.0399 + 7.0476*W - 55.534*W^2 + 159.67*W^3 - 138.41*W^4 \quad (3\text{-}10)$$

$$RHd = 1172.6*W6 - 1833*W5 + 1026.5*W4 - 235.73*W3 + 14.23*W2 + 2.3337*W - 0.0084 \quad (3\text{-}11)$$

$$RHd = 0.0027*e^{(10.837*W)} \quad (3\text{-}12)$$

$$RHd = 7.8402*W^6 - 31.319*W^5 + 45.391*W^4 - 27.049*W^3 + 3.5604*W^2 + 2.1102*W - 0.0333 \quad (3\text{-}13)$$

Equation 3-10 to 3-13 are developed using the adsorption isotherm measured by E. Elsayed [31] replotted using the relative humidity versus the water vapour uptake as shown in Figure 3-2.

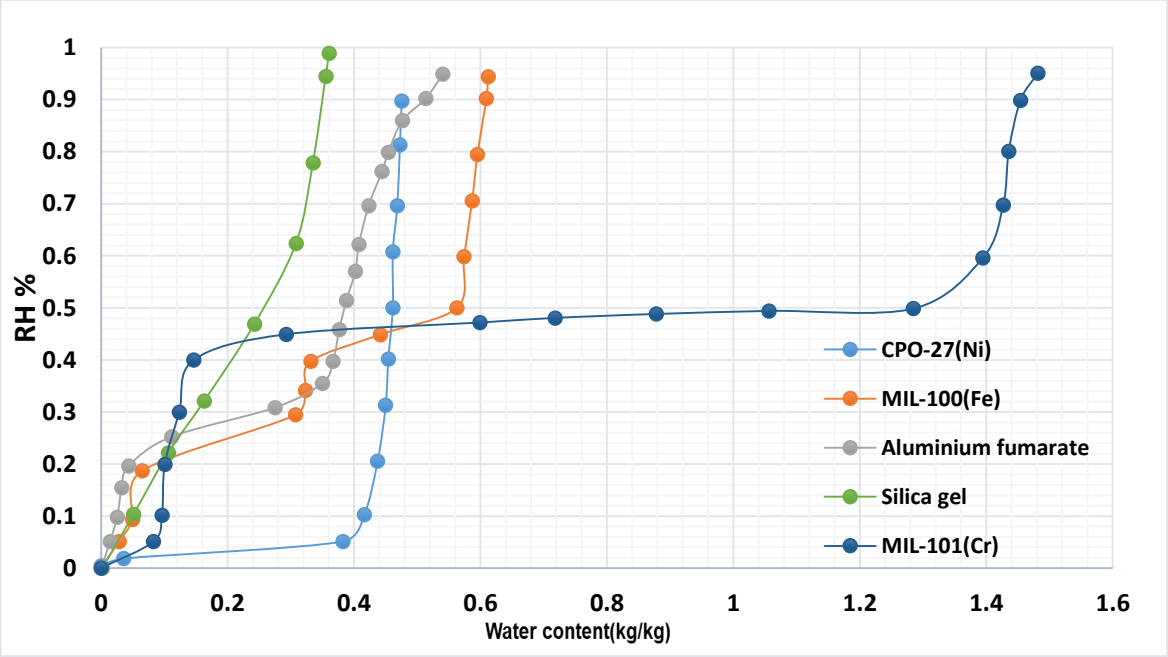



*Figure 3-2: Isotherm curve for MOF materials.*

The channel geometry is described by equations (3-14) –(3-16):

$$A_f = \pi \left(\frac{h}{2}\right)\left(\frac{w}{2}\right) \tag{3-14}$$

Where $A_f$ is the cross-sectional area of airflow passage, w is the channel width, and h is channel height.

$$A_t = \pi \left(\frac{h}{2} + \delta d\right)\left(\frac{w}{2} + \delta d\right) \tag{3-15}$$

Where $A_t$ is the total cross-sectional area of one channel, and $\delta d$ is the flet thickness.

The hydraulic diameter $D_h$ can be found as

$$D_h = \frac{4\,A_f}{p_e} \tag{3-16}$$

Where $p_e$ represents the perimeter of flow passage for one channel and can be determined by,

$$p_e = 2\pi \sqrt{\left(\frac{h}{2}\right)^2 + \left(\frac{w}{2}\right)^2} \tag{3-17}$$

Figure 3-3 shows a flow diagram of the developed mathematical model highlighting the significant steps used and the sequence of tasks. The model boundary conditions are as follow:

$$\frac{\partial T_d}{\partial x}\Big|_{x=0} = \frac{\partial T_d}{\partial x}\Big|_{x=L_w} \tag{3-18}$$

$$\frac{\partial W_d}{\partial x}\Big|_{x=0} = \frac{\partial W_d}{\partial x}\Big|_{x=L_w} \tag{3-19}$$

The initial conditions used in this modelling include the initial temperature of the air and desiccant (Tp(x,0)= Tp0 and Td(x,0)= Td0), the water content in the desiccant (W(0,t)) and the humidity ratio of the air and desiccant (Wp(x,0)= Wp0 and Wd(x,0)= Wd0) and they are assumed to be uniform. The model was developed using the finite difference method in Matlab software applied to a control volume for one channel. In this modelling, the following assumptions are made: the heat exchanger is a stationary desiccant-coated heat exchanger of square 15 cm ×15 cm with identical ellipse with height (h) and width (w) flow channel after coating with desiccant for simplicity. Heat conduction and mass diffusion in moist air are neglected. Mass diffusion of vapour in desiccant is neglected. The thermo physical properties of the dry air and the properties of the dry desiccant material as well as of the matrix, are constant. The channels were identical in coating thickness and they were adiabatic.

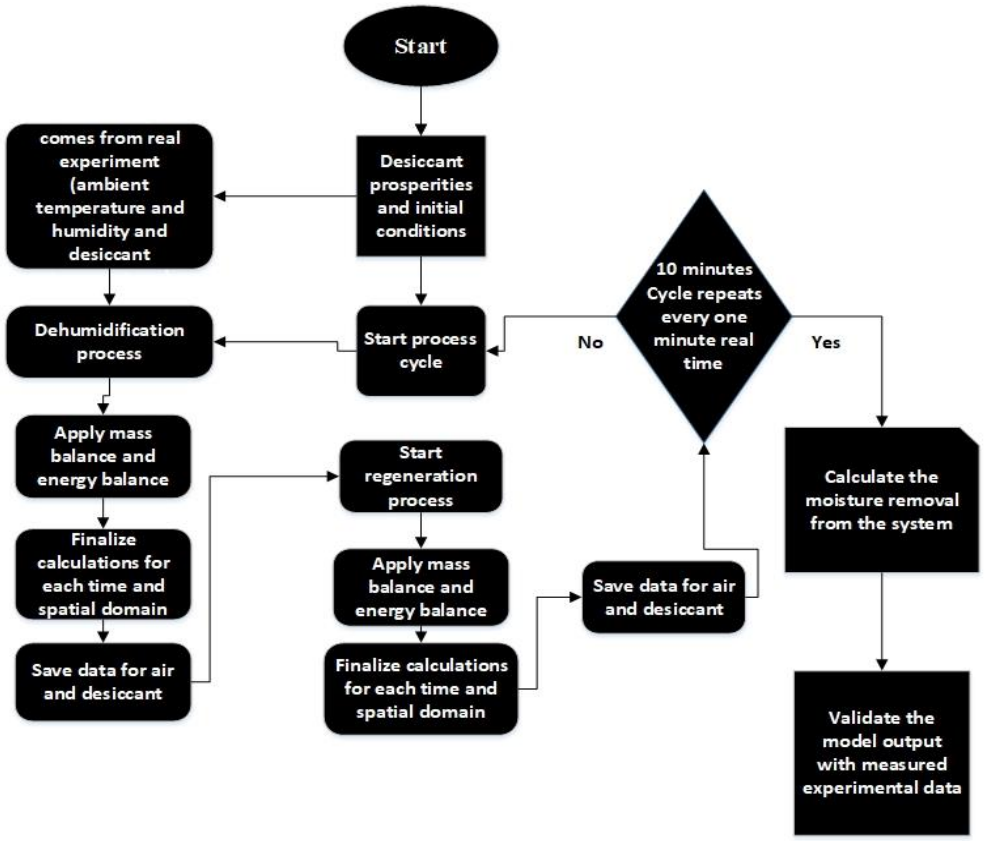



*Figure 3-3: flow chart for the stationary desiccant system process.*

Table 3-1 represents the dimensions of the modelled honeycomb channel and the properties and operating conditions of the process air. Table 3-2 represents the properties of the investigated MOF materials used as inputs parameters in the model. Such properties were measured at the University of Birmingham laboratory using helium pycnometer for density measurement, differential scanning calorimetry for specific heat capacity by E. Elsayed [31]. As for silica gel, its properties were taken from Yadav [150]. The solid tortuosity and Surface diffusivity values were brought from the literature listed in table 3-2.

*Table 3-1 Physical channel dimensions and operating conditions for process air.*

| | | |
|---|---|---|
| Desiccant width (Lw) | 0.015 | [m] |
| Channel height (h) | 0.006 | [m] |
| Channel pitch (w) | 0.008 | [m] |
| Desiccant thickness ($\delta d$) | 0.0015 | [m] |
| Air density ($\rho_a$) | 1.016 | [kg/m3] |
| Specific heat of air ($C_{pa}$) | 1005 | [kJ/kg/K] |
| Thermal conductivity of air ($K_a$) | 0.175 | [W/mK] |
| Specific heat of water vapours($C_{pv}$) | 1864 | [kJ/kg/K] |
| Nusselt number (Nu) | 2.45 | |
| Sherwood number (Sh) | 2.5 | |
| Atmospheric Pressure (P) | 1.01325 × 105 | [Pa] |
| Facial air velocity (u) | 3.1 | [m/s] |

Table 3-2 Thermophysical properties of silica gel and Aluminium fumarate MOF material.

| Material | Density ($\rho_d$) | Thermal conductivity ($K_d$ ) | Specific heat ($C_{pd}$) | Surface diffusivity | Porosity | Maximum water content | solid tortuosity ( $\tau$) |
|---|---|---|---|---|---|---|---|
| Silica gel | 550 [150] | 0.175 | 921 | 1.6e-10 [150]. | 0.4 | 0.34 | 2.8 [151] |
| Aluminium fumarate | 520 [31] | 0.08+1.4E-4$T_{bed}$ [31]. | 970 | 3.63e-14 [152]. | 0.67 | 0.54 | 2.8 |
| MIL-100(Fe) | 422 [31] | 6.5E-4$T_{bed}$-0.155[31] | 990 | 5.47e-12 [153] | 0.79 | 0.6 | 0.25 [153] |
| MIL-101(Cr) | 295.9 [31] | -2.155E-2+1.7E-4$T_{bed}$ [20] | 1100 | 1.6e-16 [154] | 0.82 | 1.4 | 1.14 [155] |
| CPO-27(Ni) | 440 [31] | 4.6E-4Tbed-0.077 [31] | 970 | 0.142e-4 [156] | 0.76 | 0.47 | 2.74 [156] |

Figure 3-4 shows the flow diagram of the input and output air passing through the stationary desiccant heat exchanger during dehumidification and regeneration processes.

In Figure 3-4, Point 1 represents the ambient air conditions, point 2 represents the output air conditions of the dehumidification process and point 3 is the input air conditions for regeneration process and point 4 is the output air conditions.

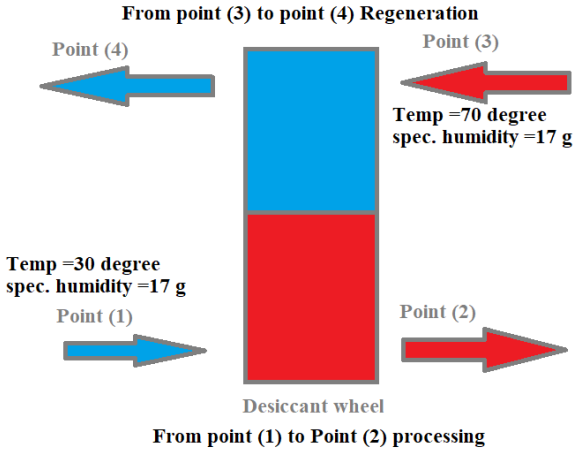



*Figure 3-4: Wheel and air flow passage presentation.*

Two main parameters are used to characterise the desiccant cooling system performance with various MOF materials namely COP and moisture removal rate. Low COP leads to an increase in the consumed energy and hence the system operating cost [157]. The other parameter is the moisture removal which depends on the selected adsorbent material and its ability to adsorb water from air [158].

The coefficient of performance for the desiccant system can be calculated using Eq. 3-20

$$\mathrm{COP} = \frac{(\mathrm{W_{p\ initial}} - \mathrm{W_{p\ Final}})q_{st}}{T_{reg} - T_{a\ initial}} \qquad (3\text{-}20)$$

Figure 3-5 shows the predicted steady-state analysis for moisture removal and coefficient of performance for silica gel compared to Yadv's modelling results showing maximum deviation of 8.4%. The validated model was then operated using Aluminium fumarate, MIL-100(Fe), MIL-101(Cr) and CPO-27(Ni) properties. Table 3-3 compares the steady-state model output including COP and Moisture removal rate at air velocity of 2.5m/s, temperature of 30°C, specific moisture content of 17g/kg, regeneration air with inlet conditions of 70°C and specific moisture content of 17g/kg. It is clear that Aluminium fumarate produced the highest COP of 0.65 with water removal rate of 12.65g/kg dry air and MIL-101(Cr) produced the highest moisture removal of 15.99 g/kg dry air but with COP of 0.44 compared to silica gel and other

MOF materials used. Therefore, Aluminium fumarate was used in the experimental testing presented in section 3.2. Figure 3-6 shows a psychrometric chart for Aluminium fumarate dehumidification and regeneration processes compared with Silica gel.

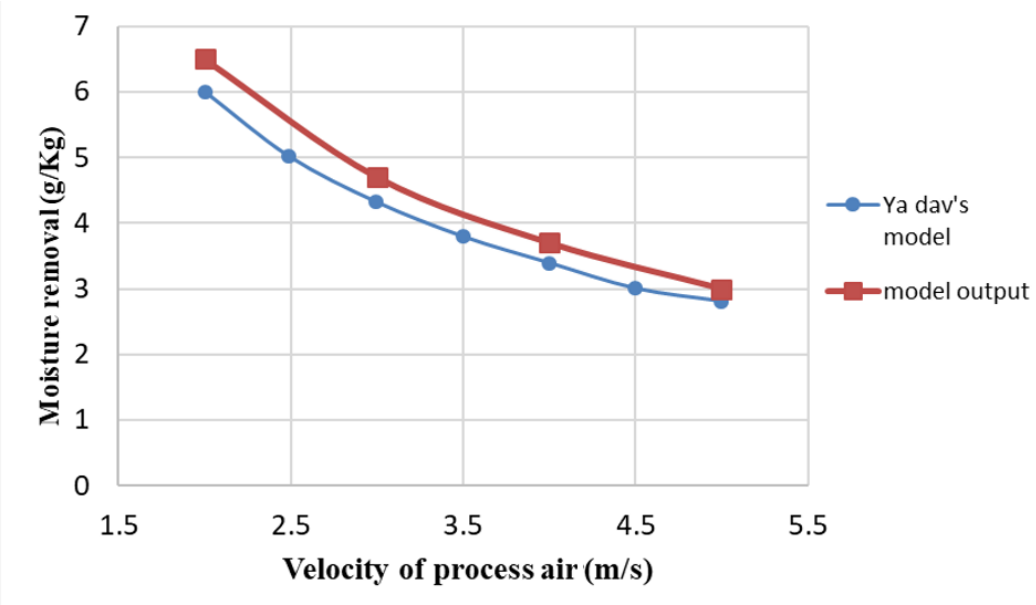
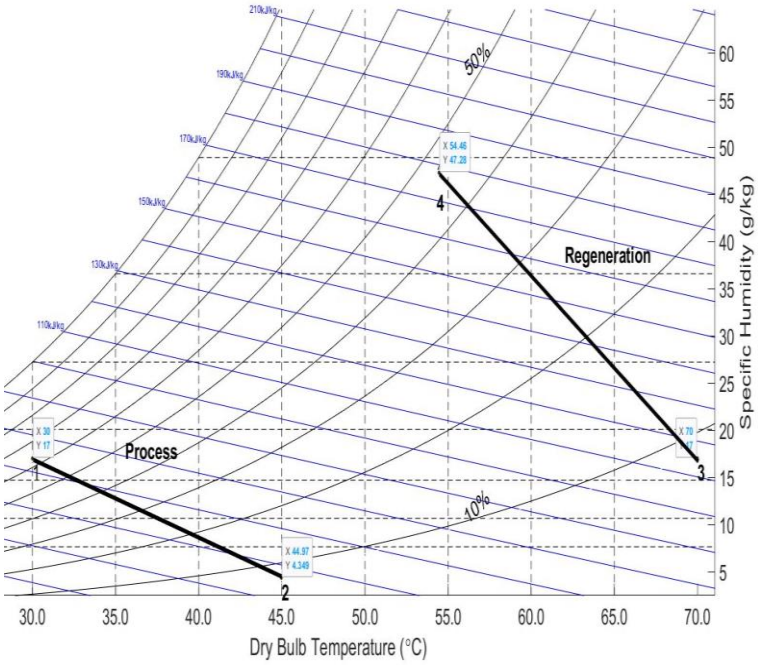


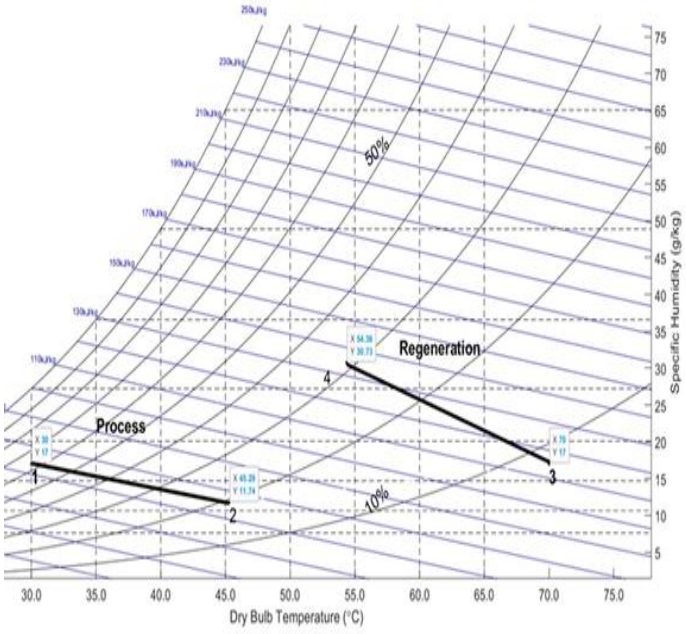

*Figure 3-5: Inlet velocity change vs moisture removal.*

Table 3-3 Model results for both regeneration and dehumidification processes.

| Material | Initial air temp. (ºC ) | Initial specific humidity | Output air temp. (ºC) | Output specific humidity (g/kg) | Initial air temp. (ºC) | Initial specific humidity | Output air temp (ºC) | Output specific humidity (g/kg) | COP For desiccant wheel | Moisture removal (Grams) |
|---|---|---|---|---|---|---|---|---|---|---|
| | **Process** | | **Process** | | **Regeneration** | | **Regeneration** | | | |
| | **Point 1** | **Point 1** | **Point 2** | **Point 2** | **Point 3** | **Point 3** | **Point 4** | **Point 4** | | |
| Silica gel | 30 | 17 | 45.29 | 11.74 | 70 | 17 | 54.36 | 30.73 | 0.3684 | 5.26 |
| Aluminium fumarate | 30 | 17 | 44.97 | 4.349 | 70 | 17 | 54.46 | 47.28 | 0.6591 | 12.651 |
| MIL-100(Fe) | 30 | 17 | 42.83 | 9.094 | 70 | 17 | 46.07 | 30.82 | 0.4253 | 7.906 |
| MIL-101(Cr) | 30 | 17 | 39.36 | 1.011 | 70 | 17 | 60.41 | 42.33 | 0.4408 | 15.989 |
| CPO-27(Ni) | 30 | 17 | 44.04 | 10.45 | 70 | 17 | 49.95 | 32.88 | 0.3963 | 6.55 |




(A)Aluminium fumarate.




(B)Silica gel

*Figure 3-6: psychrometric representation for stationary model output.*

## 3.2.Experimental setup

Figure 3-7 shows the experimental facility used to test the performance of a desiccant-coated heat exchanger with Aluminium fumarate as the adsorbent material. It consists of an evaporative cooler and a 15 cm ×15 cm × 50 cm duct, which contains a honeycomb structure coated with Aluminium fumarate and mounted on a scale to measure the weight change during the process.

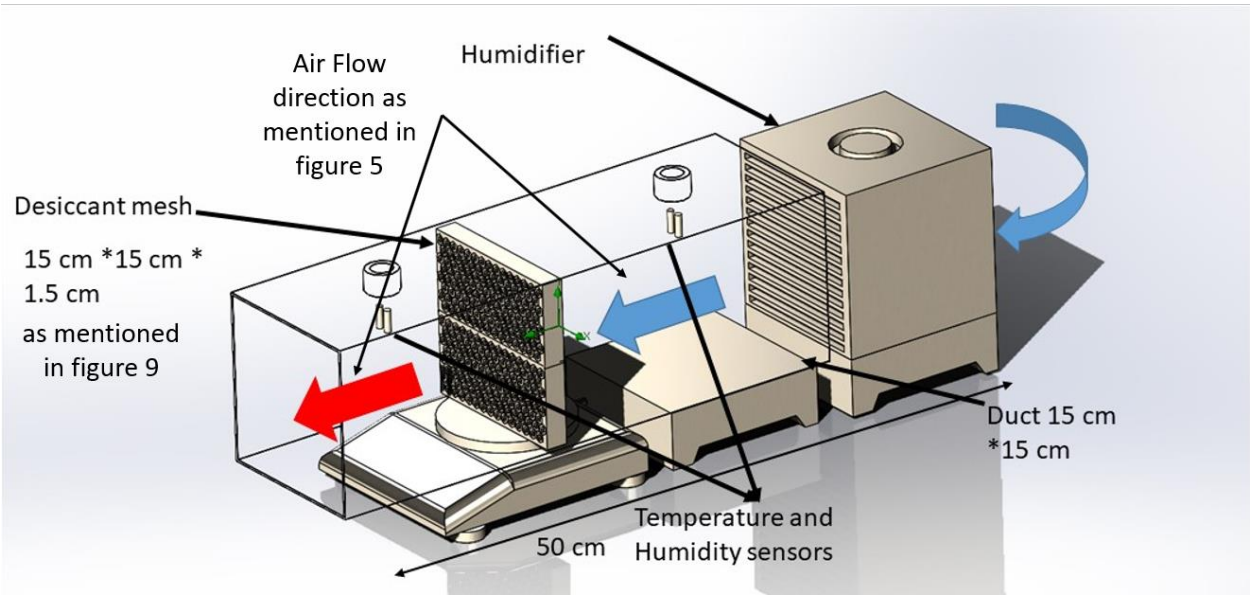



*Figure 3-7: 3-D drawing for the test facility.*

The coated honeycomb structure acts as a desiccant coated heat exchanger (DCHE). The Aluminium fumarate MOF is bought from MOF technology Limited company and the used coating process is based on a method developed by E. Elsayed et al.[31]. This coating method was tested at the University of Birmingham, showing that the adsorption capacity before and after coating is still the same. The use of desiccant coating can offer many advantages compared to packing in terms of increasing durability, improving heat transfer by reducing thermal contact resistance and, therefore, improving the adsorption/desorption process. This makes the coating better than the conventional packed technique. However, as the thickness of the coating layer increases the mass transfer rate decreases, so it needs to be optimized. In this process, a 20 grams binder is mixed with 400 grams Aluminium fumarate solution in 2 liters of distilled water. The solution is sprayed on the honeycomb structure surfaces after cleaning them from the rust and galvanic layer, then dried in an oven for 2 hours. The spraying process was repeated until a specific amount of adsorbent material was achieved. Figure 3-8 shows the coated honeycomb structure and table 3-4 lists its weight before and after coating. This prototype contains 77.5 grams of Aluminium fumarate. This amount of MOF can adsorb 38.75 grams of moisture from air at equilibrium, which can be a good indicator of the system's behaviour.

The evaporative cooler is used to supply humid air to the honeycomb desiccant wheel and it has a three-speed fan producing air with speed ranging from 1.5 m/s to 3.1 m/s. The evaporative cooler has frontal area of 15 cm × 15 cm and a length of 15 cm. Two Elitech GSP-6 Temperature and Humidity Data Loggers were used in this test facility, which can read 16000 Points, integrated with Dual Sensors one for temperature and the other for humidity. The temperature sensor measurement has a range of -40 °C to 85 °C and an accuracy of ± 0.3 °C. The humidity sensor measurement has a range of 10% to 99% RH and an accuracy of ±3% RH. Proster anemometer is used to measure the air speed through the duct, it measures the air speed ranging from 0-30m/s with an accuracy of ± 5%. Oertling JC41 electronic balance scale is used to measure the weight of the coated honeycomb structure during the testing process.

Table 3-4 Weight of honeycomb structure before and after coating.

| |
|---|
| honeycomb Mesh frontal Area = **0.15 m * 0.15 m =0.0225 m$^2$** |
| honeycomb Mesh weight before coating = **49 gm** |
| honeycomb Mesh after coating = **126.5 gm** |
| honeycomb Mesh thickness = **1.5 cm** |
| Aluminium fumurate net weight = **77.5 gm** |

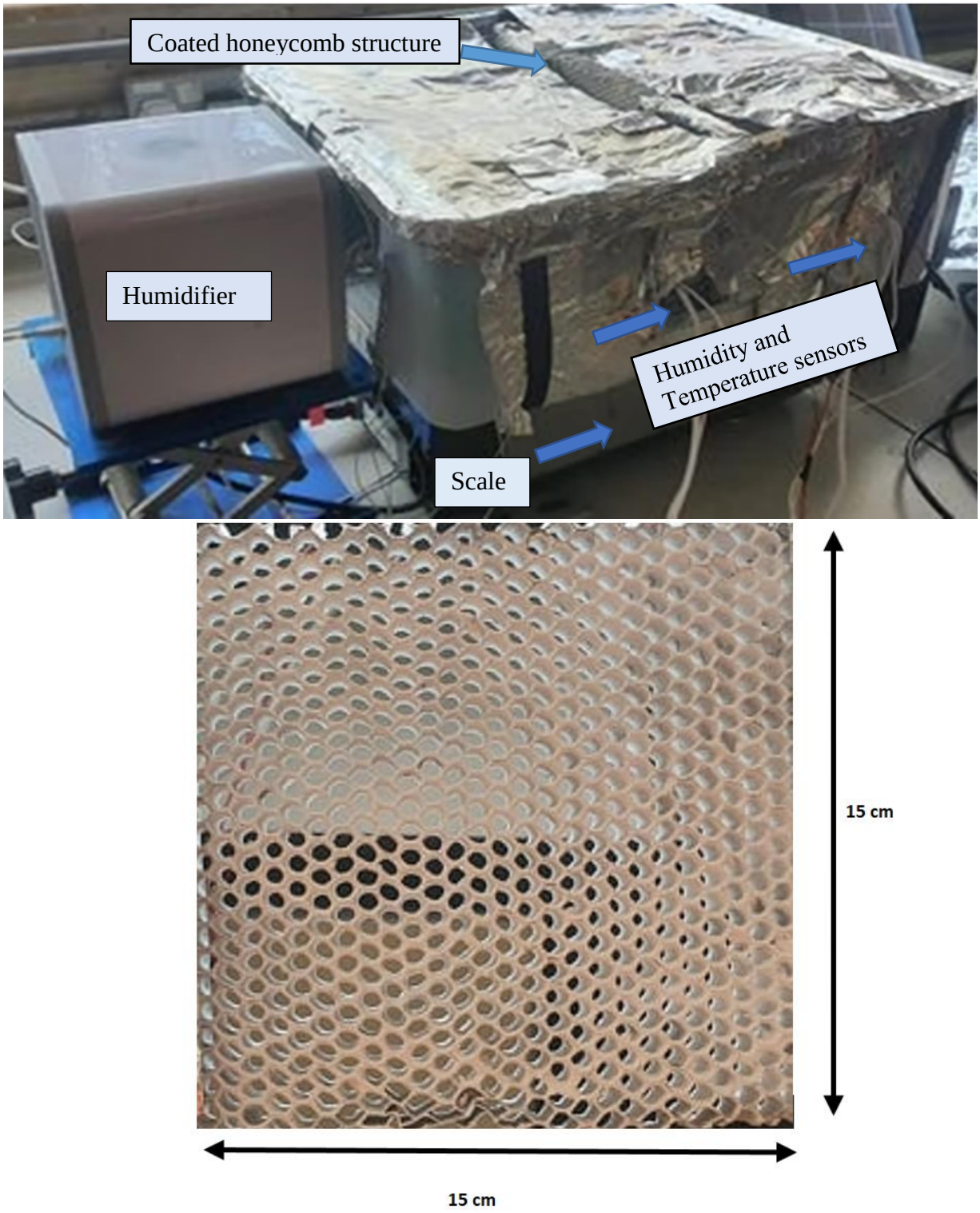



*Figure 3-8: Coated honeycomb structure integrated with the test facility.*

Table 3-5 shows the accuracy, range and uncertainty of the measuring devices used in the experimental facility. The standard uncertainty was calculated taking into account both random and systematic errors using available data from the equipment manufacturer datasheets and Eq. (3-21) [159].

$$u = \frac{a}{\sqrt{3}} \tag{3-21}$$

Where, u and a are the standard uncertainty and instrument accuracy, respectively.

Table 3-5 Accuracy, range, and standard uncertainty of measuring instruments.

| Instrument | Accuracy | Range | Standard uncertainty | |
|---|---|---|---|---|
| Humidity sensor | ± 3% RH | 10% – 99% | 1.73 % |  |
| Temperature sensor | ± 0.3 ° C | -40 ° C – 85 ° C | 0.173 V | |
| Anemometer | ± 5% | 0 – 30m/s | 2.88 % |  |

In the experimental testing, two methods were used to measure the moisture removal from the air flowing through the honeycomb DCHE. The first one is by measuring the change in the honeycomb structure weight due to moisture adsorption using the scale and recording these data with time. The second method is measuring the humidity and temperature of the air before and after the honeycomb DCHE, then calculating the moisture content using psychrometric equations then taking the difference between the input and the output. Figure 3-9 compares the measured change in weight of the honeycomb structure to the change in moisture content of the air flowing through the honeycomb DCHE. It can be seen that the two methods of evaluating the moisture removal are in good agreement with maximum difference of 11.3%.

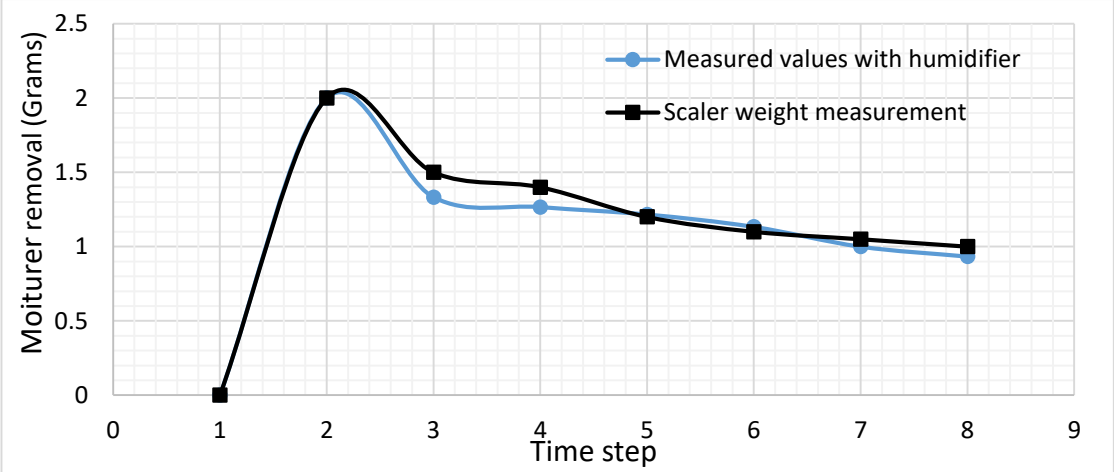



*Figure 3-9: moisture removal versus time step measured values output compared with scaler measurements.*

## 3.3. Modelling and experimental results

In this section, the results of testing Aluminium fumarate coated desiccant wheel for the dehumidification of air at various input air humidity. Two cases were investigated, one with high air humidity using the evaporative cooler and the second case is with lower humidity i.e. using the ambient humidity.

Figures 3-10 and 3-11 show the measured relative humidity and temperature of the air entering and leaving the MOF-coated honeycomb DCHE at 3.1 m/s for the case with high humidity. The blue lines in Figure 3-10 represents the input air relative humidity percentage, starting from 64%, increasing rapidly to 75%, then slowly to 78% (real time values). The orange line represents the output air relative humidity, which starts from 63 %, decreases rapidly to 45%, and then increases slowly to 52%. This figure shows that the Aluminium fumurate honeycomb DCHE can control the relative humidity by reducing it from 78% to 52%. The highest humidity change is at minute 2 to minute 4 with an average change of 34%.

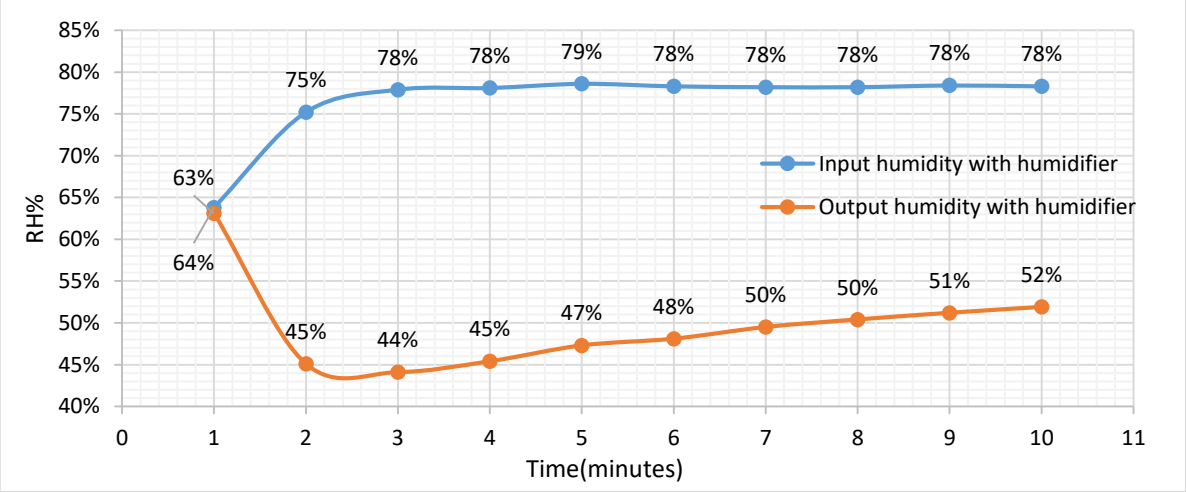



*Figure 3-10: Relative humidity change versus time when using a humidifier.*

The blue line in Figure 3-11 describes the input air temperature decreasing from 21.6 °C to 18 °C. The orange line represents the output air temperature, reaching 29.7 °C at minute 2, then decreasing to 24.4 °C at minute 10.

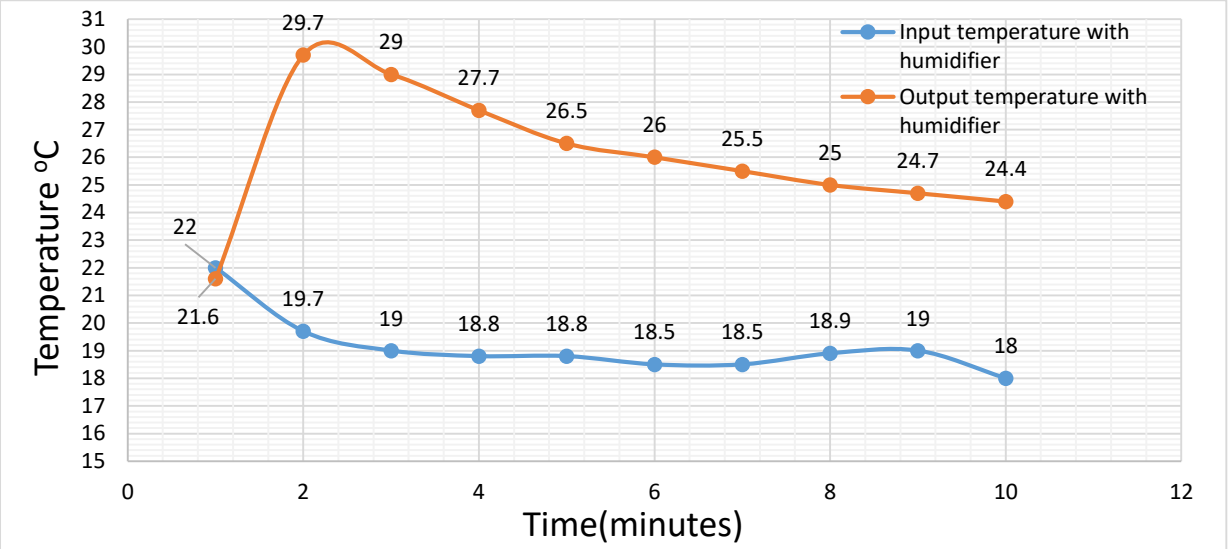



*Figure 3-11: Temperature change with a humidifier.*

Figures 3-12 and 3-13 denote the measured relative humidity and temperature of the input air and the output air using ambient conditions without a humidifier at airspeed 3.1 m/s. The blue line represents the input air relative humidity changing from 61% to 64%. The output air relative humidity started at 59%, decreased to 42%, then increased to 50%. The difference between the input and the output after 10 mins equals 14%, which is lower than the case of high humidity (with the humidifier, see Figure 3-10). The most significant change in relative humidity occurs between minute 2 to minute 4, where the rate of adsorption of the dry adsorbent material is high.

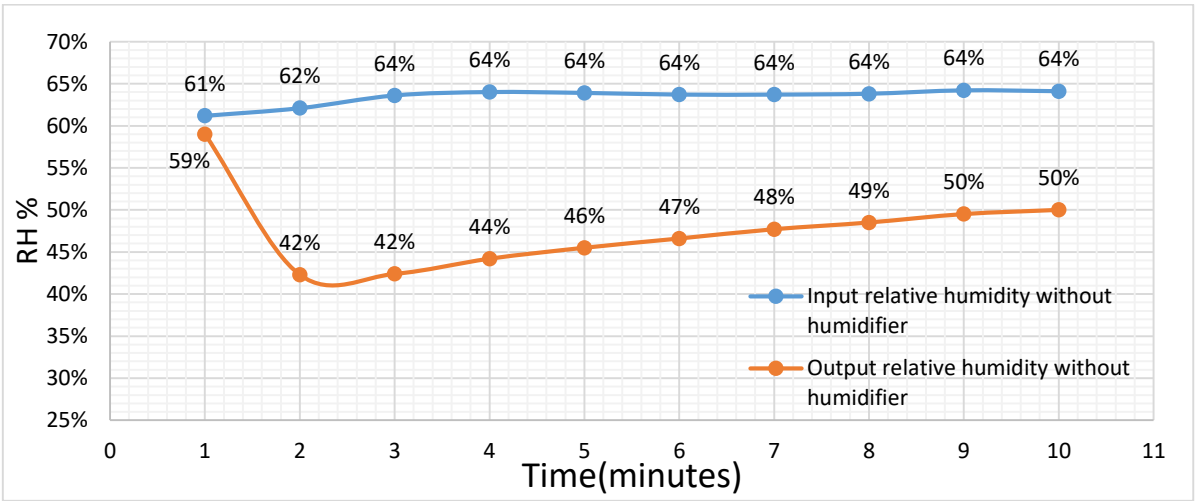



*Figure 3-12: Relative humidity change versus time without humidifier.*

The blue line in Figure 3-13 depicts the input air temperature varying from 23.4 °C to 21.4 °C. The output air peak temperature of 30.6 °C happens at 2 mins, and the lowest temperature of 24.5 °C occur after 10 mins due to the lowest adsorption rate.

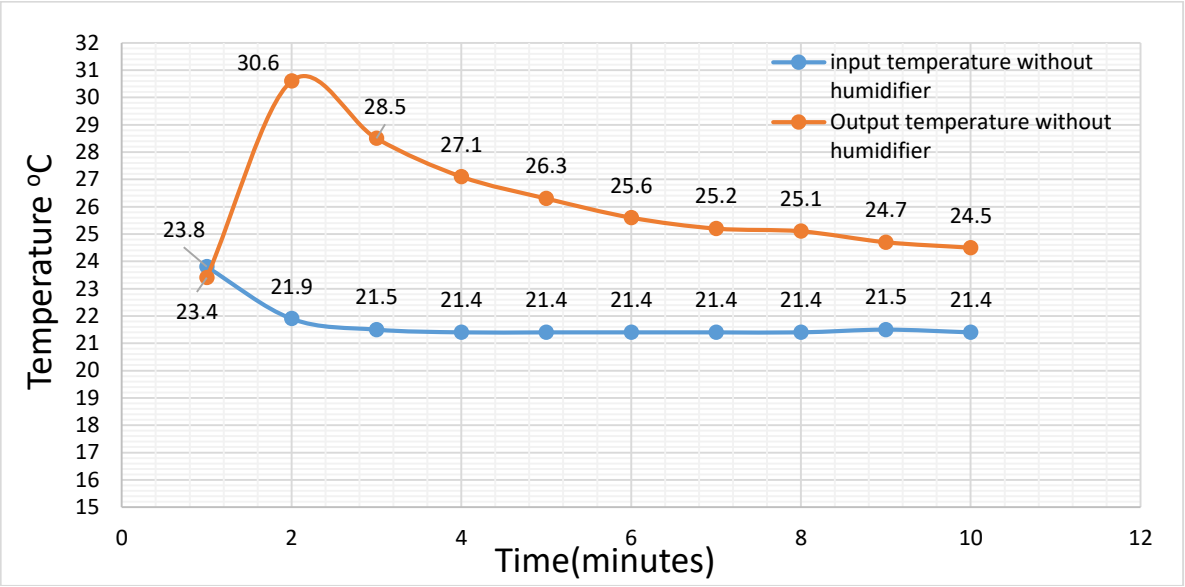



*Figure 3-13: Temperature change without a humidifier.*

Figure 3-14 compares the change in relative humidity between the input and the output air for the honeycomb desiccant wheel for the case with humidifier where relative humidity reached 78% and the case without humidifier where relative humidity reached 64%. The orange line represents the humidity change with humidifier ranging from 26% to 34%. The blue line shows that the humidity change ranging from 14% to 21%. These results indicate that as the input air relative humidity increases, the change in relative humidity due to the desiccant wheel increases. This could be attributed to the increase in water uptake of Aluminium fumarate adsorbent material as the air relative humidity increases as shown in Figure 3-2. As relative humidity changes the pressure ratio changes hence the mass transfer rate changes which affect the material behavior. This is controlled by the adsorption/desorption isotherm of Aluminium fumarate and its kinetics [31].

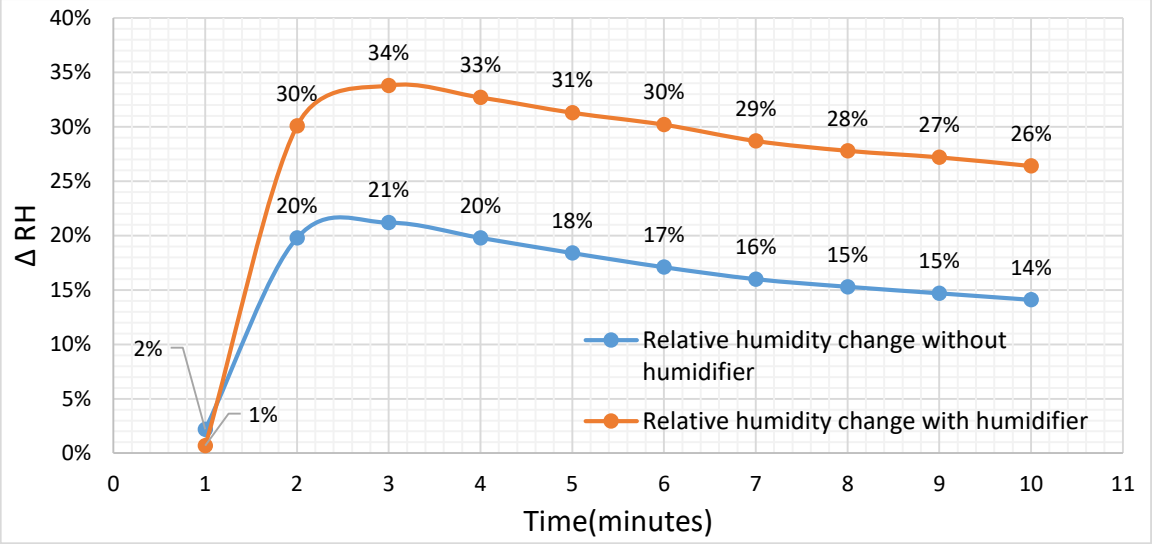
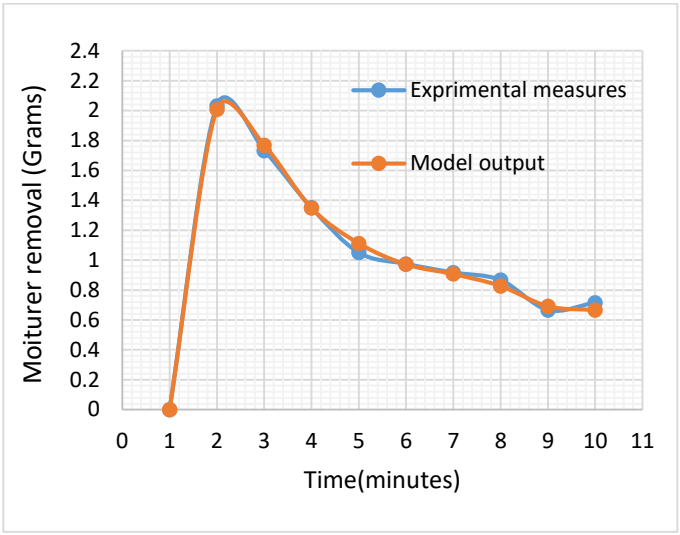


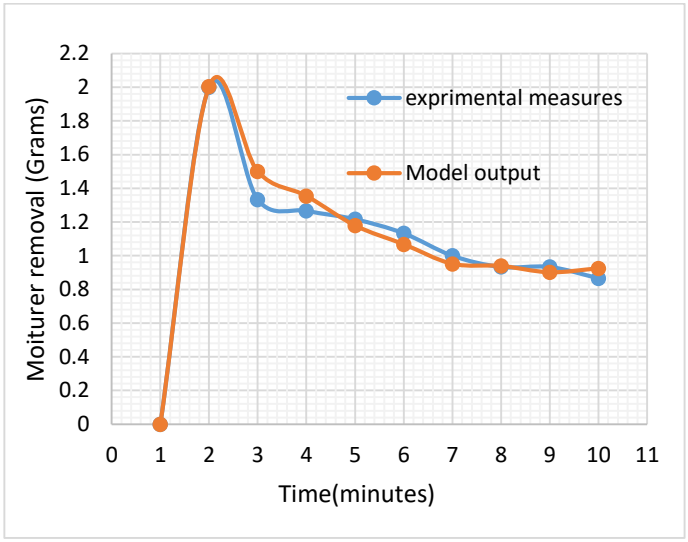

*Figure 3-14: Relative humidity change at the same conditions with and without a humidifier.*

Figure 3-15 compares the experimentally measured moisture removal to those predicted by the developed mathematical model at airspeed of 3.1 m/s, ambient temperature of 21.5°C $\pm 0.5$ °C and humidity of 64% $\pm 3\%$ (Figure 3-15a) and at input airspeed 3.1m/s, temperature after humidifier of 19 °C $\pm 0.5$ °C and humidity of 78%$\pm 1\%$ (Figure 3-15b). These results show good agreement between the experimental data and the model output, with a maximum deviation of 13%.

Figure 3-16 represents the model-predicted moisture removal variation with time at three airspeeds, air input temperature, and humidity of 19.5 °C and 50 %, respectively. It can be seen that the moisture removal increases as the inlet airspeed decreases, this is due to the increase of the resident time between the adsorbent material and the moist air. The maximum moisture removal is 3.5 grams for an airspeed of 1.5 m/s. Also, it was clear that the maximum moisture removal rate took place during the first two mins of the process, and after that, it started to decrease rapidly, which can be attributed to the saturation of the MOF material after two mins.




a) Without a humidifier




b) With a humidifier

*Figure 3-15: moisture removal variation with time experimental versus model results.*

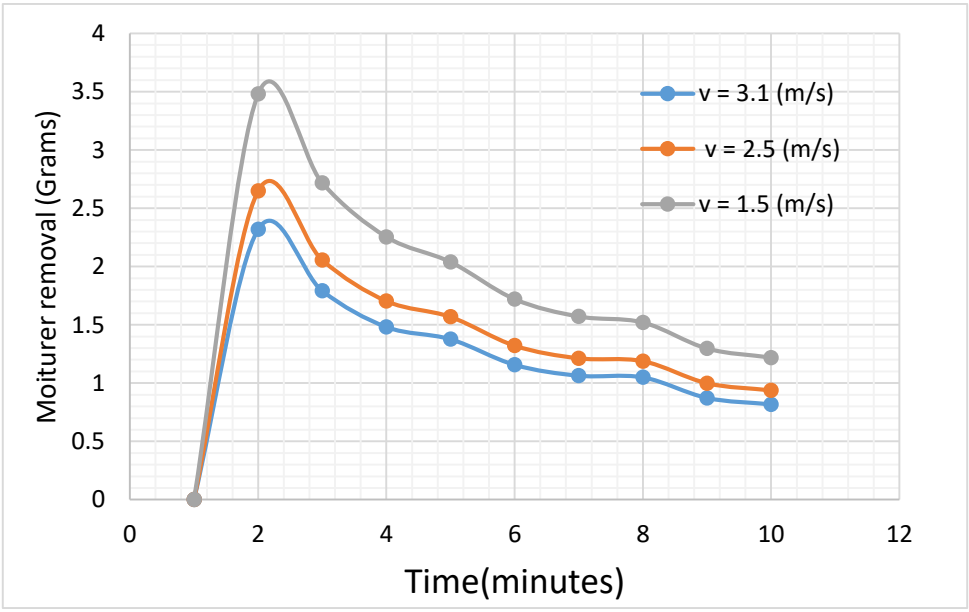



*Figure 3-16: moisture removal versus time step at different airspeeds.*

## 3.4.Summary

This chapter investigated the use of four MOF materials namely CPO27(Ni), MIL100(Fe), MIL-101(Cr) and Aluminium Fumarate compared to silica gel on the performance of stationary desiccant wheel in terms of the moisture removal rate and Coefficient of performance (COP).

Using MATLAB software, a one dimensional dynamic model to solve mass and heat transfer between air and the MOF desiccant Material coated on a honeycomb structure was developed to predict MOFs performance in terms of COP and moisture removal rate at various airflow input conditions. Numerical simulation results showed that the Aluminium

fumarate produced the highest COP of 0.65 with a water removal rate of 12.65g/kg dry air while MIL-101(Cr) produced the highest moisture removal of 15.99 g/kg dry air but with COP of 0.44. MIL-100(Fe) has a COP of 0.43 and moisture removal of 7.91 g/kg, and CPO-27(Ni) has COP of 0.4 with moisture removal of 6.55 g/kg compared with Silica gel which has COP of 0.37 and moisture removal of 5.26 g/kg.

The experimental facility was developed using a honeycomb structure coated with Aluminium fumarate as the stationary DCHE, and experimental tests were carried out at two inlet operating conditions, temperature and humidity of 18.5 $^{o}$C,78% and 21.4 $^{o}$C, 64%, respectively. It was found that increasing the incoming air humidity results in increasing the maximum change in air humidity between the inlet and the outlet, where at air humidity of 78%, the maximum change in the air humidity is 26-34%, while at air 64%, the maximum change is 14-21%.

The numerical dynamic model predictions were compared to experimental ones, showing good agreement with a maximum deviation of 13% for the moisture removal rate. Experimental and modelling results were carried out to investigate the effect of incoming air speed (1.5m/s, 2.5m/s, and 3.1m/s) on moisture removal rate for coated Aluminium fumarate. The results showed a general trend that as the incoming air speed increases, the moisture removal rate decreases, at an air speed of 1.5 m/s, the maximum moisture removal is 3.6 g/kg, while at airspeed of 3.1m/s, the moisture removal rate is 2.4 g/kg. Also, it was clear that the maximum moisture removal rate took place at the first two mins of the process and after that it is started to decrease rapidly, which can be attributed to the saturation of the MOF material after the two mins. This is a very important result since it will guide the users on the right cycle time for the system to achieve the best output.

This work highlights the significance of using MOF materials as advanced adsorbent materials in the moisture removal process in desiccant cooling applications.

The literature shows honeycomb structures are ideal for desiccant-coated heat exchangers due to their high surface area-to-volume ratio, maximising contact between air and desiccant material and enhancing moisture adsorption efficiency. They ensure uniform airflow, reduce pressure drop, and enhance heat and mass transfer, making them suitable for portable and space-constrained environments. However, their complexity and mechanical parts can lead to higher production costs and maintenance challenges, and the heating and cooling methods are still limited. On the other hand, wire-finned tubes have the potential to be easier and cheaper to manufacture, offer good heat transfer properties, and offer a variety of heating and cooling methods compared to honeycomb structures. Coating and maintenance capabilities are easier than honeycomb structures.

So, the upcoming chapter will primarily focus on developing an electrically heated desiccant-coated heat exchanger based on a wire-finned tube and establishing a laboratory test facility to evaluate its performance after selecting the appropriate MOF material from an additional set of MOF.

# Chapter 4 Development of electrically heated desiccant coated heat exchanger

In Chapter 3, the potential of using MOF material for moisture removal in desiccant cooling systems using mathematical modelling was investigated. Aluminium fumarate, MIL-100(Fe), CPO-27(Ni), and MIL-101(Cr) were studied compared to silica gel, showing that Aluminium fumarate produced the highest coefficient of performance, while MIL-101(Cr) produced the highest moisture removal rate. Experimental results using Aluminium fumarate coated on a honeycomb structure agreed with the modelling results. In this work, the honeycomb structure was heated in an oven, which limited the progress using such geometry. Employing electrical heating to heat the MOF desiccant material directly offers the potential to reduce the size and energy consumption of the DCHE. This Chapter will present the development of electrically heated stationary desiccant heat exchangers. In this chapter, additional MOF materials will also be studied.

(**This chapter is based on the previously published papers: Andrew N. Aziz, Saad Mahmoud, Raya Al-Dadah, Anil Taskin, Mohamed A. Ismail, Y.M. Fahmy, Md Mamoon Rashid, "Novel MOF-303/G coated wire-finned heat exchanger for dehumidification applications– Experimental investigation" Energy, Volume 305, 2024)**

## 4.1.Heating element configuration

Wire-finned tubes provide substantial advantages over honeycomb structures in desiccant applications and heating and cooling systems. Wire-finned tubes offer a significant benefit in being cost-effective and easy to manufacture, making them an appealing choice for applications that require large-scale production and are budget-conscious. The fins increase the surface area, improving the ability to transmit heat, which is advantageous for heating and cooling. This design enables excellent heat transfer, promoting good desiccant regeneration and maintaining the correct temperature levels. In addition, wire-finned tubes are typically easier to clean and maintain, which helps reduce operational expenses and extend their lifespan. Although wire-finned tubes do not possess the same uniform airflow and high moisture adsorption efficiency as honeycomb structures, their strong performance and economic benefits make them a practical substitute for different desiccant systems and HVAC applications. This is why this design was chosen for this study instead of honeycomb structure.

Figure 4-1 describes the development of heating configurations for the wire-finned tube to achieve the target temperature required in the desorption process for a selected MOF, showing the dimensions and the wire connections. In order to enhance the surface area and

quantity of the coated MOFs, the height of the fin is raised to 20 mm. Each tube should hold 60 grams of the selected MOFs. The wire-finned tube is manufactured by P.A.K Engineering Ltd, wrapped by the Nichrome wire between the fins, and then coated at the University of Birmingham (UOB).

Nichrome wire is widely used for heating purposes because of its melting point, electrical resistance and durability. Its efficient heat generation capability along, with its resistance to oxidation and corrosion guarantees lasting performance with upkeep. The stable resistance of Nichrome wire across a temperature range enables temperature regulation while its mechanical robustness and non magnetic properties provide versatility for various uses. Popularly utilized in ovens, industrial furnaces, and laboratory equipment Nichrome wires effectiveness and dependability make it a top choice for various heating needs [160]. In this configuration, a 1mm Nichrome wire was used and customised to wrap around the tube, allowing it to convert electrical energy into heat efficiently. The number of fins is 44 per loop with a Fin spacing of 2mm.

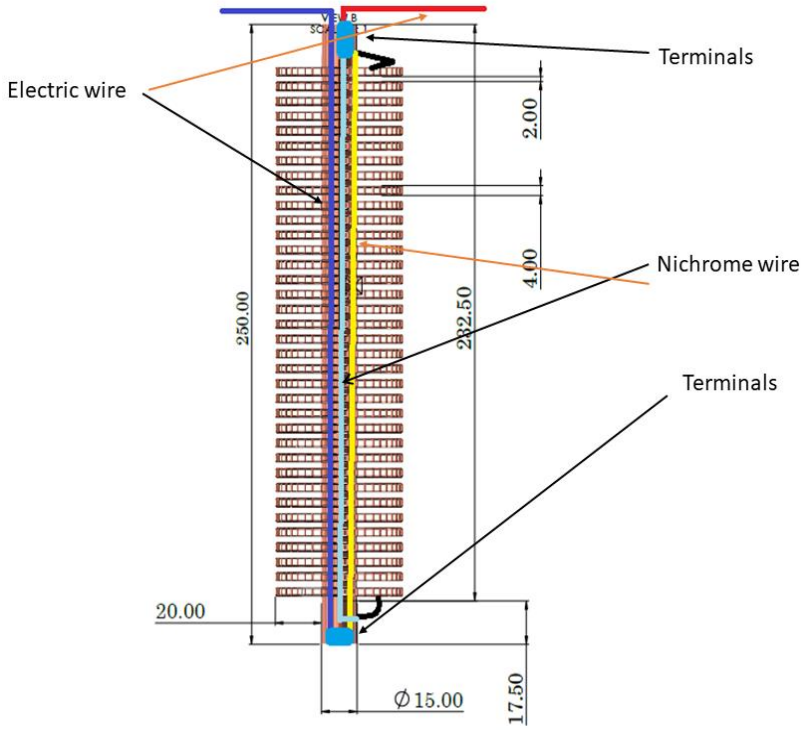



*Figure 4-1: the heating wiring diagram.*

Figure 4-2 illustrates the heating circuit that was meticulously designed and simulated using Proteus software. The heating element is designed to withstand the high temperatures generated during operation without deforming or deteriorating. It is often enclosed within a protective sheath made of ceramic to ensure safe usage and prevent direct contact with the

surrounding environment. When an electrical current is applied to the heating element, the resistance of the wire causes it to heat up. This heat is then transferred to the MOF material through conduction and convection. The target was to achieve uniform temperature distribution along the tube with low power input.

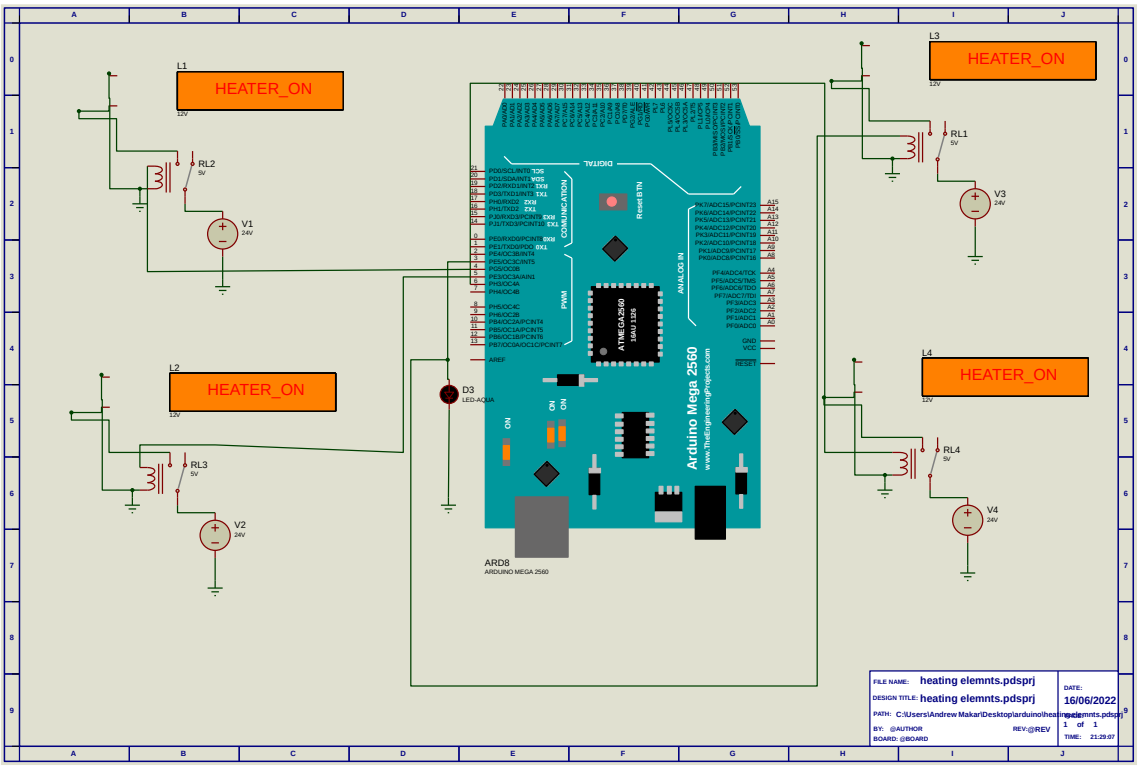



*Figure 4-2: heating control circuit.*

Figure 4-3 shows the electrical heating circuit diagram system used in the experiments, consisting of a DC-DC voltage regulator, a relay kit, and an Arduino Mega to control the power supplied during the heating (desorption) processes.

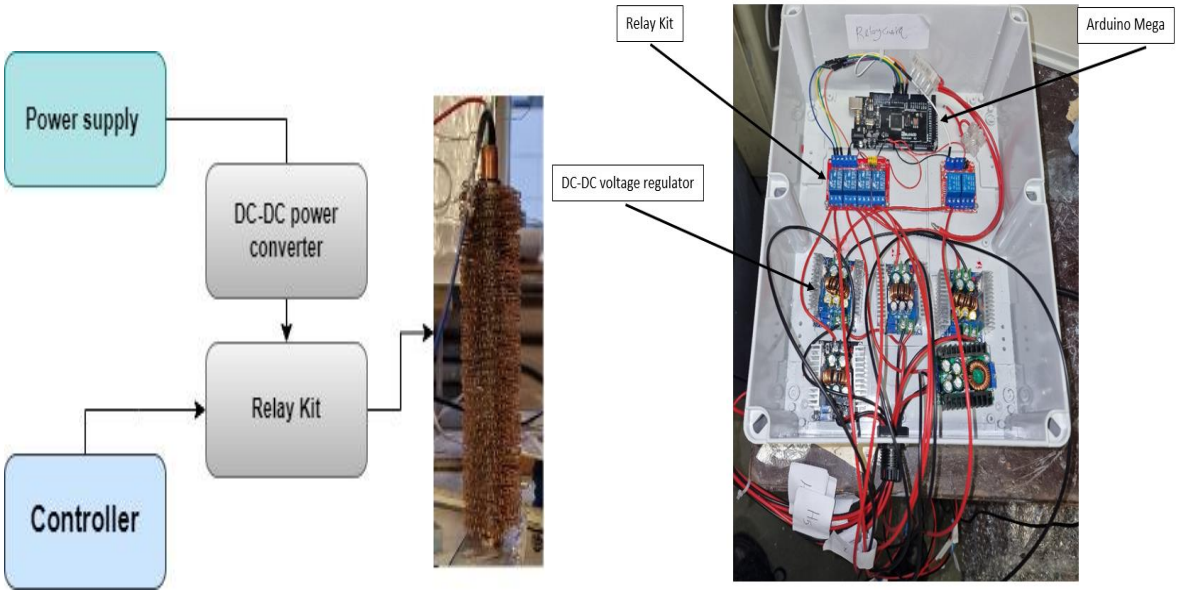



*Figure 4-3: The heating control circuit to control the desorption/adsorption process for the DCHE.*

Thermograms or infrared image was captured to show the distribution of infrared radiation emitted by the tube surface. It visually represents the temperature variations in a scene, highlighting hot and cold areas. The thermal camera is a FLIR TG165-X USB 2.0 thermal imaging camera with a temperature range of –25 → +300 °C, with an 80 x 60pixel detector resolution (see Figure 4-4). Figure 4-5 shows the electrically heated wire-finned thermal image, indicating uniformity of the heating process. Figure 4-6 depicts the K-type thermocouples with an accuracy of ± 0.3°C, the sensor's locations along the tube. Figure 4-7 represents the measured temperature values along the tube, confirming the uniformity.




*Figure 4-4: Thermal Imaging Camera.*

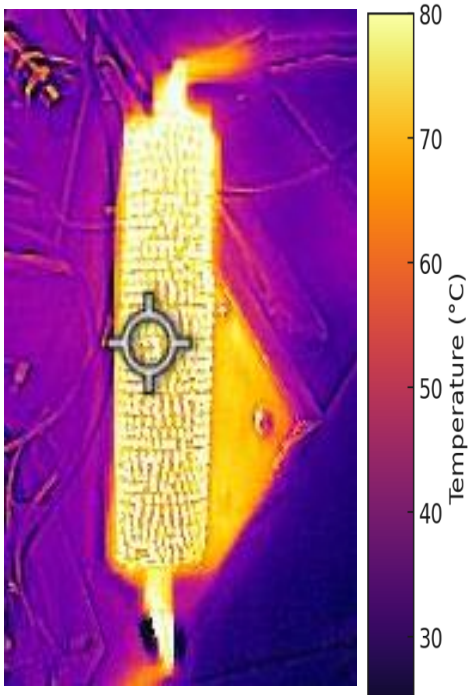
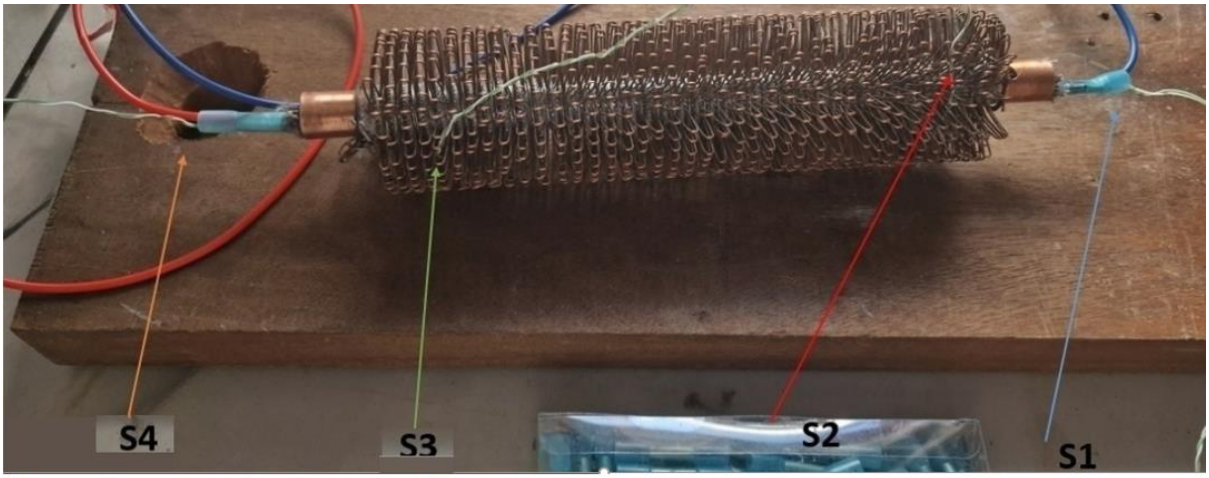



*Figure 4-5: Thermal image of the electrically heated wire finned tube with 28.8 W.*




**Where, S reprents the themocouple temperature sensor**

*Figure 4-6: Temperature sensors distribution along the tube before coating.*

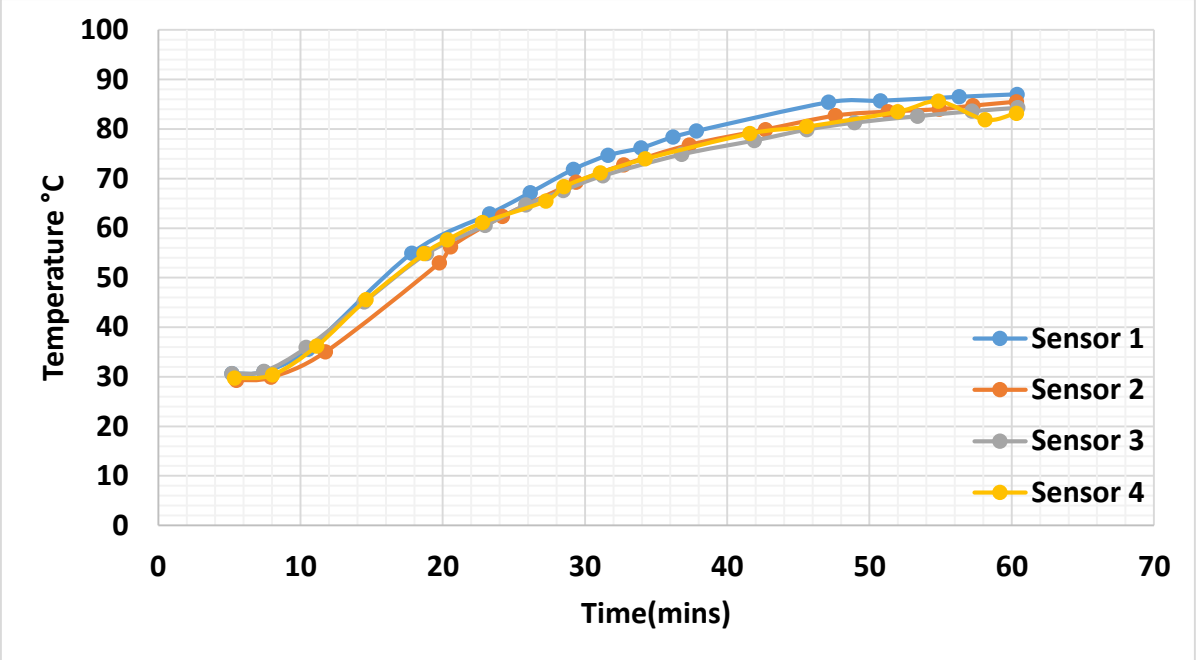



*Figure 4-7: Temperature distribution along the tube using input power of 20 W.*

## 4.2.Examining additional MOF materials

After finalising the electrically heated wire-finned tube, a number of high-performance MOF materials were investigated, namely MOF-303/G, MOF-801/G, MIL-100(Fe)/G, Aluminium fumarate, MOF-801, and MIL-100(Fe). Aluminium fumarate, known as MOF-A520, synthesised and commercially produced by MOF Technologies ltd, UK, has an equilibrium uptake of 0.53gH2Ogads$^{-1}$. MIL-100(Fe) consists of trimesic acid (H3BTC) linkers forming a three-dimensional octahedral cages network. These cages are interconnected by windows, allowing guest molecules to pass. MIL-100(Fe) has a high specific surface area of ~1,900 m²/g, which means that a considerable amount of surface is available for interaction with guest molecules. This property makes MIL-100(Fe) a good candidate for gas adsorption and separation applications. Based on previous work, the authors produced MIL-100(Fe)/G by mixing MIL-100(Fe) with 10% of graphene nanoplatelets to improve its thermal conductivity [161]. MOF-801 comprises a cubic array of interconnected metal ions, specifically zirconium ions and fumaric acid ligands, resulting in a highly porous structure. MOF-801's advantages include its ability to regenerate at low temperatures, <90°C, and having high water uptake capacity of 34% by weight at low relative humidity P/Po below 0.2. MOF-801/G was produced at the UOB lab by introducing graphene nanoplatelets during the synthesis of MOF-801 [162]. MOF-303, also known as aluminium pyrazolate, consists of a metal ion, aluminium, connected to organic ligands known as pyrazolate. The resulting structure of MOF-303 is a porous material with a high surface area, allowing it to adsorb large amounts of water. The strong chemical bonds between the aluminium ions and the pyrazolate ligands make it stable and

resistant to degradation, allowing it to adsorb and release water molecules multiple times without losing its chemical structure and performance. MOF-303/G was produced at the UOB lab by introducing graphene nanoplatelets during the synthesis of MOF-303.

Figure 4-8 shows the adsorption isotherms for these MOF materials. This is generated using the Dynamic vapour sorption device DVS system, specifically developed to determine the amount of adsorbent absorbed by detecting the change in its mass during sorption. The technique involves drying the sample at the specified temperature and duration, employing nitrogen as a purging gas, and manipulating the relative pressure by combining dry nitrogen with adsorbate vapour. The change in mass is measured, indicating the adsorption/desorption behaviour of the substance. The water vapour intake at each relative pressure step is determined to establish the equilibrium, and the adsorption rate curves are generated by plotting the weight of the sample against time. It is clear in this figure that MOF-303 and MOF-303/G have a significant jump in water adsorption at 0.2 relative pressure; this is due to the presence of specific functional groups within these MOFs, such as carboxylates (-COO-), hydroxyls (-OH), which can create sites that strongly interact with water molecules through hydrogen bonding, leading to increase water uptake at lower pressures.

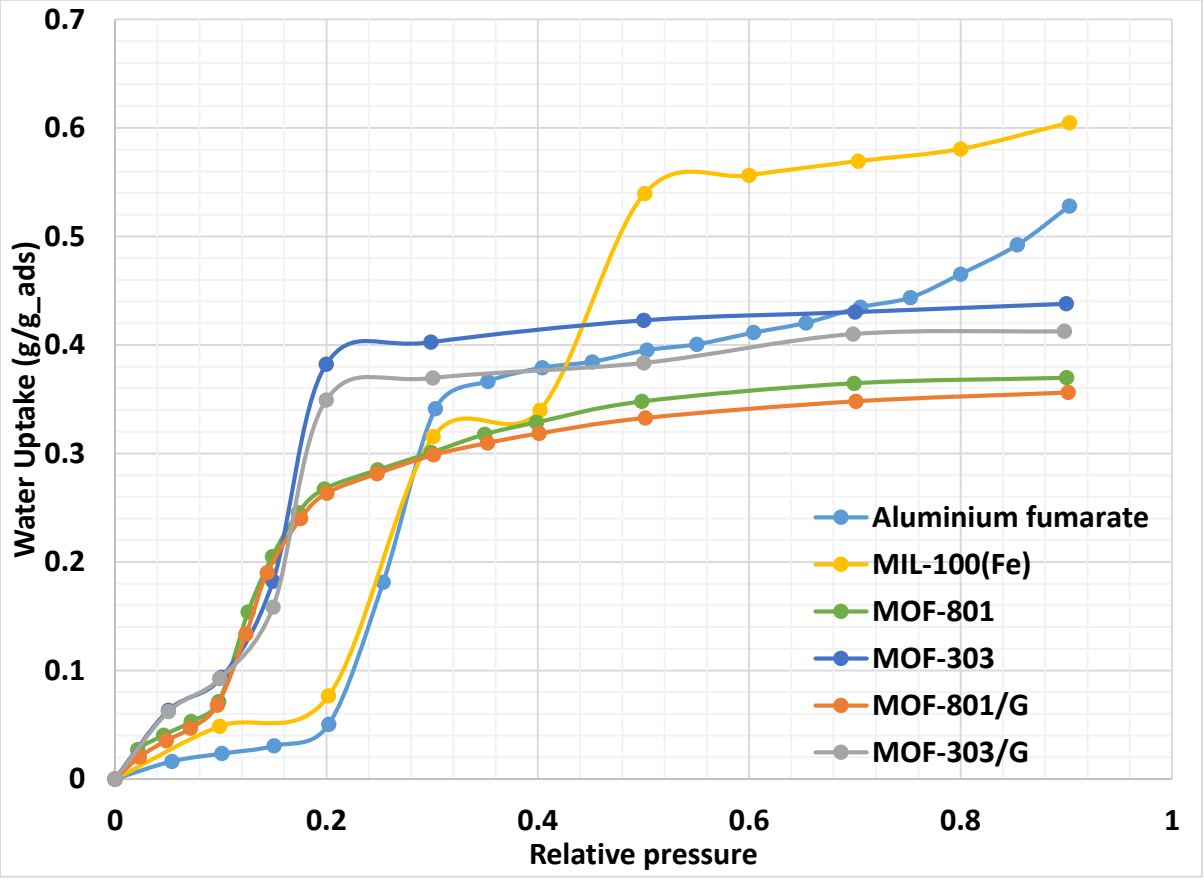



*Figure 4-8:The water adsorption isotherm of Aluminium Fumarate and MIL-100(Fe)* [31], *MOF-801 and MOF-801/G* [162], *MOF-303 and MOF-303/G.*

The addition of graphene nanoplatelets during the synthesis of MOF-303 significantly improved its thermal diffusivity, as shown in Figure 4-9. The thermal diffusivity was measured using laser flash analysis (LFA) for MOF-303, MOF-303/G and Graphene nanoplatelets, showing that MOF-303/G has thermal diffusivity ranging from 0.184 to 0.23 mm2/s at temperatures ranging between 25°C to 115°C while the thermal diffusivity of MOF-303 ranges from 0.01 to 0.0123 mm2/s at the same temperatures.

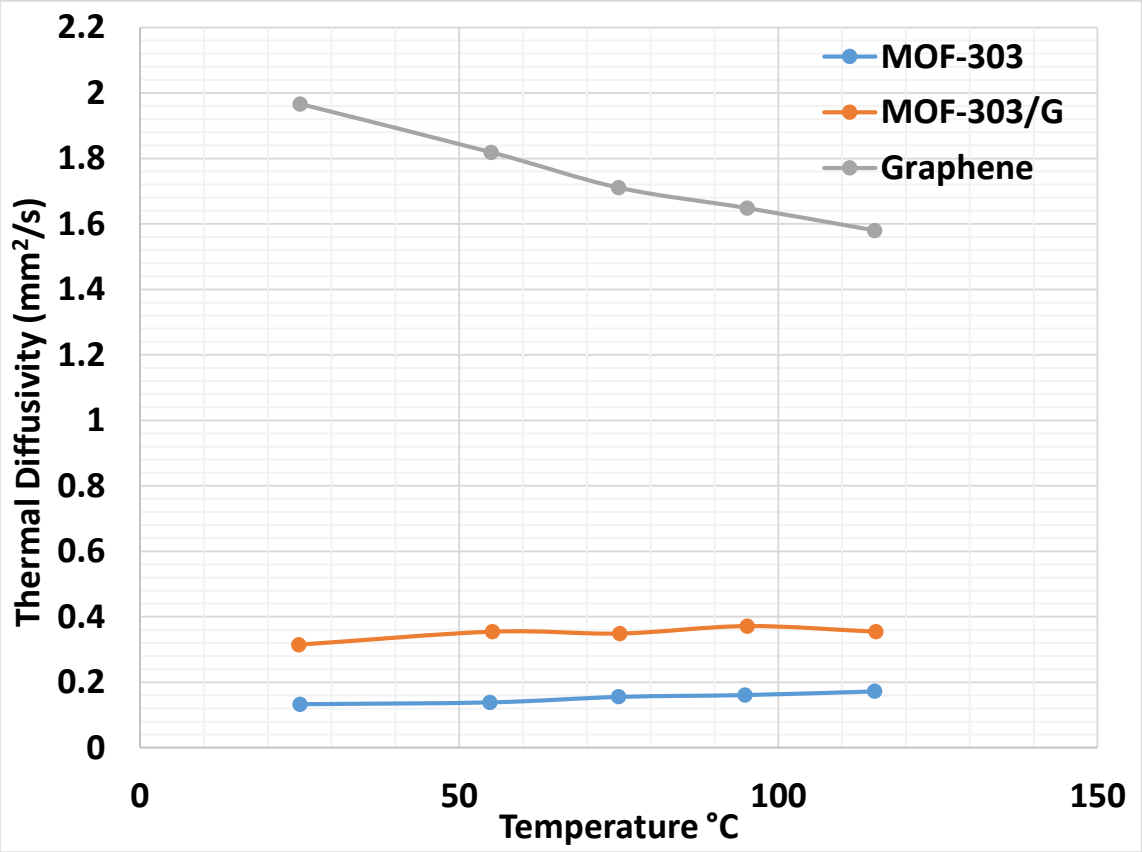



*Figure 4-9*: *Thermal diffusivity of MOF-303 and MOF-303/G* [163].

In order to assess the performance of the above-described MOF materials for application in air dehumidification, experiments were carried out using six electrically heated copper wire finned tubes with 7mm fin height, each coated with 0.3mm thick of the relevant MOF material as shown in Figure 4-10. The optical images for the proposed MOFs are presented in Figure 4-11.

The coating procedure employed in this study was derived from the methodology established by Elsayed [31] and Albaik, [83] where 40 grams of 2-Hydroxyethyl cellulose (HEC) as a binder is combined with a solution of MOFs weighing 400 grams in a volume of 2 litres of distilled water as shown in Figure 4-12. The solution is applied to the finned tube surfaces after being

cleaned from rust and galvanic layers. Subsequently the MOF-coated wire finned tube is dried in an oven for a duration of 2 hours. The wire-finned tube was subjected to repeated spraying with the MOF binder solution until a certain thickness of MOF coating was attained. The MOF-coated wire finned tubes were mounted on a digital scale and connected to a power supply, as shown in Figure 4-13. Table 4-1 represents the density and the maximum water content for the studied MOF materials.



Aluminium fumarate | MOF-303/G | MOF-801 | MIL-100(Fe) | MIL-100(Fe) | MOF-801/G

*Figure 4-10: Six electrically heated copper wire finned tubes each coated with 0.3mm thick of the relevant MOF material.*




(a) (b) (c)

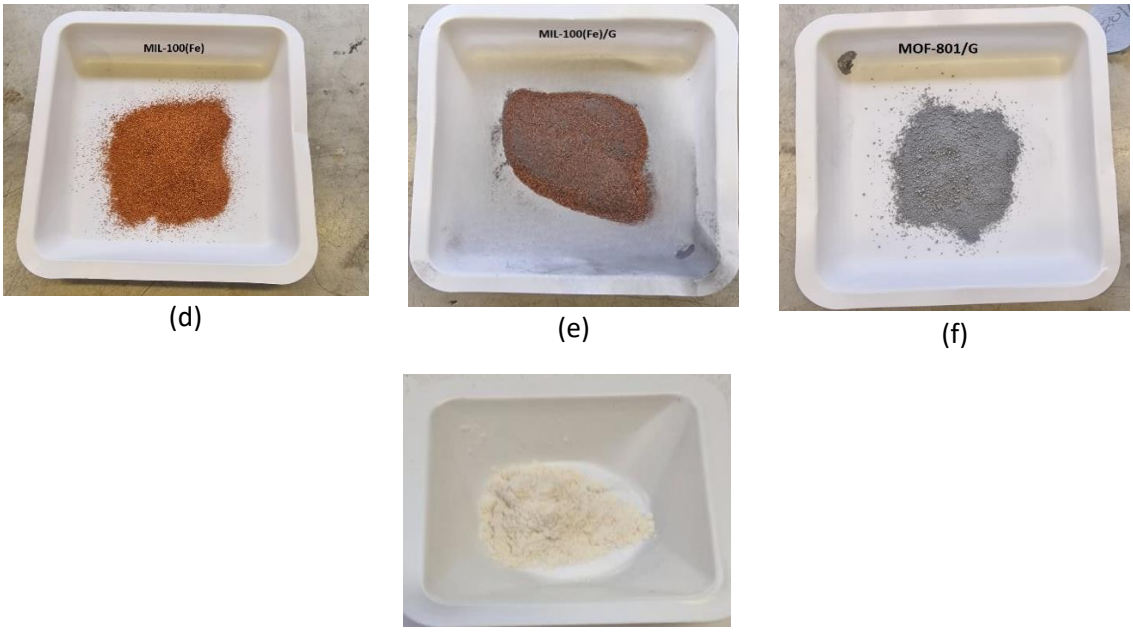



*Figure 4-11: Optical images for MOFs coating powder. (a) Aluminium fumarate, (b) MOF-303/G, (c) MOF-80, (d) MIL-100(Fe), (e) MOF-100(Fe)/G (f) MOF-801/G (g) binder.*

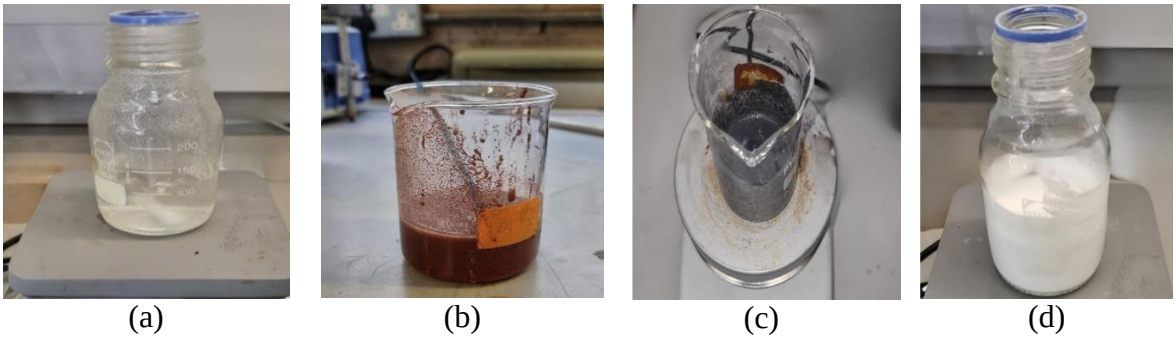



*Figure 4-12: Optical images for MOFs/binder solution(a) binder solution, (b) MIL-100 (Fe) /binder, (c) MOF-303/G/binder, (d) Aluminium fumarate/binder.*

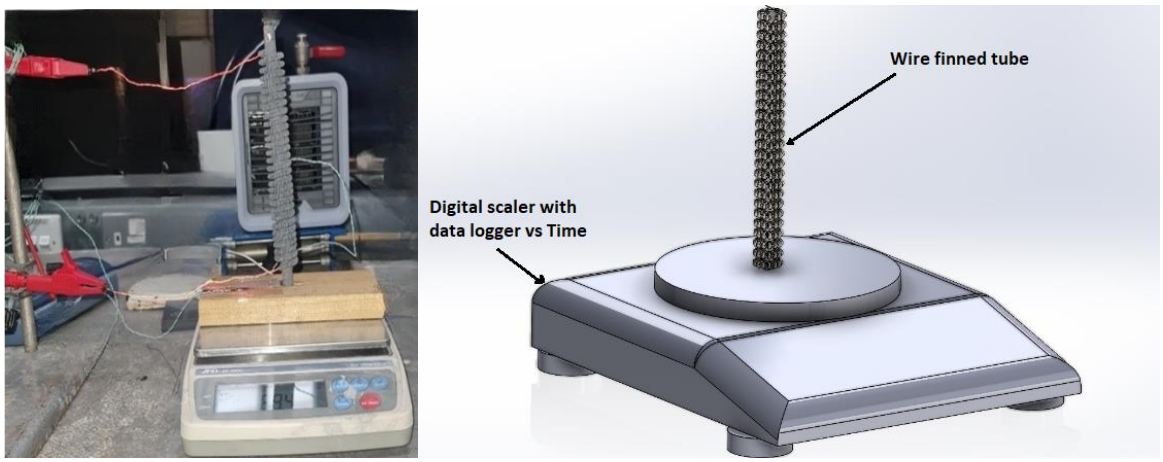



*Figure 4-13: Small tube test setup at ambient conditions.*

Table 4-1 The parameters of the used MOFs

| *Material* | *Density* | *Maximum water equilibrium uptake* |
|---|---|---|
| *Aluminum fumarate*[31] | *520* | *0.55* |
| *MOF-801*[162] | *1401* | *0.36* |
| *MOF-801/G*[162] | *1552.3* | *0.35* |
| *MIL-100(Fe)*[31] | *422* | *0.6* |
| *MOF-303/G* | *932* | *0.41* |

Each tube was heated for one hour to ensure fully desorbed MOF material, then was left to adsorb water vapour from the ambient at 21°C and 55% relative humidity. The weight of the wired finned tubes was logged with time, and the weight change indicates the amount of adsorbed water vapour. Figure 4-14 shows the percentage of water uptake variation with time for the six MOF materials. It can be seen that MIL-100(Fe)/G achieved an adsorption uptake of 19%, MOF-801 achieved 17.5%, and MIL-100(Fe) achieved a 16% adsorption uptake under the same conditions. However, aluminium fumarate performed less effectively, with less than 13% water uptake. MOF-303/G showed the highest water uptake of 22%, thus, MOF-303/G is used in this work. Figure 4-15 shows the repeatability of testing MOF-303/G coated wire finned tube, highlighting that the results are repeatable, with a maximum deviation of 0.54%.

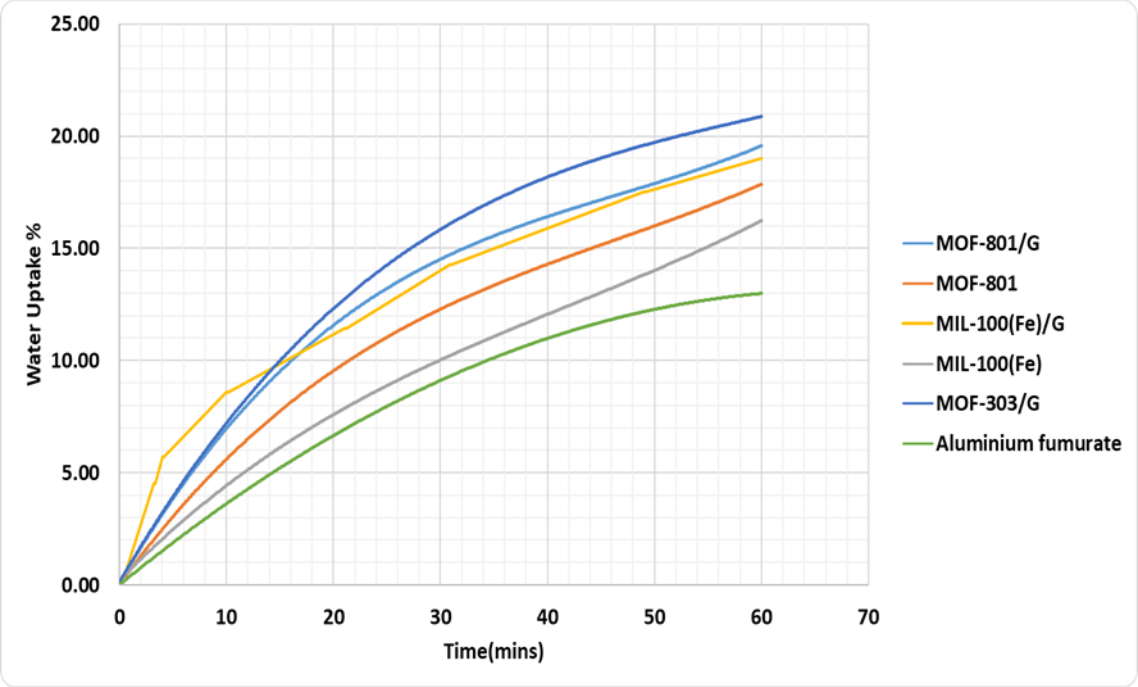



*Figure 4-14: Six wire-finned tube's water uptake at ambient conditions.*

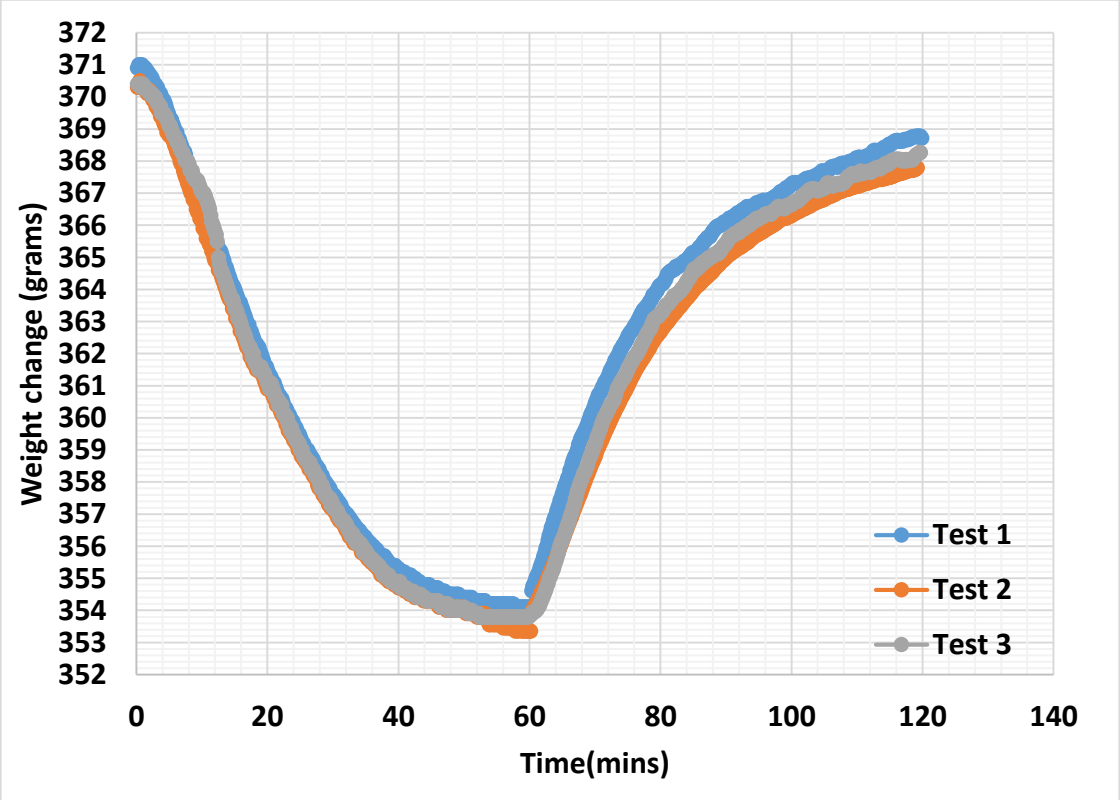



*Figure 4-15: Repeatability test for MOF-303/G.*

## 4.3.MOF-303/G characterisation

From the previous section, MOF-303/G outperforms the other MOFs in ambient conditions, so it is crucial to characterise MOF-303/G more and check its stability before coating. Figure 4-16 shows the SEM images for pure MOF-303, graphene, and MOF-303/G. Figure 4-17 shows the PXRD pattern for MOF-303 nanoparticles, graphene nanoplatelets, and MOF-303/G composite measured using a D8 Bruker X-ray powder diffractometer at room temperature. The thermal stability of MOF-303/G was assessed by conducting thermogravimetric analysis (TGA) with an air flow rate of 10°C/min throughout a temperature range of 25°C to 700°C as shown in Figure 4-18, which represents a high degree of thermal stability.

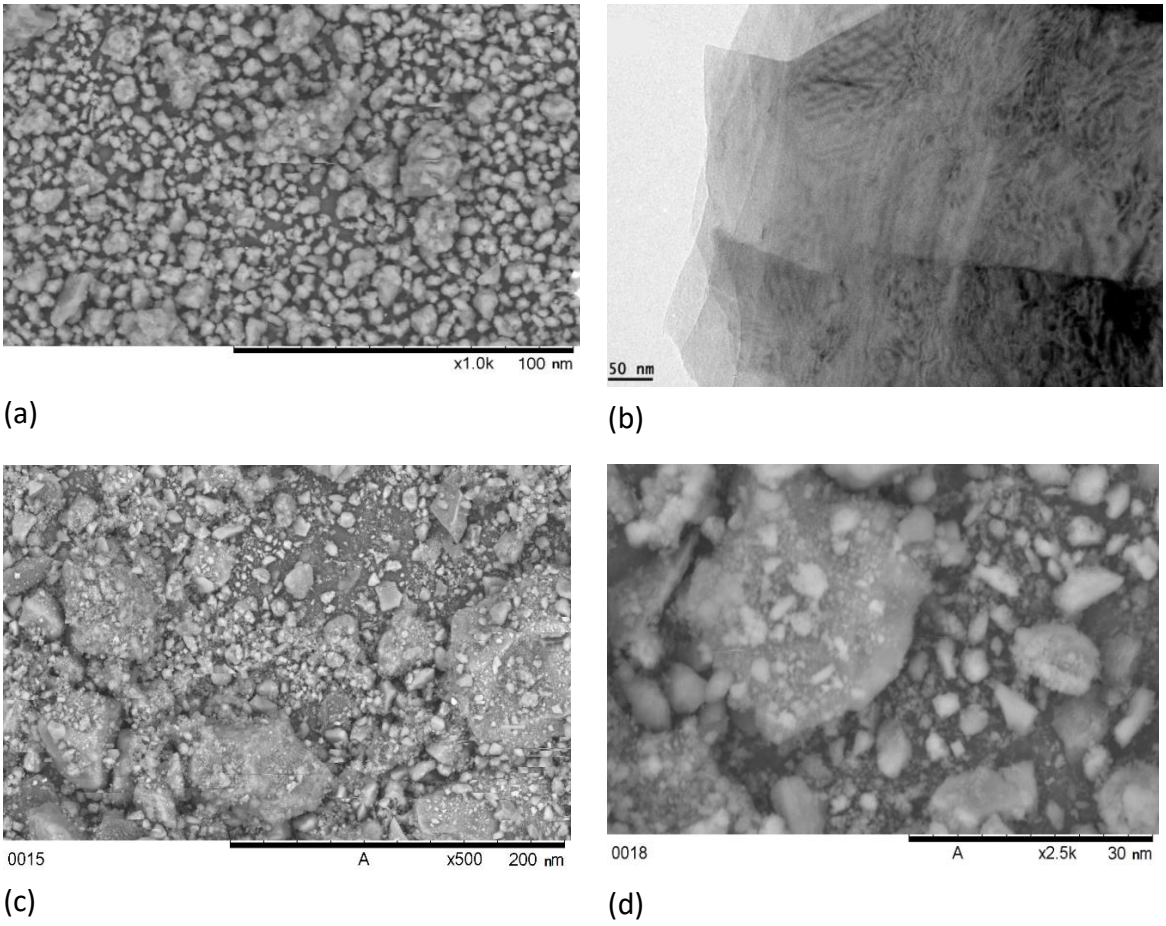



*Figure 4-16: SEM image of MOF-303 nanoparticles. (b) SEM image of graphene nanoplatelets. (c,d) SEM images of MOF-303/G.*

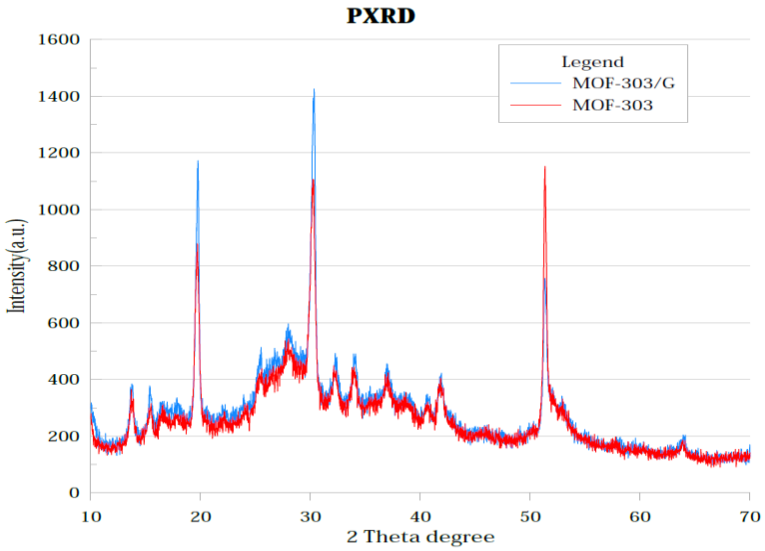



*Figure 4-17: PXRDs patterns for graphene nanoplatelets, neat MOF-303 nanoparticles, and MOF-303/G (10%) composite.*

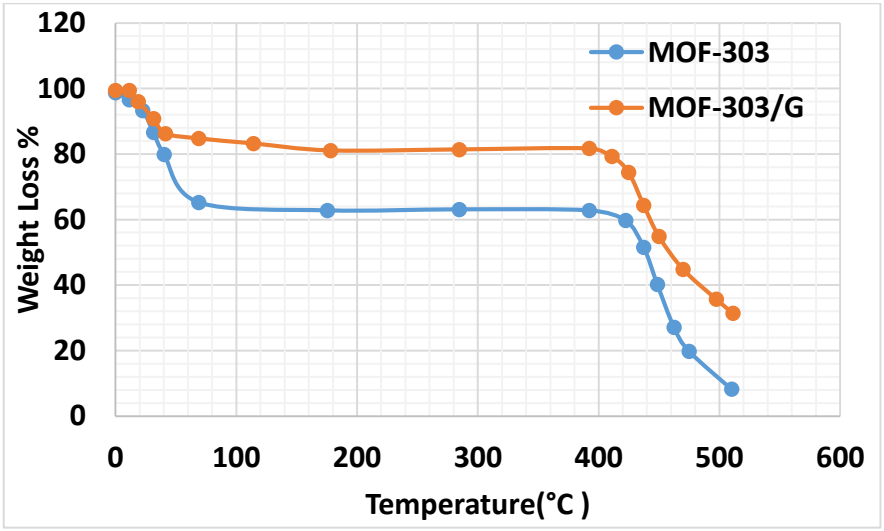



*Figure 4-18: TGA of MOF-303 and MOF-303/G* [163].

Figure 4-19 shows 16 cycles for the adsorption/desorption of MOF-303/G, indicating good stability and a desorption temperature of 90°C is enough to produce a repeatable desorption process. Adding graphene nanoplatelets reduced the cyclic time compared to the neat MOF-303.

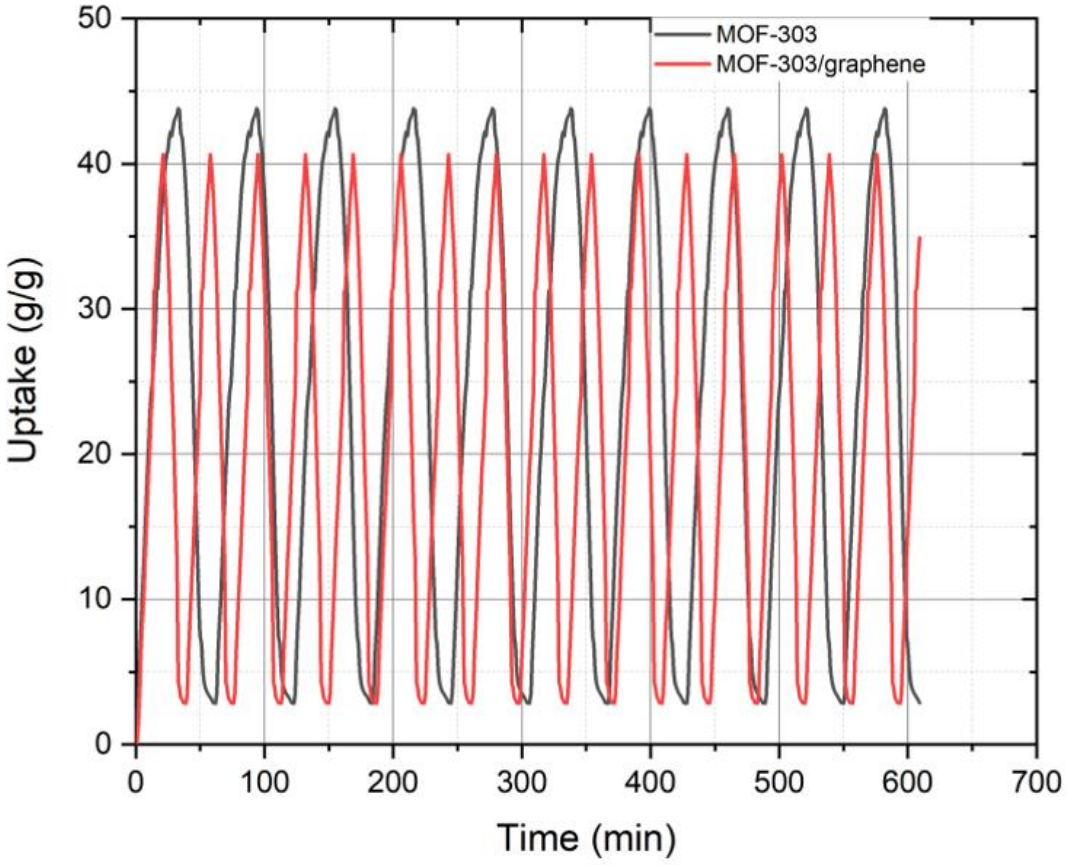



*Figure 4-19: Cyclic performance of MOF-303/G nanoparticles compared to neat MOF-303 at P/Po = 0.9 and $T_{desorption}$ of 90 °C* [163].

After checking the stability of the MOF-303/G, it is essential to study the effect of different power values on a single coated tube of MOF-303/G In order to investigate the impact of power used to desorb the water vapour from MOF-303/G coated on the wire-finned tube with 20 mm fin height, different power values were used, namely 12.8, 20 and 28.8 W. Figure 4-20 depicts the variation in the weight of the wire-finned tube coated with MOF-303/G at the three applied power levels, with an air temperature of 20°C and humidity of 60%. Figure 4-20 also shows the variation of MOF-303/G temperature with time during the supply of the power (desorption) and without the power (adsorption). It can be seen that the temperature at the end of the desorption process increases with the increase of the input power, reaching 64°C, 85°C, and 98°C at 12.8, 20, and 28.8 Watts, respectively. Increasing the adsorbent temperature resulted in lowering the MOF-303/G coated wire finned tube weight to 361, 356.5 and 355.8 grams respectively. Table 4-2 outlines the performance parameters of the MOF-303/G coated wire finned tube in terms of water removal rate per cycle, the number of cycles per day, total water removal per day, and the electrical power consumption per day.

The cycle time consists of 1 hour for desorption and various times for the adsorption process of 20, 30 and 60 mins. It is clear from this table that using a desorption time of 60 mins and a power input of 12.8 W can produce the highest daily water removal per power consumption of 0.9 (g/kgMOF)/(W.hr).

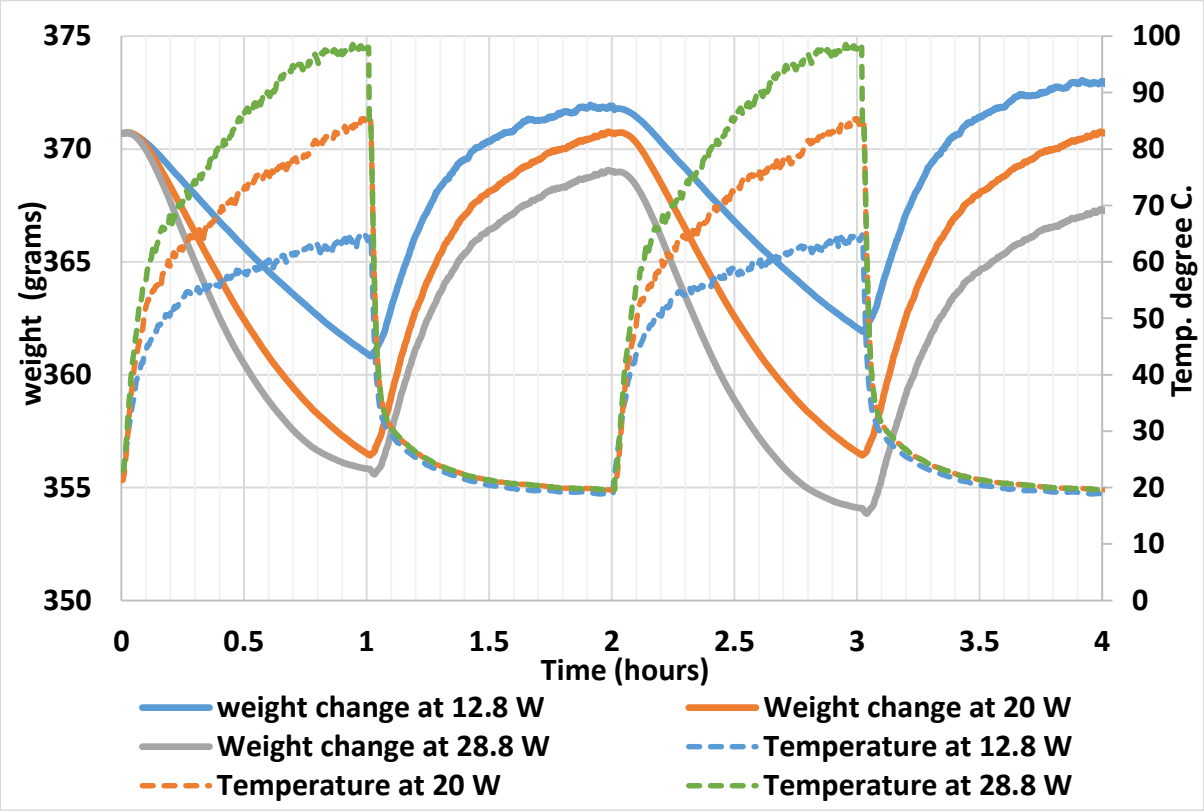



*Figure 4-20: Single wired-finned tube coated with MOF-303/G characterisation at different watts for the desorption process.*

Equations used to estimate the values in Table 4-2 are as follows

To calculate the power consumption per day(W.hr):

$$P_C = N \times P_in \tag{4-1}$$

P_C is the power consumption, N is the number of cycles per day, and P_in is the power input for a single-wire-finned tube.

To calculate the Net water adsorbed per day (g/ kgMOF) as follows:

$$N_water_day = N_water_cycle \times N \tag{4-2}$$

Where N_water is the net water adsorbed per cycle (g/kg)

The Water to power ratio (g/kgMOF/W.hr) is written as:

$$W/p = \frac{N_{water_{day}}}{P_C} \tag{4-3}$$

Table 4-2 The performance parameters of the MOF-303/G coated wire-finned tube.

| Power input (W) | Cycle adsorption time (mins) | Net water adsorbed per cycle (g/kg) | Number of cycles per day | Power consumption per day (W.hr) | Net water adsorbed per day (g/ kgMOF) | Water to power ratio (g/kgMOF/W.hr) |
|---|---|---|---|---|---|---|
| 12.8 | 20 | 6.5 | 20 | 256 | 130 | 0.508 |
| | 30 | 8.4 | 18.5 | 236.8 | 155.4 | 0.656 |
| | 60 | 11.6 | 8 | 102.4 | 92.8 | 0.906 |
| 20 | 20 | 6.1 | 20 | 400 | 122 | 0.305 |
| | 30 | 9.1 | 18.5 | 370 | 168.35 | 0.455 |
| | 60 | 14.3 | 8 | 160 | 114.4 | 0.715 |
| 28.8 | 20 | 6.2 | 20 | 576 | 124 | 0.215 |
| | 30 | 9.5 | 18.5 | 532.8 | 175.75 | 0.329 |
| | 60 | 14.7 | 8 | 230.4 | 117.6 | 0.51 |

## 4.4.MOF Coated Multi-Tube Heat Exchanger

In various dehumidification applications, large amounts of MOF will be needed; therefore, a multiple-tube desiccant-coated heat exchanger (DCHE) needs to be investigated. Figure 4-21 shows the MOF-303/G coated heat exchanger comprising five wire-finned tubes with 25 cm × 25 cm dimensions. The figure also shows a thermal image of the heat exchanger when heated using a power input of 28.8 W for each tube with no airflow. In the thermal image, different colours are used where areas of the heat exchanger coloured red, orange, or yellow have high temperatures, while areas coloured blue or purple indicate low temperatures.

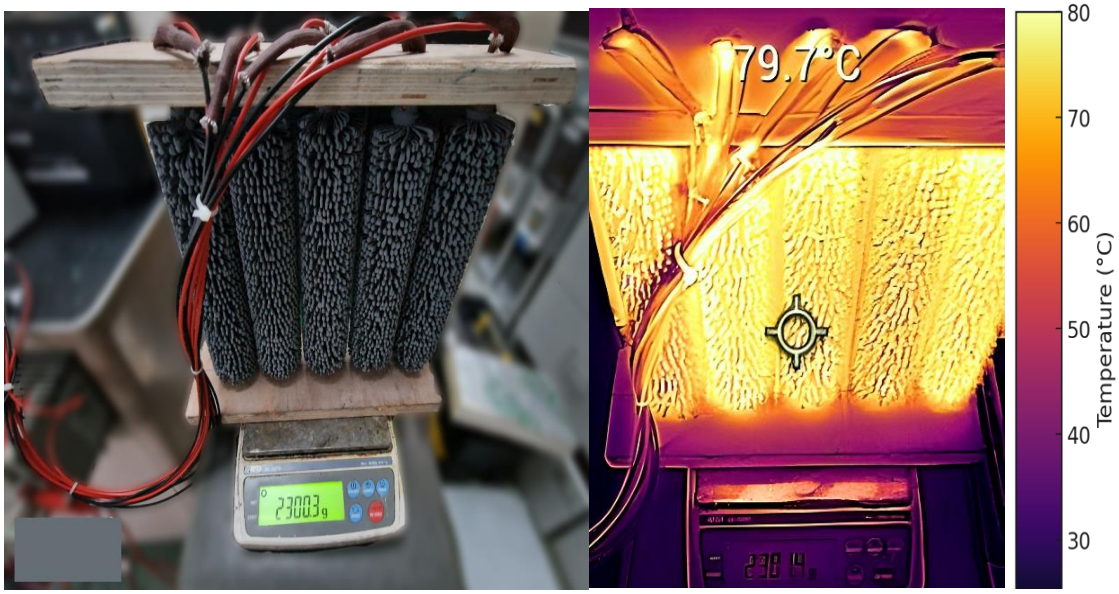



*Figure 4-21: Full-coated desiccant heat exchanger with wire connections and its Thermal image after applying power.*

Figure 4-22 depicts the test facility developed to study the performance of the MOF multi-tube DCHE at a controlled inlet temperature and humidity and different desorption temperatures. The test facility consists of an evaporative cooler that controls the inlet air temperature and humidity, the multitube DCHE mounted on a digital scale and the duct that bounds the airflow onto the DCHE. Various measuring instruments (see Figure 4-23) were used in the experiments, including k-type thermocouples connected to Picologer TC-08 with temperature accuracy of a sum of ±0.2% of reading and ±0.5°C to measure the MOF surface temperature. For measuring the air humidity and temperature, two Elitech humidity and temperature sensors with accuracy $\pm 3RH$ and $\pm 0.3℃$ with uncertainty of 1.73% are installed before and after the DCHE. The scale used to measure the DCHE weight is A&D FZ-5000i integrated with data logger AD-1688 with a minimum unit weight of 0.01g, screen regeneration speed five times/second, and sensitivity fluctuation (10°C to 30°C) of ±2ppm / °C.

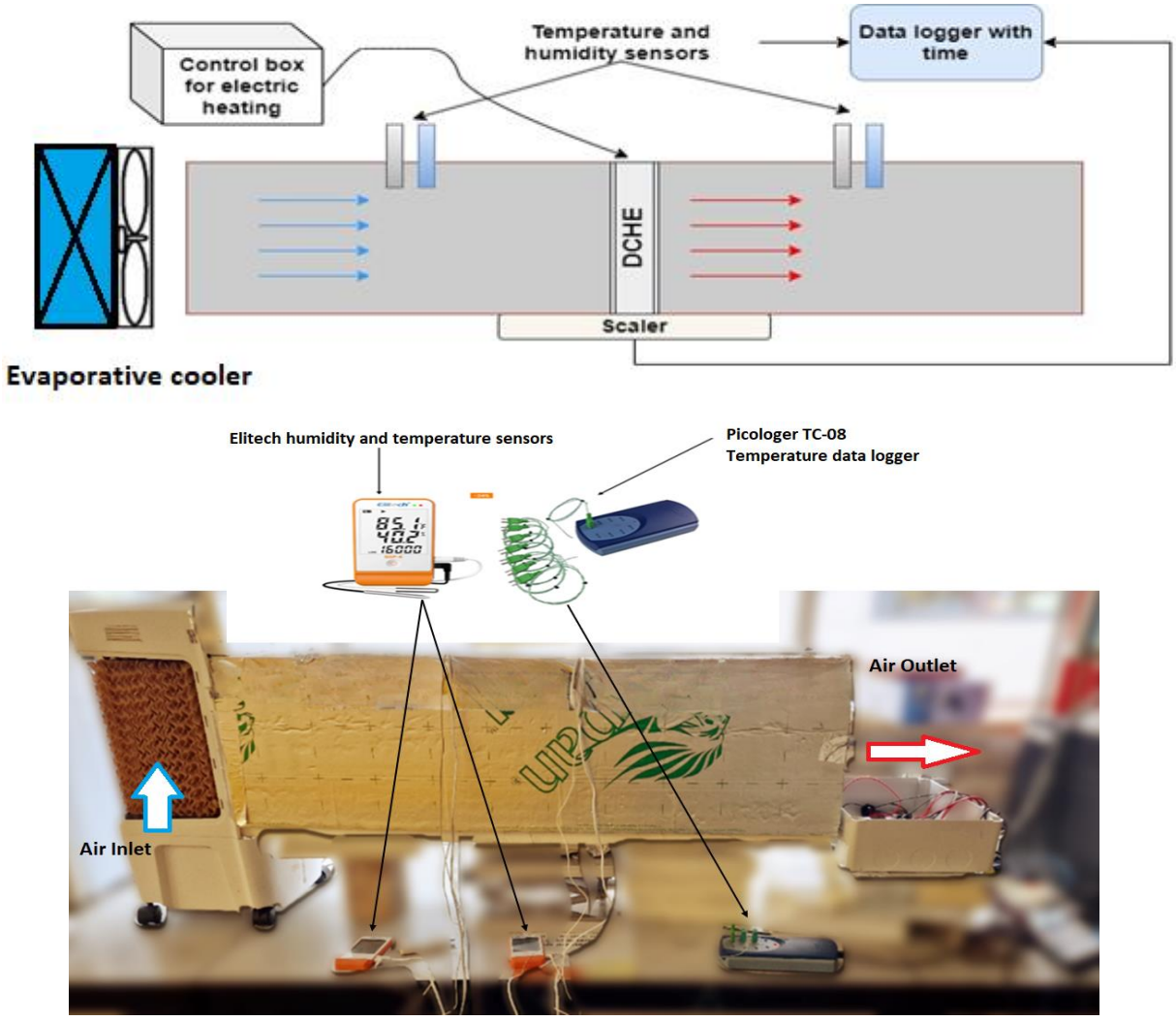



*Figure 4-22: Test facility to characterise the single tube and the complete heat exchanger.*




*Figure 4-23: Temperature, humidity sensors and weight scaler used to collect the data for the dehumidification test facility.*

Table 4-3 presents the accuracy, range, and level of uncertainty associated with the measurement instruments employed within the experimental facility. The calculation of the standard uncertainty considered both random and systematic errors. This was done by utilising data obtained from the equipment manufacturer's datasheets and employing Equation (4-4) [159].

$$u = \frac{a}{\sqrt{3}} \tag{4-4}$$

Where u and a are the standard uncertainty and instrument accuracy, respectively.

Table 4-3 Accuracy, range, and standard uncertainty of measuring instruments**.**

| Instrument | Accuracy | Range | Standard uncertainty |
|---|---|---|---|
| **Humidity sensor** | ± 3% RH | 10% – 99% | 1.73 % |
| **Temperature sensor** | ± 0.3 ° C | -40 ° C – 85 ° C | 0.173 V |
| **Anemometer** | ± 5% | 0 m/s – 30m/s | 2.88 % |
| **Scale** | ± 1% | 0.01 g - 3200 g | 0.577% |

The multi-tube DCHE was tested to characterise its performance at air inlet humidity of 75% and temperature of 20°C and desorption at three different power levels, achieving MOF-303/G temperatures of 45°C, 60°C, and 70°C at 25 watts, 30 watts, and 35 watts per tube respectively during 30 mins. Figure 4-24 represents the desorption rate at three different temperatures: 45°C, 60°C and 70°C; this temperature range is chosen based on the literature for comparison. The higher desorption rate was achieved at 35 watts at a surface temperature

of 70°C, and the lowest desorption rate was achieved at 25 watts at a surface temperature of 45°C.

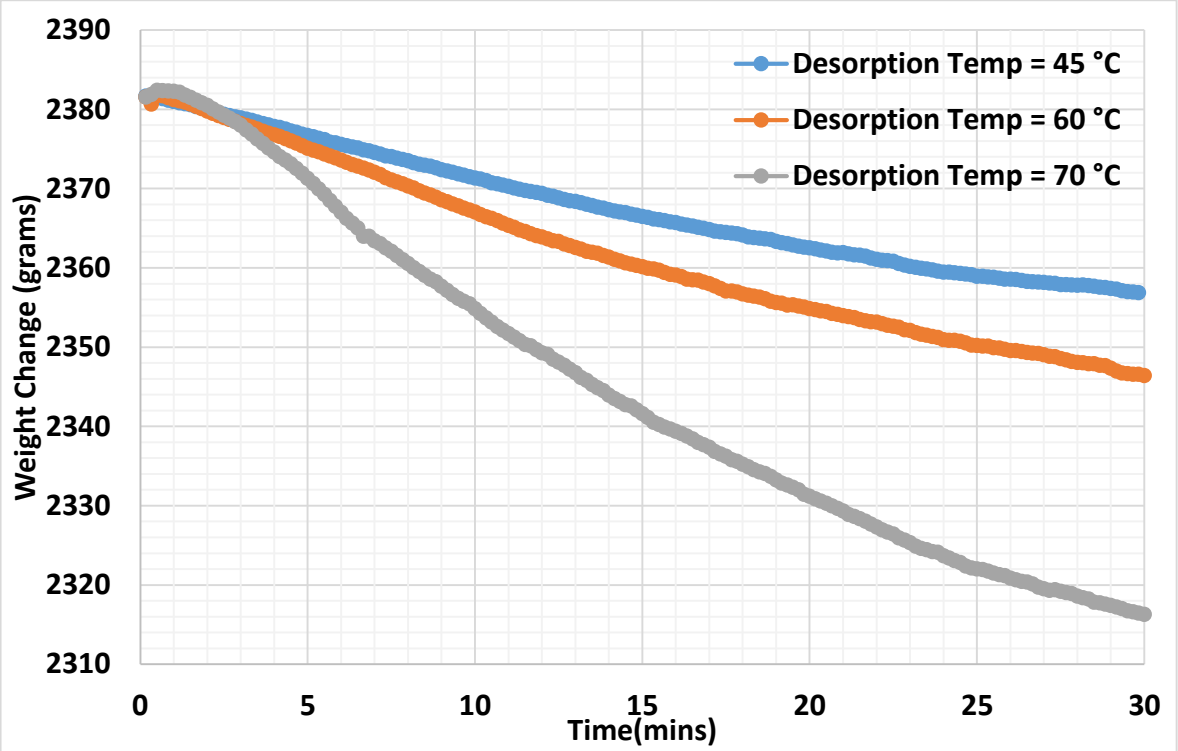



*Figure 4-24: desorption process at three different MOF-303/G surface temperatures: 45°C,60°C and 70°C.*

Figure 4-25 illustrates the variation of the surface temperature of MOF-303/G and its water uptake during the adsorption process at inlet air temperature and relative humidity 20.4°C, 74%, respectively of 20 mins after desorption using a power input of 25 Watts, 30 Watts, and 35 Watts where MOF-303/G surface temperature reached 45°C, 60°C, and 70°C, respectively. The Figure shows that the maximum water uptake achieved was 6.3%, 11.25%, and 17.15%, respectively. The increase in the material surface temperature increased the desorption rate and caused the material to lose more water vapour, as shown in Figure 4-24.

Figure 4-26 shows the air temperature variations before and after the multi-tube DCHE during the adsorption process of 20 mins and incoming air of 20°C. For MOF surface temperature of 45°C, the temperature after the DCHE rapidly increases during the first two mins, reaching 27°C. Subsequently, at the 5-minute mark, there is a noticeable decline in temperature, dropping to around 22.5°C. The trend stabilises after that, and from the 5-minute mark to the 20-minute mark, the temperature remains relatively constant at 20.4°C. For MOF surface temperature of 60°C, the temperature after the DCHE rapidly increases during the first two mins, reaching 29°C. Subsequently, at the 5-minute mark, there is a

noticeable decline in temperature, dropping to around 25°C. The trend stabilises after that, and from the 5-minute mark to the 20-minute mark, the temperature remains relatively constant at 20.4 °C. That means the temperature curve takes longer to reach a lower and stabilised temperature. For a surface temperature of 70°C, the temperature after the DCHE rapidly increases during the first two mins, reaching 34°C. Subsequently, at the 6-minute mark, there is a noticeable decline in temperature, dropping to around 25°C. The trend stabilises after that, and from the 6-minute mark to the 20-minute mark, the temperature remains relatively constant at 20.4°C.

Figure 4-27 shows the humidity variation with time before and after the DCHE during adsorption. The humidity of the incoming air is 75%. For MOF surface temperature of 45°C, the humidity after the DCHE significantly decreased during the first 2 mins, reaching 50%. There is a noticeable increase in the humidity from 5 mins to 10. Afterwards, it starts to settle at 72.5% till the end of the 20 mins. That means that the MOF-303/G becomes saturated. For MOF surface temperature of 60°C, the humidity after the DCHE significantly decreased during the first 2 mins, reaching 44%. There is a noticeable increase in the humidity from 5 mins to 10. Afterwards, it starts to settle at 70% till the end of the 20 mins. That means the MOF-303/G becomes saturated slower than in the previous case due to increasing the surface temperature by 15°C. For MOF surface temperature of 70°C, the humidity after the DCHE significantly decreased during the first 2 mins, reaching 35%. There is a noticeable increase in the humidity from 5 mins to 10. Afterwards, it starts to settle at 70% till the end of the 20 mins.

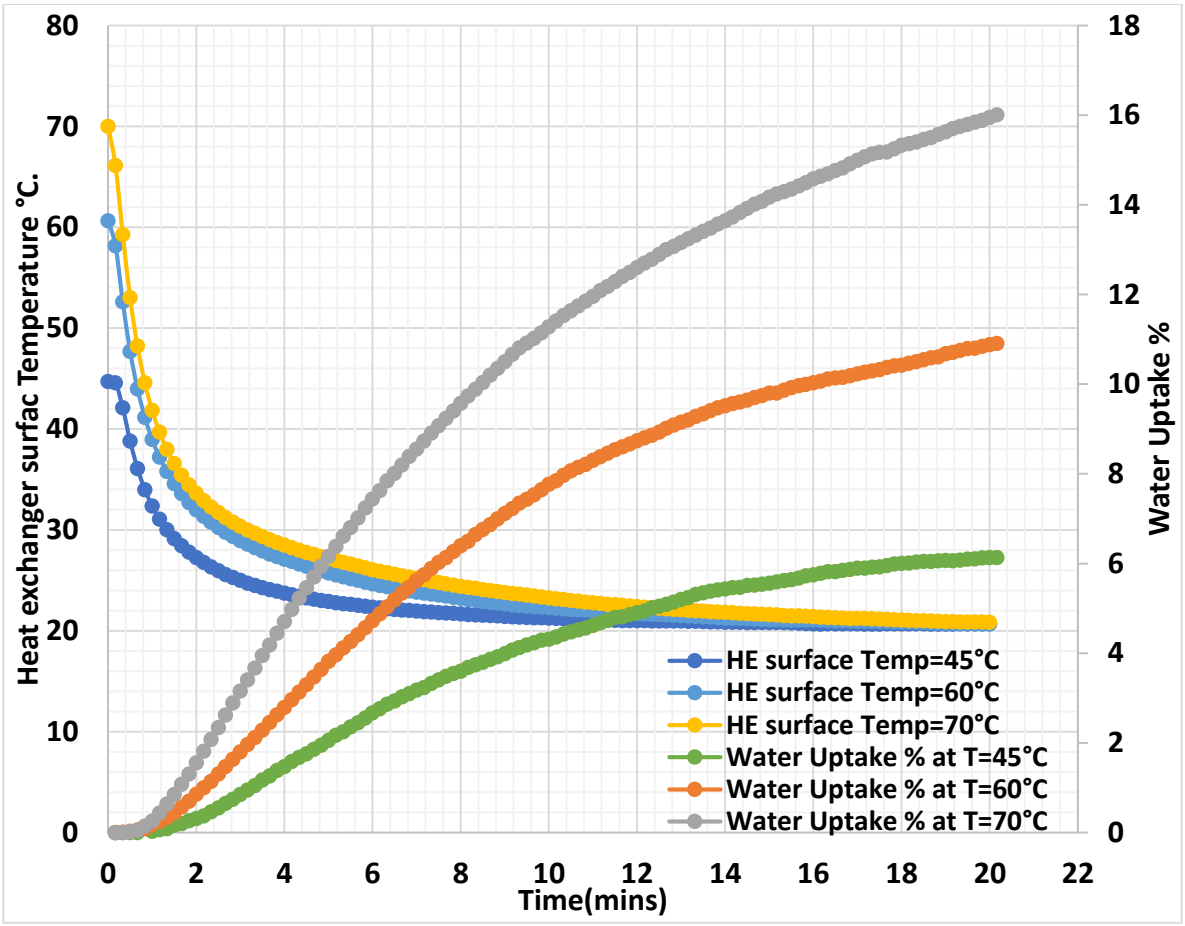



*Figure 4-25: The water uptake of MOF-303/G versus time at MOF surface temperature of 45, 60, and 70°C*

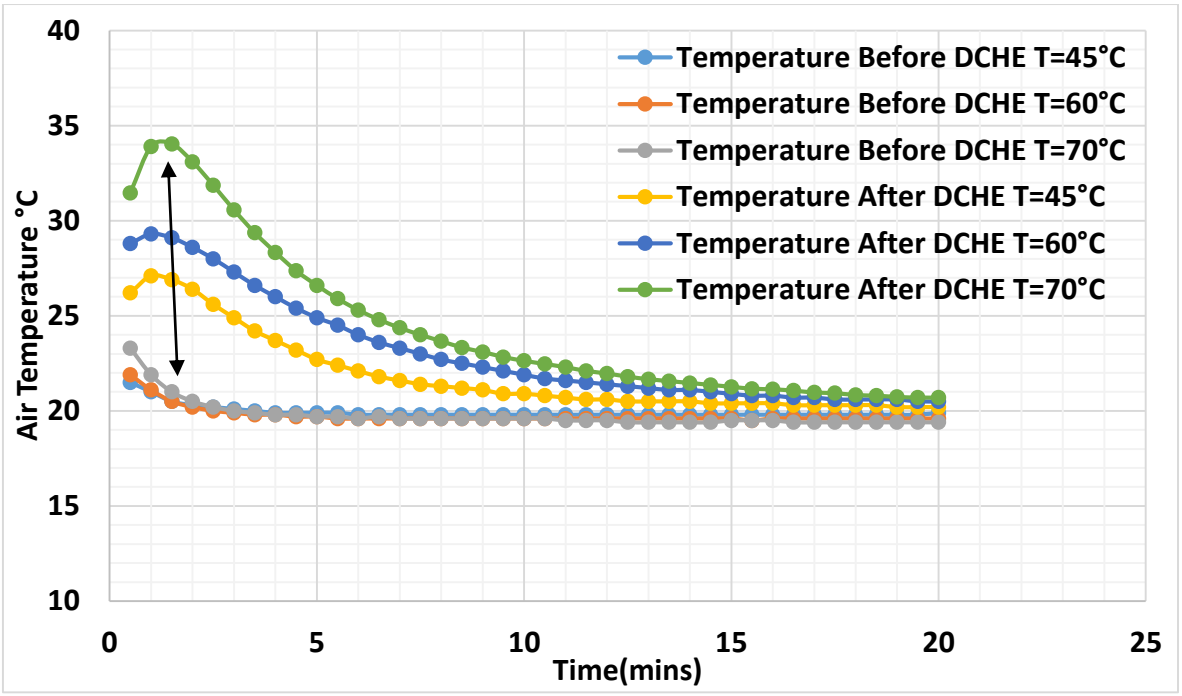



*Figure 4-26: Temperature before and after the heat exchanger at MOF surface temperature of 45°C, 60°C, 70°C*

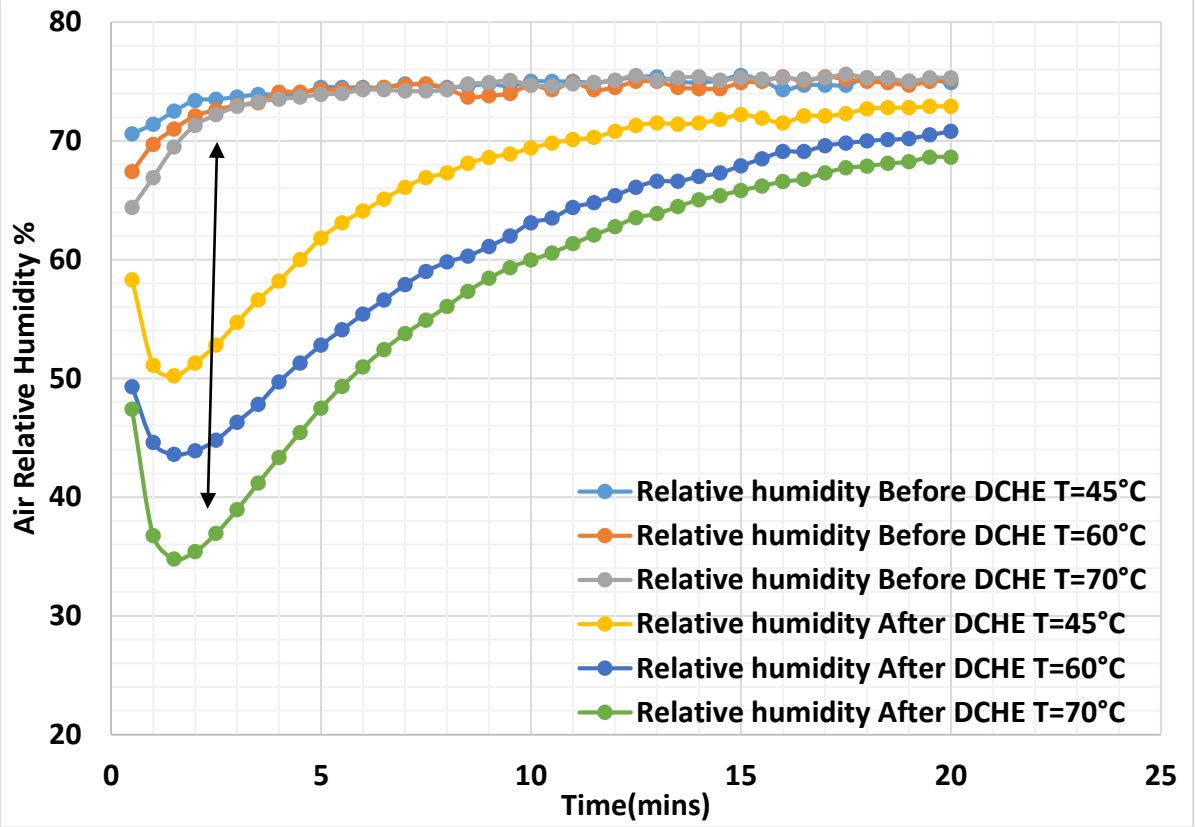



*Figure 4-27: Relative humidity before and after the heat exchanger at MOF surface temperature of 45°C, 60°C, 70°C.*

Figure 4-28 depicts the air dehumidification process on psychrometric chart after duration of 10 mins at the three MOF surface temperatures of 45, 60 and 70°C. Process 1-2 shown in the figure with red line is for the case of MOF surface temperature of 45°C where at point 1, the air inlet temperature and specific humidity are recorded as 19.8°C and 10.69 g/kg_dair. At point 2 the air exit temperature and specific humidity were measured to be 21.3°C and 10.59 g/kg_dair leading to moisture removal of 0.1g/kg_dair. Process 1-2 shown in the figure with blue line is for the case of MOF surface temperature of 60°C where at point 1, the air inlet temperature and specific humidity are found to be 19.6 °C and 10.54 g/kg_dair respectively. At point 2, the air exit temperature and specific humidity were recorded as 22.4°C and 10.36 g/kg_dair respectively leading to moisture removal rate of 0.18g/kg_dair. Process 1-2 shown in the figure with green line is for the case of MOF surface temperature of 70°C. At point 1, the air inlet temperature and specific humidity were recorded as 19.6 °C and 10.6 g/kg_dair while at point 2 the air exit temperature and specific humidity were measured to be 22.9°C and 10.18 g/kg_dair respectively leading to moisture removal rate of 0.42g/kg_dair. Therefore, it can be concluded that as the MOF surface temperature increases, the moisture removal rate increases.

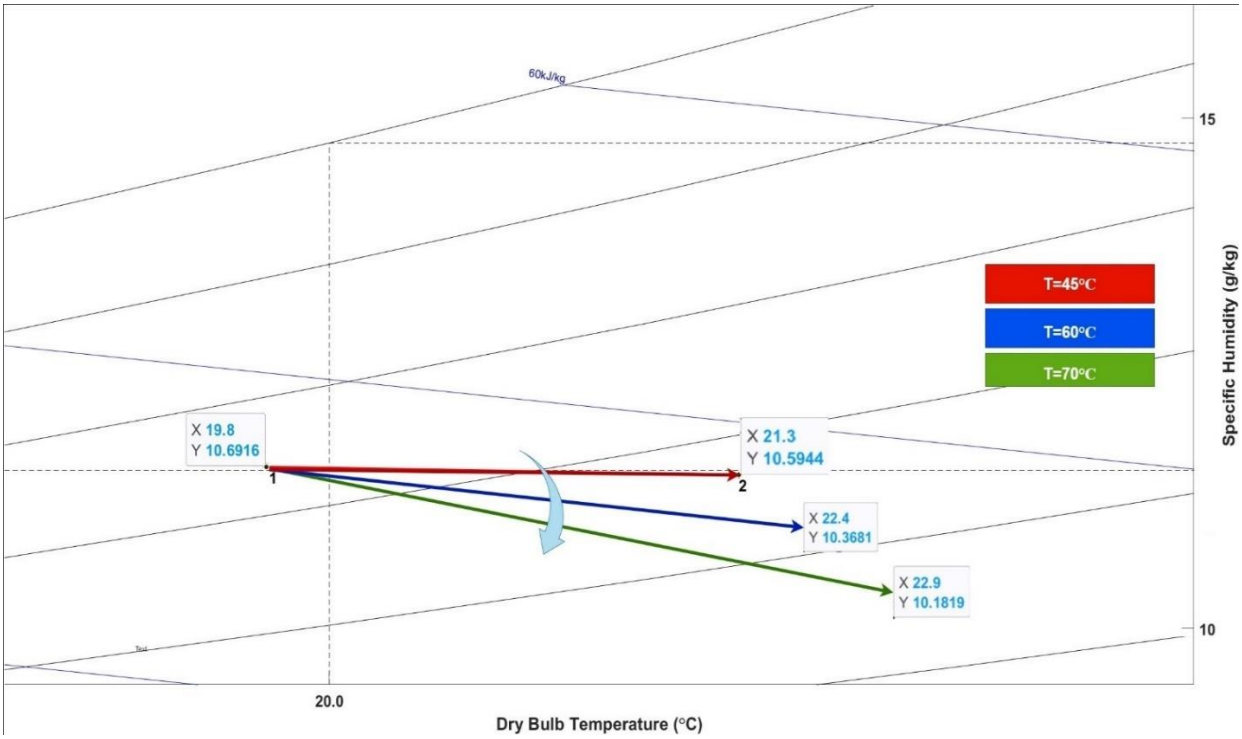



*Figure 4-28: Temperature/humidity ratio before and after the heat exchanger at MOF surface temperature of 45°C,60°C, and 70°C after 10 mins on psychrometric chart.*

Table 4-4 presents specific humidity, temperature, and relative humidity values at three different MOF-303/G surface temperature values: Low (45 °C), Medium (60 °C), and High (70°C). At the Low-temperature, upcoming air-specific humidity is 10.670g/kg(d.a), the air temperature is 20.4°C and air relative humidity is 74.1%, with an associated uptake percentage of 6.3%. In the Medium temperature (60 °C), the upcoming air-specific humidity is 11.045g/kg(d.a), the air temperature is 20.5°C, and the air relative humidity is 73.2%, resulting in an uptake percentage of 11.25%. Finally, at the High-temperature (70 °C), upcoming air-specific humidity is 11.200g/kg(d.a), the air temperature is 20.7°C, and air relative humidity is 73.1%, with the highest uptake percentage of 17.15%.

Table 4-4 *Summary of the effect of changing the DCHE surface temperature desorption/ adsorption process versus the water uptake.*

| | | Low(45°C) | Mid(60°C) | High (70°C) |
|---|---|---|---|---|
| **Input conditions for air** | **Specific humidity** | **10.670** | **11.045** | **11.200** |
| | **Temperature** | **20.4°C** | **20.5°C** | **20.7** |
| | **Relative humidity** | **74.1%** | **73.2%** | **73.1%** |
| **Output desorbed (grams$_{water}$)** | **Water Uptake %** | **6.3%**<br>**23.09** | **11.25%**<br>**33.57** | **17.15%**<br>**64.05** |

The Coefficient of Performance (COP) provides a metric to compare the effectiveness of different desiccant systems against their energy consumption. A higher COP indicates a system extracts more moisture (latent cooling) per unit of energy used for regeneration (typically heat). Optimising COP is critical in ensuring efficient and sustainable operation of desiccant systems. It allows for lowering energy consumption, which translates to saving money on electricity or fuel used for regeneration. Also, by using less energy, desiccant systems contribute less to greenhouse gas emissions and pollution.

To determine the effectiveness of the MOF-303/G DCHE, the coefficient of performance (COP) is defined as:

$$COP = \frac{\int_0^\tau m_a \times (h_{a,out} - h_{a,in})}{Q_{in}} \quad (1)$$

$$Q_{in} = P * N + P_fan \quad (2)$$

Where N is Number of tubes, and P is power of one single tube, $P_fan$ is a fan power, $m_a$ is the air mass flow rate, $h_{a,in}\ and\ h_{a,out}$ are the air-specific enthalpy before and after the DCHE.

Figure 4-29 shows the COP values determined for the three different MOF-303/G surface temperatures of 45°C, 60°C and 70°C and different cycle times. The fan input power is 50 watts. By increasing the MOF surface temperature, the COP increases while it decreases by increasing the cycle time. The best COP was achieved with a cycle time of five mins and a MOF-303/G surface temperature of 70°C, while the lowest COP was achieved with a cycle time of 20 mins and a MOF-303/G surface temperature of 45°C.

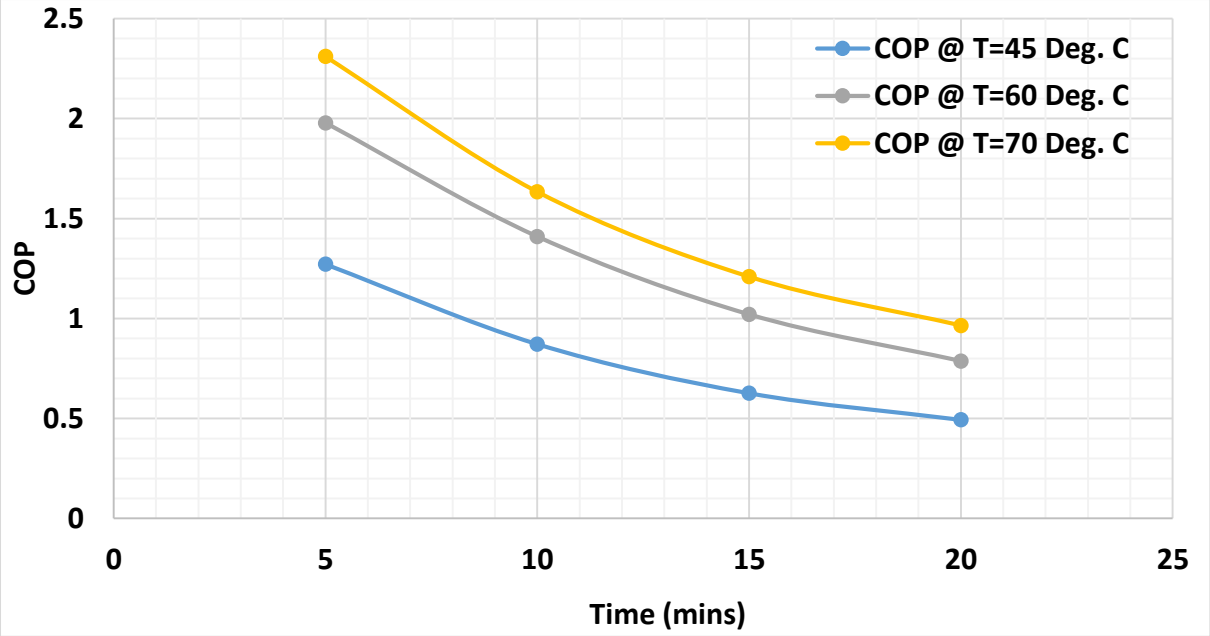



*Figure 4-29: The COP of MOF-303/G versus time at MOF surface temperature of 45°C, 60°C, 70°C.*

To evaluate the performance of the developed MOF-coated wire-finned heat exchanger, its COP values were compared to those reported in the literature. Table 4-5 lists the material used, regeneration temperature, cycle time, types of heat exchanger and the achieved COP. It is clear from this table that the developed MOF-303/G DCHE outperforms those reported in the literature by achieving the highest COP values.

Table 4-5 *intended design in comparison to previously published designs.*

| Reference | Material used | Heat exchanger type | Total fin area | Regeneration temperature | Cycle time | COP |
|---|---|---|---|---|---|---|
| W. J. Luo [164] | silica gel sodium polyacrylate | Single row finned-tube | 7.26m² | 50 | 15 mins | 0.253 |
| | | | | 50 | 15 mins | 0.294 |
| M. Qin [116] | MIL-100(Fe) | Rectangular finned heat sinks | 1.452m² | 50 | 15mins | 0.42 |
| Current work | MOF-303/G | Wire-finned tube | 0.994752m² | 45 | 15mins | 0.6264 |
| | | | | 60 | 15mins | 1.02 |
| | | | | 70 | 15mins | 1.2 |

## 4.5.Summary

In this chapter, six MOF materials were coated on wire-finned tubes as described in chapter 3 and their water vapour removal rate from ambient air at 21°C and 55% relative humidity were experimentally tested. Results showed that MOF-303/G achieved the highest water uptake of 22% compared to 19% for MIL-100(Fe)/G, 17.5% for MOF-801, and 16% for MOF-100(Fe).

Therefore, MOF-303/G was used to develop an electrically heated wire-finned multi-tube heat exchanger, which was tested at various power input values, achieving MOF surface temperatures of 45°C, 60°C, and 70°C. Increasing the MOF-303/G surface temperature during the desorption process (regeneration) resulted in drying the desiccant material, leading to the increase in water uptake from 6.3% at 45°C to 11.25% at 60°C to 17.15% at 70°C during the adsorption process.

The Coefficient of Performance (COP) measures the effectiveness of different desiccant systems against their energy consumption. A high COP indicates a system extracts more moisture (latent cooling) per unit of energy used for regeneration (typically heat). The COP of the developed MOF-303/G DCHE was determined and compared to other desiccant-coated heat exchangers in the literature. Results showed that COP values range from 0.6264 to 1.02 to 1.2 at the regeneration temperatures of 45°C, 60°C, and 70 °C, respectively, outperforming those reported in the literature with COP range from 0.253 to 0.42.

This investigation illustrated that the wire-finned tube heat exchanger coated with MOF-303/G possesses substantial potential compared to conventional heat exchanger designs. As a result, this design has been chosen for desiccant air conditioning applications and will undergo additional testing in the subsequent chapter.

# Chapter 5 Case study for DCHEs to control the greenhouse's climate

From the preceding chapter, we identified six materials, MOF-303/G, that exhibited the most significant adsorption under normal conditions. This chapter focuses on the development of a 3D model using COMSOL Multiphysics for finite element analysis of desorption/adsorption processes using MOF-303/Graphene (MOF-303/G). The objective is to investigate the relationship between desorption duration and input power and determine the scenario that yields the best water removal rate per unit of power consumption. Furthermore, the outcomes derived from the 3D model were correlated with a macroscopic analysis to regulate the climate within a greenhouse with $2m^3$ volume.

**(This chapter is based on the previously published paper: Andrew N. Aziz , Raya Al-Dadah , Saad Mahmoud, Mohamed A. Ismail, Mohammed K. Almesfer, Marwa F. El-Kady, and Hassan Shokry "MOF-801/Graphene Adsorbent Material for Greenhouse Climate Control System—Numerical Investigation," Energies, vol. 16, no. 9, 2023.)**

## 5.1. Computational Fluid Dynamic Modelling of MOF-303/G

This section has developed a 3D computational Fluid Dynamic model for a copper wire finned tube heat exchanger coated with a 0.3mm thick layer of MOF-303/G. Figure 5-1 shows a 3D CAD drawing of this wire-finned tube imported to COMSOL Multiphysics to simulate water vapour's adsorption/desorption processes on the coated MOF. In addition, this wire-finned tube was integrated with Nichrome wire to provide electrical heating for the desorption process. In the COMSOL model, the following modules were used: (i) electrical heating module to simulate the heating process, (ii) heat transfer in solids and fluids module to simulate the heating effect through the body and the MOF material, (iii) Darcy's law to describe the momentum of fluid flow in the porous domain, and (iv) Linear Driving Force (LDF) to model the MOF domain's water uptake taking into account the MOF's adsorption isotherm and kinetics.

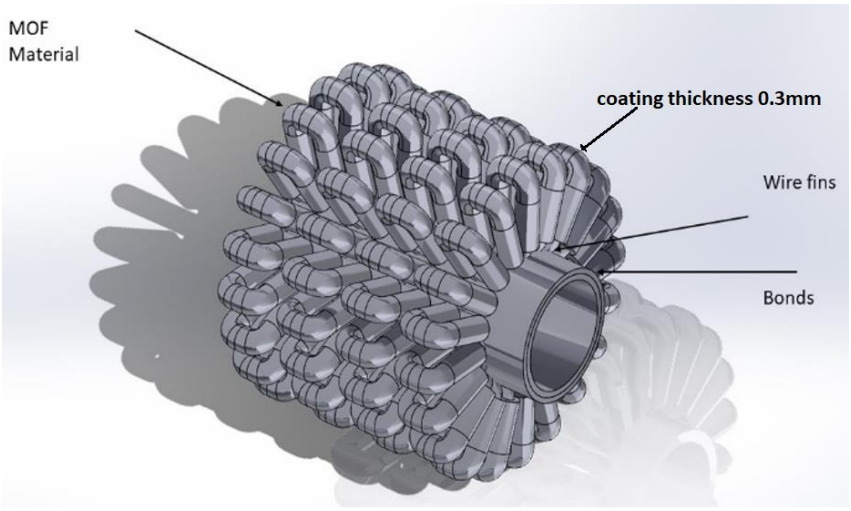



*Figure 5-1: MOF-303/G-coated wire finned tube and its 3D CAD model.*

Equation 5-1 describes the heat transfer in solids and fluid $where\ Q_{ted}$ Is the thermoelastic damping [165]

$$\rho C_p \frac{\partial T}{\partial t} + \rho C_p \mathbf{u} \nabla T + \nabla(-k \cdot \nabla T) = Q_e + Q_{ted} \quad (5\text{-}1)$$

Equations 5-2 to 5-4 describe the electrical heating process [166]. $Q_e$ (W/m3) is the resistive heating in the heat equation represented in equation 2

$$\rho C_p \frac{\partial T}{\partial t} + \nabla(-ks \cdot \nabla T) = Q_e \quad (5\text{-}2)$$

$\boldsymbol{J}$ is the current density (A/m2), and E is the electric field strength (V/m) are presented in equations 3 and 4

$$J = \frac{E}{Q_e} \quad (5\text{-}3)$$

$$E = \nabla V \quad (5\text{-}4)$$

Equation 5 presents the Darcy law equation [167]

$$\frac{\partial}{\partial t}(\rho\epsilon) + \nabla \cdot \left(\rho\left(\frac{-K_d}{\mu}\nabla p_v\right)\right) = Q_m \quad (5\text{-}5)$$

Equation 5-6 shows the Linear Driving Force (LDF), where $W_{inf}$ and $W$ are the final and initial instantaneous water uptake, respectively [10].

$$\frac{\partial W}{\partial t} = k\left(W_{inf} - W\right) \quad (5\text{-}6)$$

Where k is the overall mass transfer coefficient , $k_0$ is the LDF empirical constants and $E_a$ Is the activation energy given by equation 5-7 [31]:

$$k = k_0 e^{\left(\frac{-E_a}{RT}\right)} \quad (5\text{-}7)$$

The MOF permeability $(K_d)$ is expressed as follows [168]

$$K_d = \frac{d_p^2 \epsilon^3}{150(1-\epsilon)^2} \quad (5\text{-}8)$$

$Q_m$ in equation 9 is the mass source of the adsorbate through the adsorbent material

$$Q_m = -(1-\epsilon)\rho_{ads}\frac{\partial W}{\partial t} \quad (5\text{-}9)$$

The pressure of the vapour was calculated using ideal gas as follows [169]

$$p_v = \rho_v R_v T \quad (5\text{-}10)$$

The equilibrium water uptake ($W_{inf}$) of MOF-303/G was determined using equations (5-11)-(5-14) [36-28]:

$$A = -RT\ln(\frac{p}{p_o}) \quad (5\text{-}11)$$

$$D_s = D_{so}\, e^{\left(\frac{-Ea}{RT}\right)} \quad (5\text{-}12)$$

$$W_{inf} = 3.4741 * e^{(-0.0006362 * A)} \text{ for } A > 3987 \quad (5\text{-}13)$$

$$W_{inf} = -6.6724\times10-10\cdot A2-7.112\times10-6\cdot A+0.30933 \text{ for } A < 3987 \quad (5\text{-}14)$$

Table 5-1 shows the thermophysical properties of the MOF-303/G used in the model.

Table 5-1 Thermophysical parameters [27-28].

| Properties | MOF-303/G |
|---|---|
| **Powder particle Density** | 0.932 g cm-3 |
| **Tortuosity** | 1.56 |
| **$C_p$ values** | 715 J kg-1 K-1 |
| **Bulk Density** | 0.51 g/cm3 |
| **$Q_{st}$** | 2400 kJ kg-1 |
| **Particle size** | 100-200 nm |
| **Skeletal Density** | 1.5 |
| **$K_d$** | 160 W/m.k |
| **Particle radius Rp(m)** | 120 E-9 |

All physics were coupled and solved numerically using a time-dependent solver, which solves the equations simultaneously to give accurate results with minimum solving iteration time for the non-linear equations. The initial boundary conditions are set by assuming that the adsorbent material is fully saturated with a water uptake of 0.35 kg/kg and material temperature of 30°C. During the desorption process, the heating is enabled by applying electrical power of 28.8 W for a period of 40mins. During the adsorption process, the electrical power is switched off, and the MOF-303/G material was exposed to atmospheric conditions

for a period of 40 mins. During this simulation, a quarter of the tube is used due to symmetry at the two sides of the 3D wire finned tube.

Figure 5-2 shows the temperature and water uptake variation with time during one desorption and adsorption cycle with a desorption time of 40 mins at an input power of 28.8 W and an adsorption time of 40 mins at an ambient temperature of 23°C and humidity of 55%. The blue line represents the temperature variation with time, while the green line represents the water uptake variation with time. It can be seen that the temperature reaches a steady state after 25 mins of heating, reaching 82°C, and the water uptake decreased to 0.01 kg/kg. During the adsorption process, the water uptake increased with time till reaching an uptake of 0.20 kg/kg at 80 mins.

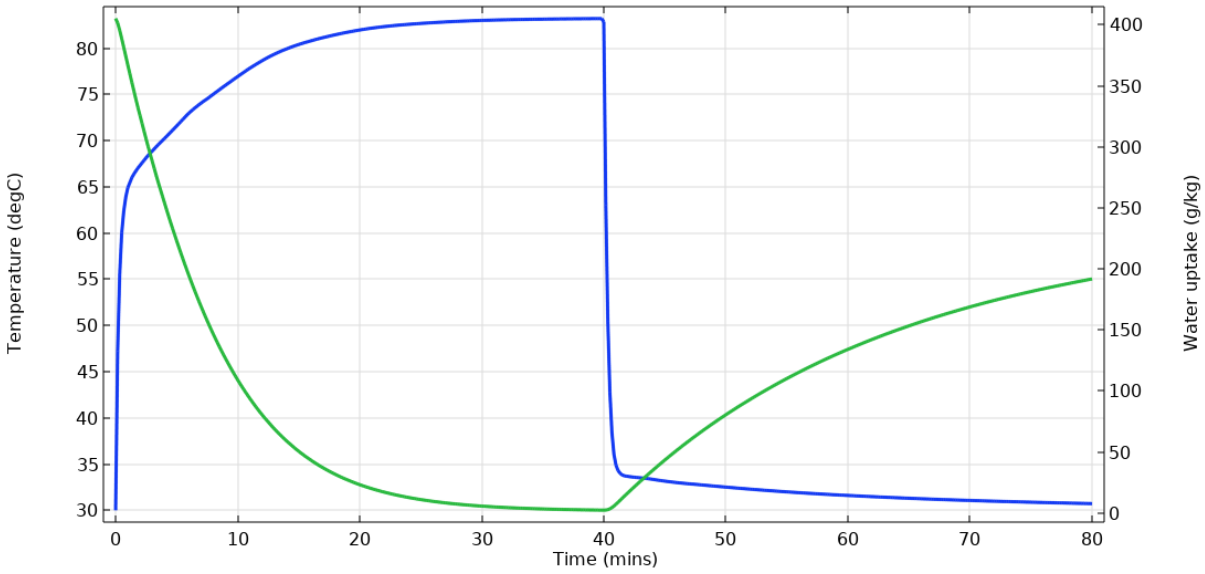



*Figure 5-2: Simulation results at ambient operating conditions.*

Figures 5-3 and 5-4 show 3D images of predicted temperature and water uptake during the heating process (desorption) at 10 and 34 mins and during the adsorption process at 40 and 80 mins for a 15cm wire-finned tube coated with 10 grams of MOF303/Graphene. It is clear from figure 5-3 that as the time increases, the temperature increases and the MOF-303/G water uptake decreases, while figure 5-4 shows that the water uptake increases with time during the adsorption process.

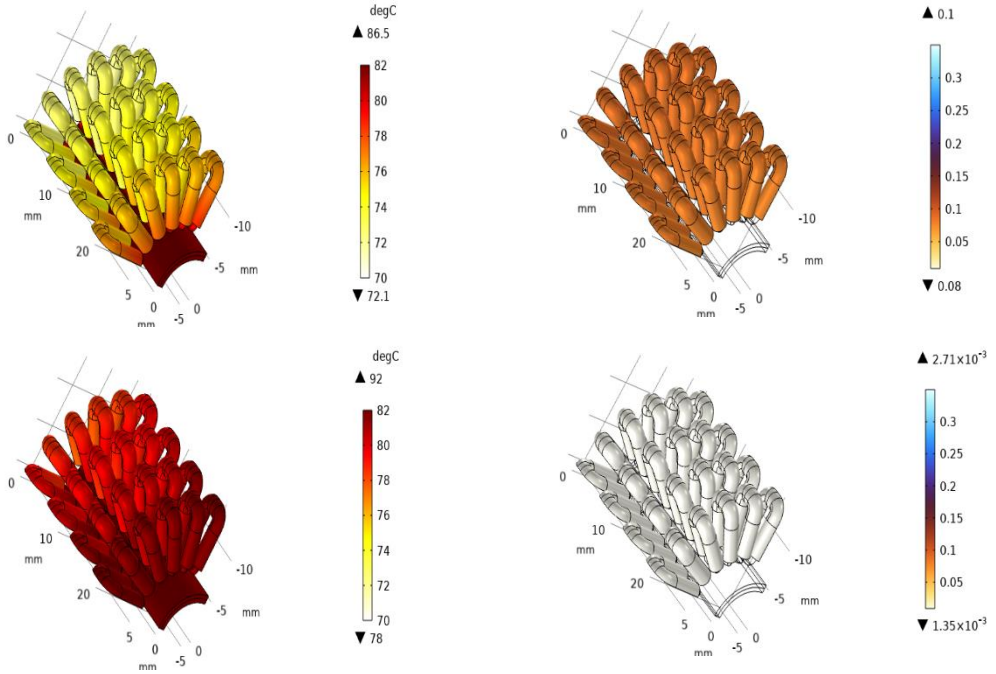



*Figure 5-3: Shows the temperature and the water uptake variation during the desorption process for a 15cm wire-finned tube coated with 10 grams after 10, 34 mins.*

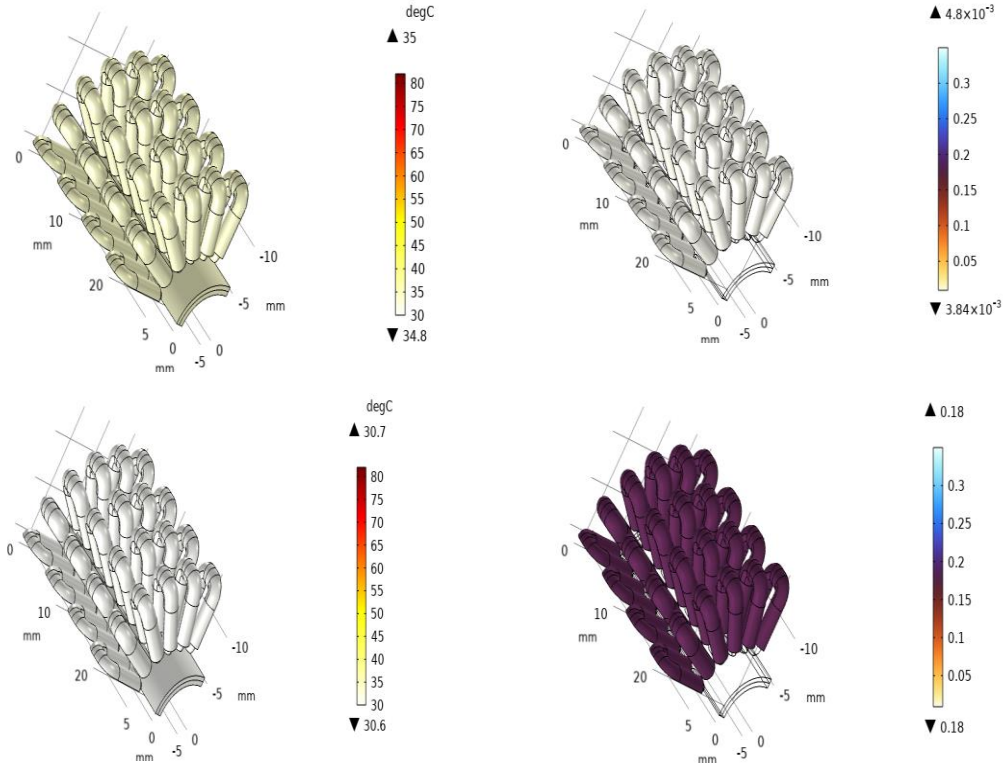
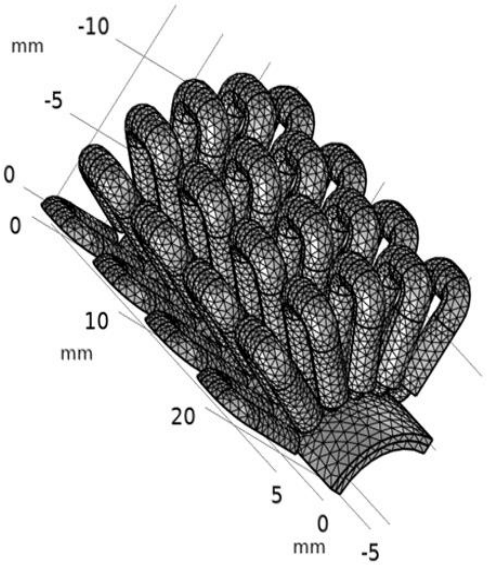



*Figure 5-4: Shows the temperature and the water uptake variation during the adsorption process for a 15cm wire-finned tube coated with 10 grams after 40, 80 mins.*

The mesh sensitivity test is carried out using the physics-controlled mesh option in COMSOL, where tetrahedron mesh shape was selected with four different sizes applied,

namely Extra coarse, coarse, normal, fine and finer. Table 5-2 shows the number of elements used in the various options, and Figure 5-5 shows the predicted temperature variation with time using the four mesh sizes. It is clear that using the coarse mesh option produces similar results to the other mesh sizes but with lower computational times of 20 mins. All the simulation cases were carried out using PC Intel core i7 processor, 48 GB RAM, 1 TB SSD Hard Drive.



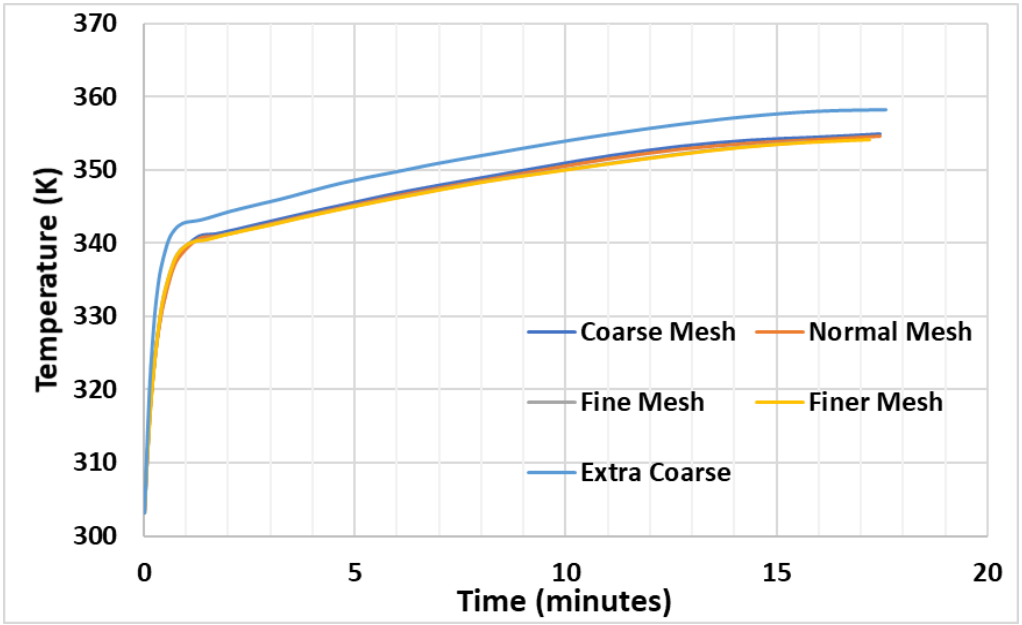




*Figure 5-6: Mesh sensitivity analysis.*

Table 5-2 mesh sensitivity analysis.

| Mesh size | Domain elements | Boundary elements | Edge elements | Simulation time (mins) |
|---|---|---|---|---|
| Extra coarse | 14189 | 10482 | 4404 | 14 |
| Coarse | 43672 | 28864 | 7128 | 20 |
| Normal | 87350 | 50786 | 10331 | 30 |
| Fine | 347294 | 122756 | 16041 | 80 |
| Finer | 806964 | 208410 | 21526 | 127 |

### 5.1.1. CFD Model Validation and Results

The modelled wire finned tube was coated with 10g of MOF-303/G using a 0.3mm thick layer and equipped with 0.41 mm thickness Nichrome wire to provide the heating required for the desorption process. Also, the tube was instrumented with surface thermocouples and mounted on a sensitive scale to measure the variation of its weight with time during the desorption process due to electrical heating and the adsorption process due to moisture capture from the atmosphere, as shown in Figure 5-6. Tests were carried out at an ambient temperature of 23$^{o}$C and relative humidity of 55%, similar to those used in the model. Figure 5-7 compares the model-predicted water uptake during the adsorption process (shown in Figure 5-2) with the experimental measurements with time, showing good agreement with a maximum deviation of ±6%. In addition, the results are repeatable, with a maximum deviation of 5%, as shown in Figure 5-8.

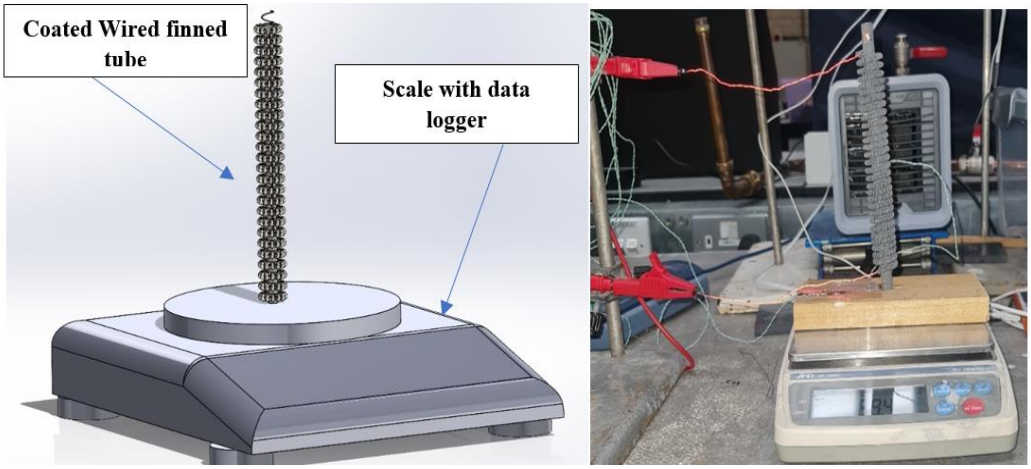



*Figure 5-6: Validation test setup.*

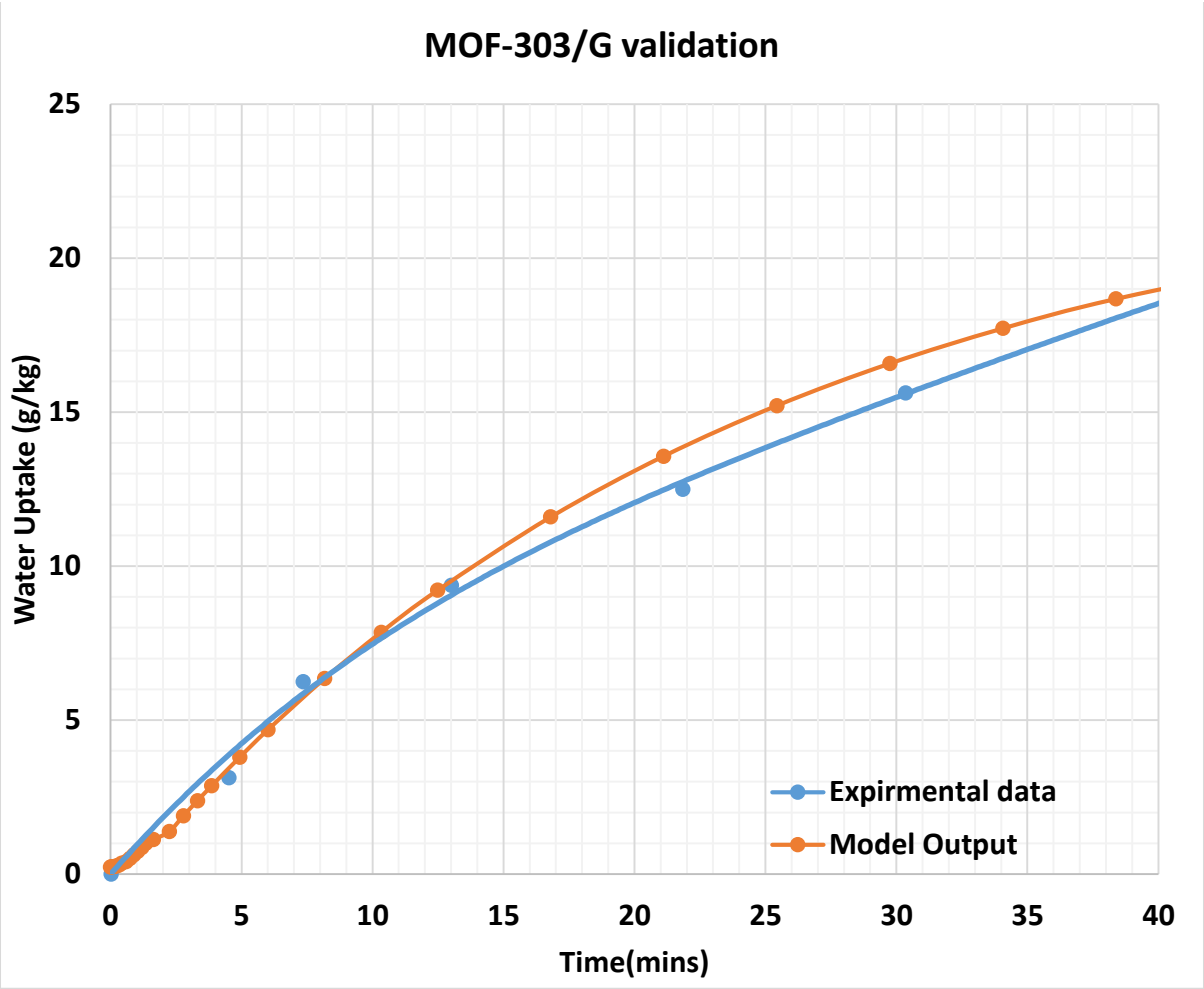
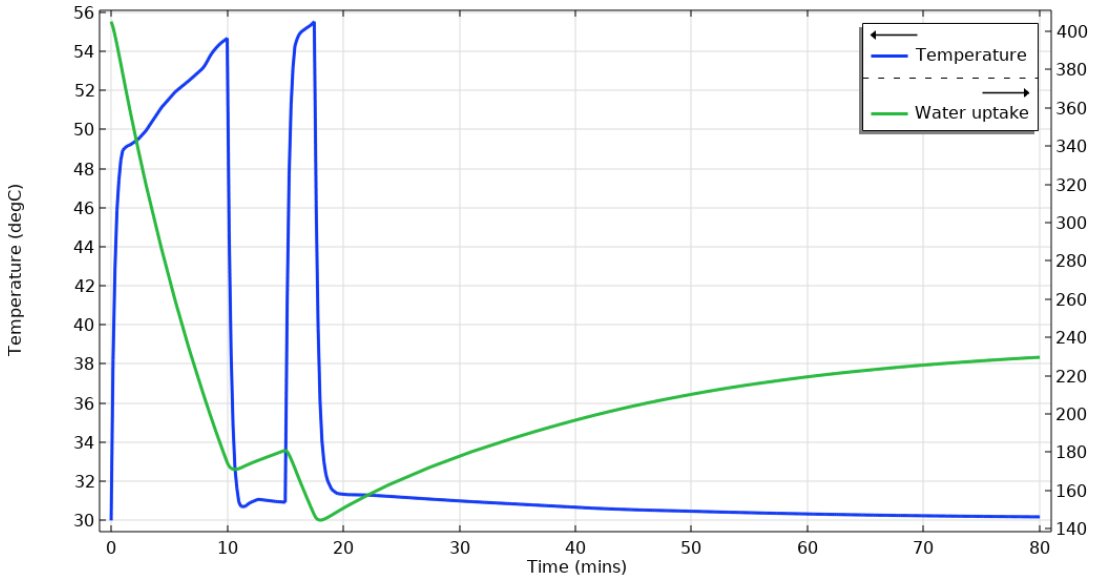


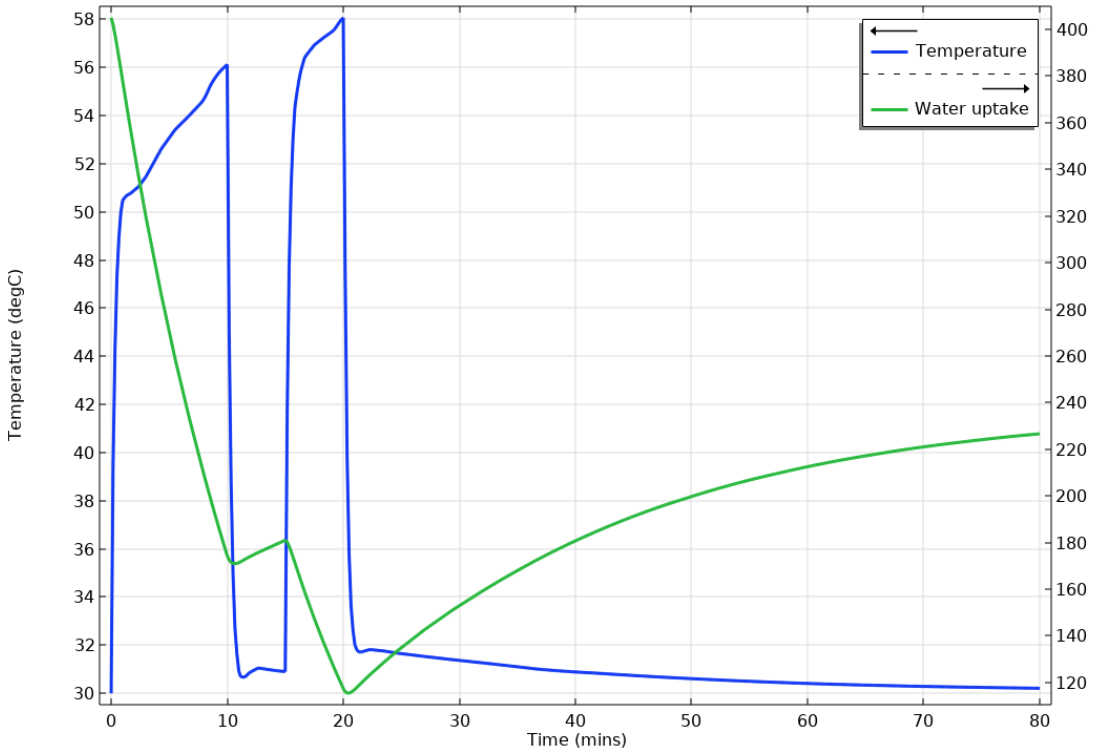

*Figure 5-7: Comparison of the simulation results with experimental data.*




*Figure 5-8: Repeatability test.*

The validated CFD model for the adsorption/desorption cycle of MOF-303/G-coated on wire finned tube was used to investigate the effect of changing the desorption time (2.5mins, 5mins, 10mins, and 40mins) and the applied electrical power on the overall water uptake during the adsorption process of 40mins, the first 10 mins are initialisation. Figures 5-9, 5-10, and 5-11 show the temperature and water uptake variation with time for the power input of 12.8W, 20W, and 28.8W, respectively.


Temperature (degC)
Time (mins)
Temperature
Water uptake


Temperature (degC)
Time (mins)
Temperature
Water uptake

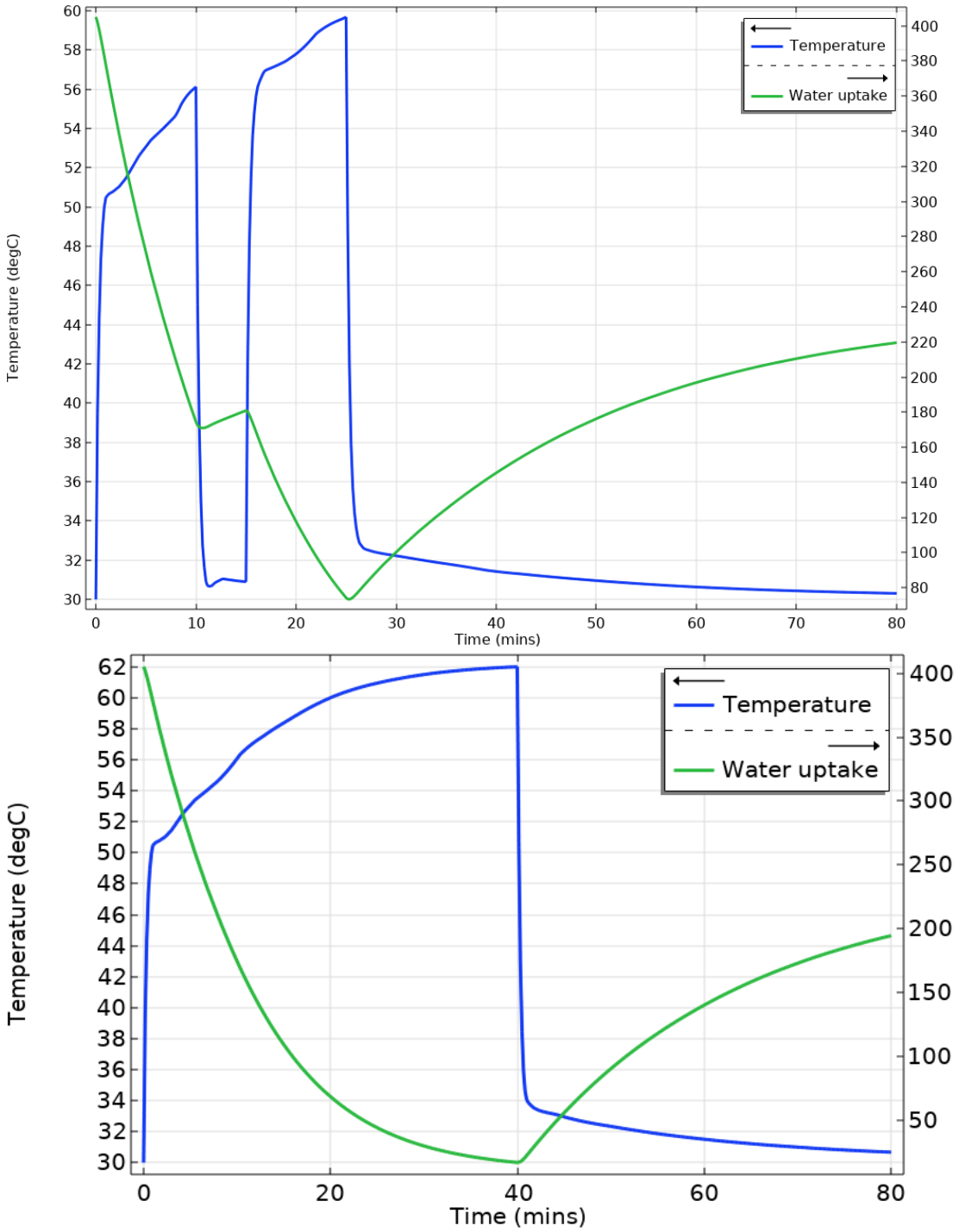
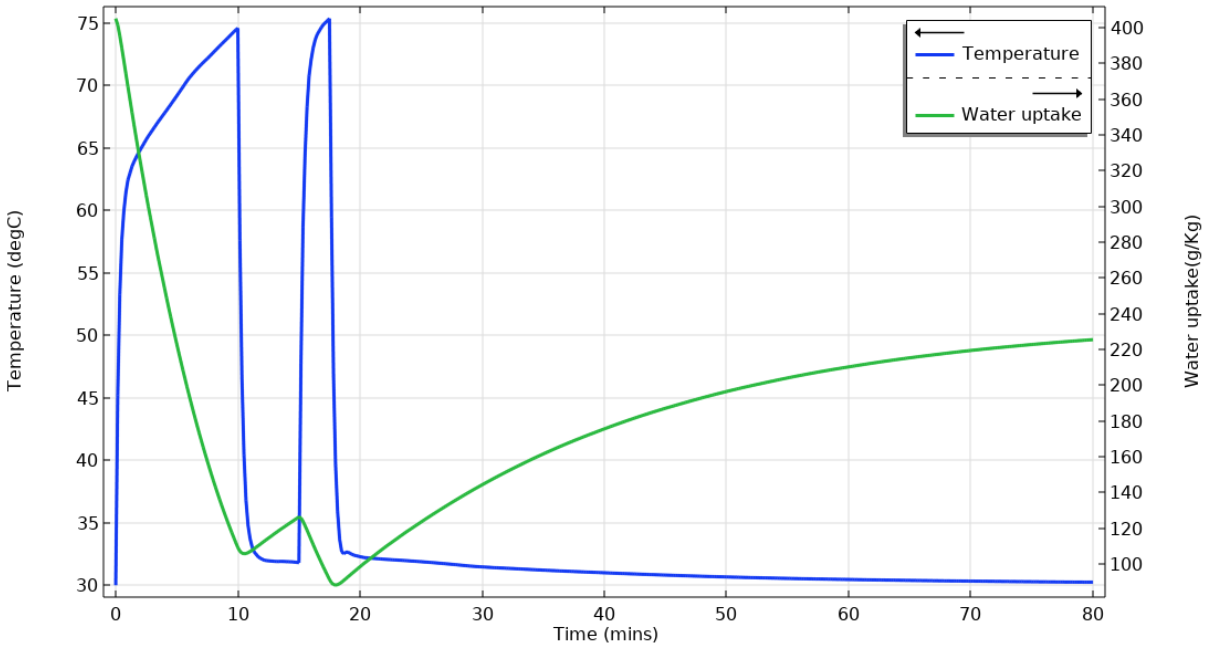
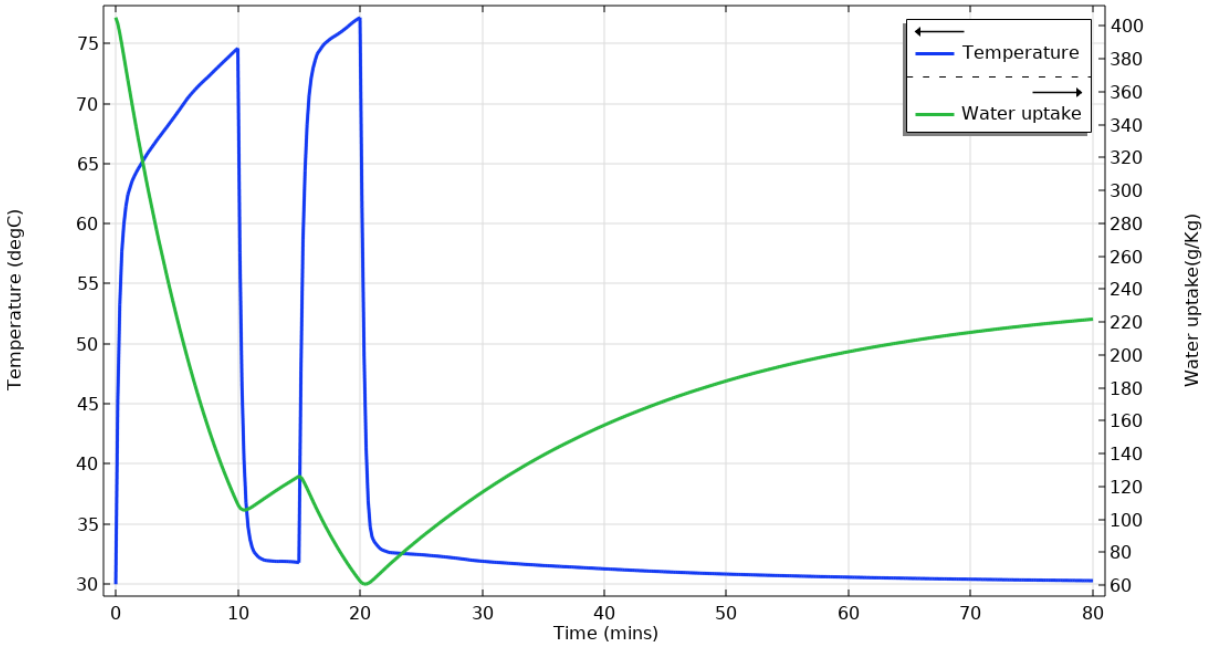



*Figure 5-9: Temperature and water uptake variation with time during desorption and adsorption processes at input power of 12.8W and adsorption time of 40 mins.*


Temperature (degC)
Water uptake(g/Kg)
Time (mins)
Temperature
Water uptake


Temperature (degC)
Water uptake(g/Kg)
Time (mins)
Temperature
Water uptake

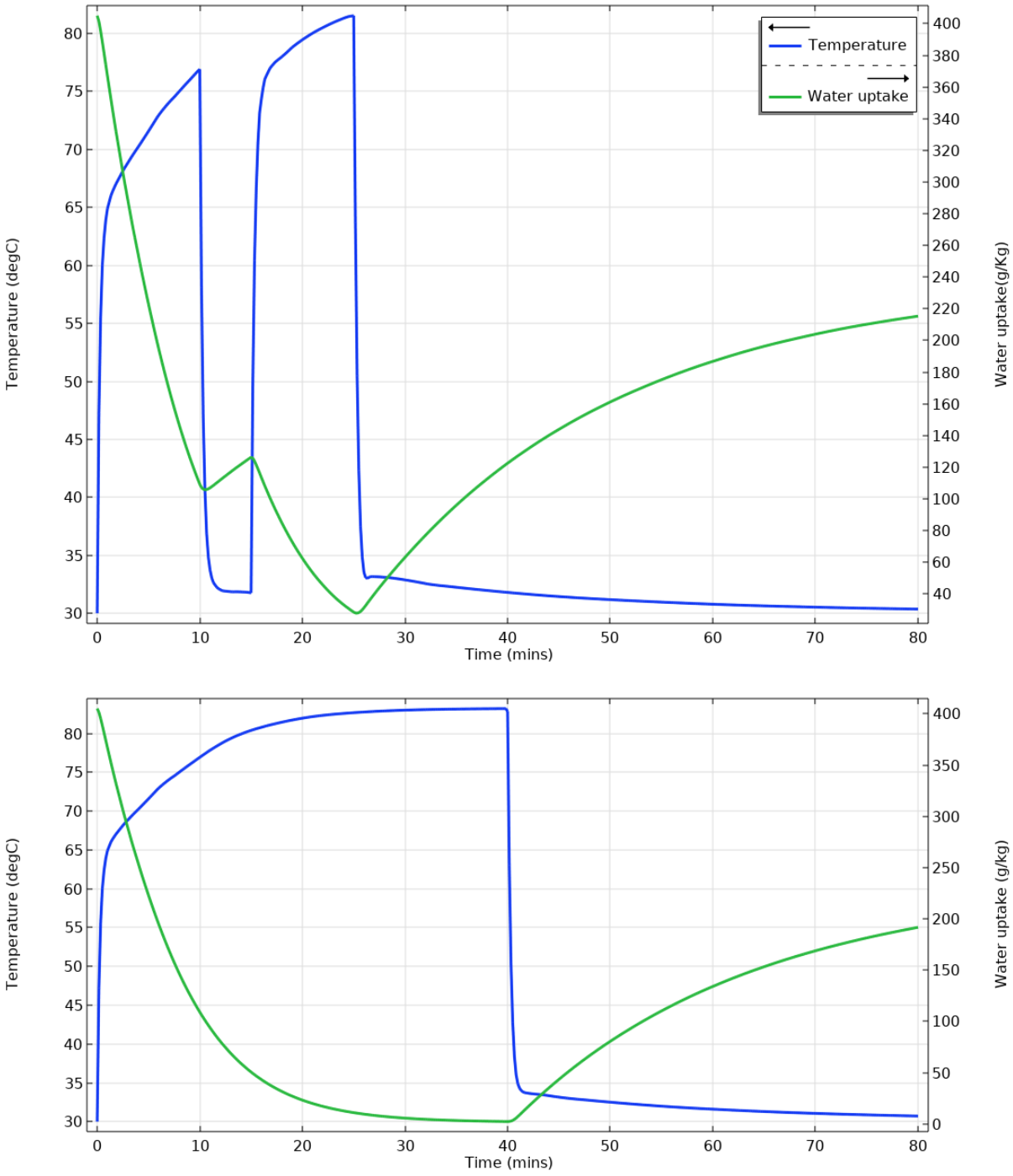
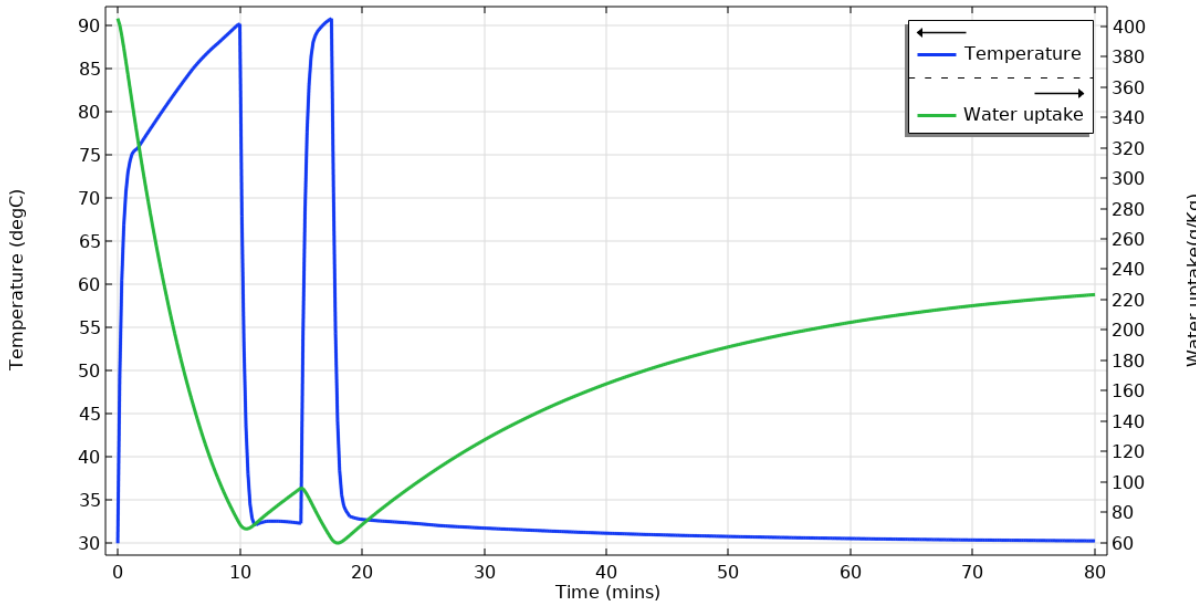
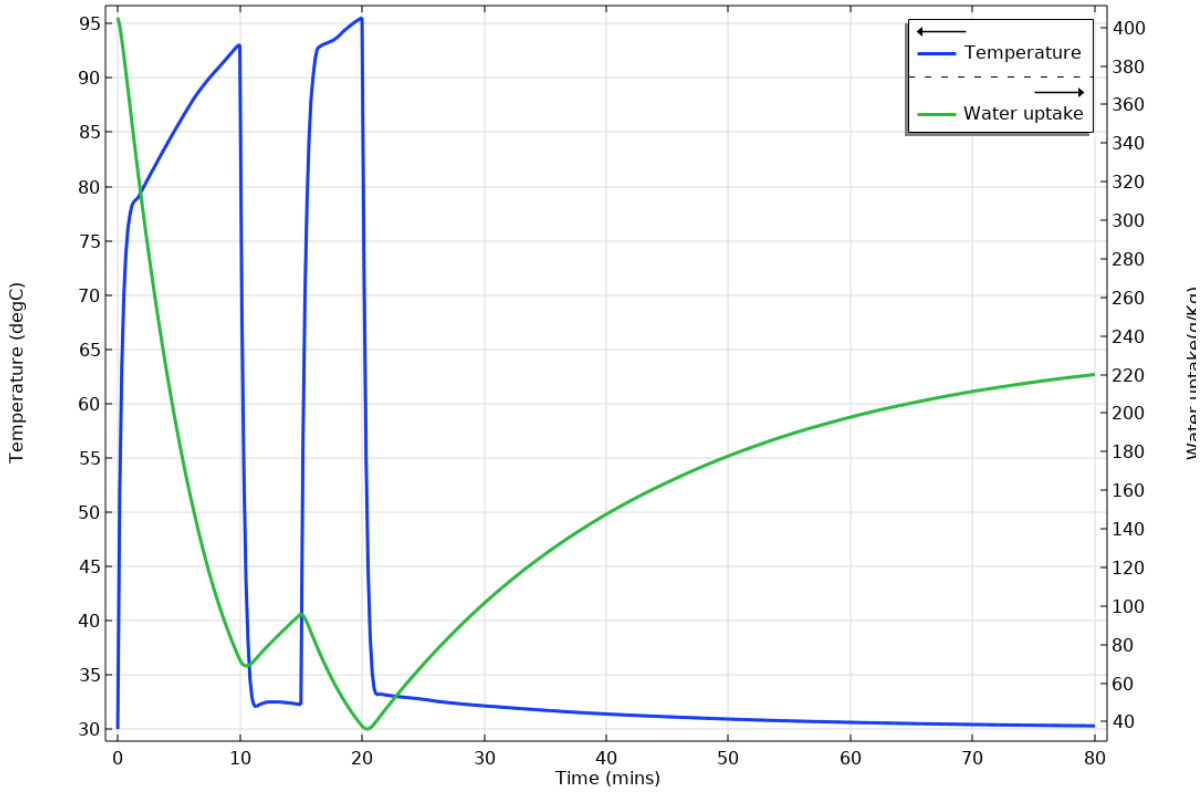



*Figure 5-10: Temperature and water uptake variation with time during desorption and adsorption processes at input power of 20W and adsorption time of 40 mins.*


Temperature
Water uptake
Temperature (degC)
Time (mins)


Temperature
Water uptake
Temperature (degC)
Time (mins)

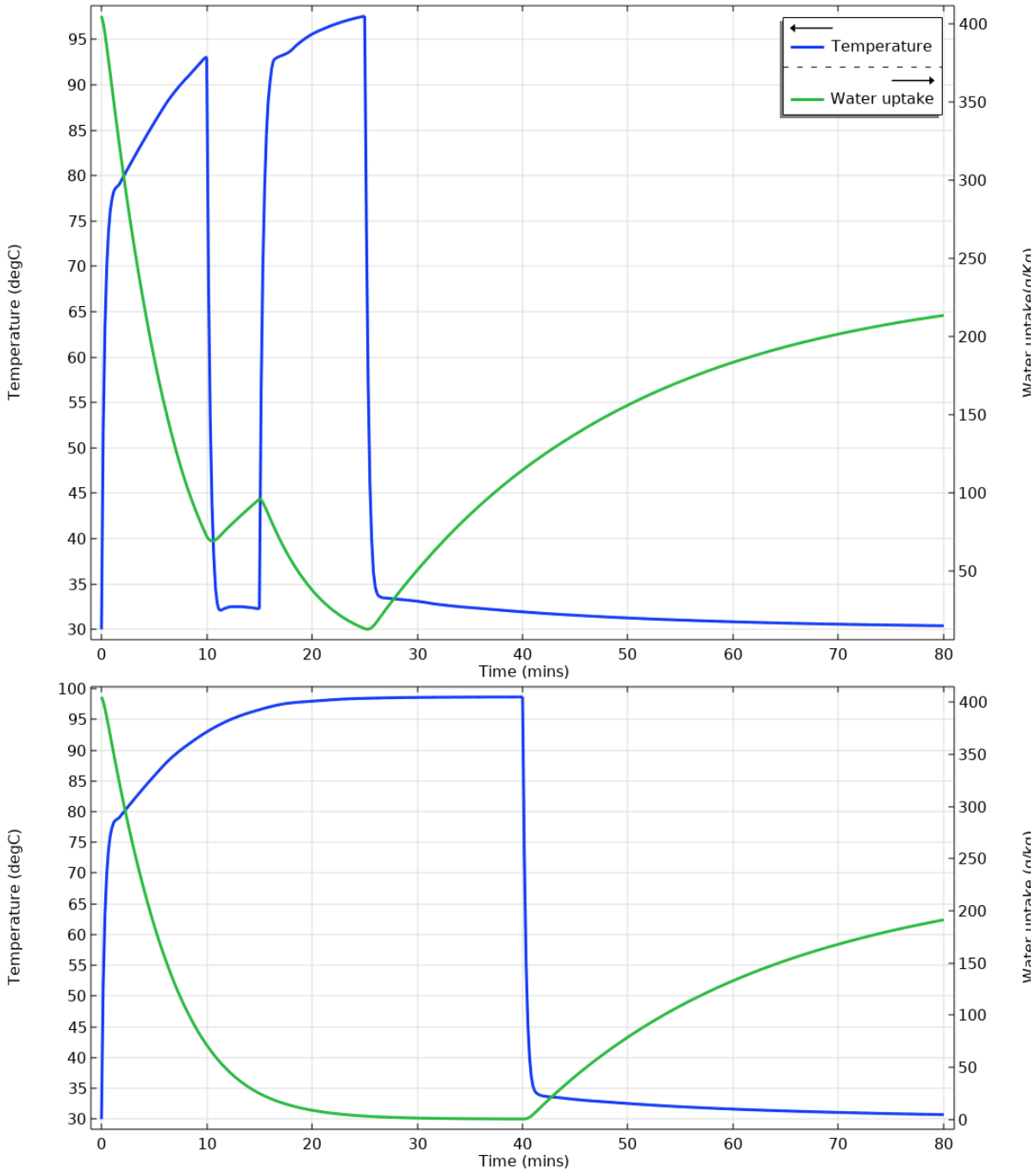



*Figure 5-11: Temperature and water uptake variation with time during desorption and adsorption processes at input power of 28.8W and adsorption time of 40 mins.*

Table 5-3 summarises the results shown in Figures 5-9,5-10,5-11 in terms of water removal rate per cycle, number of cycles per day, total water removal per day and the electrical power consumption per day. It is clear from this table that using a desorption time of 2.5mins and power input of 20W can produce the highest daily water removal per power consumption of 2.69(g/kgMOF)/(W.hr).

Table 5-3 Effect of Desorption time and power input on the daily water adsorbed and power consumption.

| Power Input (W) | Desorption time (mins) | Water uptake at end of desorption process (g/kg) | Water uptake at end of adsorption process (g/kg) | Net water adsorbed per cycle (g/kg) | Number of cycles per day | Net water adsorbed per day (g/kg) | Power Consumption per day (W.hr) | Water to Power ratio ($g/kg_{MOF}$/W.hr) |
|---|---|---|---|---|---|---|---|---|
| 12.8 | 2.5 | 147.5 | 229.83 | 82.33 | 33.88 | 2789.53 | 1084.24 | 2.57 |
| | 5 | 117.47 | 227.12 | 109.65 | 32 | 3508.80 | 2048 | 1.71 |
| | 10 | 74.29 | 221.62 | 147.33 | 28.8 | 4243.10 | 3686.40 | 1.15 |
| | 40 | 17.231 | 194.67 | 177.44 | 18 | 3193.90 | 9216 | 0.35 |
| 20 | 2.5 | 91.189 | 225.68 | 134.49 | 33.88 | 4556.87 | 1694.12 | 2.69 |
| | 5 | 62.46 | 225.1 | 162.64 | 32 | 5204.48 | 3200 | 1.63 |
| | 10 | 28.43 | 217.98 | 189.55 | 28.8 | 5459.04 | 5760 | 0.95 |
| | 40 | 2.28 | 200.95 | 198.67 | 18 | 3576.06 | 14400 | 0.25 |
| 28.8 | 2.5 | 62.37 | 223.73 | 161.36 | 33.88 | 5467.26 | 2439.53 | 2.24 |
| | 5 | 37.8 | 223.38 | 185.58 | 32 | 5938.56 | 4608 | 1.29 |
| | 10 | 12.89 | 217.26 | 204.37 | 28.8 | 5885.86 | 8294.40 | 0.71 |
| | 40 | 0.478 | 199.8 | 199.32 | 18 | 3587.8 | 20736 | 0.17 |

## 5.2. Green House Climate Control System Air-to-Air heat exchanger

Figure 5-12 shows a schematic diagram of the proposed greenhouse climate control system to achieve the required temperature and humidity levels. This system consists mainly of two MOF-303/G-coated heat exchangers, an air-to-air heat exchanger and an evaporative cooler that will deliver the input air at the target temperature and humidity to the greenhouse. In this system, the incoming humid air from the greenhouse at (1) will pass through the air-to-air heat exchanger to reduce the temperature of air coming from the MOF-coated heat exchanger. The air leaving the air-to-air heat exchanger (2) will pass through the MOF-303/G-coated heat exchanger (DCHE), where the MOF material will adsorb the air moisture content, thus reducing its humidity (3). During this process, the air temperature will increase due to the released heat of adsorption. The dehumidified hot air will then pass through the air-to-air heat exchanger where it is cooled down while its moisture content remains constant. A further cooling will be applied to the air (4) using the evaporative cooler, where the target temperature and humidity will be achieved and delivered to the greenhouse (5). In this system, two DCHEs are needed to enable continuous air dehumidification, where they will alternate between adsorption and desorption processes. During the desorption process, the desorbed water vapour can be condensed in the water vapour condenser and used for irrigation of the greenhouse. D1 to D6 are dampers to control the airflow direction

at various locations according to the required operating scenario. More details on this code are presented in Appendix I.

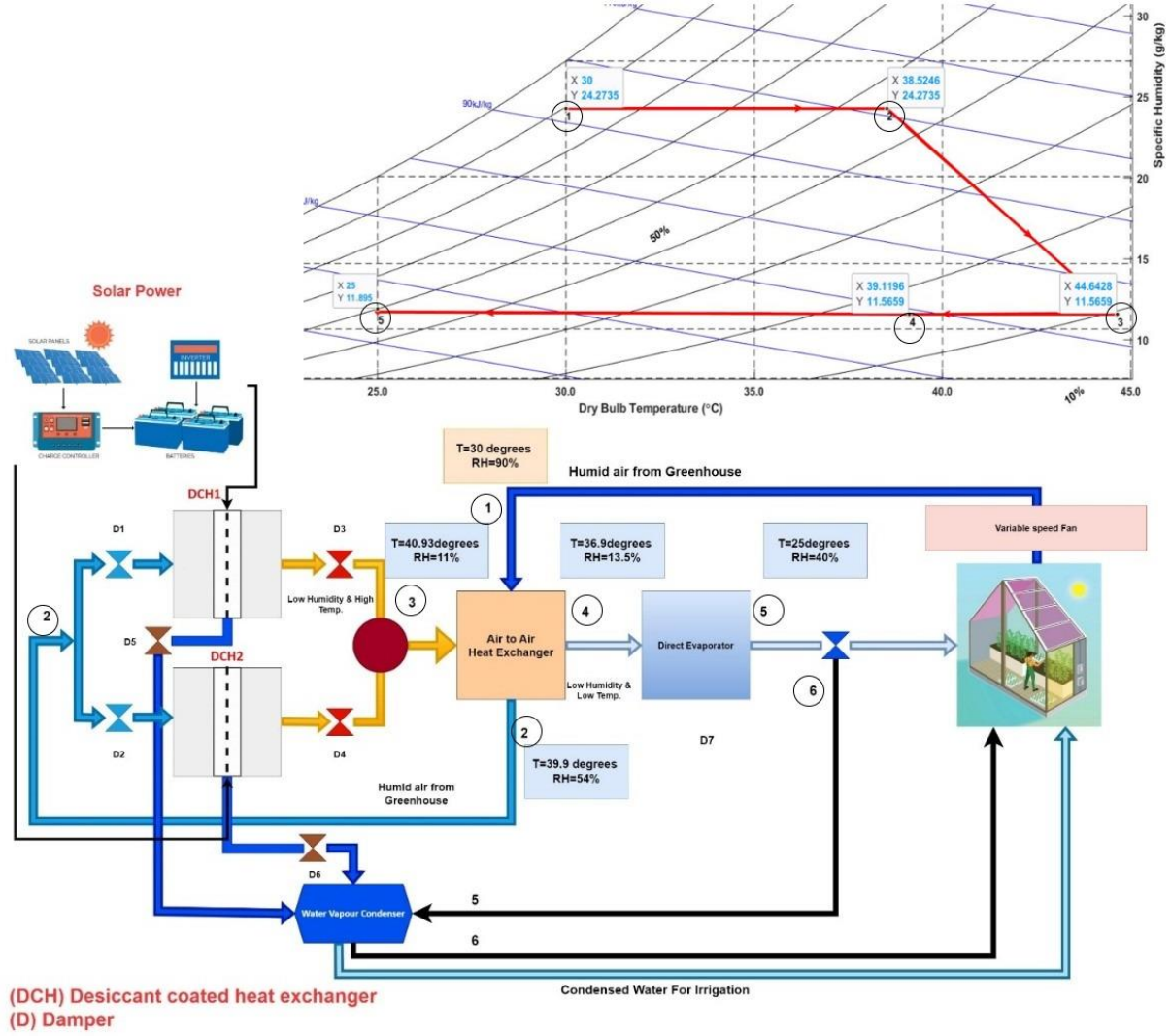



*Figure 5-12: Greenhouse climate control based on a desiccant cooling system using MOF-303/G material.*

The governing equations for heat and mass transfer for the major components of the system are listed below where equations 15 to 23 describe the conservation of mass and energy for the DCHEs.

Equation 5-15 describes the conservation of moisture in the air [147] as:

$$\rho_a \, d_e \left(\frac{\partial W_p}{\partial t} + u \frac{\partial W_p}{\partial x}\right) = K_y (W_d - W_p) \tag{5-15}$$

The energy conservation for the air is given in equation 5-16 [147] as:

$$\rho_a C_{pa} d_e \left(\frac{\partial T_p}{\partial t} + u \frac{\partial T_p}{\partial x}\right) = h \left(T_d - T_p\right) + K_y \, C_{pv} (W_d - W_p)(T_d - T_p) \tag{5-16}$$

Desiccant moisture conservation is determined by equation 5-17 [147]:

$$\delta d\ \rho_d \left(\frac{\partial W}{\partial t} - De\frac{\partial W}{\partial x^2}\right) = K_y\left(W_p - W_d\right) \quad (5\text{-}17)$$

Desiccant energy conservation can be written in equation 5-18 [147] as follows:

$$\left(\frac{\partial T_d}{\partial t} - \frac{K_d}{C_{pd}\,\rho_d}\frac{\partial T_d}{\partial x^2}\right)\delta d.\,\rho_d\,.\,C_{pd} = h\left(T_p - T_d\right) + q_{st}\,.\,K_y\left(W_p - W_d\right) + C_{pv}\,K_y\left(T_p - T_d\right)\left(W_p - W_d\right) \quad (5\text{-}18)$$

Where $W_d$ is the adsorbent material equilibrium uptake expressed as a function of the MOF relative humidity as [148]:

$$W_d = 0.62188\frac{P_v}{P_{atm} - P_v} = 0.62188\frac{RHd}{(P_{atm} - P_{vs}) - RHd} \quad (5\text{-}19)$$

The effective diffusivity (De) is determined as [149]:

$$De = D_s\frac{1.6\times 10^{-6}}{\tau}e^{\left(-0.974\times 10^{-6}\frac{q_{st}}{T_d}\right)} (20)$$

Where $q_{st}$ is the heat of adsorption given as [148];

$$q_{st} = A = h_{fg}[1 + 0.2843e^{(-10.28W)}] \quad (5\text{-}20)$$

Where $h_{fg}$ is the latent heat of evaporation for water and is given by[171]:

$$h_{fg} = (2504.4 - 2.4425\ T_d)\ 1000 \quad (5\text{-}21)$$

The desiccant relative humidity equation for MOF-303/G:

$$RHd = 302.92*W^4 - 182.23*W^3 + 29.271*W^2 - 0.0066 \quad (5\text{-}22)$$

Equations 23- 29 describe the heat transfer equations for the air-to-air heat exchanger [172]:

$$T_{po} = (T_{pi} - T_w).\,e^{Ax} + T_w \quad (5\text{-}23)$$

$$A = \frac{-h_p\times a\times n}{m_p\times c_p} \quad (5\text{-}24)$$

$$R_e = \frac{V\times L}{\nu} \quad (5\text{-}25)$$

$$h_p = (0.664\times (R_e{}^{0.5}))\times\frac{(P_r^{\frac{1}{3}}\times k)}{L} \quad (5\text{-}26)$$

$$A = a\times n\times\frac{\delta}{2} \quad (5\text{-}27)$$

$$At = n\times a\times L \quad (5\text{-}28)$$

$$m_p = \rho.V.A \quad (5\text{-}29)$$

Equations 5-30 to 5-44 describe the heat and mass transfer equations [173] for the evaporative cooler shown schematically in figure 5-13:

$$\dot{m}_a.\partial h_m = \delta\dot{Q}_S + \delta\dot{Q}_L \quad (5\text{-}30)$$

$$\delta\dot{Q}_S = h_T.(T_W - T).\partial A \quad (5\text{-}31)$$

$$\delta\dot{Q}_L = \partial\dot{m}_W.\left(C_{pv}T_w + h_{fg}\right) \quad (5\text{-}32)$$

$$\partial\dot{m}_W = h_m.\rho_a(W_s - W) \quad (5\text{-}33)$$

$$\partial\dot{m}_W = \dot{m}_a.\partial W \quad (5\text{-}34)$$

$$\left(C_{pa} + W.C_{pv}\right).\frac{\partial T}{\partial x} = \left[\frac{\mathrm{P}.h_T}{\dot{m}_a} + C_{pv}.\frac{\partial W}{\partial x}\right].(T_w - T) \quad (5\text{-}35)$$

$$\frac{\partial W}{\partial x}.\dot{m}_a = \mathrm{P}.h_m.\rho_a(W_s - W) \quad (5\text{-}36)$$

$$R_e = \frac{U.D_h}{\upsilon_a} \quad (5\text{-}37)$$

$$D_h = 2.D \quad (5\text{-}38)$$

$$\mathrm{Nu}=\mathrm{Sh}=7.54 \quad (5\text{-}39)$$

$$h_T = \frac{D_{va}.\mathrm{Sh}}{D_h} \quad (5\text{-}40)$$

$$h_m = \frac{k_a.\mathrm{Nu}}{D_h} \quad (5\text{-}41)$$

$$D_{va} = 1.87 * 10^{-10} * T^{2.072} \quad (5\text{-}42)$$

Boundary conditions

$$T_W = T_{wb}(T_{in}, \varphi_{in}) \quad (5\text{-}43)$$

$$W_s = \mathrm{W}(T_w, \varphi = 100\%) \quad (5\text{-}44)$$

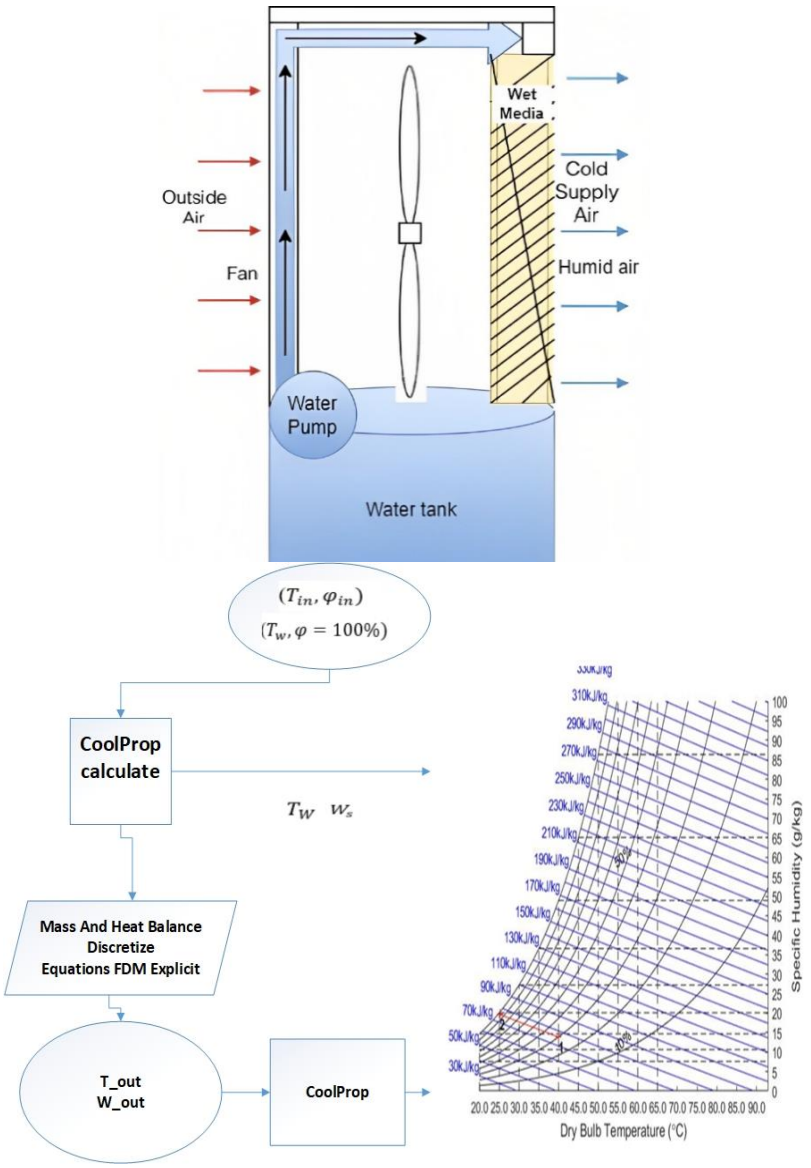



*Figure 5-13: Schematic diagram of direct evaporative cooler/model flow chart.*

The above equations for the DCHEs, air-to-air heat exchanger, and evaporative cooler are solved using MATLAB according to the flow chart in Figure 5-14 using the inputs listed in Table 5-4 coupled with CoolProp [174] for air properties.

Table 5-4 Input parameters to the greenhouse climate control system.

| Model inputs | Value | Units |
|---|---|---|
| Air relative humidity (RH_air) | 65, 75,90 | % |
| Air temperature (T_air) | 30 | $^{o}C$ |
| Air velocity (U) | 1.5, 2.5,3.5 | m/s |
| Air density (Roh_air) | 1.2 | kg/m3 |
| Desiccant density (Roh_desiccant) | 600 | kg/m3 |
| Sher wood number (Sh) | 2.5 | - |
| Specific heat of air | 1005 | kJ/kg/K |
| Air Thermal conductivity | 0.175 | W/mK |
| Nusselt number | 2.45 | - |
| The thickness of plates (t) | 0.4 | m |
| Length of plates (L) | 0.6 | m |
| Width of plates (a) | 0.4 | m |
| Channel width (sigma) | 4e-3 | m |
| No of plates | 70 | - |
| Total heat exchange area(At) | 16.8 | $m^2$ |
| Prandtl number (Pr) | 0.711 | - |
| Dynamic viscosity (neu) | 16.97*10^-6 | Ns/m |

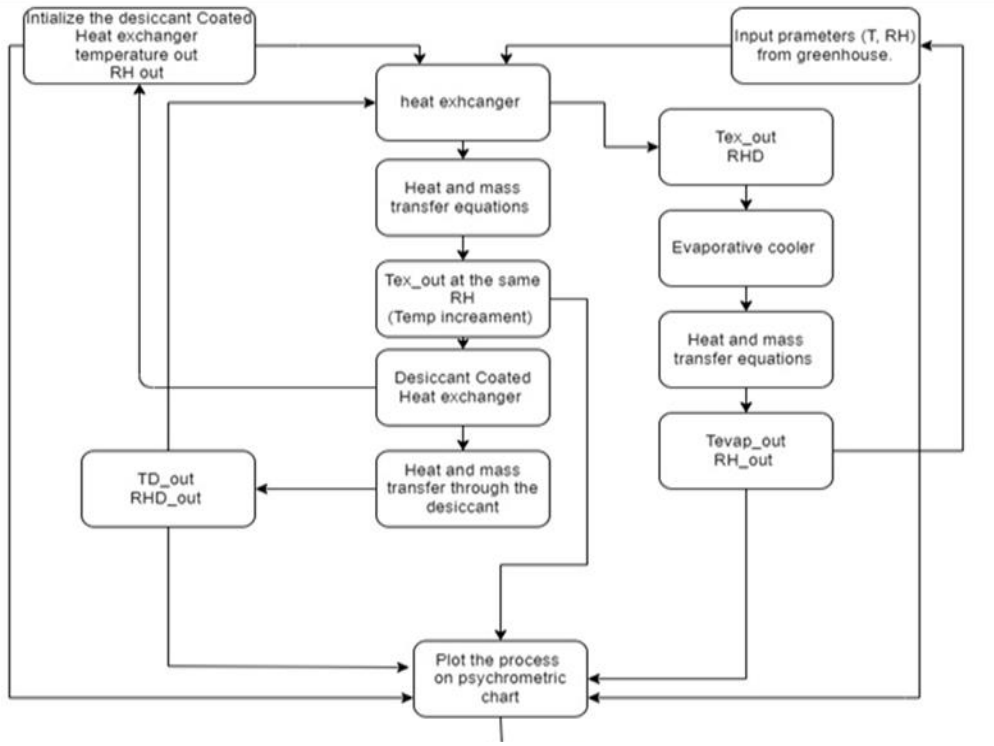



*Figure 5-14: The flow chart of the integrated cycle for the greenhouse climate control system.*

The submodels of the major components of the system, like the DCHEs, the air-to-air heat exchanger and the evaporative cooler, were validated using published literature. Table 5-5 presents the results of validating the evaporative cooler submodel using three conditions

at T= 40°C and relative humidity 30%, 50% and 70%. The Direct evaporative cooler model's outputs agree with published modelling and experimental data by Igor Kovačević [173], with a maximum difference of less than 1% for output temperature and relative humidity.

Table 5-5 Evaporative cooler model validation.

| | | Case 1 | | |
|---|---|---|---|---|
| Parameter | **Inputs** | **Current model outputs** | **Published data** | **Experimental** |
| Temperature (°C) | 40 | 25.13 | 25.34 | 25.3 |
| Relative humidity | 30% | 97.16% | 97.16% | 97.16% |
| Specific humidity (g/g) | 13.9 | 19.7 | 19.9 | 19.9 |
| | | Case 2 | | |
| Parameter | Inputs | Model outputs | Published data | experimental |
| Temperature (°C) | 40 | 30.33 | 30.47 | 30.5 |
| Relative humidity | 50% | 98.46% | 98.46% | 98.46% |
| Specific humidity (g/g) | 23.5 | 27.3 | 27.5 | 27.6 |
| | | Case 3 | | |
| Parameter | Inputs | Model outputs | Published data | experimental |
| Temperature (°C) | 40 | 34.65 | 34.72 | n/a |
| Relative humidity | 70% | 99.12% | 99.12% | n/a |
| Specific humidity (g/g) | 33.4 | 35.51 | 35.6 | 27.6 |

The air-to-air heat exchanger submodel was validated using published results of R. S. Bindu [172] with no deviation, as shown in figure 5-15.

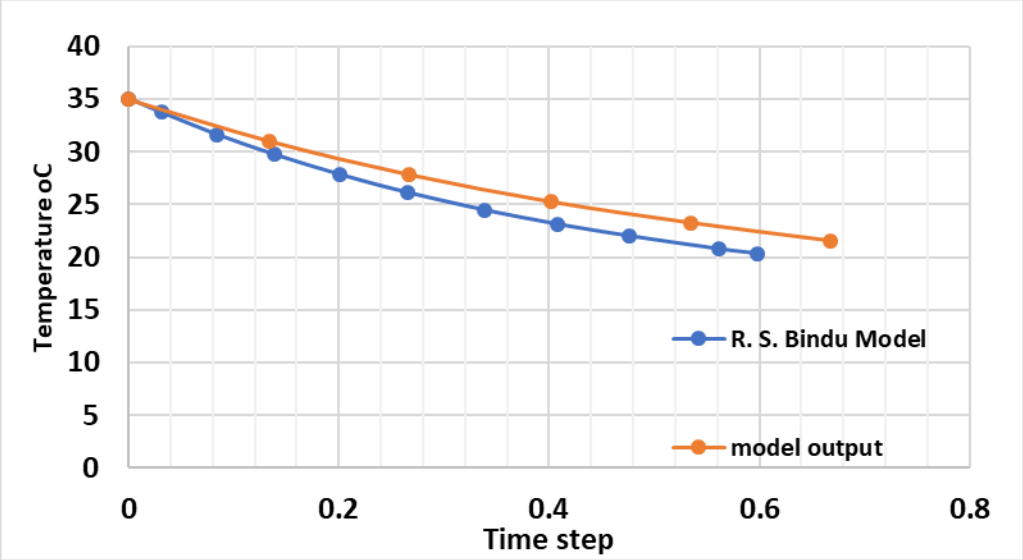



*Figure 5-15: Air-to-air heat exchanger model validation.*

Figure 5-16 compares the desiccant-coated heat exchanger submodel results to those published by Yadav et al. [36], showing good agreement with a maximum deviation of 13%.

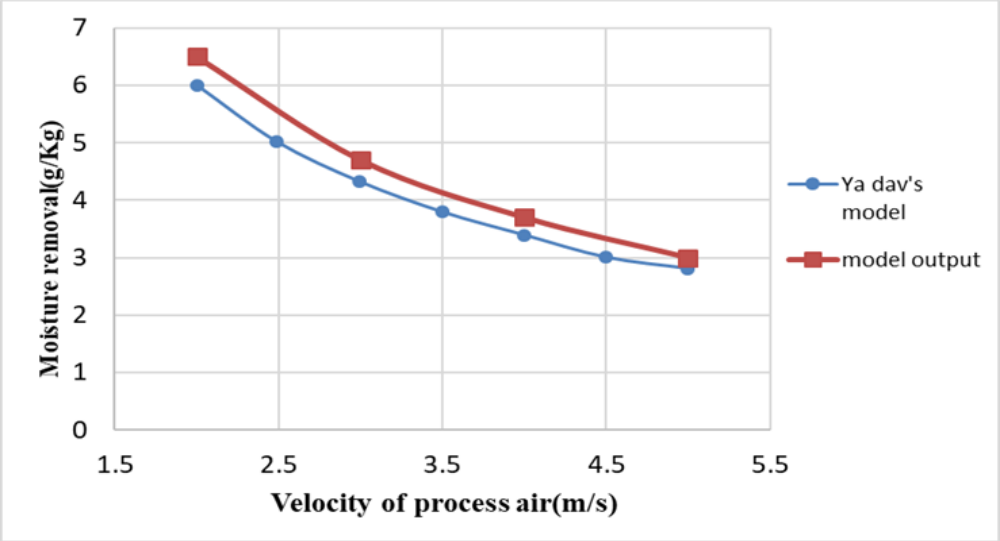



*Figure 5-16: DCHE model validation.*

## 5.3.Overall System Performance Results

The above-developed model for the greenhouse climate control system was used to predict its performance in the case of a greenhouse with initial conditions of 30°C temperature and 90% relative humidity. For the MOF DCHE, the initial condition of the MOF material was obtained from the CFD analysis, where the temperature and water uptake of the desiccant are 44.6°C and 0.115kg/kg. These conditions were achieved using a desorption time of 2.5 mins for 40 mins of continuous operation and a power input of 28.8W, which had the highest water removal rate per power consumption unit. Figure 5-17 shows the psychrometric chart for the air as it flows through various parts of the system where the air coming from the greenhouse is heated up in the air to air heat exchanger from 30°C to 38.5°C. Then the hot and humid air will pass through the MOF DCHE, where the specific humidity of the air is reduced significantly from 24.27g/kg to 11.56g/kg. As the dehumidified and hot air flows through the air-to-air heat exchanger, its temperature will decrease from 44.64°C to 39.11°C. In the evaporative cooler, the dehumidified and hot air is further cooled and humidified to achieve the target air temperature and relative humidity of 25°C and 60% and specific humidity of 11.8 g/kg, respectively, at the inlet to the greenhouse.

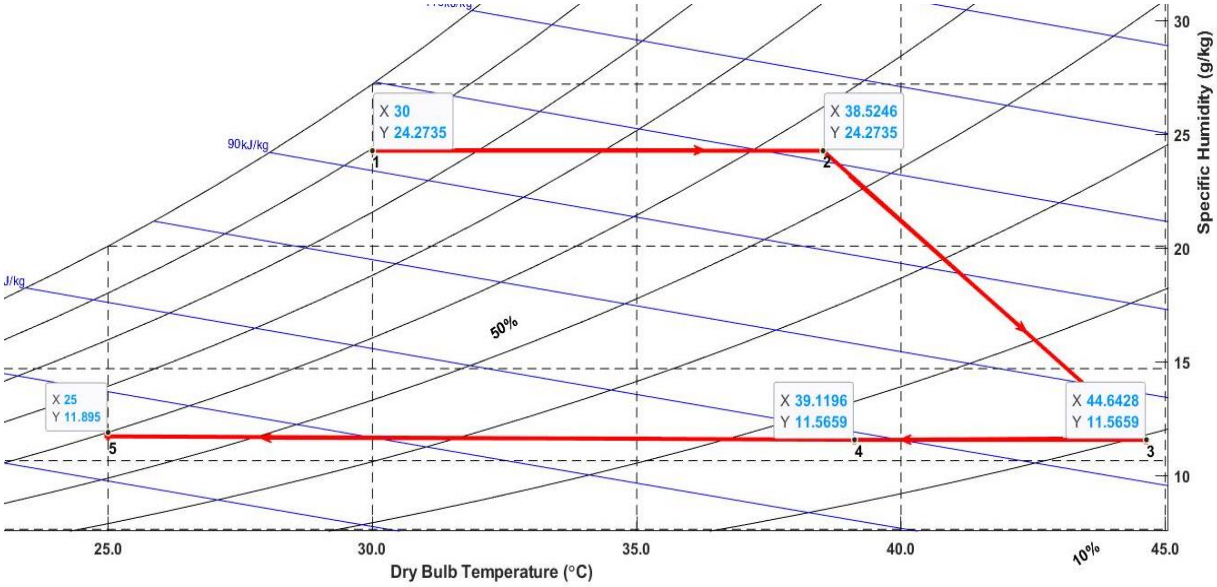



*Figure 5-17: Psychrometric chart output.*

Figure 5-18 shows the effect of changing the relative humidity inside the greenhouse at 65%, 75%, and 90% and its impact on the system performance. By increasing the relative humidity value at point (1) from 65% to 75% and then to 90%, the specific humidity for the air at point (5) increased from 10.2 g/kg to 10.81 g/kg and then to 11.895 g/kg, respectively. Using 2.5mins of heating (desorption) and 40mins of adsorption, the total number of cycles/day is 33.88, producing 2.278435 kg/day Litre of water per day collected from one DCHE used in this system.

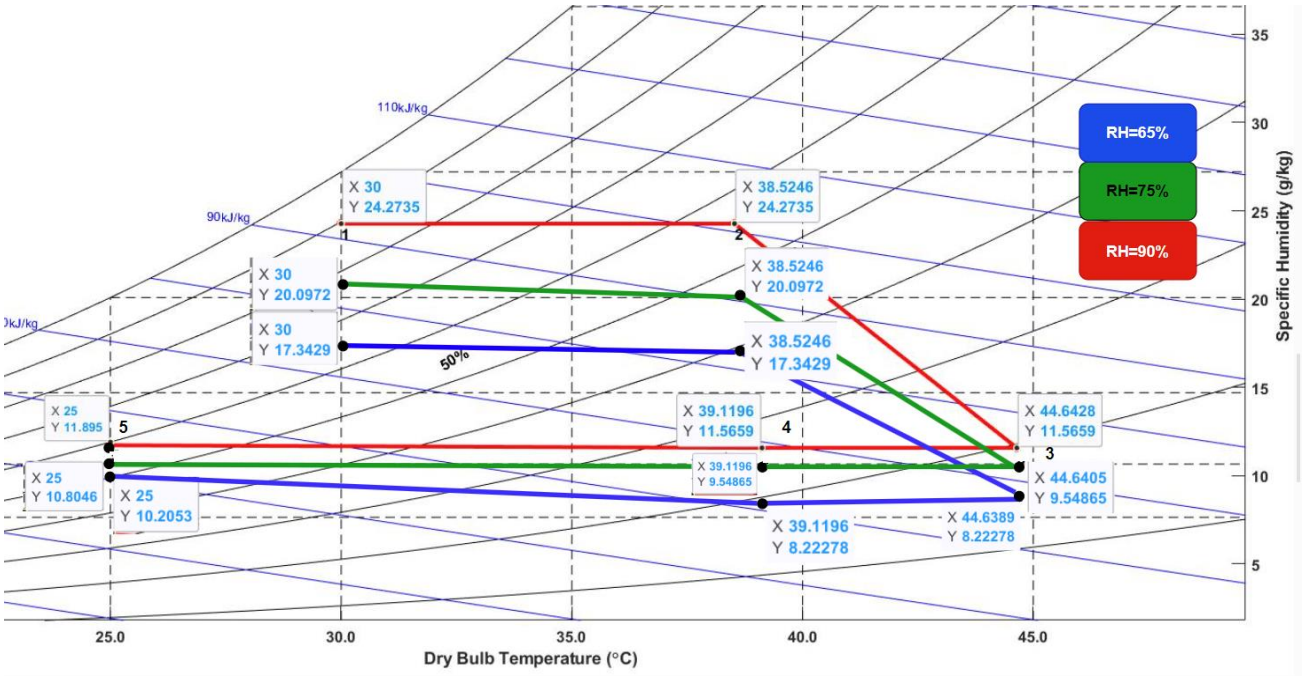



*Figure 5-18: Relative humidity change for the greenhouse and studies its effect on the system behaviour on a psychrometric chart.*

## 5.4.Summary

Food security depends on adequate crops production which is adversely affected by the extreme temperatures in hot climates, lack of irrigation water and poor soil quality. Greenhouses with controlled environment can enhance food security particularly in areas with high temperature and water scarcity by growing crops throughout the year independently from weather conditions. In this thesis, a novel system for greenhouse climate control was developed using Metal Organic Framework based desiccant coated heat exchanger integrated with air to air heat exchanger and evaporative cooler. Coupled with this model, computational fluid dynamics modelling for MOF-303/G coated heat exchanger was developed to predict the best desorption time and power consumption. Results showed that:

1. Adding graphene nanoplatelets to the synthesis of MOF-303 creates nucleating surfaces where the MOFs particles adhere to forming MOF-303/G composite. The MOF-303/G is highly porous with enhanced water sorption kinetics, and cyclic performance, but with a slight decrease in the water uptake and enhanced thermal stability.
2. The CFD modelling of MOF-303/G coated on wire finned heat exchanger showed that using power input of 20W and desorption time of 2.5mins, the MOF-303/G coated heat exchanger produces the highest water removal rate per unit power consumption of 2.69g/kgMOF/W.hr.
3. The developed system can handle greenhouses' high relative humidity of 90% and achieve the target return air relative humidity of 50%. Similarly, the system can achieve other desired return air conditions starting from different greenhouse relative humidity.
4. The developed system shows the ability to recover the water from reducing the greenhouse relative humidity to be used either for irrigation or any other applications. The daily water recovery is found to be 4.55 Litre/kgMOF used.

# Chapter 6 Experimental test facility

Results from chapter 4 and 5 highlighted the potential of MOF-303/G coated on wire finned heat exchanger in developing environmental control system that can be used for space cooling and heating while precisely controlling the space humidity. this chapter presents the construction, commissioning, and operation of a more advanced double-bed adsorption system for continuous space cooling and heating. In addition, control system for operating the system at different conditions are presented in detail.

## 6.1.Test facility description

This adsorption system has two adsorber beds, a driving fan, air to water heat exchanger and an evaporative cooler. It is connected to a 2 $m^3$ chamber, as shown conceptually in Figure 6-1 and visually in Figure 6-2. Each adsorber bed contains two parallel electrically heated multi-tube heat exchangers, coated with a maximum of 0.5 kg of adsorbent material MOF-303/G per adsorbent bed. Six electrically powered dampers are utilised to alternate between the two beds and switch airflow from the adsorption line to the desorption line. A single fan is used to provide airflow via a duct. The evaporative cooler is modified by positioning the moist medium in the forward-facing of the duct. The following section will include a detailed description of each component, the measuring instruments and control devices used in the system.

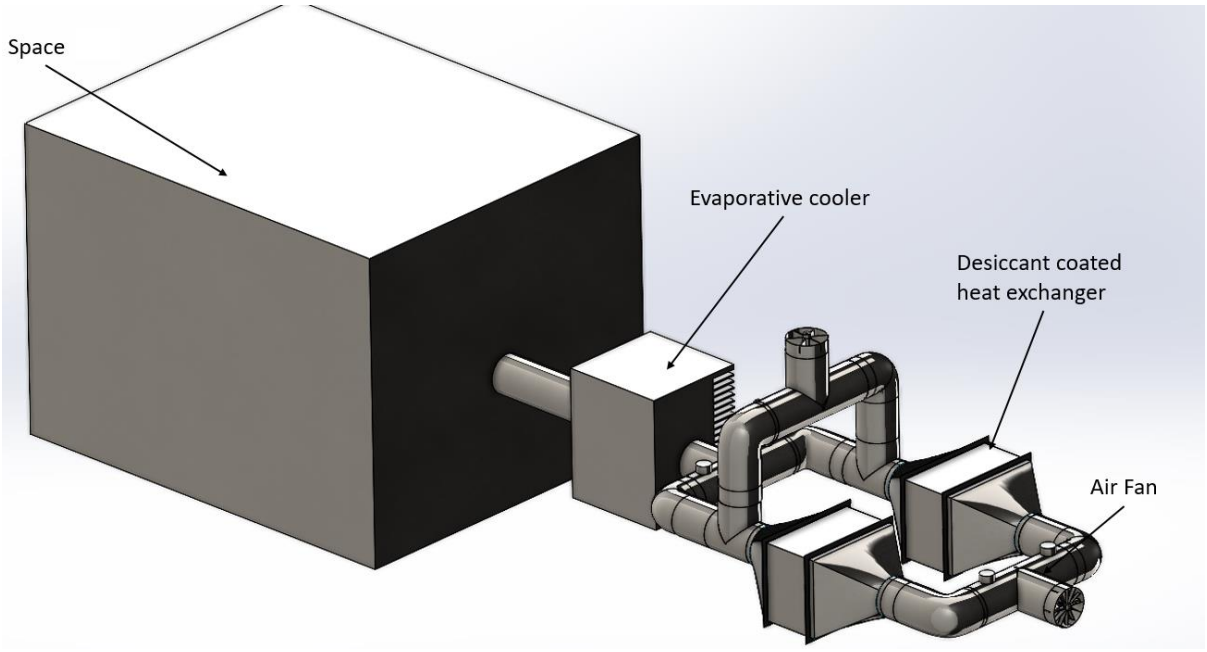



*Figure 6-1: 3D CAD model for the desiccant air conditioning system.*

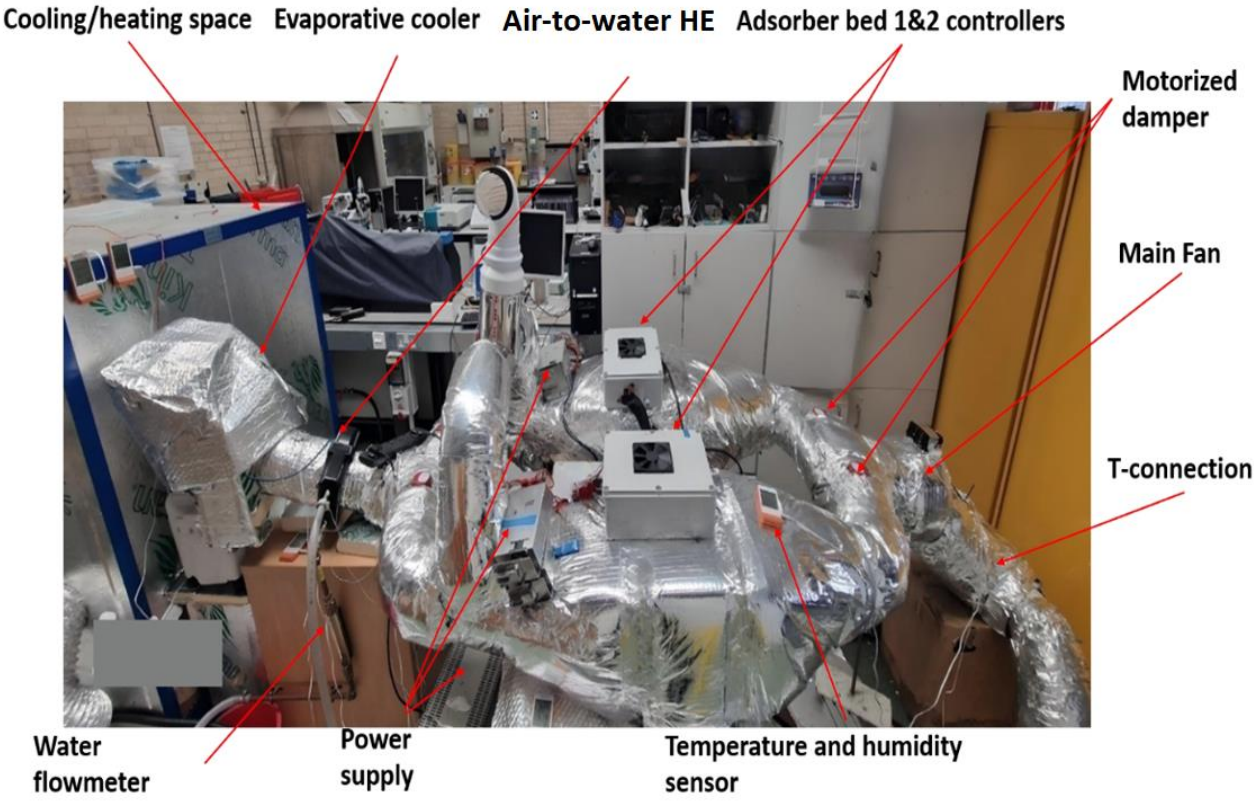



*Figure 6-2: Testing facility of the double-bed adsorption air conditioning system.*

### 6.1.1. Adsorber bed

Two identical adsorber beds are the main components of the adsorption air conditioning system, responsible for adsorbing water vapour from the incoming air and desorbing it back to the exhaust. It consists of a galvanised mild steel rectangular duct straight of 400x300mm with a length of 250mm. This duct is manufactured by "DuctStore" with the model number of "RDS400-300". Rectangular to Round 400mm Width, 300mm Depth and diameter 150 mm is attached to the rectangular duct with a Dopy frame 20mm with the model number of "SQRD400-300" as shown In figure 6-3.

Inside the tube sourcing map, 5M/16.4ft 1mm$^2$ 500C heat resistance white fibreglass-covered copper conductor. High-Temperature wire cable is used to resist heat when heating, increasing the coil's reliability, as presented in Figure 6-5. The wire-finned tubes are electrically heated using 1 mm Nichrome wire, which is connected to by 6-14 AWG waterproof shown in figure 6-4.inside each adsorber bead, two heat exchangers each consisting of five wire-finned tubes coated with 250 grams of MOF-303/G as presented in Chapter 4, section 4.4 and attached together by a wood base, as shown in Figure 6-6. The whole adsorber assembly is presented in Figure 6-7.

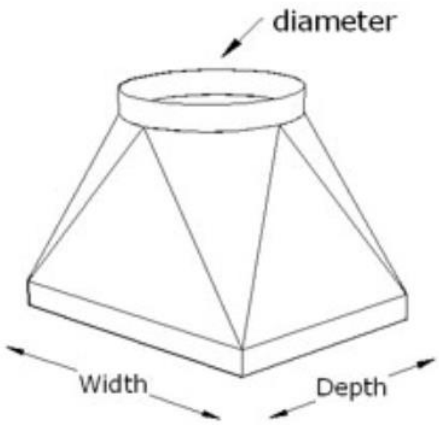



*Figure 6-3: Square to Round fitting for the adsorber bed.*




*Figure 6-4: 6-14 AWG Waterproof Wire Connectors.*

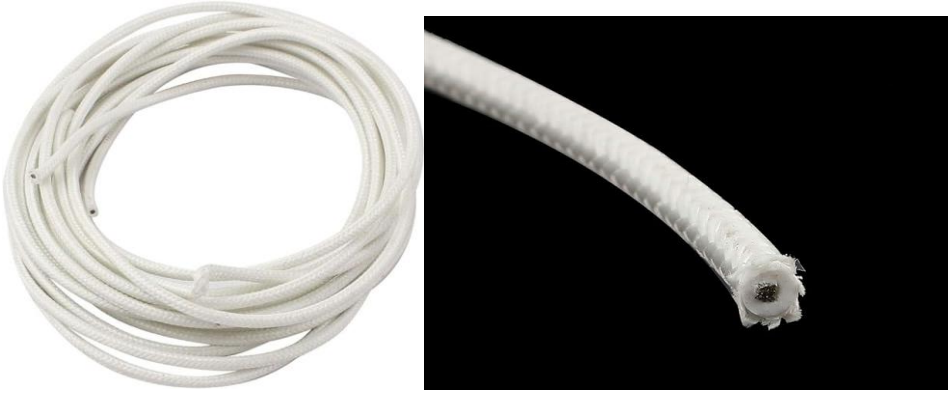


*Figure 6-5: High-Temperature Wire Cable.*

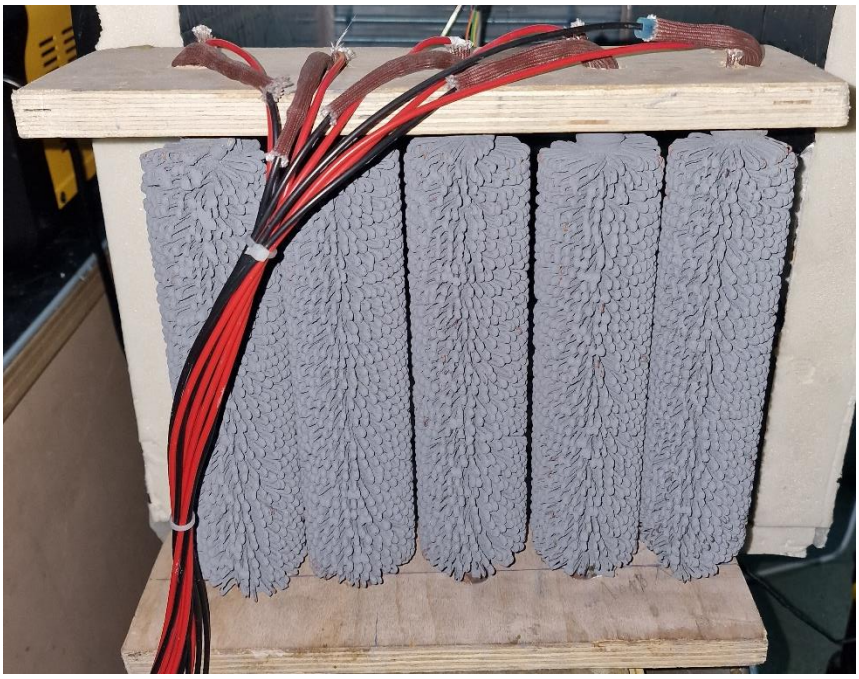


*Figure 6-6: Heat exchanger and wiring connections assembly.*

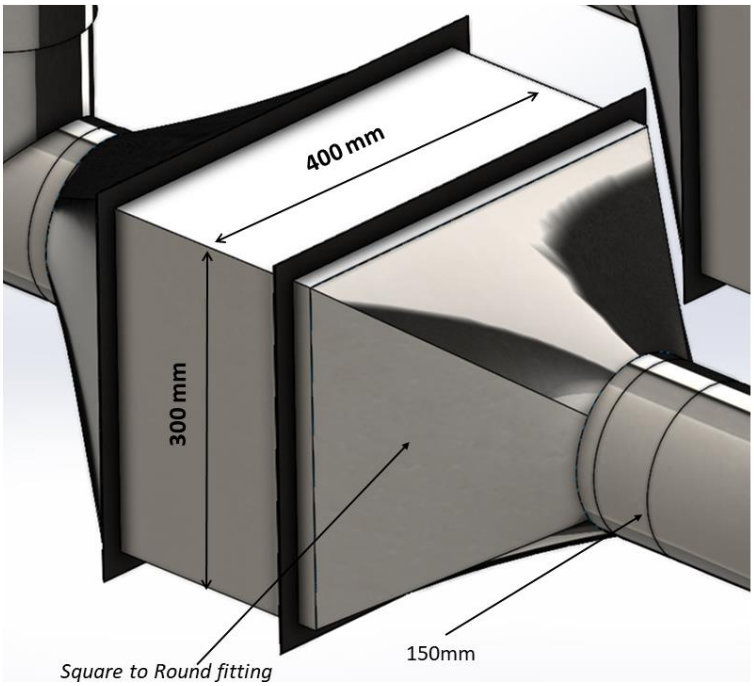



*Figure 6-7: Adsorber bed 3D assembly.*

### 6.1.2. Motorized damper

Figure 6-8 shows an electric motorized damper designed for air ducts and manufactured by "Jufjsfy". It operates using 220VAC and controls the airflow by changing the angle from 0° to 90° of the ventilation tube. The damper diameter is 150 mm, with a maximum closing and opening time of 5 seconds. Six motorized dampers were used to operate the system. Figure 6-9 shows the T-connection air duct with the motorised dampers to switch the airflow between the two adsorber beds, with it a diameter of 150 mm, width of 150mm and length of 450mm.




*Figure 6-8: 220V electric motorized damper air duct.*




*Figure 6-9: 220V Damper bypass motorized damper electric air duct vent fittings.*

.

### 6.1.3. Elbows

Six identical 150 mm diameter 90° pressed bends with seals, with model number of “7-BPL90-150”, were used as fitting between the beds and dampers in the system, as shown in figure 6-10. Also, plastic tee connections with 150mm diameter.




*Figure 6-10: 90° Elbow and plastic t connection.*

### 6.1.4. Control circuit for the two adsorber beds

In Figure 6-11, the relay kit with the brand name “Hailege” 12V with OPTO-isolated support high and low-level trigger is responsible for switching on/off the power source supplied to each DC-DC voltage regulator. The Arduino Mega controls the relays, enabling it to selectively activate or deactivate the power supply to each finned tube as required during the alternating adsorption and desorption operations. Figure 6-12 depicts the control system of a multi-tube DCHE. Four of these circuits were used to control four multi-tube heat exchangers. This system includes individual DC-DC voltage regulators for each tube, a relay kit, and an Arduino Mega. The purpose of this system is to manage the power input during the desorption process. DC-DC Voltage Regulators: Each finned tube has its own unique DC-DC voltage regulator. These regulators enable precise control of the voltage supplied to each tube, allowing for individualised adjustment of the power needed for the desorption process of the MOF on each tube. The Arduino Mega is the primary control device that supplies the necessary power for desorption operations. It establishes communication with the relay kit to regulate each finned tube's power supply. The Arduino Mega collects data from different

sensors, such as temperature, pressure, or humidity, to monitor and control adsorption/desorption cycling according to predetermined parameters or control algorithms.

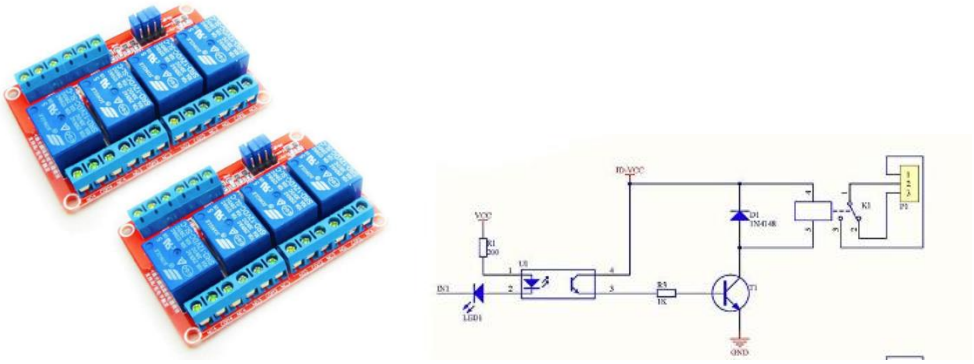


*Figure 6-11: Inlet velocity change for the desiccant wheel and studies its effect on the system behaviour on a psychrometric chart.*

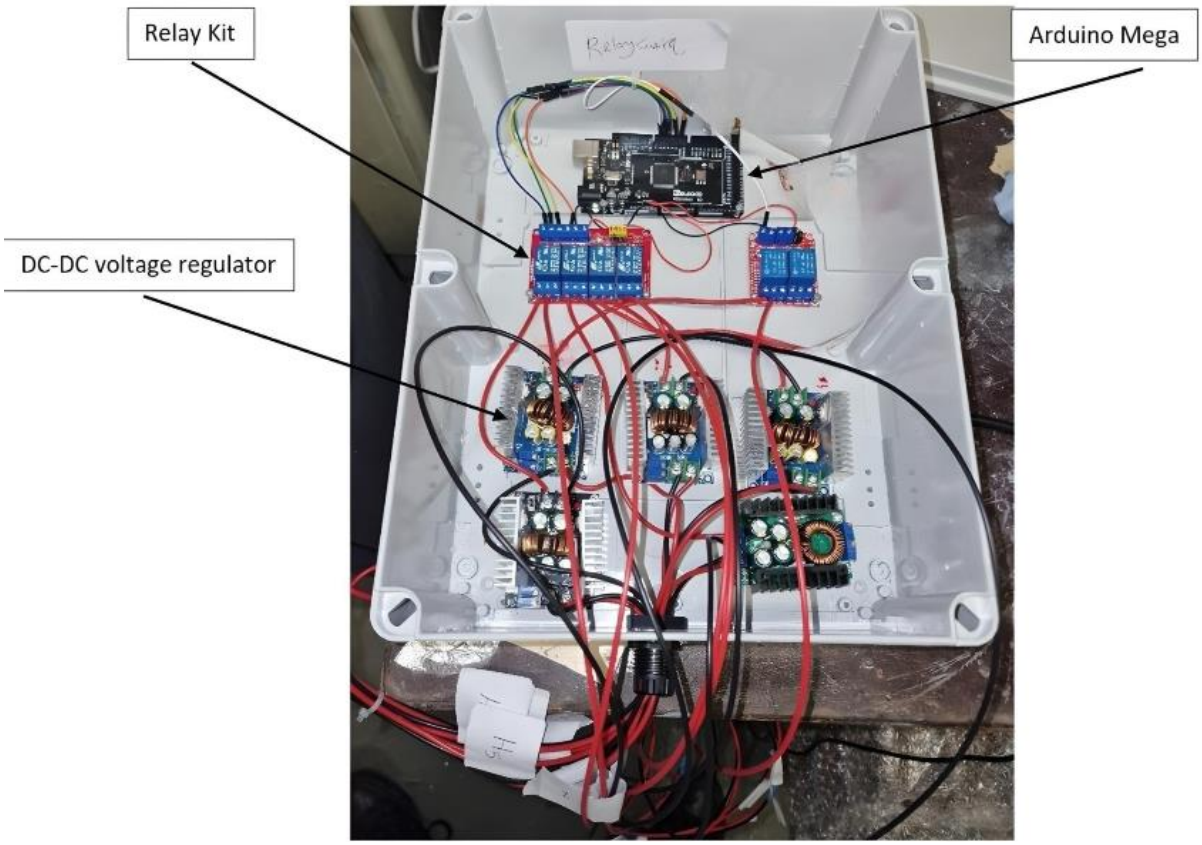



*Figure 6-12: DCHE electric control circuit.*

Control Algorithm: The Arduino Mega has a programmed control algorithm to determine the appropriate timing for turning on or off the power supply to each wire-finned tube. Adsorption Process: The control system consistently monitors the conditions inside the heat exchanger and uses the relay kit to activate the suitable DC-DC voltage regulators. This is done

to attain the desired heat of desorption for each finned tube. This control enables effective and accurate management of the desorption process. More details on this code are presented in Appendix II.

### 6.1.5. Main Fan

Figure 6-13 shows the 150mm diameter inline duct fan, which operates on a 220VAC and is used to circulate the air at different speeds, produced by DuctStore company. The PWM AC voltage dimmer 50/60Hz 80-240VAC connected with the Arduino Megawas used for fan speed control, the wiring diagram and the interface circuit are presented in Figure 6-14.

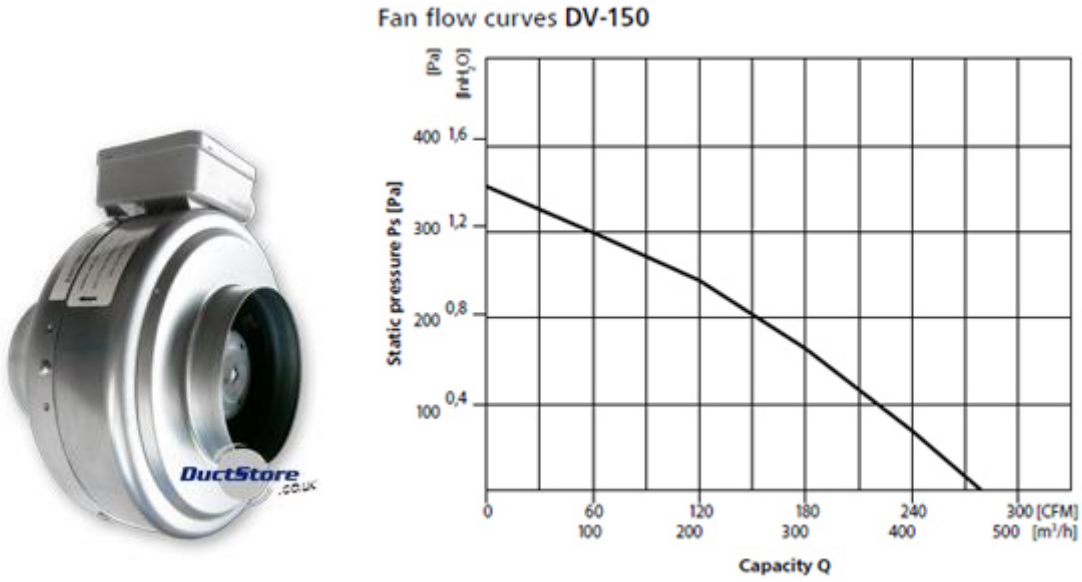



*Figure 6-13: DuctStore 150mm main fan.*

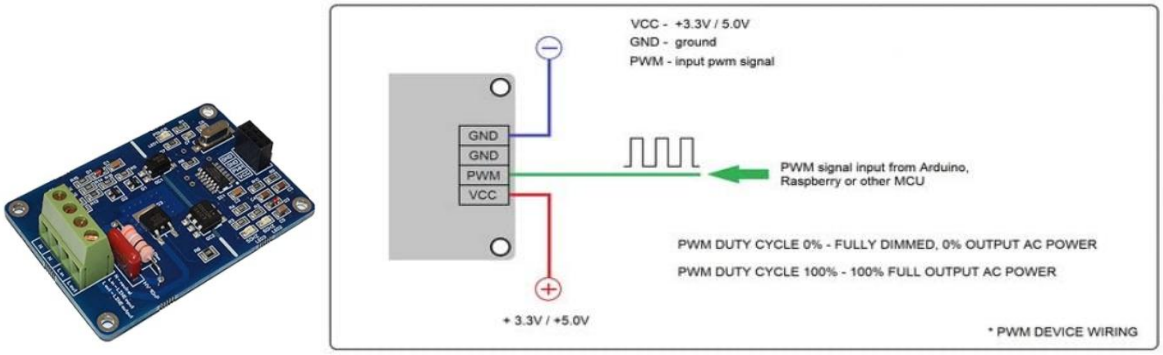



*Figure 6-14: PWM speed control circuit.*

### 6.1.1. Evaporative cooler

Figure 6-15 shows the evaporative cooler used in the experimental facility; it is a Honeywell type; the air cooler features a slim design with honeycomb cooling media and a mesh filter, offering efficient cooling with a mechanical control panel and accessible water refilling through a dedicated door. It has a 9L tank capacity, operates at a maximum air flow of 300 $m^3$/hr (176 CFM), and is powered by 65W, making it energy-efficient. The cooler covers up to 10 $m^2$ and comes with three-speed settings and oscillating louvres for better air distribution. With dimensions of 280 mm in depth, 660 mm in height, and 301 mm in width, it is compact and easily movable, running on 230V.

The evaporative cooler was modified by removing the internal fan and its pump and connecting a custom feedback control circuit to regulate the new variable speed pump to control the air humidity level independently following the adsorption process from the bed. This device is optimal for areas up to $10m^2$, as it has a water capacity of 9 litres and a low power consumption of 65W. It boasts a robust circulation of 300 $m^3$ per hour. The variable speed Kamoer pump was ordered separately to control the water flow rate needed for the wet medium. The pump specs: High flow peristaltic pump 12V brushed DC motor 400ml/min with a model number of “KPHM400”, as seen in Figure 6-16. Figure 6-17 represents the water flowrate control circuit: MOSFET Driver Module controls the pump using PWM output controlled by Arduino (3.5V/5V). Omron S8FS-G Switched Mode DIN Rail power supply to feed the circuit with specs: 100 → 240V AC AC Input, 12V DC DC output, 50A output, 600W. The flow rate relation curve with PWM is presented in Figure 6-18. This relation is used in the Arduino code to control the pump flow rate for the wet honeycomb medium of the evaporative cooler. More details on this code are presented in Appendix III.




*Figure 6-15: Honeywell evaporative cooler.*

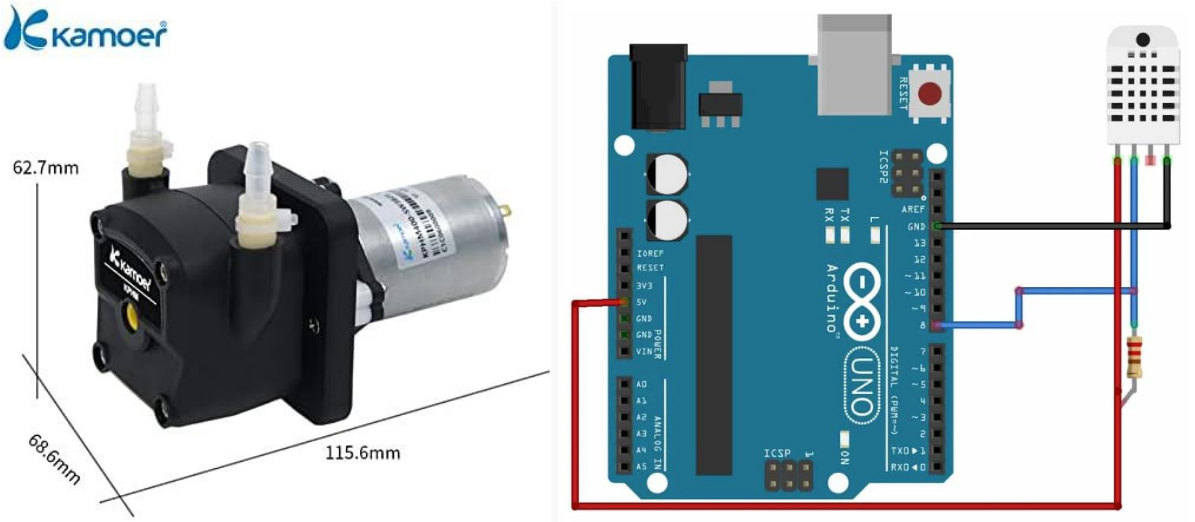



*Figure 6-16: High flow peristaltic pump 12V.*

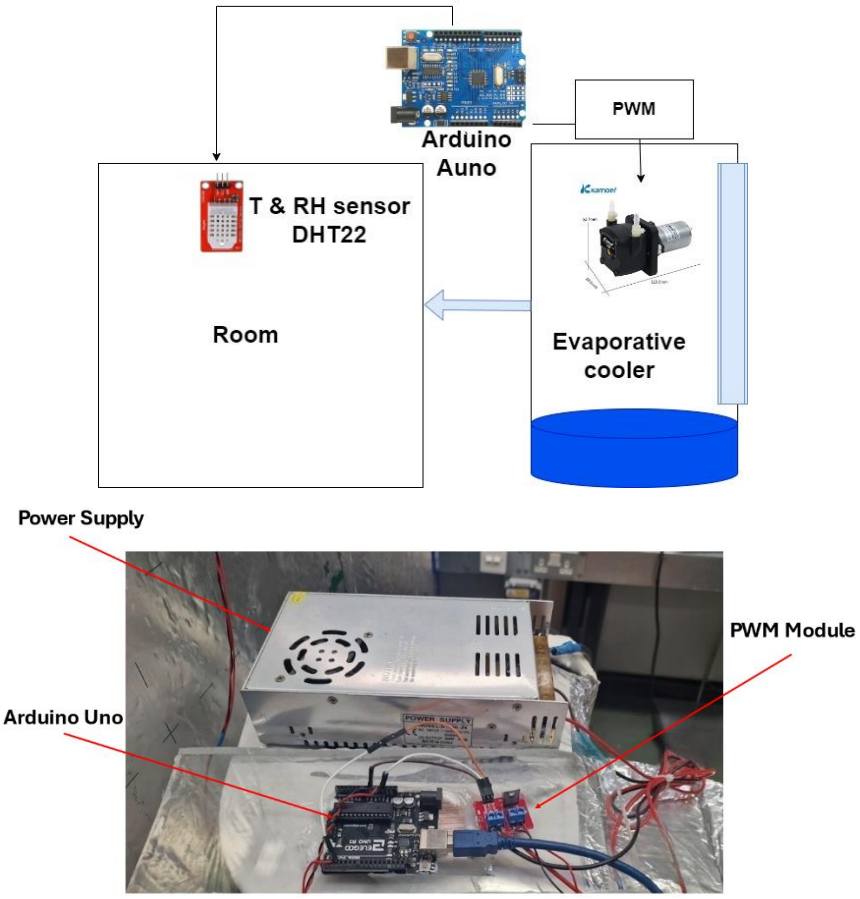



*Figure 6-17: Water flowrate control circuit for evaporative cooler.*

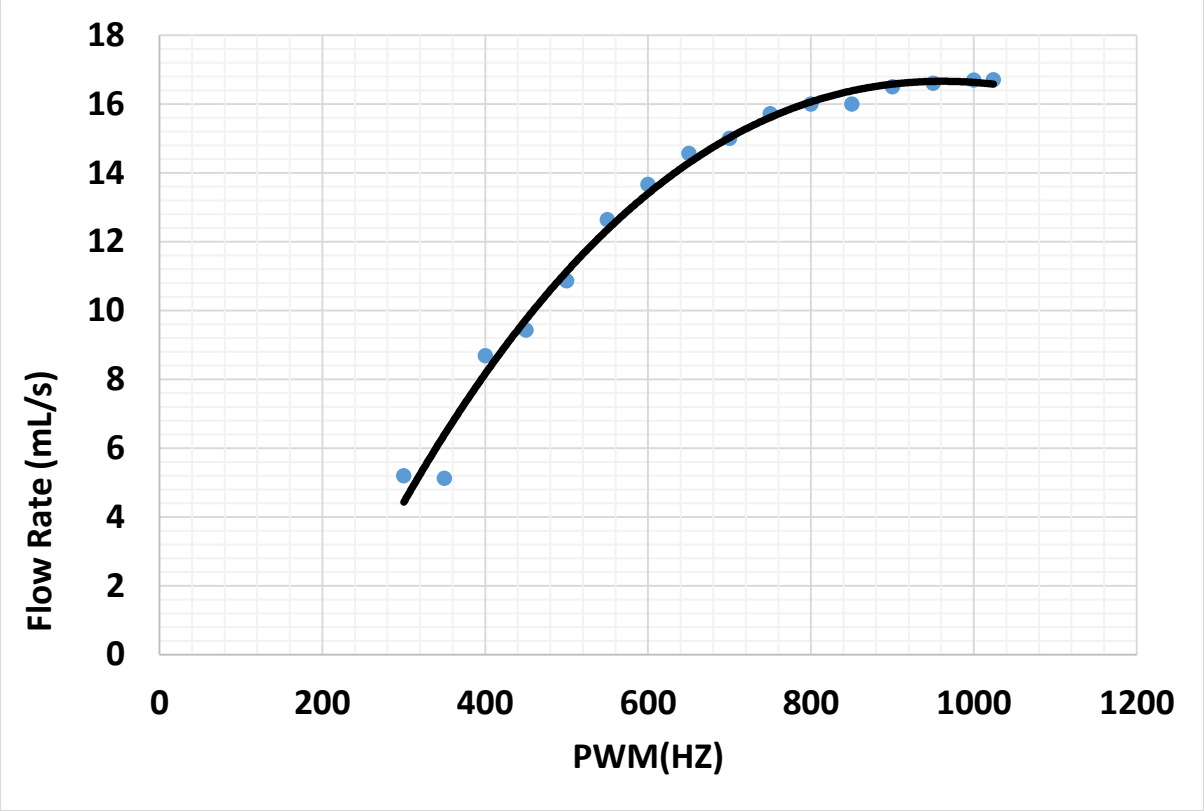



*Figure 6-18: Water flow rate control vs PWM(Hz).*

### 6.1.2. Air-to-water heat exchanger

Figure 6-19 shows the air-to-water heat exchanger HDW-150 with a circular duct of 150 mm, which cools the air temperature after the two adsorber beds; the dimensions are presented in Figure 6-20. RS UCC 2 litres to 22 litres variable area liquid flow meter was added to adjust the tap water flow rate. Two k-type thermocouples are added to the inlet and the outlet of the heat exchanger.

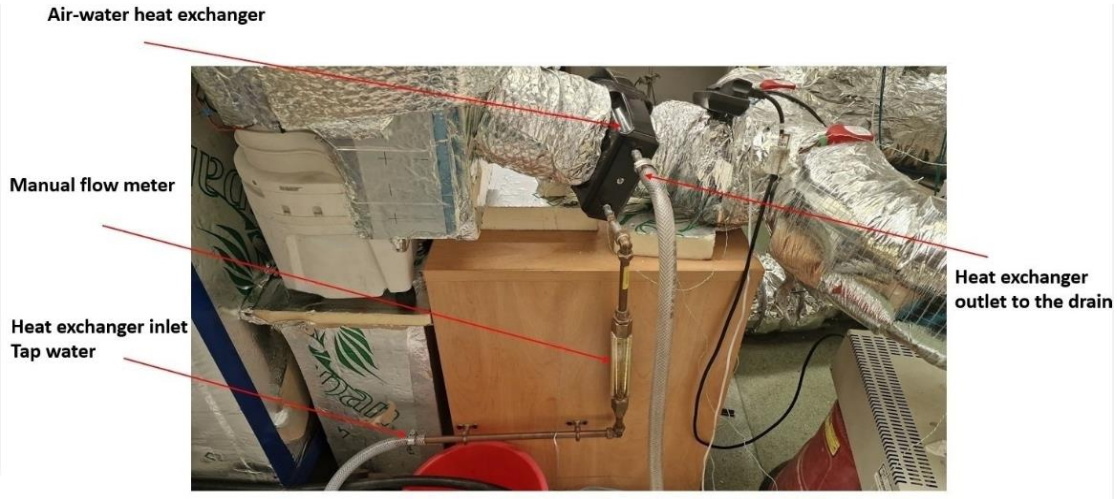
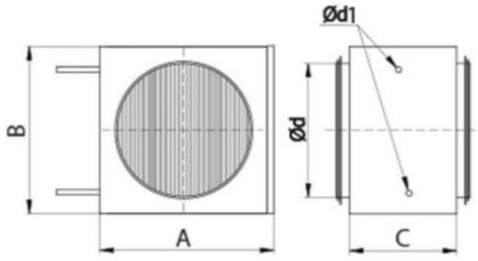



*Figure 6-19: Air-to-water heat exchanger configuration.*




| Type | Ød [mm] | A [mm] | B [mm] | C [mm] | Ød, [mm] |
|---|---|---|---|---|---|
| HDW-100 | 100 | 215 | 190 | 220 | 9,52 |
| HDW-125 | 125 | 215 | 190 | 220 | 9,52 |
| HDW-150 | 150 | 290 | 265 | 220 | 12,0 |
| HDW-160 | 160 | 290 | 265 | 220 | 12,0 |
| HDW-200 | 200 | 290 | 265 | 220 | 12,0 |
| HDW-250 | 250 | 395 | 365 | 260 | 18,0 |
| HDW-315 | 315 | 460 | 440 | 260 | 18,0 |
| HDW-400 | 400 | 560 | 525 | 270 | 18,0 |
| HDW-500 | 500 | 740 | 650 | 270 | 22,0 |

*Figure 6-20: Air-to-water heat exchanger dimensions.*

### 6.1.3. Room description and insulation

Figure 6-21 shows the room used as a space to be air-conditioned; this room is fully insulated with a vapour barrier and waterproof thermal Insulation. As shown in Figure 6-22, aluminium foil flexible ducting ventilation hydroponic was used to insulate all the piping and its connections.

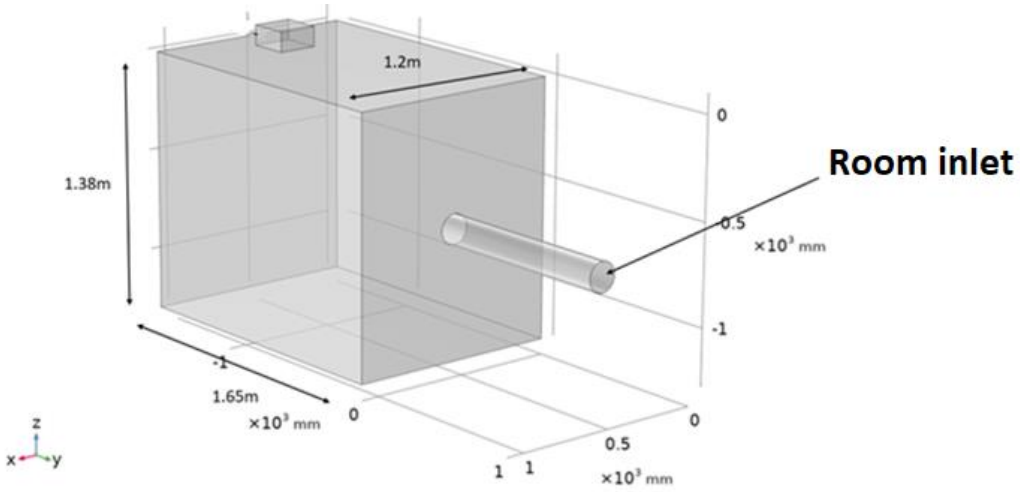



*Figure 6-21: 3D CAD drawing of the the room.*



*Figure 6-22: Piping insulation and Aluminium foil ducting.*

### 6.1.4. Sensors and data loggers

Figure 6-23a shows a schematic diagram of the developed system highlighting the position of temperature, humidity, and air flow rate used to evaluate the system performance.

Figure 6-23b shows the temperature and humidity sensors attached before and after the component. Five Elitech humidity and temperature sensors with an accuracy of ±3% RH and ±0.3°C and an uncertainty of 1.73% are used to measure air temperature and humidity. To measure the temperature of the MOF material coated on the DCHE. The two thermocouples are attached to the surface of the Multi-tube DCHEs. The k-type thermocouples were attached and connected to a data logger called Picologer TC-08, which has a temperature accuracy of ±0.2% of the reading and ±0.5°C.

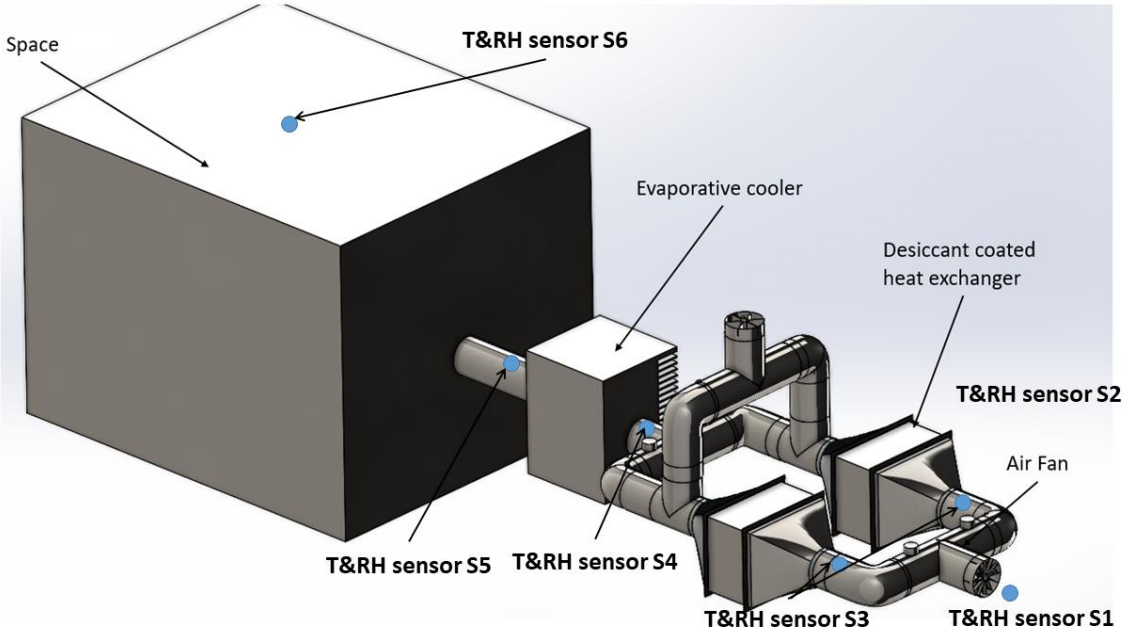



*Figure 6-23a: Temperature and humidity sensors positions for all the system.*

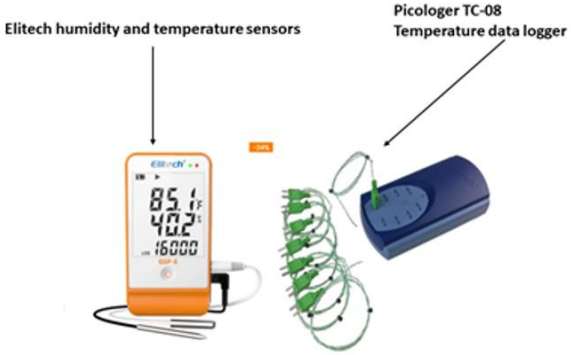



*Figure 6-23b: Temperature and humidity Sensors used for all the system.*

## 6.2.Test rig commissioning

The system was constructed according to the schematic diagram in Figure 6-1 and the visual representation in Figure 6-2. All temperature and humidity sensors and thermocouples were installed and connected to the data recording equipment, and all electrically actuated dampers were connected to their respective control board (Arduino Mega). Leakage tests were conducted on every system component, such as the adsorber beds, fittings, and air-to-water heat exchangers' circulating water pipes. Also, all air dampers and the pump for the evaporative cooler pump with its developed control system were tested for functionality using the "Arduino IDE" software.

## 6.3.Testing procedure

The testing procedure includes three stages namely: initialization, testing and data collection.

### 6.3.1. Initialization

- The pico logger, the air temperature and humidity sensors are connected to the PC and their software are reseted, and the data is ready to record with time.
- Select the half-cycle time between the two beds for cooling or heating the room.
- The motorized damper's positions are closed before starting the cycle.
- For the heating scenario, the flexible foil ducting comes from the T-connection attached to the window to supply fresh air from outside the lab.
- Initiate the room's humidity and temperature to become the same levels as the ambient conditions when heating the room.
- Initiate the room’s humidity and temperature to become 90% and 30 oC when cooling the room.
- For the heating process, the evaporative cooler pump is as off until the sensors detect a low humidity level inside the room.
- For the cooling process, the tap water circulation starts to feed the air-to-water heat exchanger's inlet with the required temperature to control the final air condition that goes to the room.
- When the room is initiated, the scenario starts cycling.

### 6.3.2. Cycling

a. To begin system operation, start button on Arduino IDE software is clicked to upload the code for cooling or heating.
b. For adsorber bed 1, the relay kit feeds the required current to the two multi-tube DCHEs to heat the MOF material until it reaches the desired time for the cycle.
c. Damper 1 D-1, D-2, D-4, D-5 are open automatically, while D-3 and D-6 are closed.
d. Then the main Fan is switched on.
e. After the half-cycle desorption time for bed 1 is finished, D-1 and D-2 are closed, and the Fan is switched off.
f. The relay kit stops feeding the current to the two multi-tube DCHEs going through the desorption process.

g. For adsorber bed 2, the relay kit feeds the required current to the two multi-tube DCHEs to heat the MOF material.
h. D-1, D2, D-3, D-6 are opened automatically, while D-4 and D-5 are closed.
i. The desorption/ adsorption process is repeated till the half-cycle time is completed.
j. For the heating process after half-cycle time completion, the evaporative cooler pump is switched on to reach the required humidity level by the feedback control system.
k. For the cooling process, the tap water is fed to the air-to-water heat exchanger from the beginning while the evaporative cooler is off throughout the process.
l. Once a cycle of adsorption and desorption processes is complete, the above steps are repeated to operate the system for several cycles required.

### 6.3.3. Data collection and switching off

a. All dampers that have been opened will close immediately when the system stops, and then all pumps must be turned off.
b. The data taker uploads and stores all measured data into the PC.
c. For post-processing, data are fed to a Matlab code to calculate the moisture removal rate and the COP of the system and plot the points before and after the adsorber beds, before and after the evaporative cooler, and before and after the air-water heat exchanger, and inside the room on a psychrometric chart.

# Chapter 7 System Experimental Results

This chapter presents the experimental results of operating the developed MOF-303/G desiccant air conditioning system. Measurements of the air temperature and humidity before and after the adsorber beds, the evaporative cooler, the air-to-water heat exchanger, and inside the room are plotted and used to determine the MOF-303/G desiccant coated heat exchanger (DCHE) moisture removal rate and the system coefficient of performance (COP). Section 7.1 describes the performance testing of a single adsorber bed system, while section 7.2 describes the results of two adsorber bed systems for heating and section 7.3 describes the results of two adsorber bed systems for cooling.

## 7.1. Performance of single adsorber bed

Figure 7-1 shows a schematic diagram of a single adsorber bed. To evaluate the single adsorber bed performance, the temperature and the relative humidity are measured, logged to the data logger and then exported to a MATLAB code to calculate the moisture removal rate and the COP of the system. The experiments were carried using single-row DCHE, two rows of DCHEs, and three rows of DCHEs inside the adsorber bed.

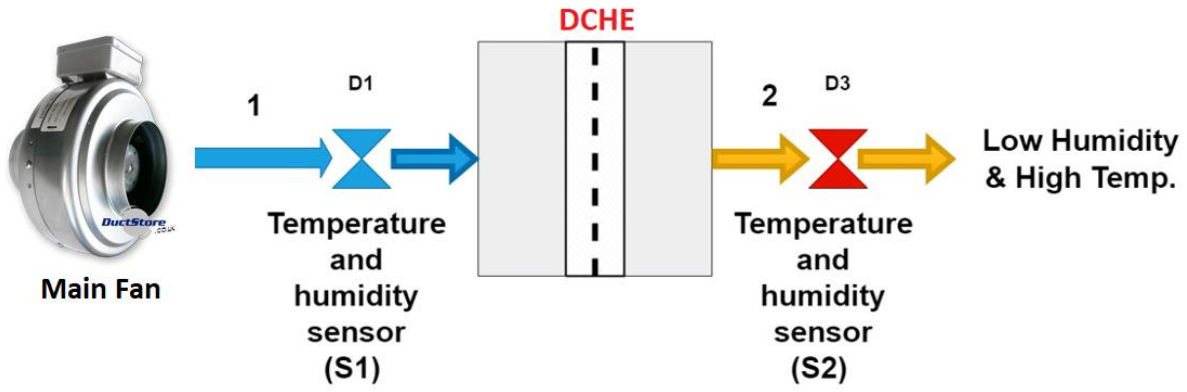



*Figure 7-1: Schematic diagram of single adsorber bed.*

Figure 7-2 shows two cycles of desorption/adsorption with a half-cycle time of 30 minutes using a single row DCHE at an inlet air temperature of 20.5°C, relative humidity of 75%, and specific humidity of 11.4 g/kg(da), It shows the variation of MOF surface temperature and its moisture removal/uptake capability with time. The moisture removal/uptake was calculated by:

$$\mathrm{MRC} = \dot{m}\left(\omega_{a,in} - \omega_{a,out}\right) \tag{7-1}$$

A positive value means the amount of water adsorbed in grams, while a negative value indicates the desorbed grams of water. The repeating cycles highlight the system's consistency in managing moisture with significant desorption in each cycle, achieving a total adsorbed grams of water per cycle of 38.9 grams per cycle with a water uptake of 12%. The power used to reach this target temperature during desorption is 30 watts.

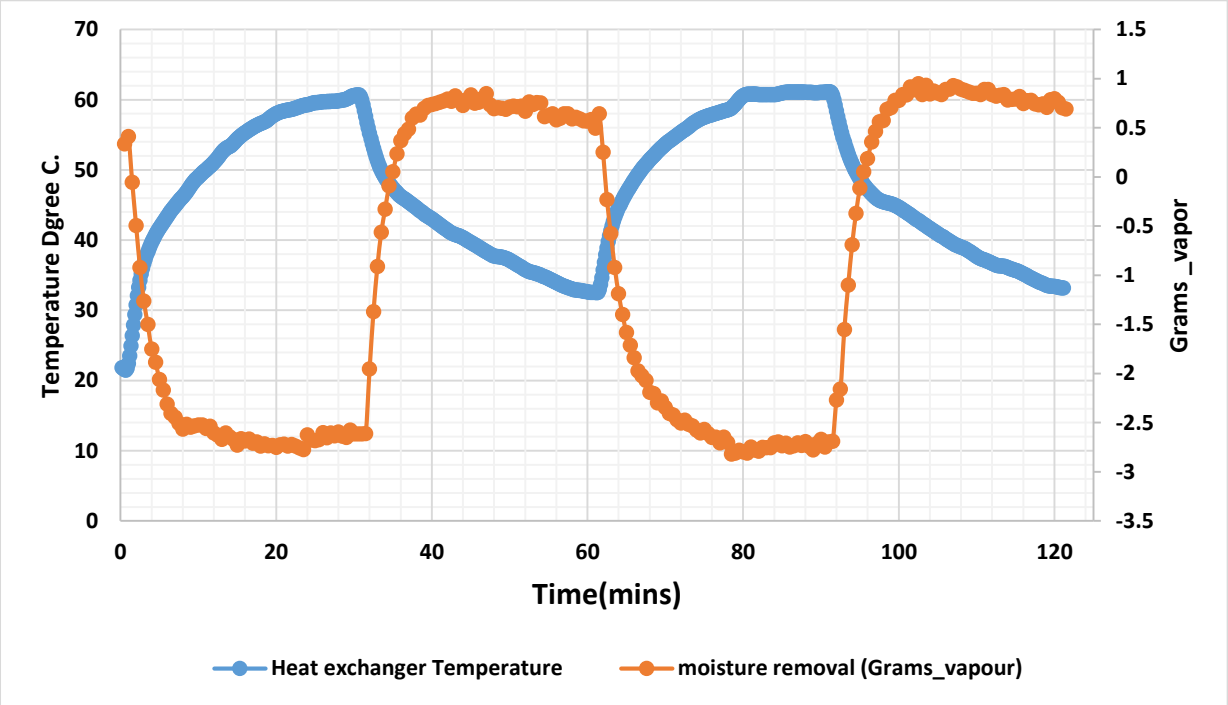



*Figure 7-2: Single-row DCHE moisture removal/uptake and MOF-surface temperature.*

Figure 7-3 shows the variation of the air inlet and outlet moisture content with time. It can be seen that the air inlet-specific humidity is relatively constant at 11.4 g/kg(d.a), indicating consistent ambient conditions. The air outlet-specific humidity increases during the desorption process and decreases during the adsorption process. The consistent cyclical pattern in the outlet air-specific humidity W_out of 10.54 g/kg(d.a) for adsorption and W_out of 15 g/kg(d.a) for the desorption process demonstrates the periodic removal of moisture, which is in sync with the heat exchanger's operational cycles. This reduction in air-specific humidity is associated with the heat exchanger's ability to manage moisture content, enhancing its air conditioning efficiency.

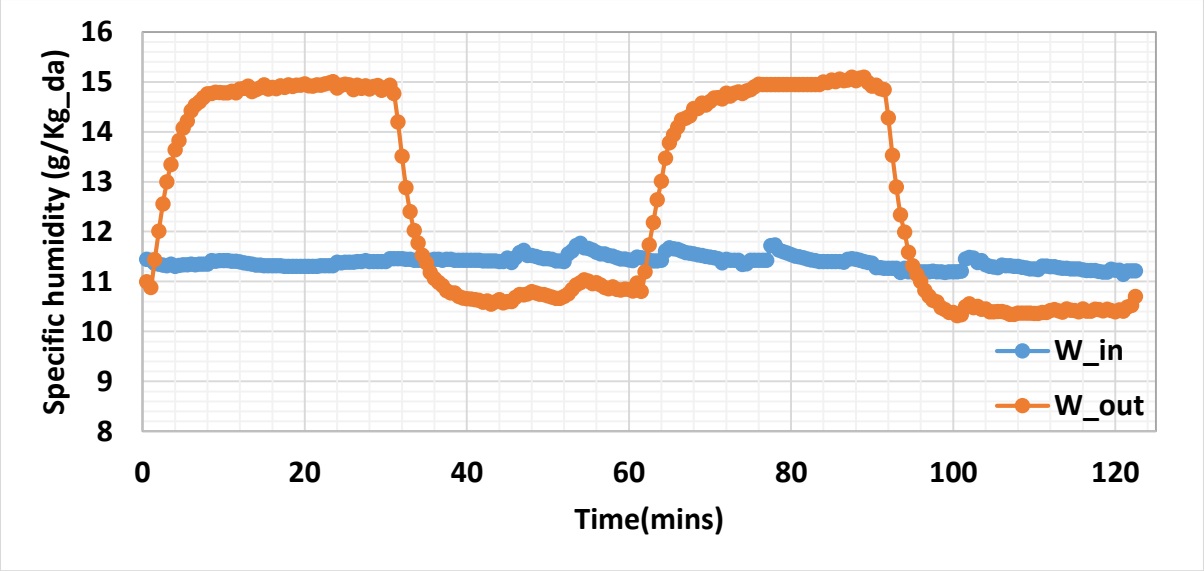



*Figure 7-3: Moisture content difference of single-row DCHE adsorber bed using MOF-303/G.*

Figure 7-4 illustrates the cyclic performance of using two rows of MOF-303/G coated heat exchangers in the adsorber bed at air inlet conditions of a temperature of 21°C, relative humidity of 75%, and specific humidity of 12 g/kg(d.a). The heat exchanger shows effective moisture removal during adsorption, with a total adsorbed moisture of 55 grams per cycle. The consistent cyclical patterns in temperature and moisture removal highlight the heat exchanger's efficiency in managing moisture content over 120 mins with a water uptake of 11%.

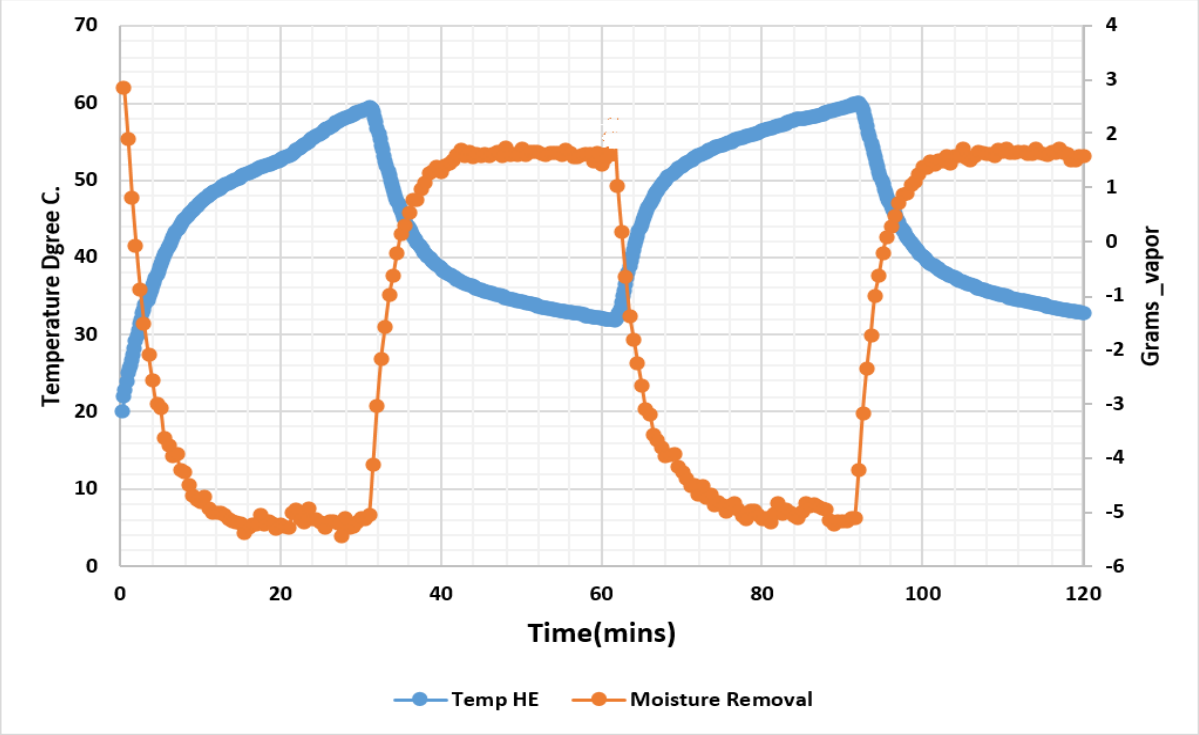



*Figure 7-4: Two-rows DCHEs adsorber bed moisture removal/uptake and MOF-surface temperature.*

Figure 7-5 shows the air inlet and outlet-specific humidity variation over time. The air inlet-specific humidity W_in remains stable at 12 g/kg(d.a), indicating consistent ambient conditions. As for the air outlet-specific humidity W_out, it varies from 10.11 g/kg(d.a) during adsorption and increases to W_out of 19.5 g/kg(d.a) for the desorption process demonstrating the periodic removal of moisture, which is in sync with the heat exchanger's operational cycles.

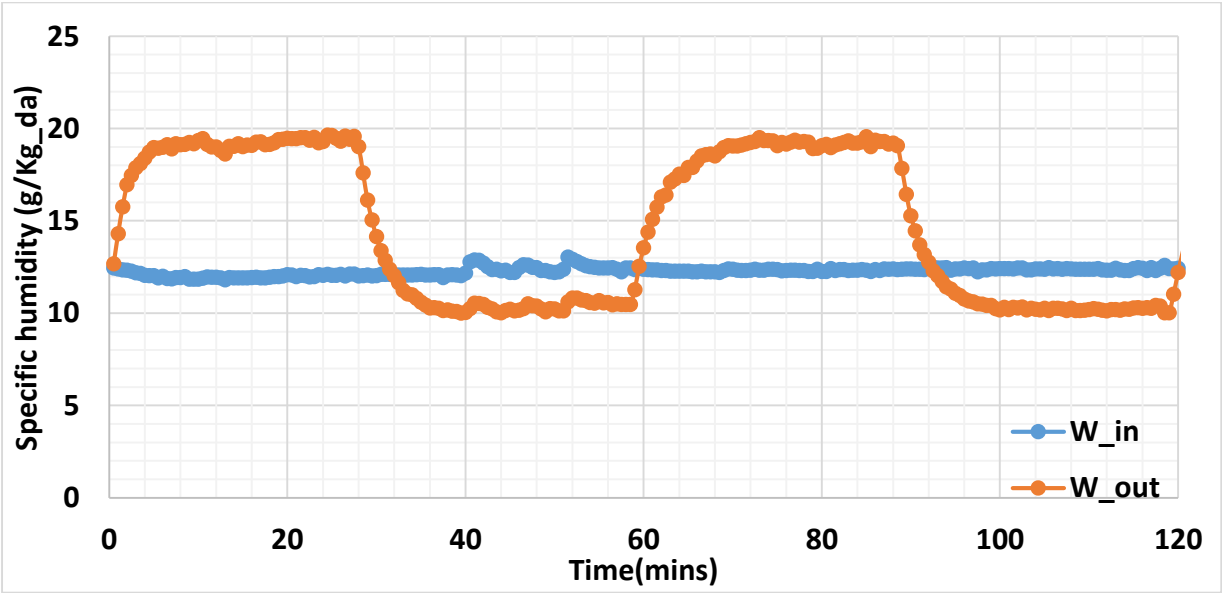



*Figure 7-5: Moisture content difference of two-rows of adsorber bed using MOF-303/G.*

Figure 7-6 shows the dynamic performance of three rows of DCHE over 120 mins, showing the relationship between its MOF surface temperature and moisture removal/uptake capability overtime at an inlet temperature of 19.2oC, inlet relative humidity of 78%, and specific humidity of 10.88 g/kg(d.a), effectively managing moisture with significant desorption in each cycle, achieving total desorbed grams of water per cycle of 69.5 grams with water uptake of 9.3%.

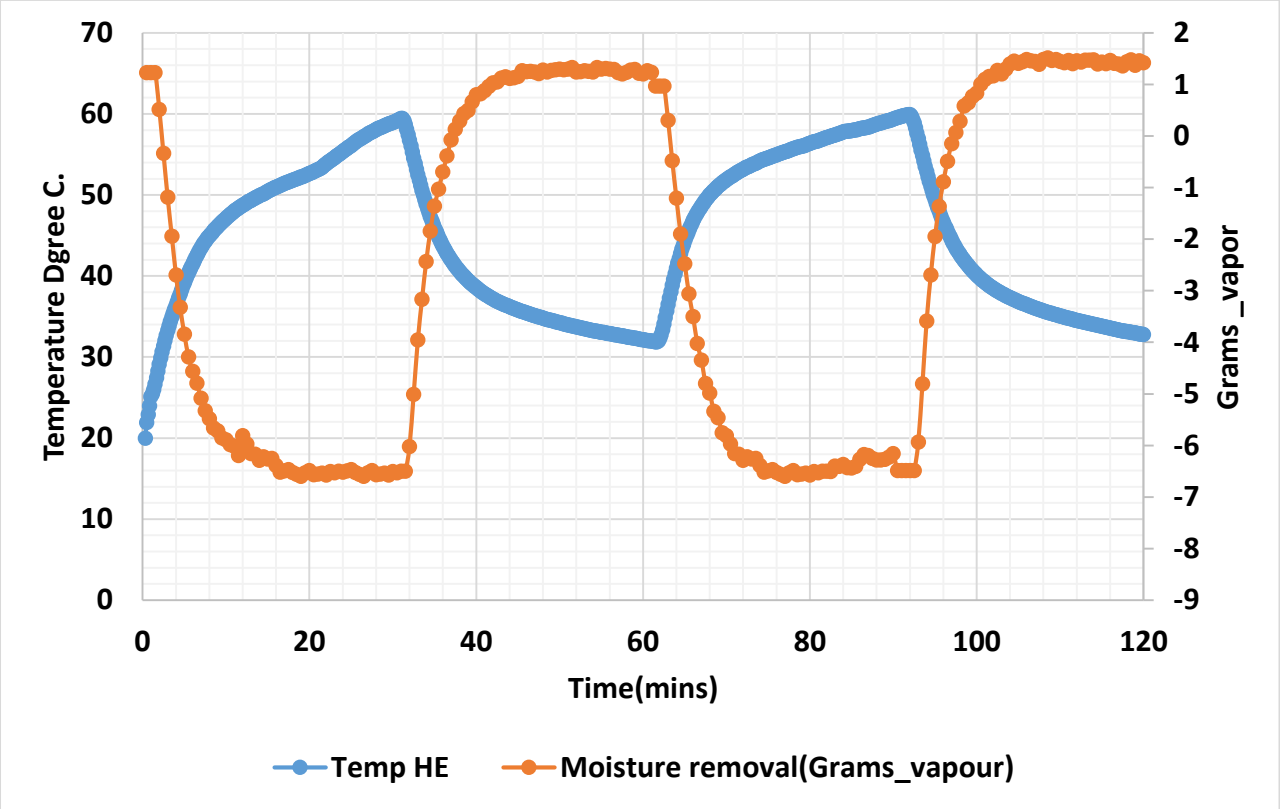



*Figure 7-6: Three-rows moisture removal rate and MOF-surface temperature.*

Figure 7-7 shows the air inlet and outlet-specific humidity variation over time. The incoming specific humidity, denoted as W_in, remains constant at 9.3 g/kg(d.a), showing a persistent state of the surrounding environment. As for the air outlet-specific humidity W_out, it varies from a value of 8 g/kg(d.a) during adsorption to 16.1 g/kg(d.a) during desorption, indicating the periodic change in moisture. This pattern is synchronised with the operational cycles of the heat exchanger.

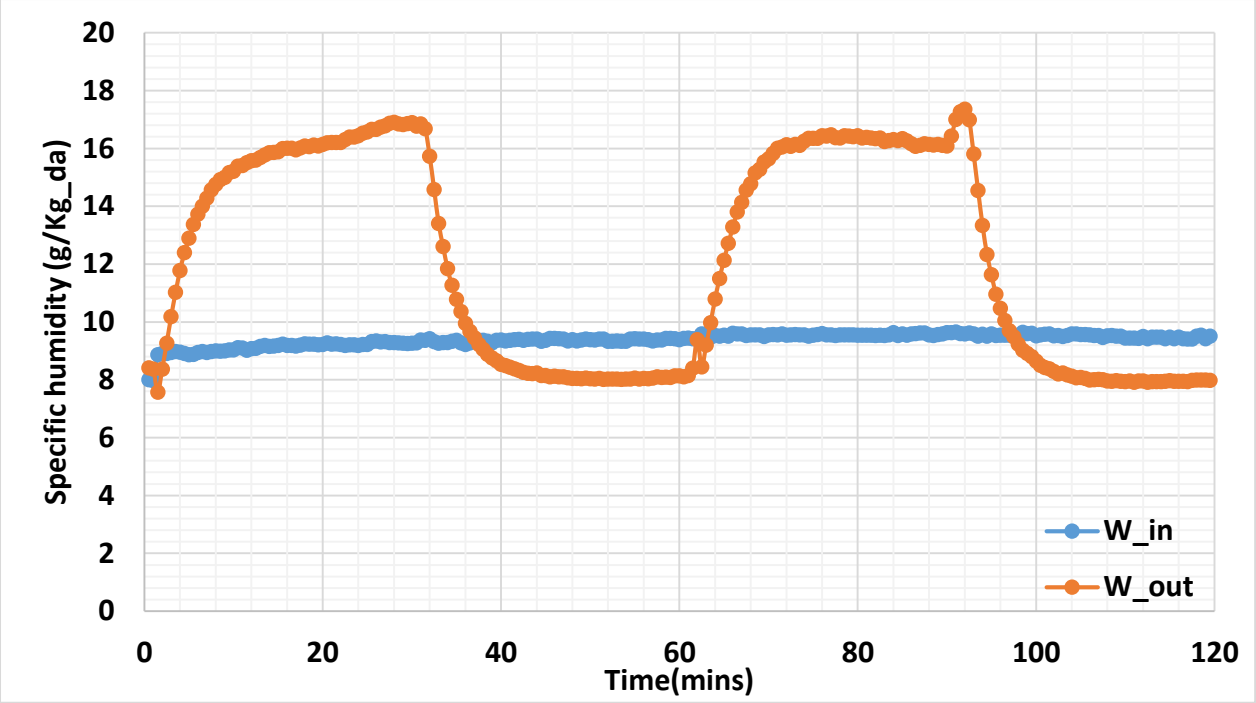



*Figure 7-7: Moisture content difference of three DCHEs rows in adsorber bed using MOF-303/G.*

## 7.2.Desiccant air conditioning system for heating

This section presents the performance of the two adsorber beds desiccant air conditioning system for heating applications. The heating system consists of two adsorber beds; each adsorber bed consists of two rows of DCHEs, each holding 250 grams of MOF. (this selection is based on calculating the air exchange rate for the room and combined with the adsorption rate of the two rows of DCHEs from the previous section and comparing the effect from that amount of MOF 500grams per bed with the commercial desiccant wheel holding the same amount of MOF designed for the same room volume), an evaporative cooler, and a room as heating space with a volume of 2 $m^3$ as shown in Figure 7-8. The system performance is presented at different operating conditions, air mixing ratios, and different half-cycle times of 10 mins, 5 mins, and 2.5 mins. The system performance is evaluated using the COP determined using equations 7-2 and 7-3.

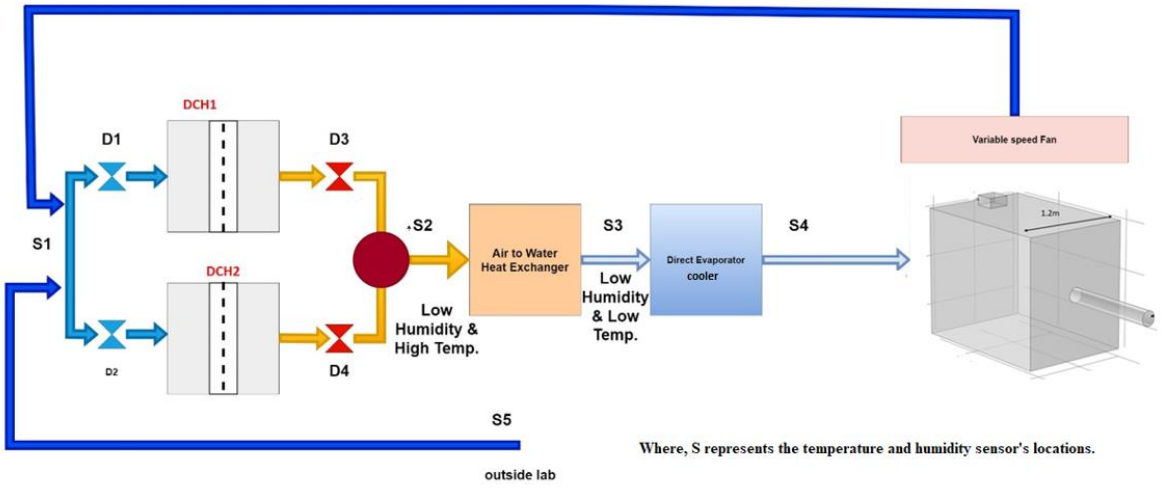



*Figure 7-8: Desiccant heating system with temperature and humidity sensors positions.*

$$COP = \frac{\int_0^{\tau} m_a \times (h_{a,out} - h_{a,in})}{Q_{in}} \quad (7\text{-}2)$$

$$Q_{in} = P * N + P_fan + \text{P_pump} \quad (7\text{-}3)$$

Where N is number of tubes, and P is the power of one single tube, $P_fan$ is a fan power, P_pump is the pump power, where $m_a$ is the air mass flow rate, $h_{a,in}$ $and$ $h_{a,out}$ are the air-specific enthalpy before and after the DCHE. $Q_{in}$ is the energy input during the system's operation determined by equation 7-3.

### 7.2.1. Adsorber beds performance without evaporative cooler

In order to investigate the performance of the two adsorber beds system for heating applications, the effect of the mixing ratio between fresh air and return air from the room at different ambient conditions and the half-cycle time were studied. Figure 7-9a illustrates the temperature variation of the ambient air and the room's interior air during 20 mins of operation. The zigzag points represent the switching moment. It can be seen that the ambient conditions are constant at 10.4°C, 56.88% relative humidity (RH), and specific humidity of 5.8 g/kg(d.a.). The main fan's air velocity is 1.5 m/s, with a 50% fresh air mixing ratio. The cycle times are adjusted to 2.5 mins, 5 mins, and 10 mins. Figure 7-9a shows that the room temperature increased to 30.4°C, 31.4°C, and 32.4°C with half-cycle times of 10, 5 and 2.5 mins, respectively.

Figure 7-9b depicts the relative humidity variation of the ambient air and the room air during the 20 mins period. It can be seen that the ambient relative humidity is constant at a value of 60%, starting with the same humidity level in the room and applying the initialisation by

operating the two adsorber beds once for 15 mins before switching between the two adsorber beds. The room's relative humidity stabilized at 25%. After passing through the DCHE, the humidity dropped to 20%, with the temperature rising to 37°C, as shown in Figures 7-9c and 7-9d.

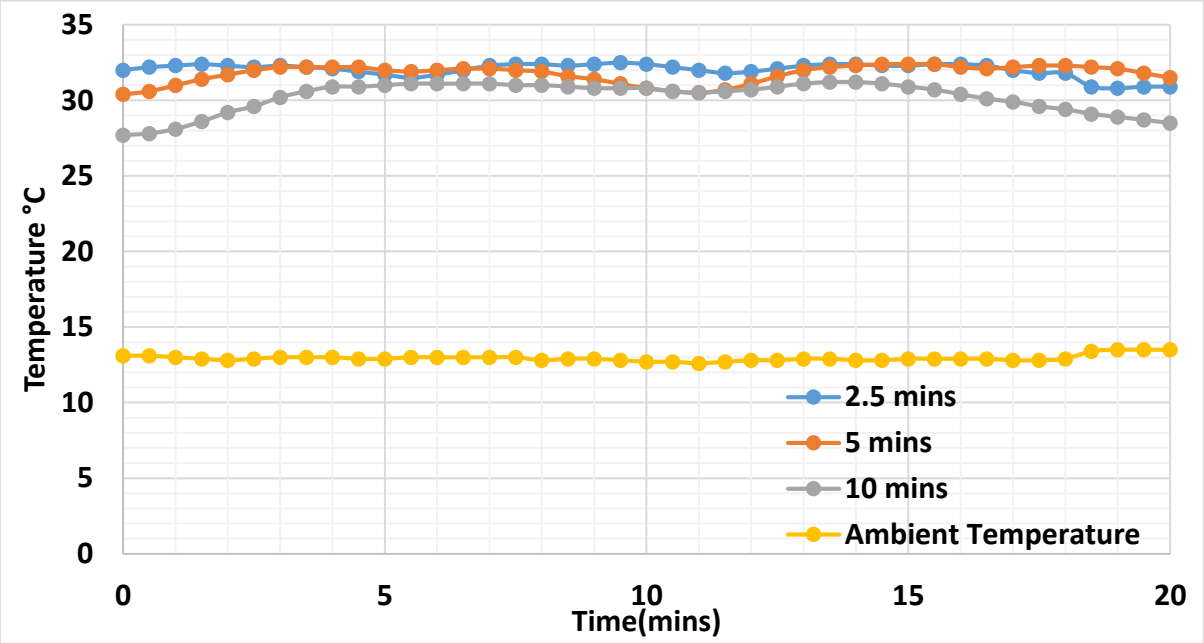



*Figure 7-9a: Room air temperature at different half-cycle times and 50% fresh air.*

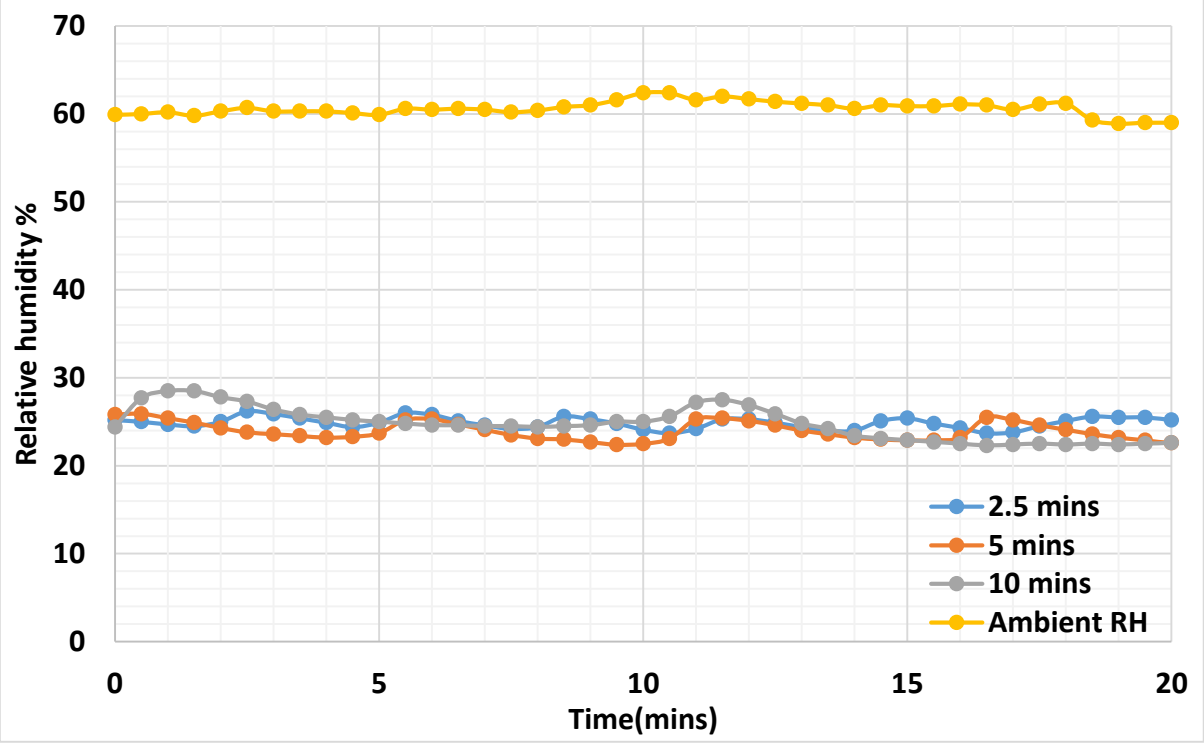



*Figure 7-9b: Room Relative humidity at different half-cycle time s and 50% fresh air.*

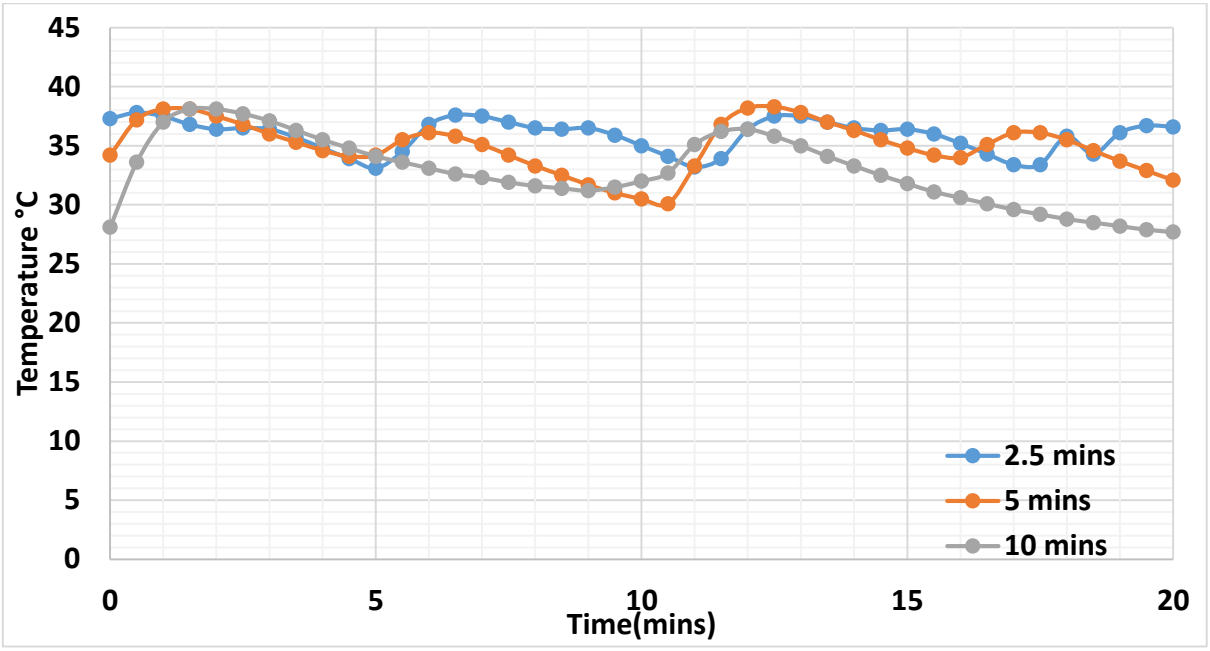



*Figure 7-9c: Air temperature after DCHE at different half-cycle time s and 50% fresh air.*

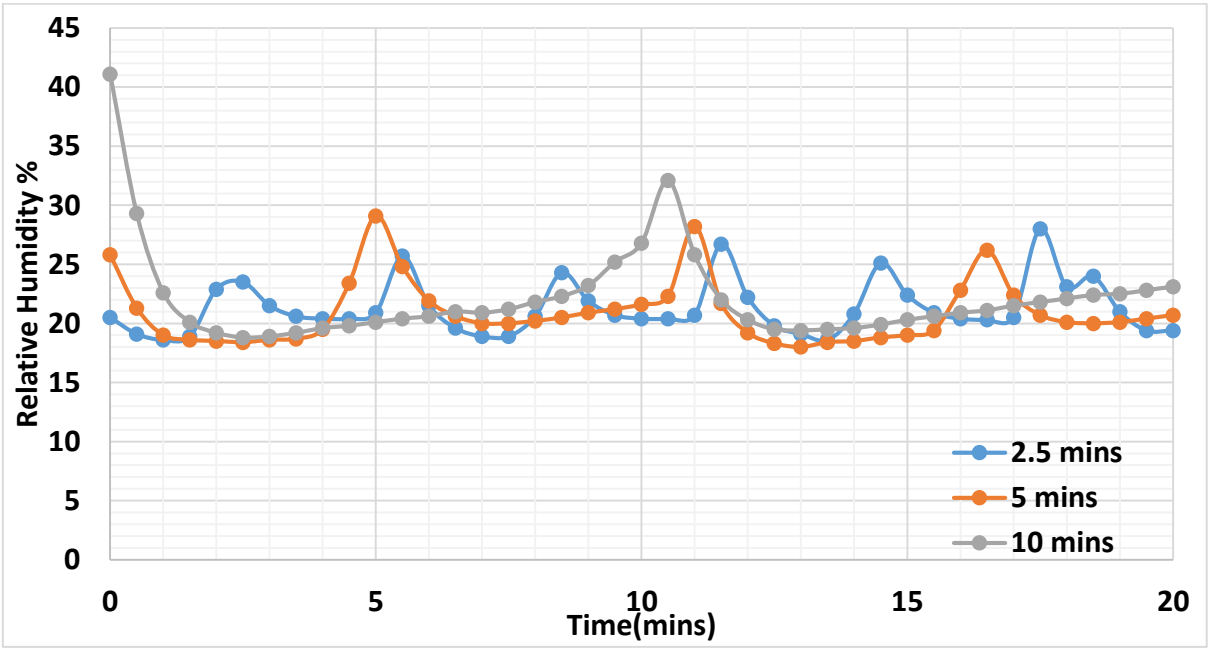



*Figure 7-9d: Air relative humidity after DCHE at different half-cycle times and 50% fresh air.*

Figure 7-9e shows the changes to the air conditions as it passes through DCHE as depicted on a psychrometric chart. The process is carried out with inlet air temperature and specific humidity of 13°C and 5.6 g/kg(d.a.), respectively and a 50% mixing ratio between fresh air and return air from the room.

It can be seen that the output-specific humidity and temperature are 7.5g/kg(d.a.), 32.4°C, respectively, for 2.5 mins, 7.1g/kg(d.a.), 31.4°C, respectively, for 5 mins, and 6.8g/kg(d.a.), 30.8°C, respectively for 10 mins.

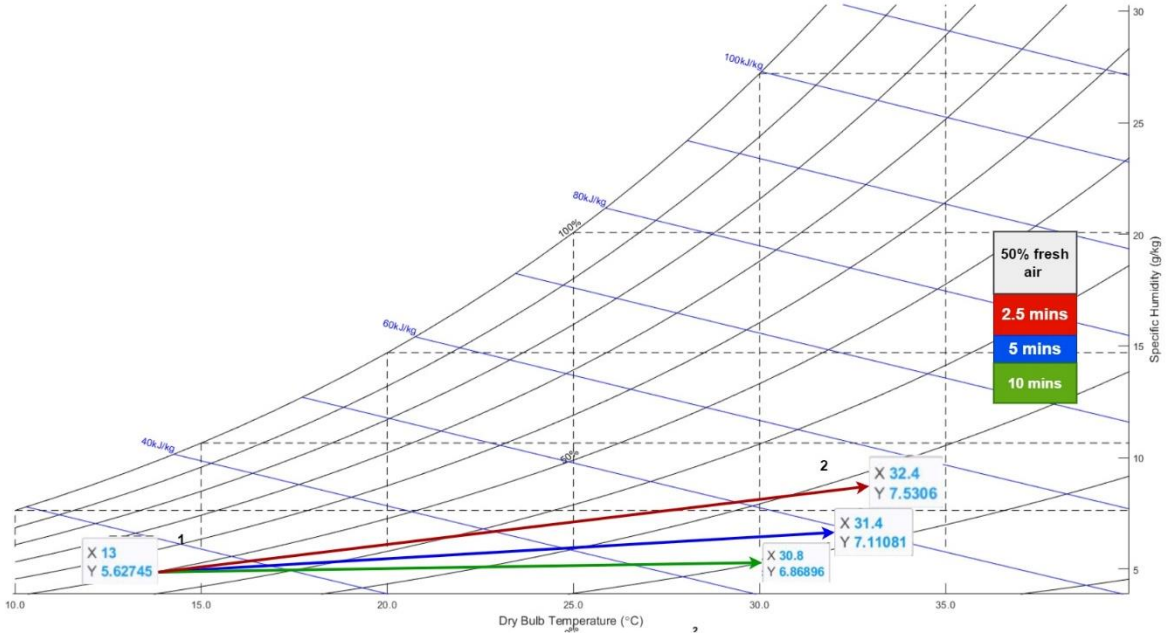



*Figure 7-9e*: *Psychrometric at different half-cycle times and 50% fresh air at 13°C, 5.6 g/kg(d.a.) inlet Temperature and specific humidity.*

Figure 7-10a illustrates the temperature variation with time between the ambient air and the room air. The ambient air conditions remain constant at 10.4°C, 56.88% relative humidity (RH), and specific humidity of 5.8 g/kg(d.a.). The main fan's air velocity is 1.5 m/s, with 100% fresh air. The half-cycle times are adjusted to 2.5 mins, 5 mins, and 10 mins. Figure 7-10b depicts the relative humidity variation between the ambient air and the room. It can be seen that the ambient relative humidity is constant at a value of 56%, starting with the same humidity level in the room and applying the initialisation by operating the two adsorber beds once for 15 mins before switching between the two adsorber beds. The room's relative humidity stabilized at 25.6%. After passing through the DCHE, the humidity dropped to 20%, with the temperature rising to 37°C, as shown in Figures 7-10c and 7-10d.

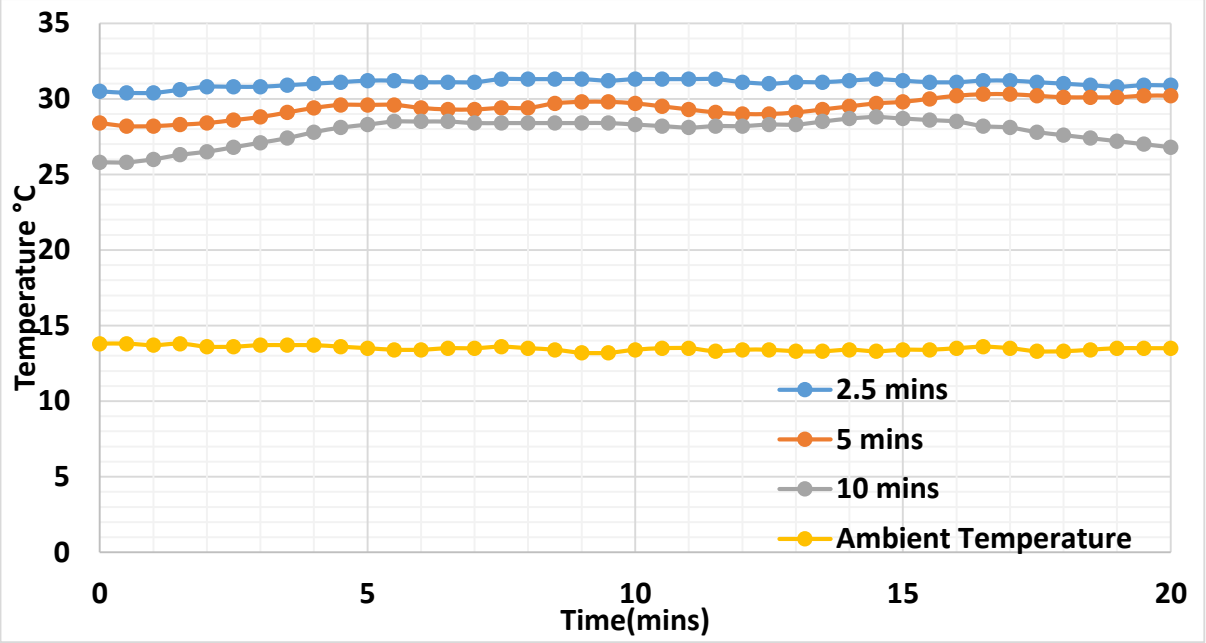



*Figure 7-10a: Room air temperature at different half-cycle times and 100% fresh air.*

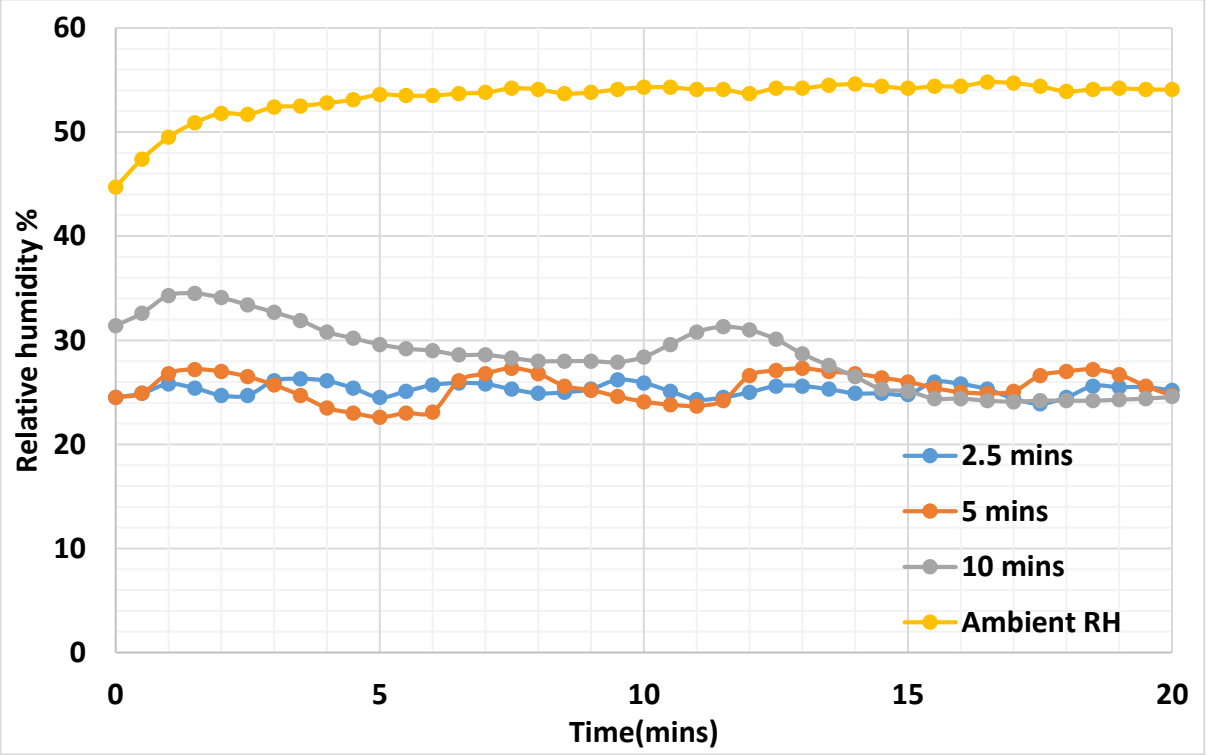



*Figure 7-10b: Room air relative humidity at different half-cycle times and 100% fresh air.*

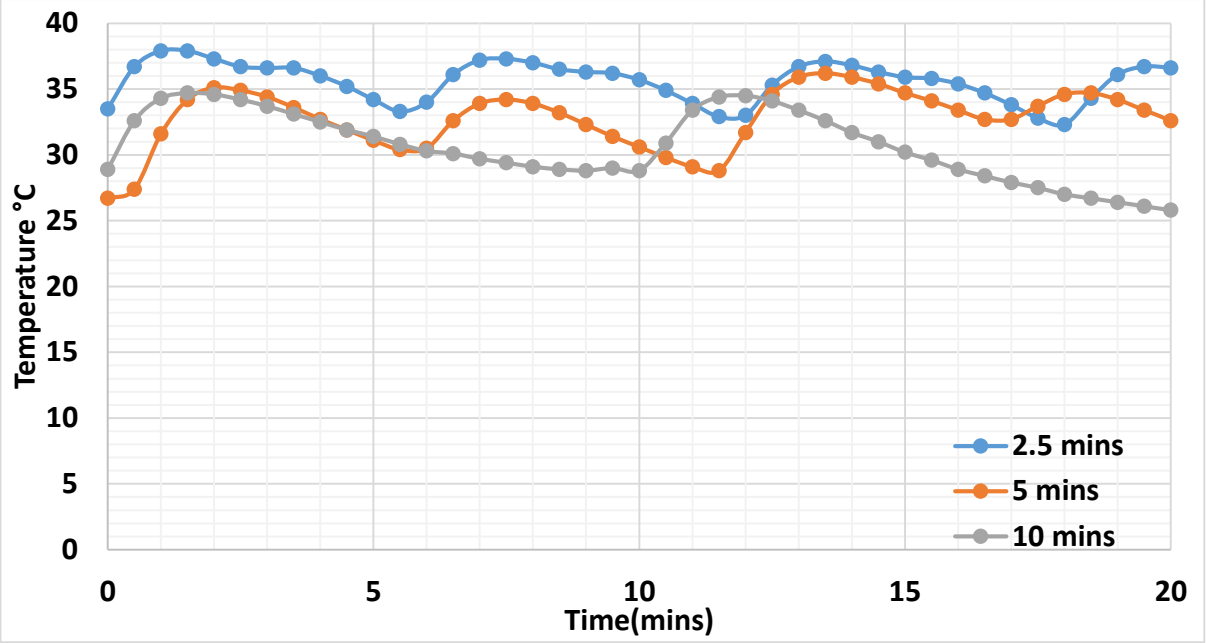



*Figure 6-10c: Air temperature change after DCHE at different half-cycle times and 100% fresh air.*

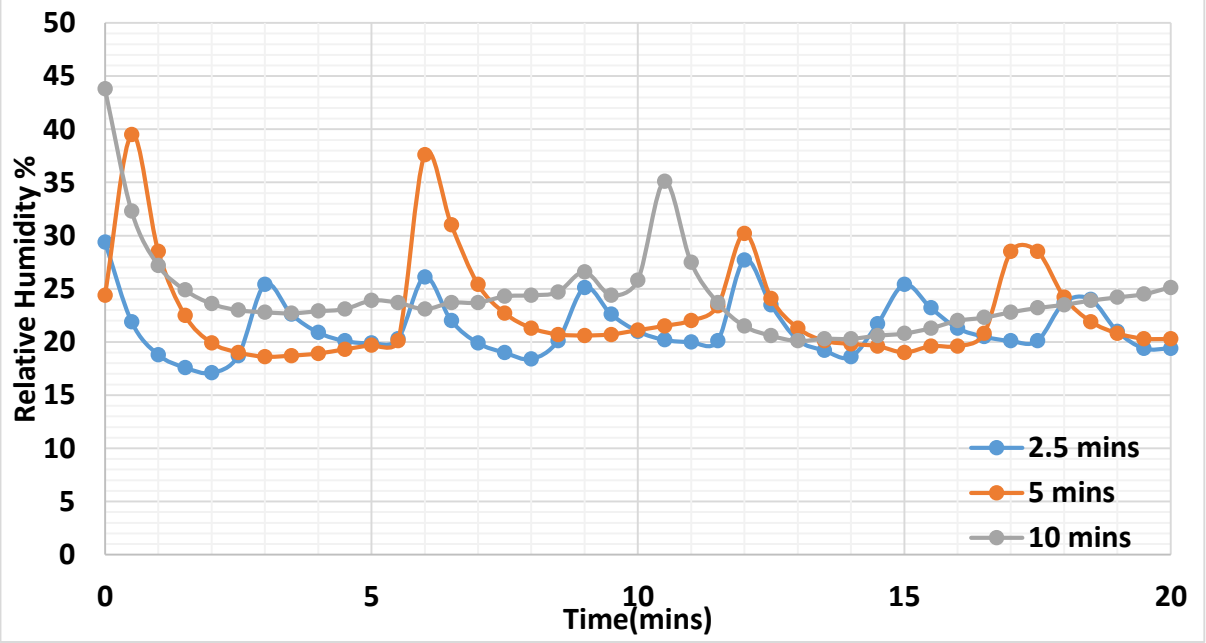



*Figure 6-10d: Air relative humidity change after DCHE at different half-cycle times and 100% fresh air.*

Figure 7-10e shows the changes to the air conditions as it passes through DCHE as depicted on a psychrometric chart. The process is carried out with inlet air temperature and specific humidity of 13.4°C and 5.014 g/kg(d.a.), respectively and a 100% mixing ratio between fresh air and return air from the room. It can be seen that the output-specific humidity and

temperature are 7g/kg(d.a.), 31.3°C, respectively, for 2.5 mins, 6.18g/kg(d.a.), 29.7°C, respectively, for 5 mins, and 5.9 g/kg(d.a.), 28.4°C, respectively for 10 mins.

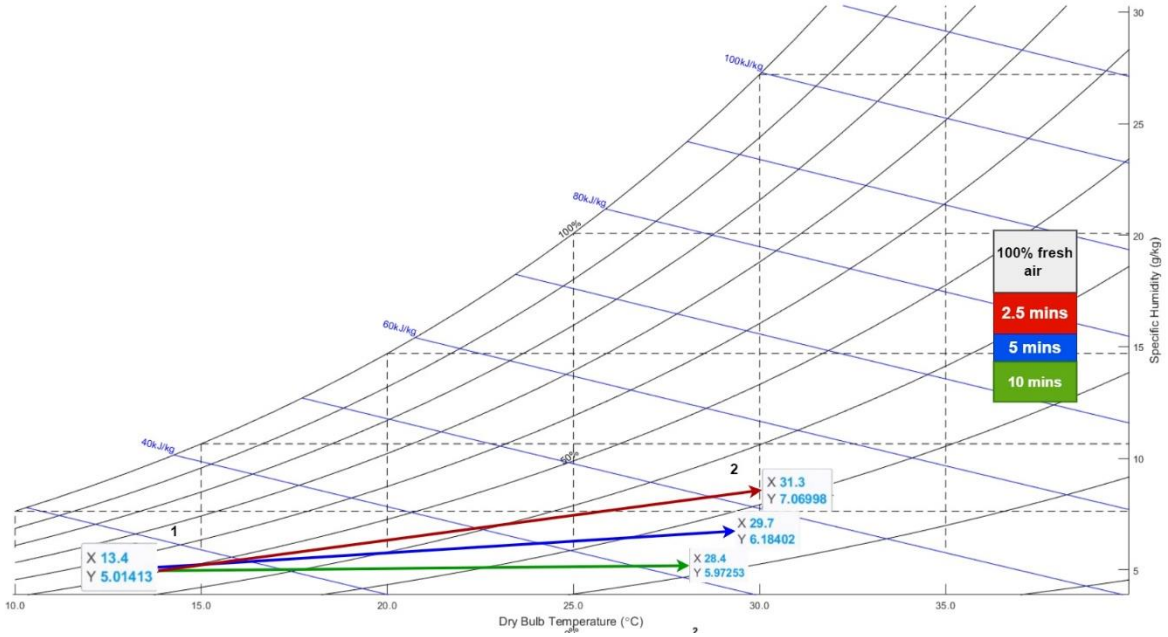



*Figure 7-10e: Psychrometric chart output at different half-cycle times and 100% fresh air at 13.4 °C, 5.01 g/kg(d.a.) inlet Temperature and specific humidity.*

Figure 7-11 highlights the Coefficient of Performance (COP) as a function of half-cycle time for two fresh air ratios: 100% and 50%. The blue line represents the COP for 100% fresh air, while the orange line represents the COP for 50% fresh air. As the half-cycle time increases from 2.5 mins to 10 mins, the COP decreases for both fresh air ratios. However, the system with 100% fresh air consistently shows a higher COP than the one with 50% fresh air and at a half-cycle time of 2.5 mins, it reaches 1.3.

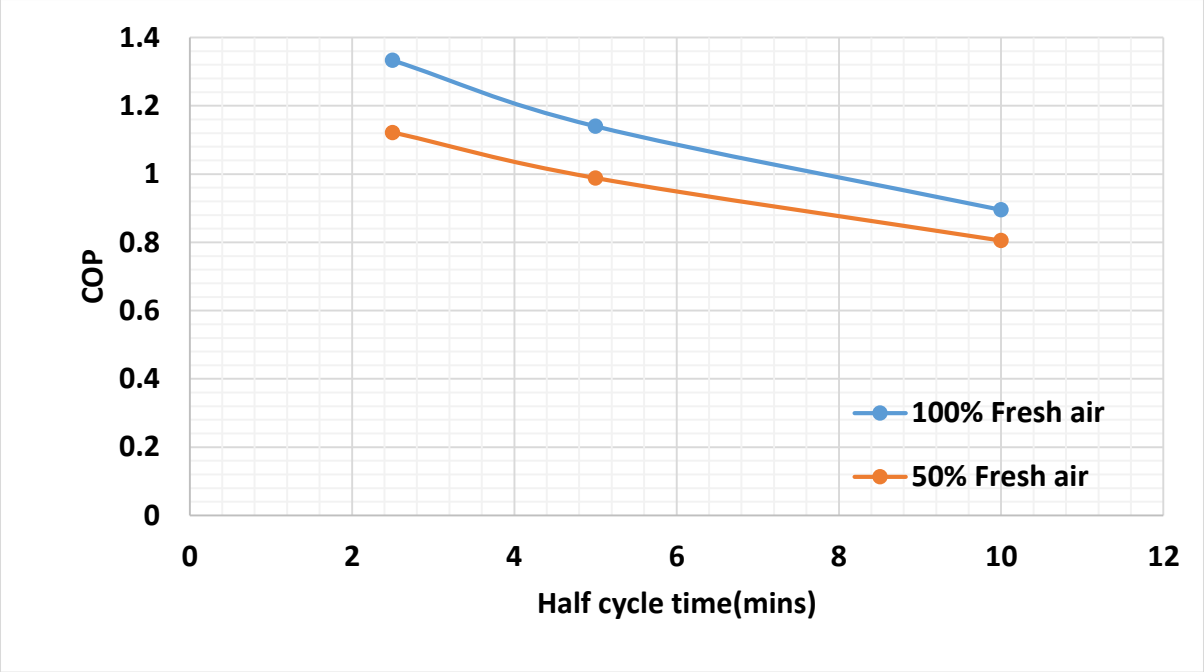



*Figure 7-11: Effect of half-cycle time and mixing ratio on the COP of the desiccant air conditioning system for heating.*

Figure 7-12a illustrates the temperature variation with time of the ambient air and the room air. The initial average ambient conditions are a relative humidity constant of 13.65°C, 50% relative humidity (RH), and specific humidity of 4.861 g/kg(d.a.). The main fan's air velocity is 1.5 m/s, with a 50% fresh air mixing ratio. The cycle times are adjusted to 2.5 mins, 5 mins, and 10 mins. Figure 7-12b depicts the relative humidity variation with time of the ambient air and the room. It can be seen that the ambient relative humidity is constant at a value of 50%, starting with the same humidity level in the room and applying the initialisation by operating the two adsorber beds once for 15 mins before switching between the two adsorber beds. The room's relative humidity stabilized at 21%. After passing through the DCHE, the humidity dropped to 17%, with the temperature rising to 35°C, as shown in Figures 7-12c and 7-12d.

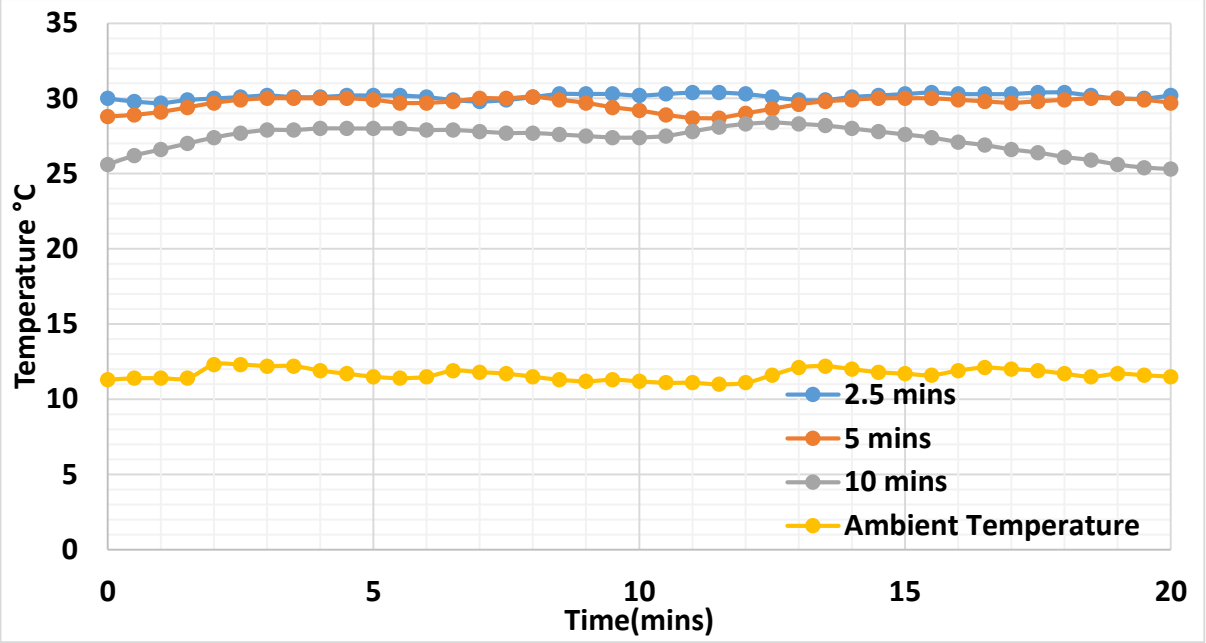



*Figure 7-12a: Room air temperature at different half-cycle times and 50% fresh air.*

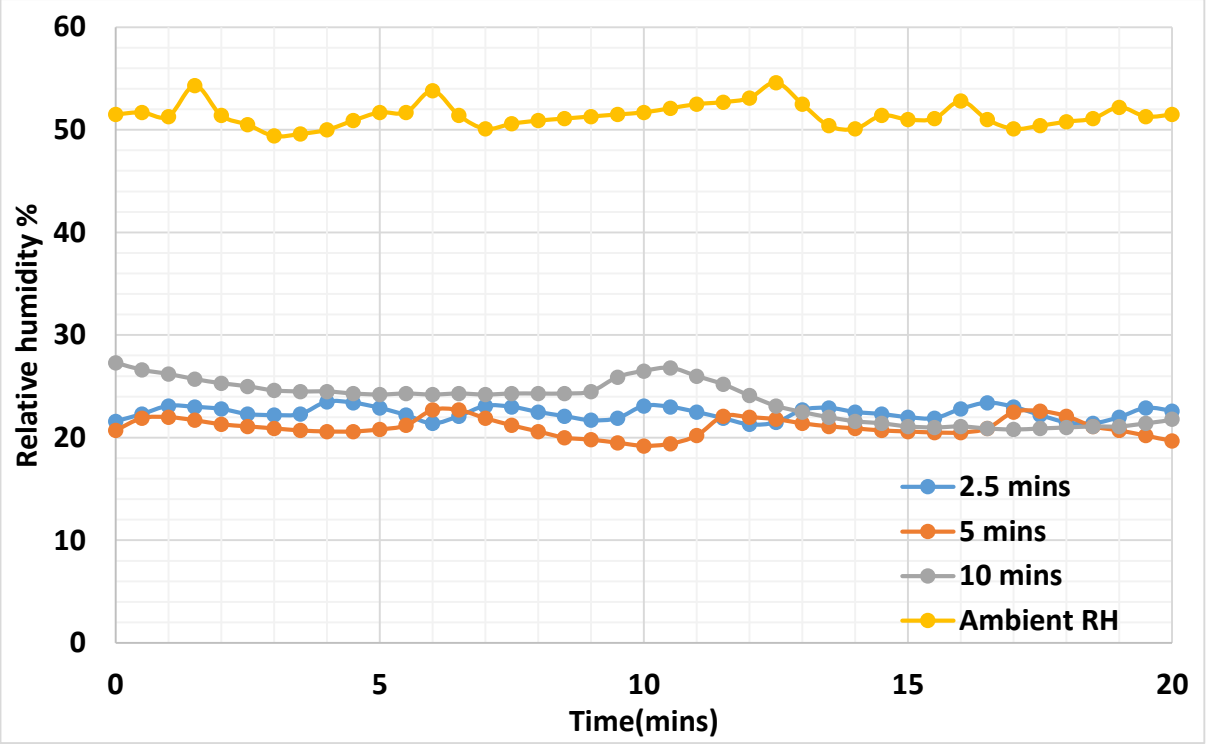



*Figure 7-12b: Room air relative humidity at different half-cycle times and 50% fresh air.*

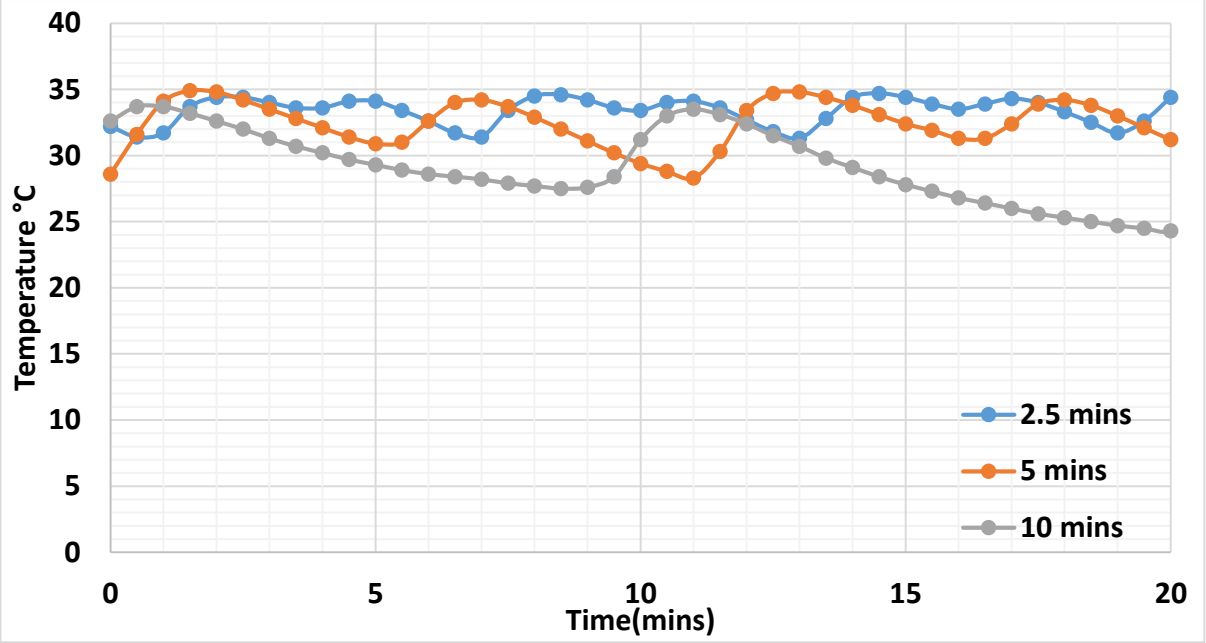



*Figure 7-12c: Air temperature after DCHE at different half-cycle times and 50% fresh air.*

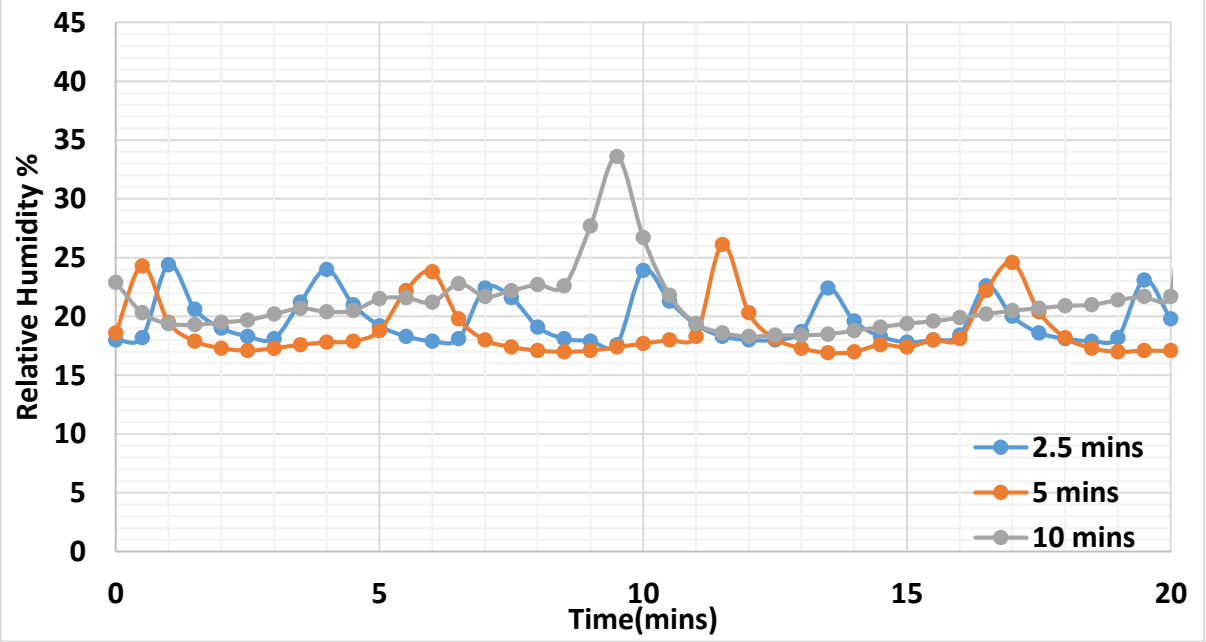



*Figure 7-12d: Air relative humidity after DCHE at different half-cycle times and 50% fresh air.*

Figure 7-12e shows the changes to the air conditions as it passes through DCHE as depicted on a psychrometric chart. The process is carried out with inlet air temperature and specific humidity of 11.2°C and 4.16 g/kg(d.a.), respectively and a 50% mixing ratio between fresh air and return air from the room. It can be seen that the output-specific humidity and temperature are 6 g/kg(d.a.), 30°C, respectively, for 2.5 mins, 4.7 g/kg(d.a.), 29.2°C, respectively for 5 mins, and 6.3 g/kg(d.a.), 28.8°C, respectively for 10 mins.

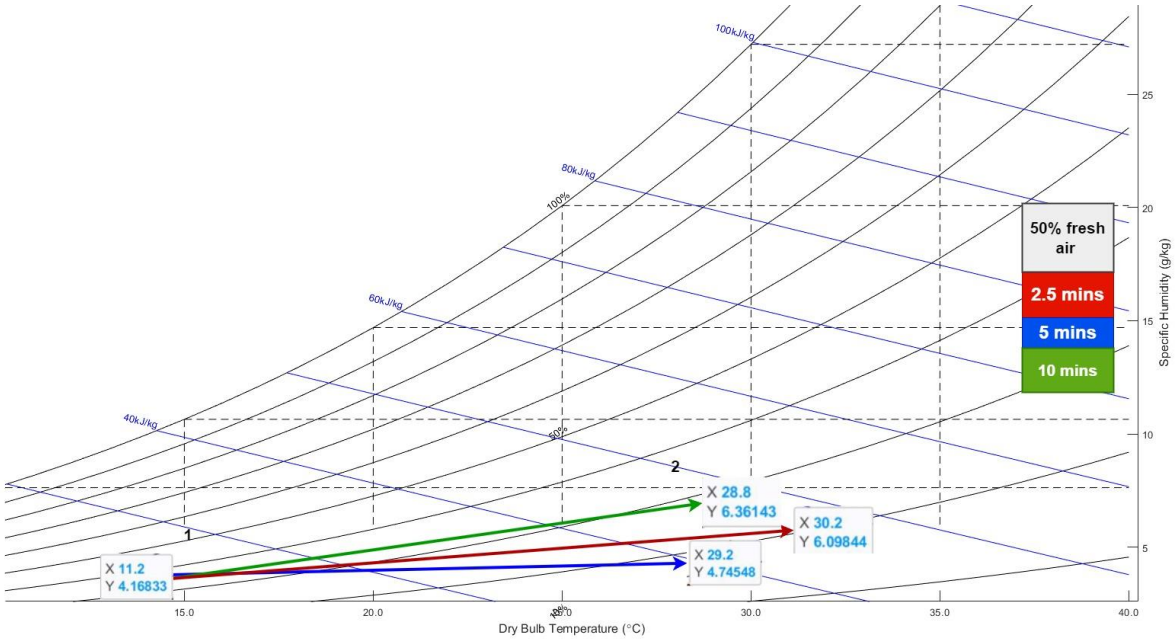



*Figure 7-12e*: *Psychrometric chart output at different half-cycle times and 50% fresh air at 11.2 °C, 4.16 g/kg(d.a.) inlet Temperature and specific humidity.*

Figure 7-13a illustrates the temperature variation with time of the ambient air and the room air. The ambient air conditions remain constant at 14°C, 45.5% relative humidity (RH), and specific humidity of 4.86 g/kg(d.a.). The main fan's air velocity is 1.5 m/s, with 100% fresh air. The half-cycle times are adjusted to 2.5 mins, 5 mins, and 10 mins. Figure 7-13b depicts the relative humidity variation between the ambient air and the room. It can be seen that the ambient relative humidity is constant at a value of 56%, starting with the same humidity level in the room and applying the initialisation by operating the two adsorber beds once for 15 mins before switching between the two adsorber beds. The room's relative humidity stabilized at 25.6% . After passing through the DCHE, the humidity dropped to 20%, with the temperature rising to 33°C, as shown in Figures 7-13c and 7-13d.

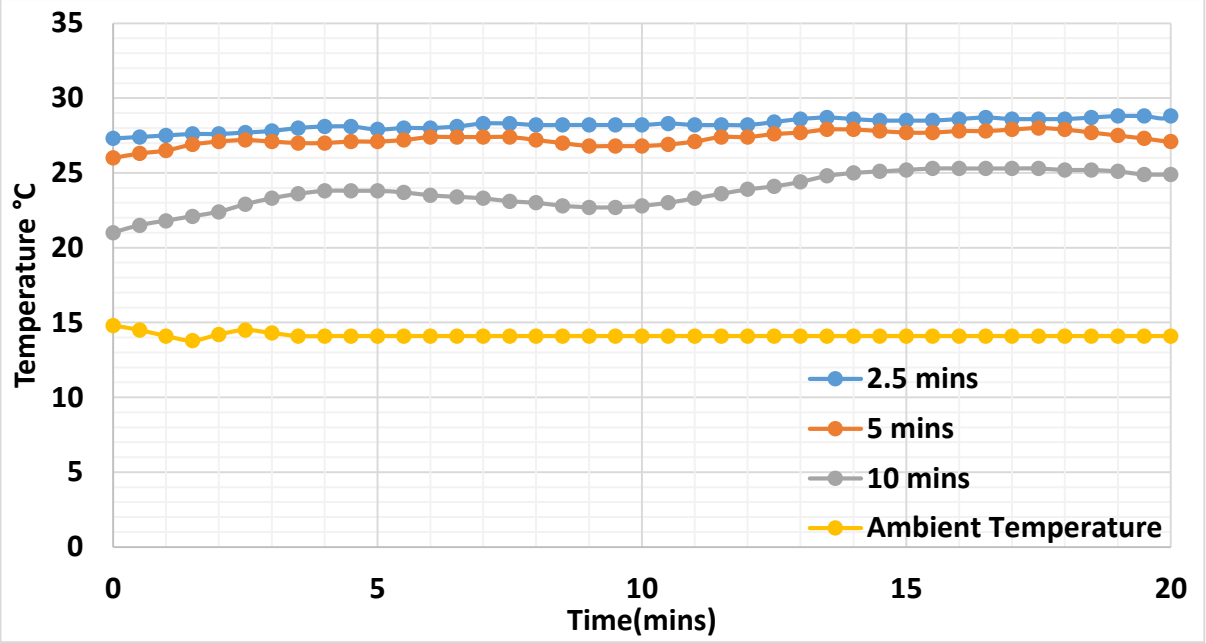



*Figure 7-13a: Room air temperature at different half-cycle times and 100% fresh air.*

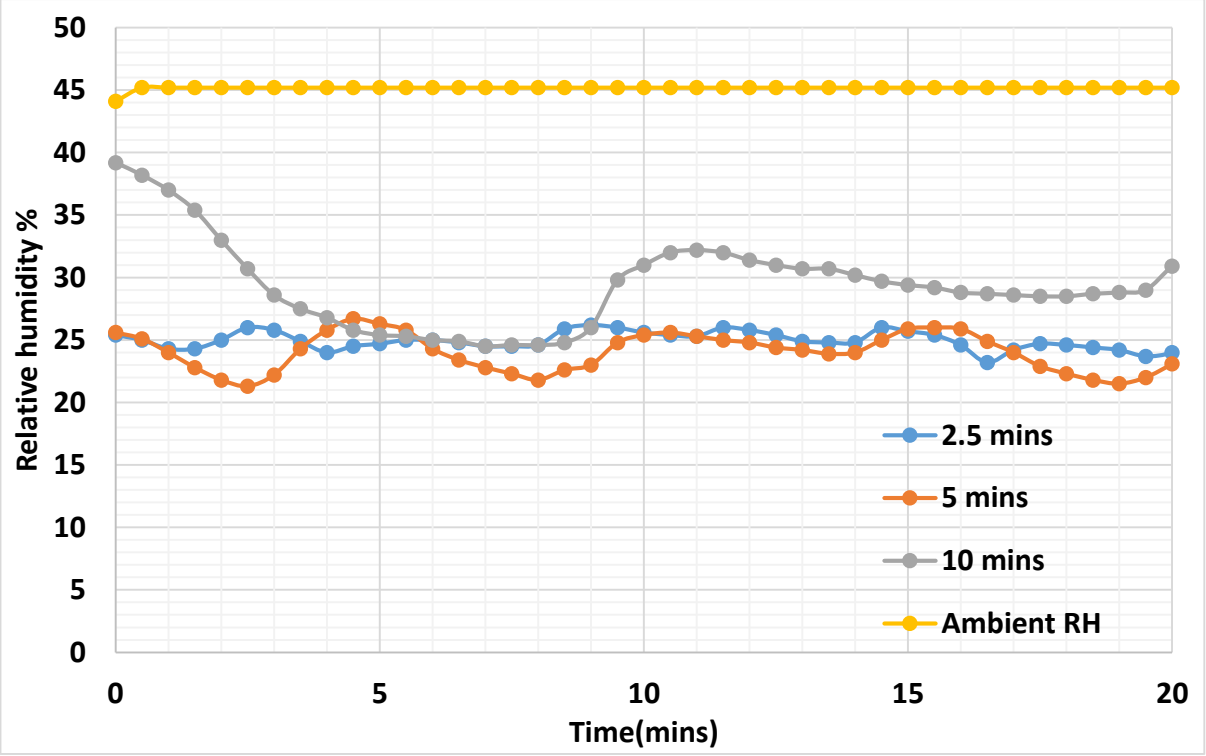



*Figure 7-13b: Room air relative humidity at different half-cycle times and 100% fresh air.*

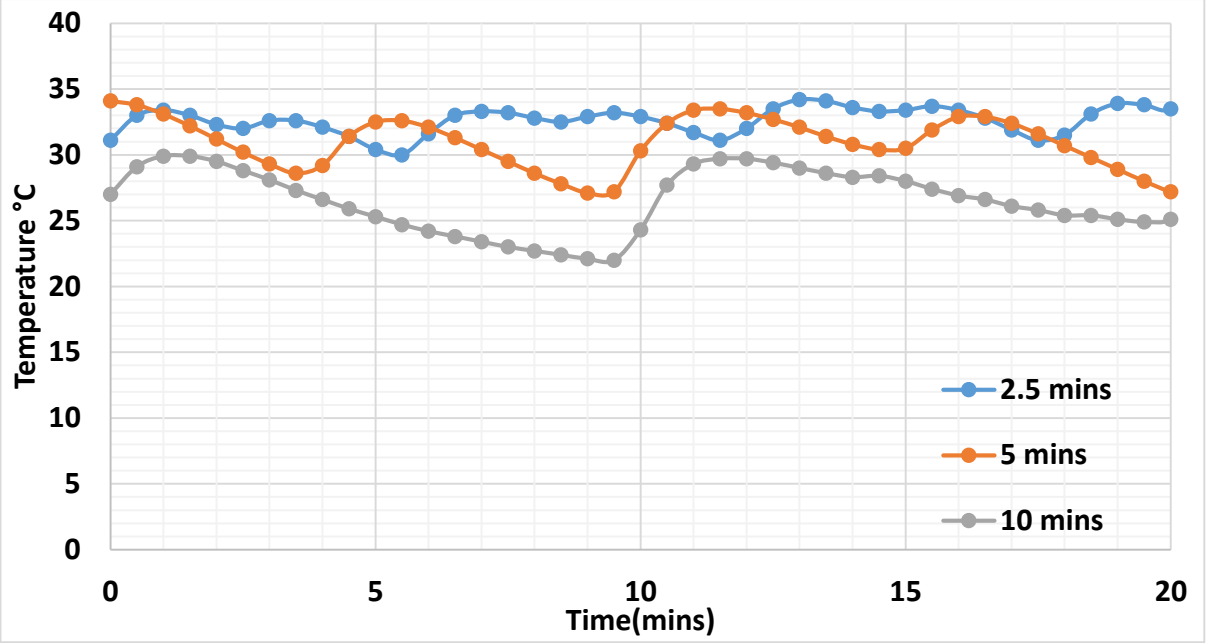



*Figure 7-13c: Air temperature after DCHE at different half-cycle times and 100% fresh air.*

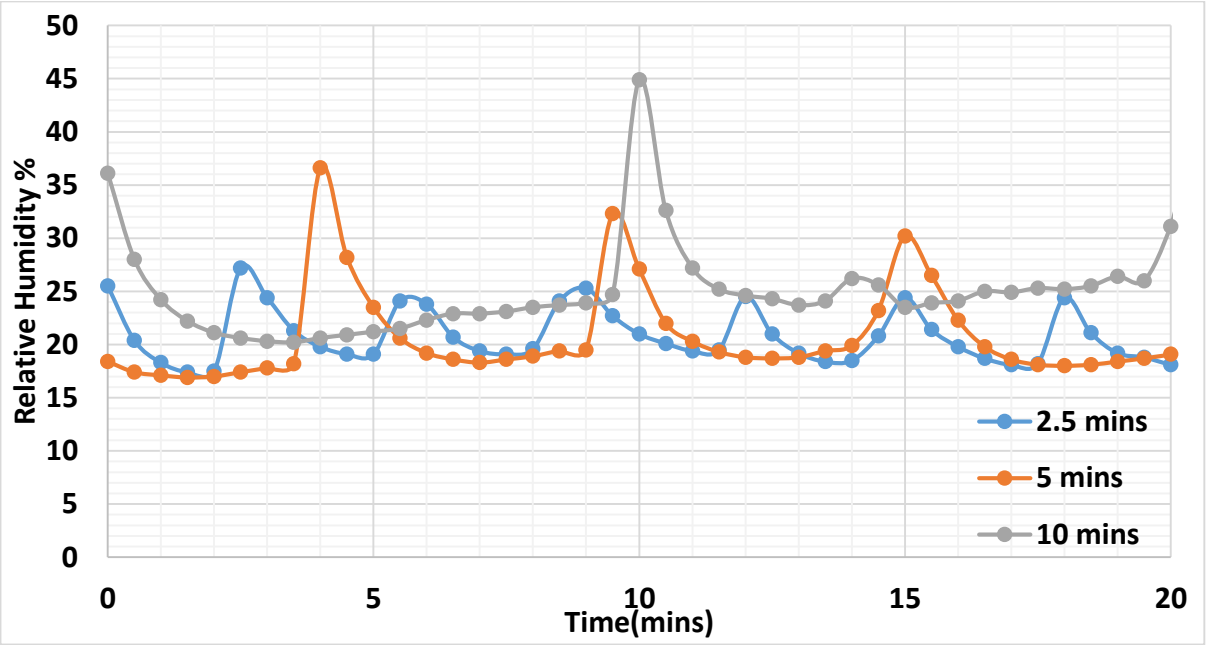



*Figure 7-13d: Air relative humidity after DCHE at different half-cycle times and 100% fresh air.*

Figure 7-13e shows the changes to the air conditions as it passes through DCHE as depicted on a psychrometric chart. The process is carried out with inlet air temperature and specific humidity of 14.7°C and 4.6 g/kg(d.a.), respectively and a 100% mixing ratio between fresh air and return air from the room. It can be seen that the output-specific humidity and temperature are 5.9 g/kg(d.a.), 28.2°C, respectively for 2.5mins, 5.4 g/kg(d.a.), 26.8°C, respectively for 5mins, and 7.3 g/kg(d.a.), 28.2°C, respectively for 10mins.

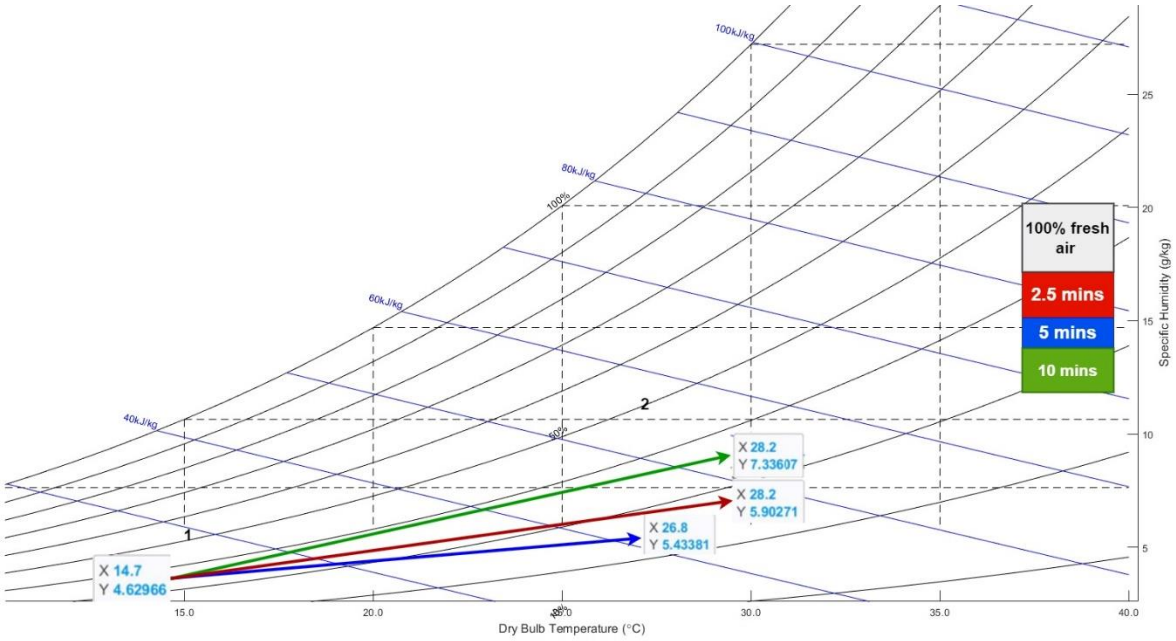



*Figure 7-13e: Psychrometric chart output at different half-cycle times and 100% fresh air at 14.7 °C, 4.6 g/kg(d.a.) inlet Temperature and specific humidity.*

Figure 7-14 highlights the Coefficient of Performance (COP) as a function of half-cycle time for two fresh air ratios: 100% and 50%. The blue line represents the COP for 100% fresh air, while the orange line represents the COP for 50% fresh air. As the half-cycle time increases from 2.5 mins to 10 mins, the COP decreases for both fresh air ratios. However, the system with 100% fresh air consistently shows a higher COP than the one with 50% fresh air at a half-cycle time of 2.5 mins, the COP is 1.2.

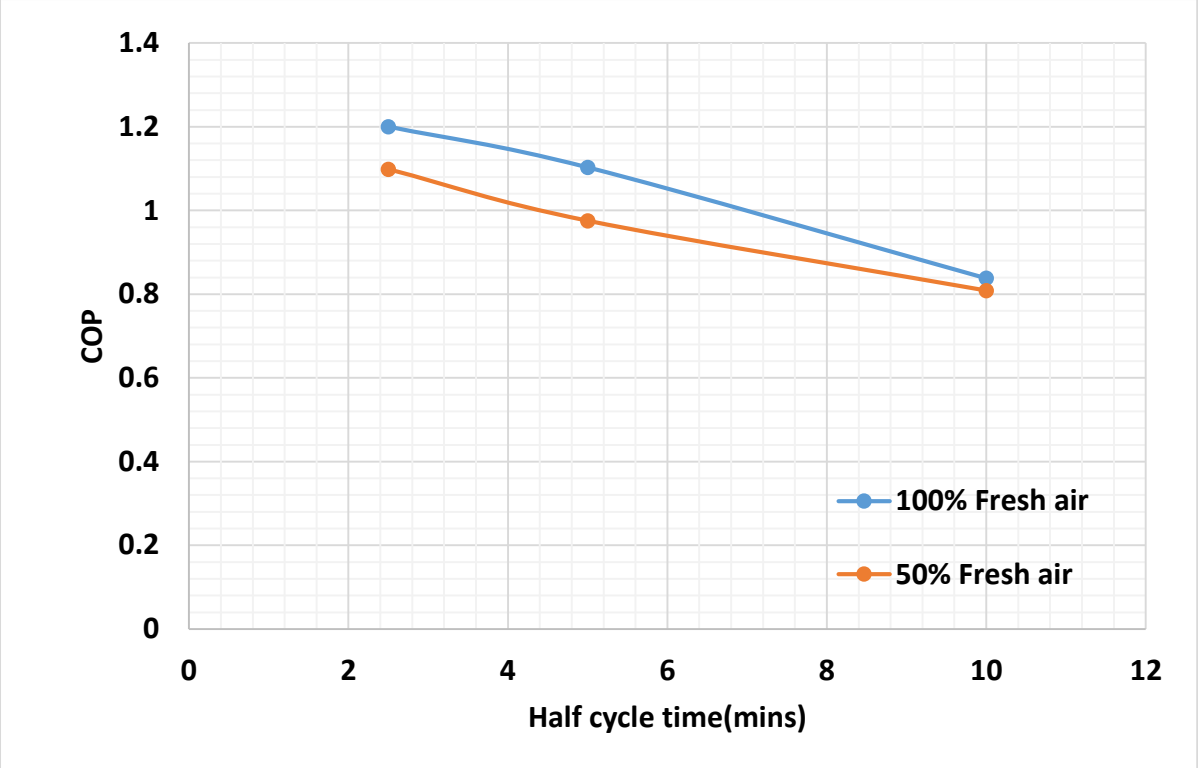



*Figure 7-14: Effect of half-cycle time and mixing ratio on the COP of the desiccant air conditioning system.*

Figure 7-15a illustrates the temperature variation with time of the ambient air and the room air. The ambient air conditions remain constant at 10.3°C, 67% relative humidity (RH), and specific humidity of 4.86 g/kg(d.a.). The main fan's air velocity is 1.5 m/s, with 50% fresh air. The half-cycle times are adjusted to 2.5 mins, 5 mins, and 10 mins. Figure 7-15b depicts the relative humidity variation between the ambient air and the room. It can be seen that the ambient relative humidity is constant at a value of 67%, starting with the same humidity level in the room and applying the initialisation by operating the two adsorber beds once for 15 mins before switching between the two adsorber beds. The room's relative humidity stabilized at 21%. After passing through the DCHE, the humidity dropped to 17.5%, with the temperature rising to 35.6°C, as shown in Figures 7-15c and 7-15d.

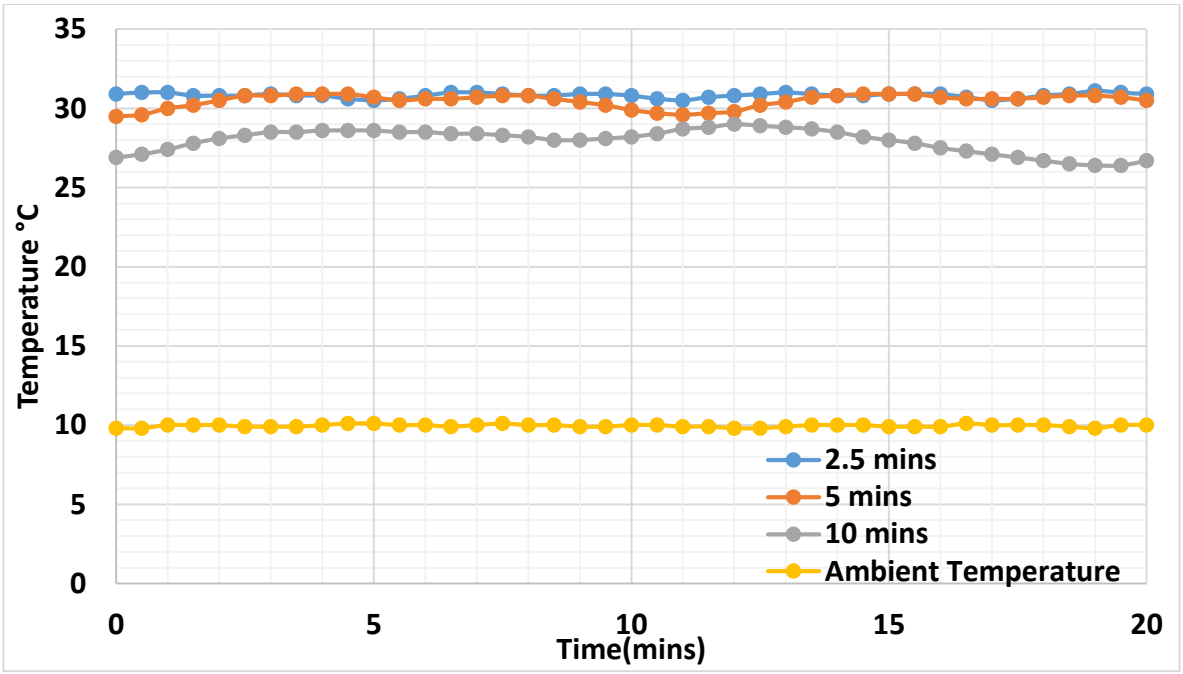



*Figure 7-15a Room air temperature at different half-cycle times and 50% fresh air.*

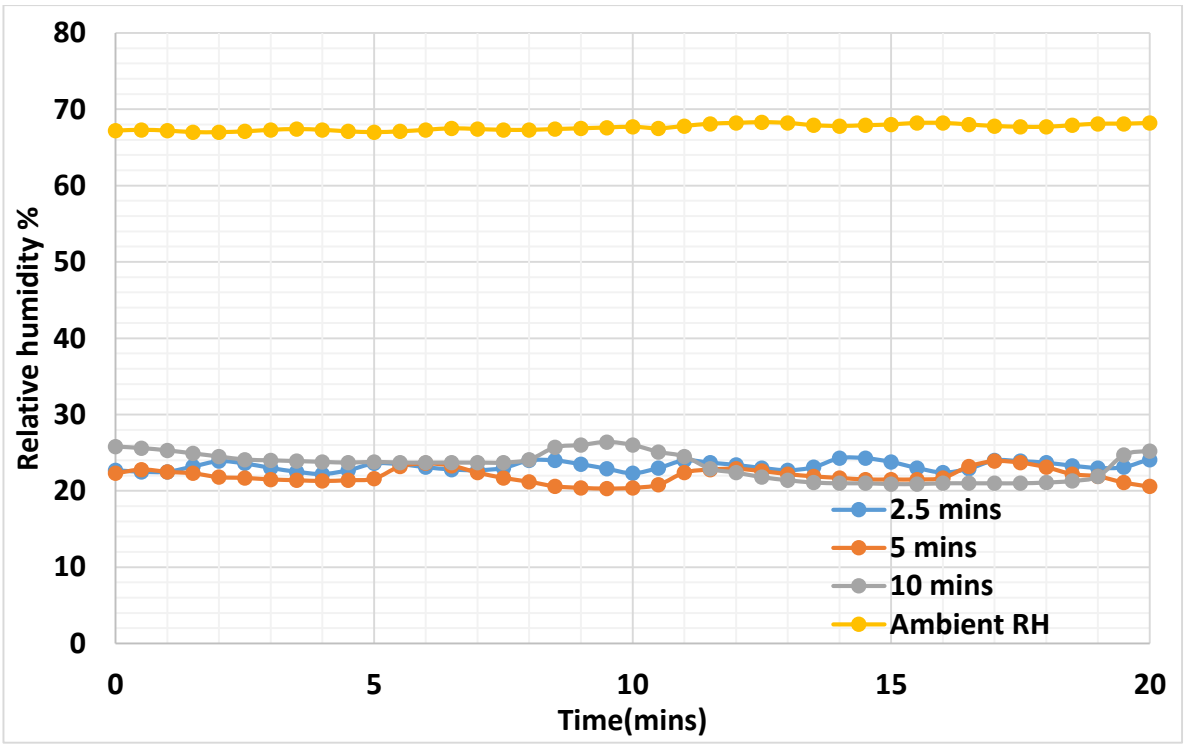



*Figure 7-15b: Room air relative humidity at different half-cycle times and 50% fresh air.*

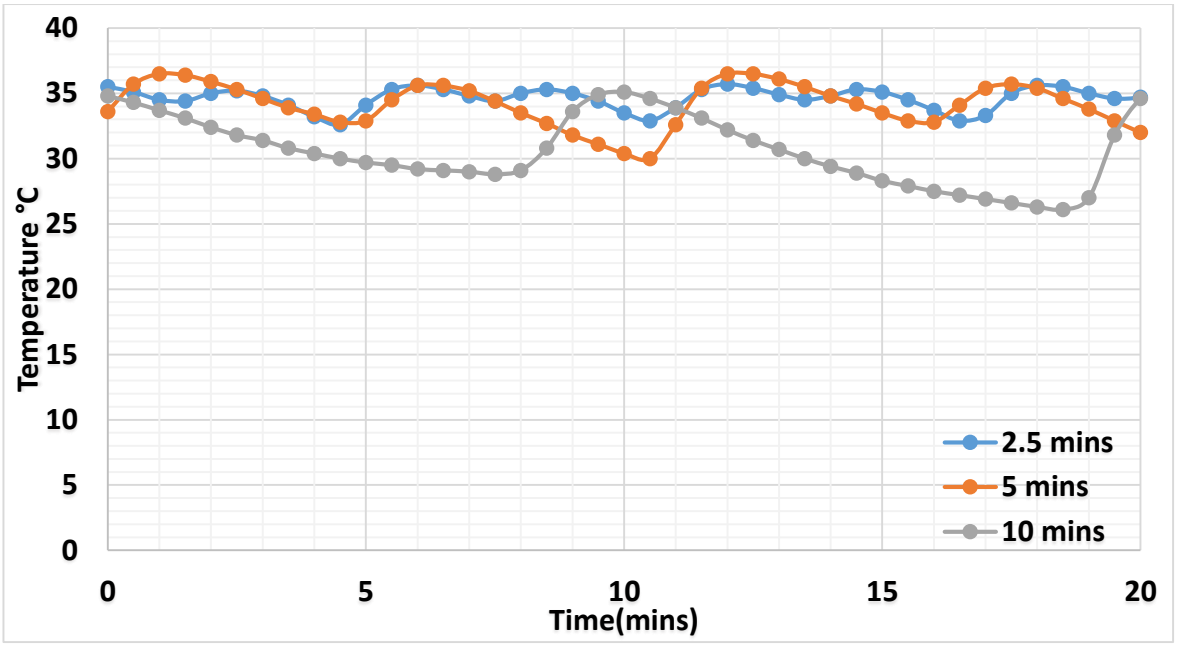



*Figure 7-15c: Temperature after DCHE at different half-cycle times and 50% fresh air.*

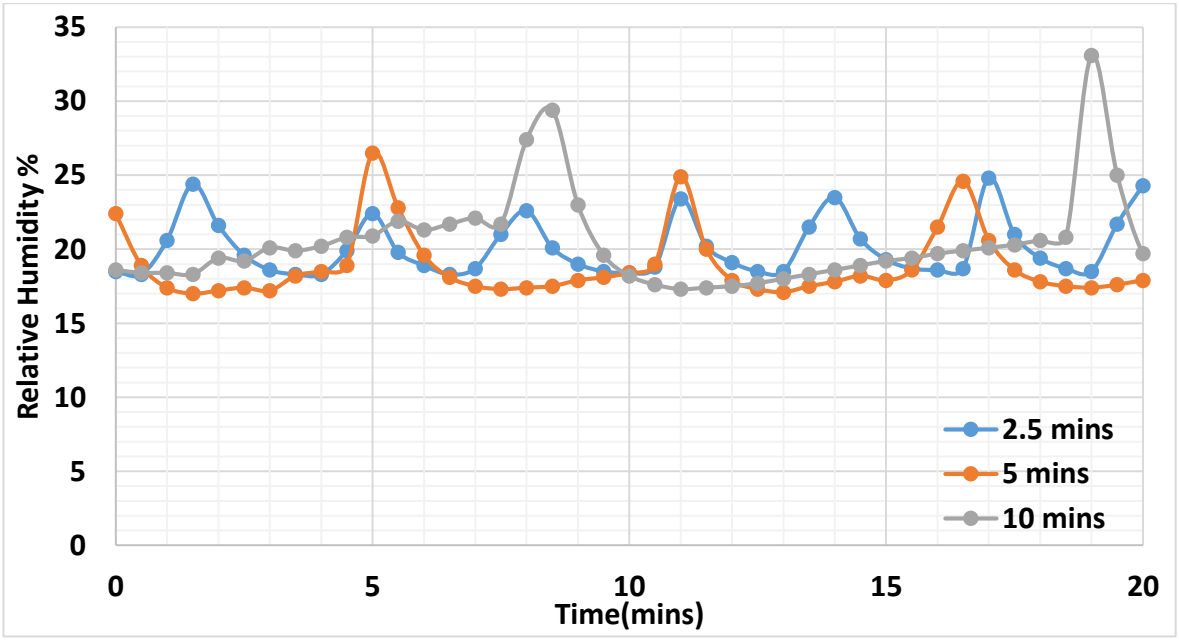



*Figure 7-15d: Air relative humidity after DCHE at different half-cycle times at 50% fresh air.*

Figure 7-15e shows the changes to the air conditions as it passes through DCHE as depicted on a psychrometric chart. The process is carried out with inlet air temperature and specific humidity of 10°C and 5.06 g/kg(d.a.), respectively and a 50% mixing ratio between fresh air and return air from the room. It can be seen that the output-specific humidity and temperature are 6 g/kg(d.a.), 30.8°C, respectively for 2.5 mins, and 5.2g/kg(d.a.), 23°C for 5 mins and 6.14 g/kg(d.a.), 28.20 °C for 10 mins, respectively.

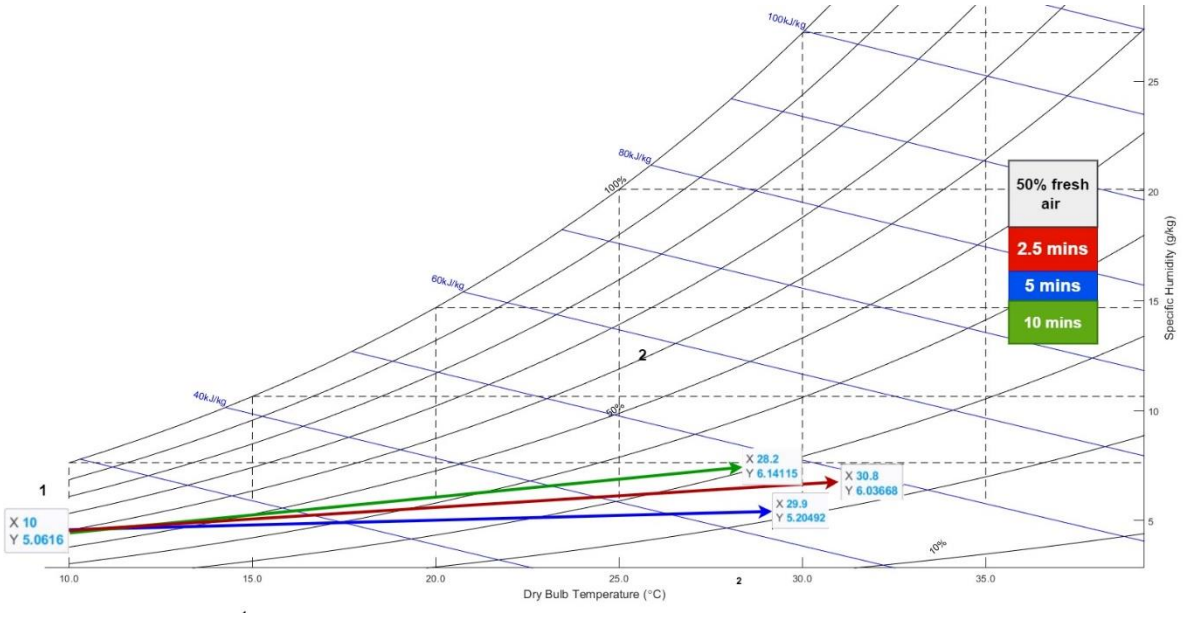



*Figure 7-15e: Psychrometric chart output at different half-cycle times and 50% fresh air at 10 °C, 5.06 g/kg(d.a.) inlet Temperature and specific humidity.*

Figure 7-16a illustrates the temperature variation with time between the ambient air and the room air. The ambient air conditions remain constant at 10.3°C, 58% relative humidity (RH), and specific humidity of 4.5 g/kg(d.a.). The main fan's air velocity is 1.5 m/s, with 100% fresh air. The half-cycle times are adjusted to 2.5 mins, 5 mins, and 10 mins. Figure 7-16b depicts the relative humidity variation between the ambient air and the room. It can be seen that the ambient relative humidity is constant at a value of 58%, starting with the same humidity level in the room and applying the initialisation by operating the two adsorber beds once for 15 mins before switching between the two adsorber beds. The room's relative humidity stabilized at 23.4%. After passing through the DCHE, the humidity dropped to 18%, with the temperature rising to 36°C, as shown in Figures 7-16c and 7-16d.

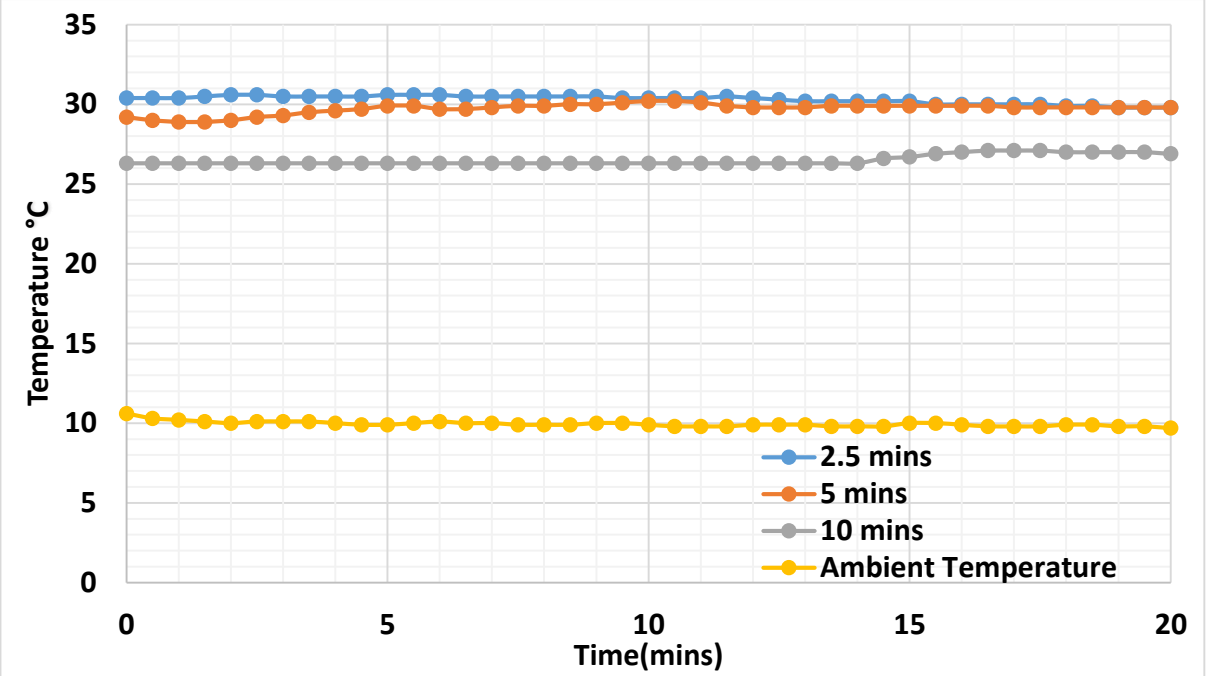



*Figure 7-16a: Room air temperature at different half-cycle times and 100% fresh air.*

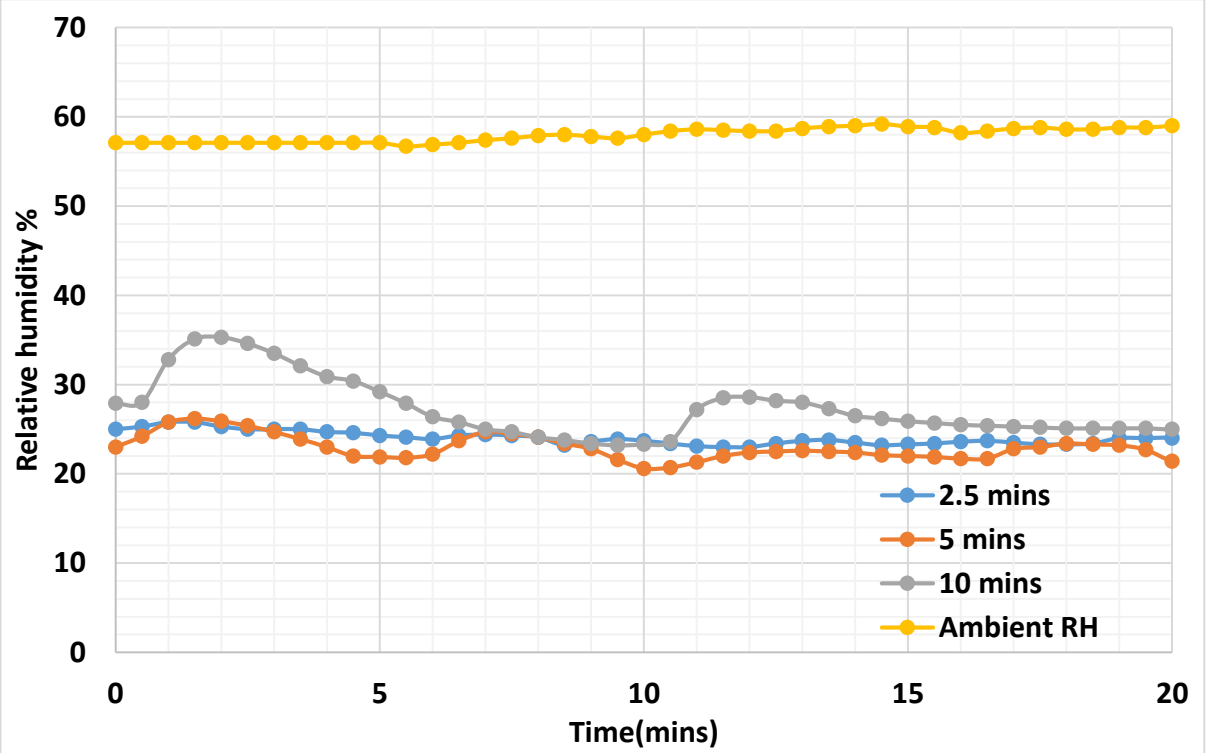



*Figure 7-16b: Room air relative humidity at different half-cycle times and 100% fresh air.*

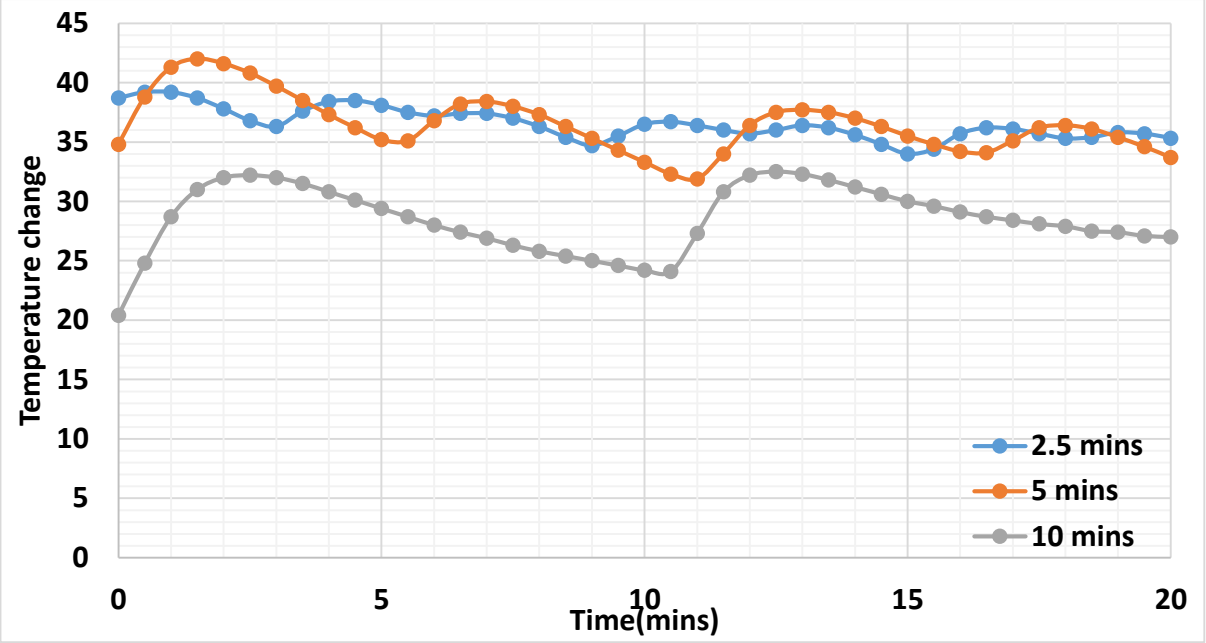



*Figure 7-16c: Air temperature after DCHE at different half-cycle times and 100% fresh air.*

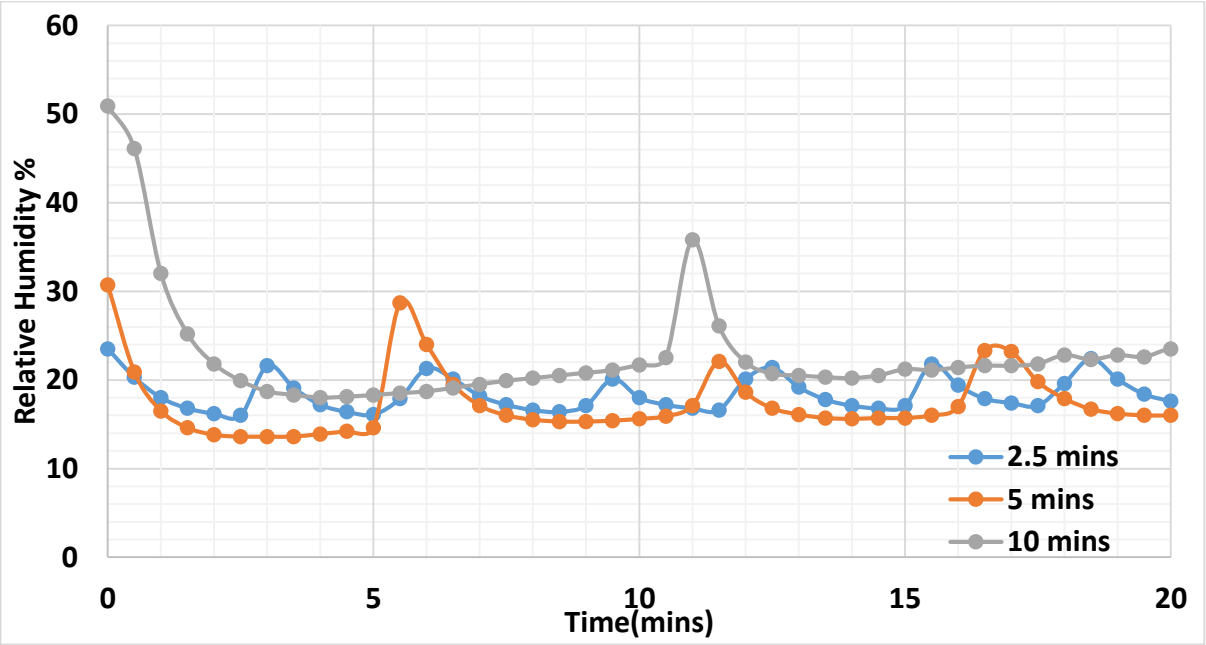



*Figure 7-16d: Air relative humidity after DCHE at different half-cycle times and 100% fresh air.*

Figure 7-16e shows the changes to the air conditioner as it passes through DCHE as depicted on a psychrometric chart. The process is carried out with inlet air temperature, and specific humidity of 10°C and 4.3 g/kg(d.a.), respectively and a 100% mixing ratio between fresh air and return air from the room. It can be seen that the output-specific humidity and temperature are 6 g/kg(d.a.), 30.2°C, respectively, for 5 mins and 2.5 mins, which is better than switching to 10 mins.

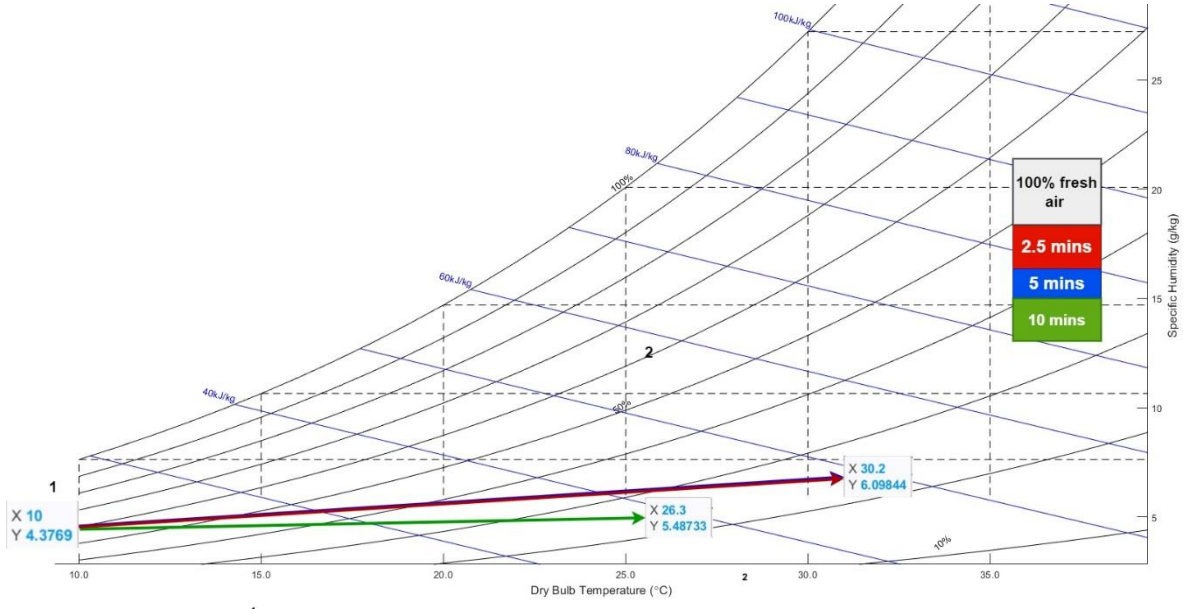



*Figure 7-16e: Psychrometric chart output at different half-cycle times and 100% fresh air at 10 °C, 4.38 g/kg(d.a.) inlet Temperature and specific humidity.*

Figure 7-17 highlights the Coefficient of Performance (COP) variation of half-cycle time for two fresh air ratios of 100% and 50%. The blue line represents the COP for 100% fresh air, while the orange line represents the COP for 50% fresh air. As the half-cycle time increases from 2.5 mins to 10 mins, the COP decreases for both fresh air ratios. However, the system with 100% fresh air consistently shows a higher COP than the one with 50% fresh air at a half-cycle time of 2.5 mins, the COP is 1.54.

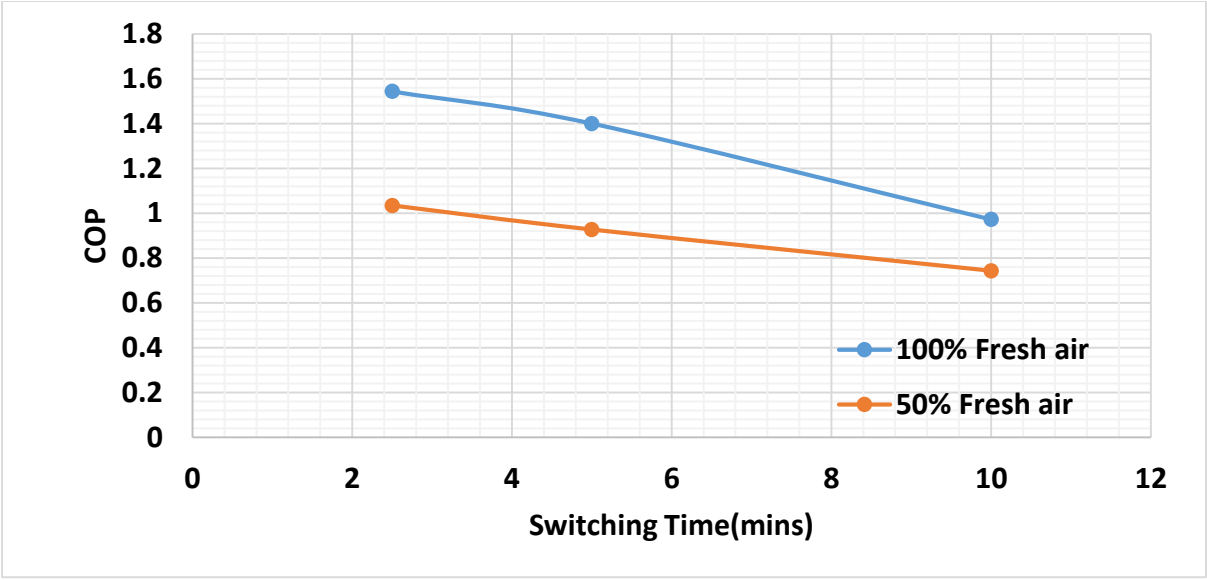



*Figure 7-17: Effect of half-cycle time and mixing ratio on the COP of the desiccant air conditioning system.*

Figure 7-18 shows the Coefficient of Performance (COP) versus air speed for a half-cycle time of 2.5, 5, and 10 mins, indicating that COP decreases as airspeed increases for all times. The process is carried out with inlet air temperature, humidity, and specific humidity of 10.8°C, 62.2% and 5 g/kg(d.a.), respectively and a 100% mixing ratio between fresh air and return air from the room. The highest COP is observed for the 2.5-mins half-cycle time across all airspeeds, followed by the 5-mins duration, then with the 10-mins duration having the lowest COP. Specifically, at 0.75 m/s airspeed for each bed, the COPs are slightly above 1, around 0.94, and approximately 0.85 for 2.5, 5, and 10 mins, respectively. At 2.25 m/s, the COP values are around 0.6, 0.57, and 0.47 for 2.5, 5, and 10 mins, respectively. The system is most efficient at lower air speeds and shorter durations, with 2.5 mins half-cycle time, with efficiency decreasing as airspeed increases or half-cycle time.

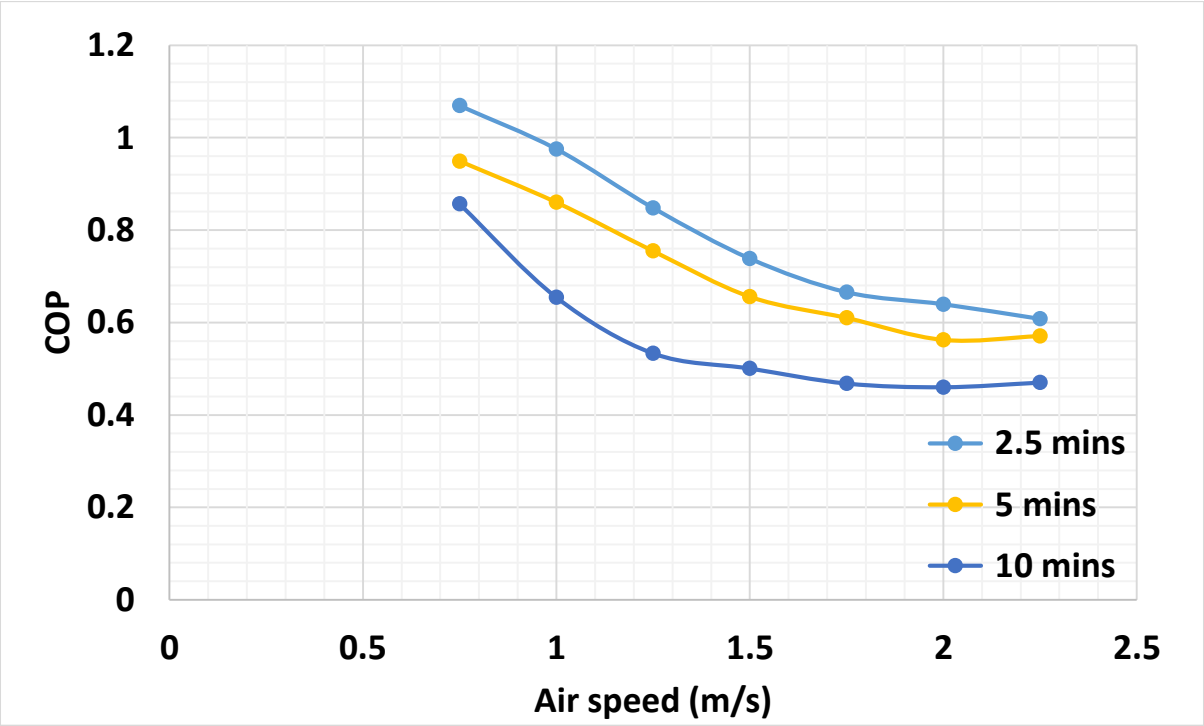



*Figure 7-18: Coefficient of Performance (COP) versus airspeed for 2.5, 5, and 10-mins half-cycle times.*

As a conclusion from the previous experiments, Figure 7-19 shows the output air temperature and specific humidity vs half-cycle time for 50% and 100% fresh air. The temperature decreases as the half-cycle time increases for both mixing ratios, with the 50% fresh air mixture generally resulting in higher output temperatures. As half-cycle time increases, the specific humidity decreases for both mixing ratios, with the 100% fresh air mixture consistently having lower specific humidity levels.

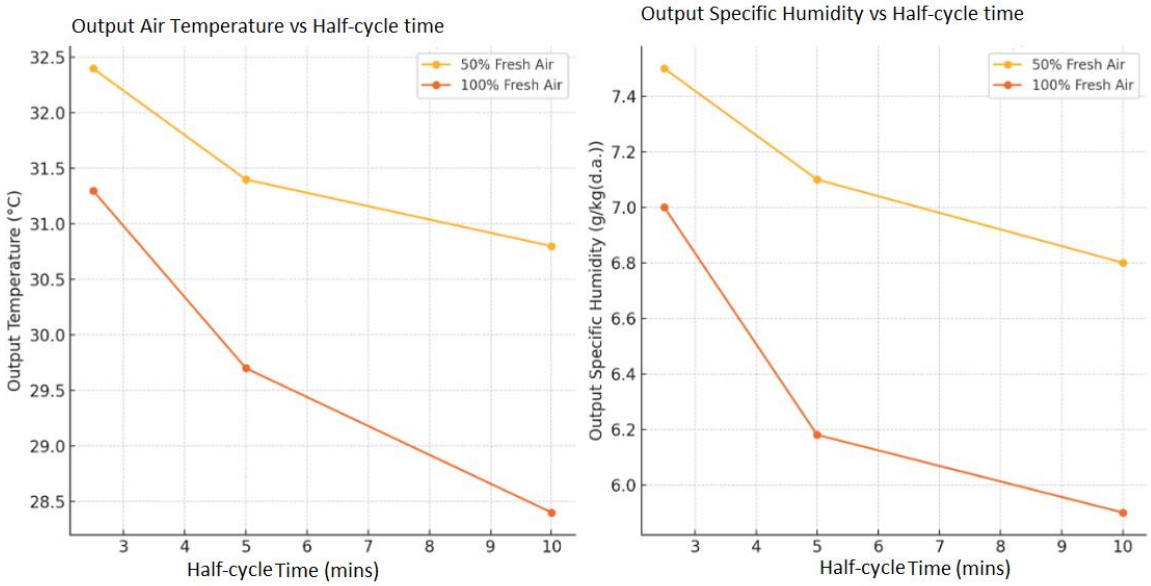



*Figure 7-19: Output air temperature vs. half-cycle time and output air specific humidity vs. half-cycle time.*

- **Higher Efficiency**: The system with 100% fresh air consistently shows a higher Coefficient of Performance (COP) across all half-cycle times compared to the 50% fresh air scenario. These results indicate that using more fresh air enhances the system's efficiency for heating applications.
- **Lower Output Temperatures and Humidities**: Employing 100% fresh air typically results in lower output air temperatures and specific humidities compared to the scenario with 50% fresh air. This phenomenon can be attributed to the higher capacity of fresh air to remove moisture, enhancing dehumidification and producing drier and relatively cooler air.
- **Effect of Half-cycle time**: As the half-cycle time increases, the temperature and humidity levels slightly decrease. However, at 2.5 mins, the system shows optimal performance, balancing energy consumption and output conditions effectively. The system is less efficient at longer half-cycle times, resulting in lower temperatures and humidity removal rates.

### 7.2.2. Impact of Evaporative Cooling on Humidity and Temperature Control

The previous section concluded that the optimum half-cycle time is 2.5 mins, the mixing ratio is 100 %, and the airspeed is 0.75 m/s for each adsorber bed. In this section, the effect of adding the evaporative cooler after the DCHE, as shown in Figure 7-8, on the system's

performance for heating applications. This investigation was carried out at various evaporative coolers' water pump flow rates and the air speed of the main fan. The evaporative cooler starts when the room's humidity level reaches the set value of 40% relative humidity.

Figures 7-20 and 7-21 present air temperature and humidity variations over 75 mins, measured at different points in an experimental facility, namely: after the DCHE, after the evaporative cooler, the room and the ambient temperature. Figure 7-20 shows the temperature variation during the first 35 mins of the heating process, representing the initialization of the room in this period. The yellow line represents the room temperature, which increased from 15.8°C to 25°C, and the relative humidity dropped from 61% to 31.7%. Afterwards, the two adsorber beds will operate and alternate between adsorption and desorption. The room temperature reaches 26°C, and the relative humidity is 41.6% at the time of 54 minute, and then the evaporative cooler starts to cool down the room temperature to 24°C and increases the room relative humidity level to 55-60% as shown in figure 7-20. This controlling method allows the temperature and the relative humidity levels to be controlled independently based on the amount of MOF-303/G material for each adsorber bed and the amount of water sprayed in the wet media of the evaporative cooler under the same main airspeed. From 0 to 15 mins, the system activated the two adsorber beds.

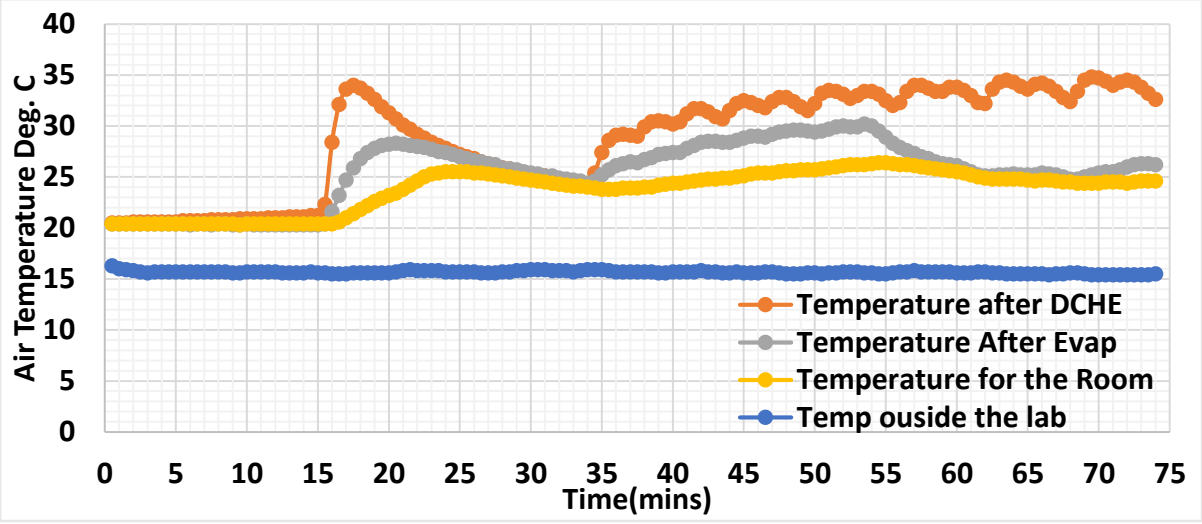



*Figure 7-20: Air temperature change for a dynamic cycle for the desiccant air-conditioning system for heating.*

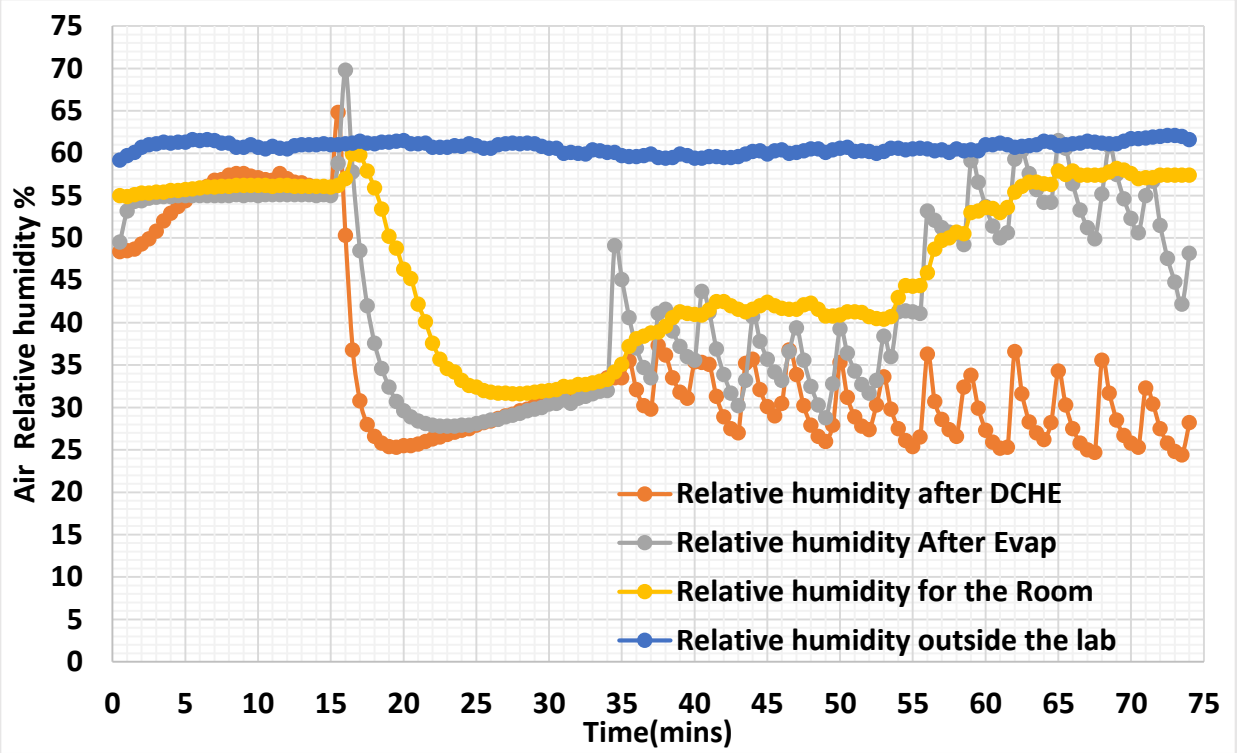



*Figure 7-21: Air relative humidity change for a dynamic cycle for the desiccant air-conditioning system for heating.*

### 7.2.3. Impact of Varying Water Flow Rates in the Evaporative Cooler Pump on System Performance

Figures 7-22 and 7-23 present the temperature variation of various locations in the test facility, namely after the DCHE, after the evaporative cooler, inside the room and the ambient with a pump water flow rate of 5ml/s, an airspeed of 1.5m/s, and a cyclic half-cycle time of 2.5 mins over 40 mins. The ambient air temperature is 11.7°C, and the relative humidity is 67.1%. In Figure 7-22, the orange line represents the air temperature after DCHE, which increases to 32°C. The results show that the room temperature increases from 22°C to 25°C. After the evaporative cooler was activated at 25°C, the room temperature decreased to about 22.8°C due to the swamp effect.

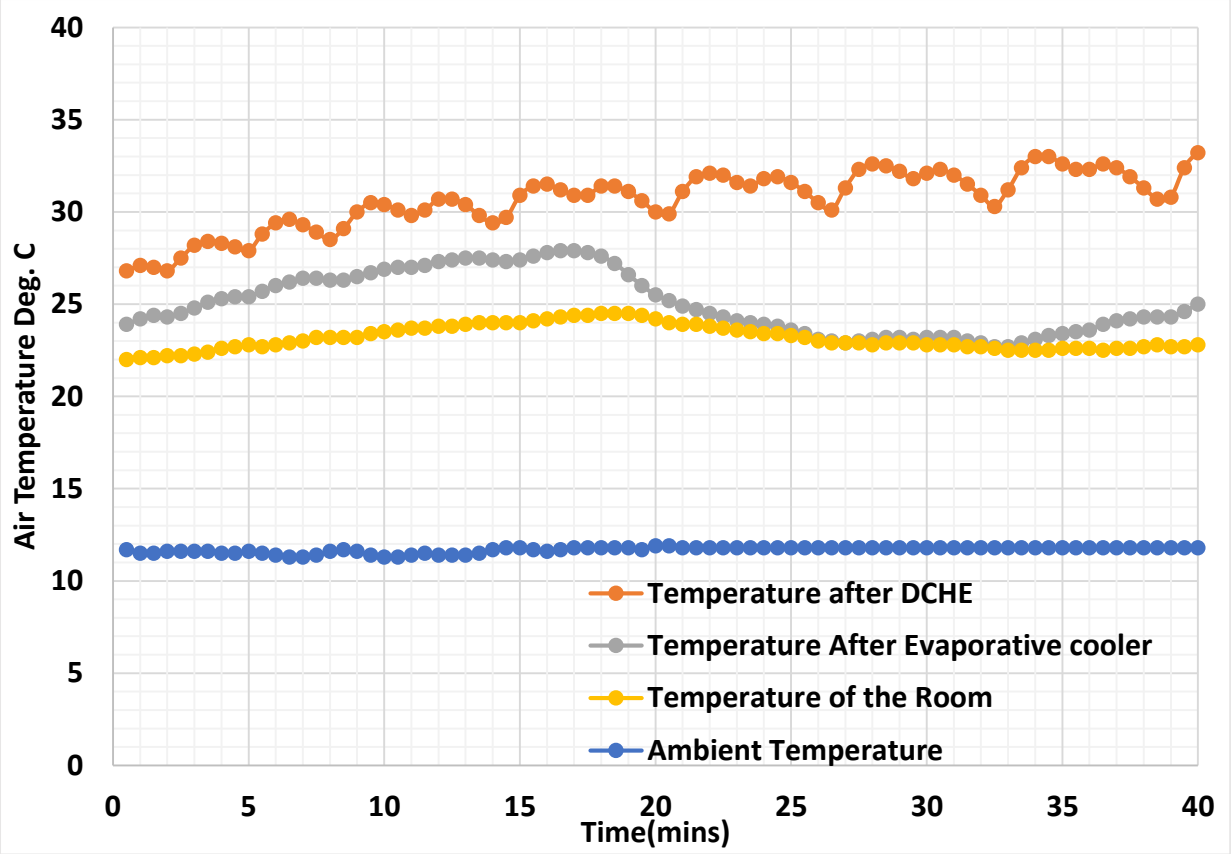



*Figure 7-22: Air temperature variation with time in the desiccant air-conditioning system for heating at a water flow rate of 5ml/s.*

Figure 7-23 shows the variation in the relative humidity where the humidity after the DCHE, as represented by the orange line, varies from 25% at the end of the adsorption process to 35% at the end of the desorption process. The grey line represents the humidity after the evaporative cooler. The room humidity reached 41% in the first 20 mins, but after the evaporative cooler pump is switched on, the room humidity starts to increase, reaching 58%, achieving the comfort condition for humidity. The process is presented on a Psychrometric chart in Figure 7-24. Processes 1-2 are the dehumidification and heating process as air passes through the DCHE, while processes 2-3 are the humidification and cooling process as the air passes through the evaporative cooler. The two processes resulted in heating the ambient air from 11.9°C to 22.8°C while reducing the air relative humidity from 65% to around 58%.

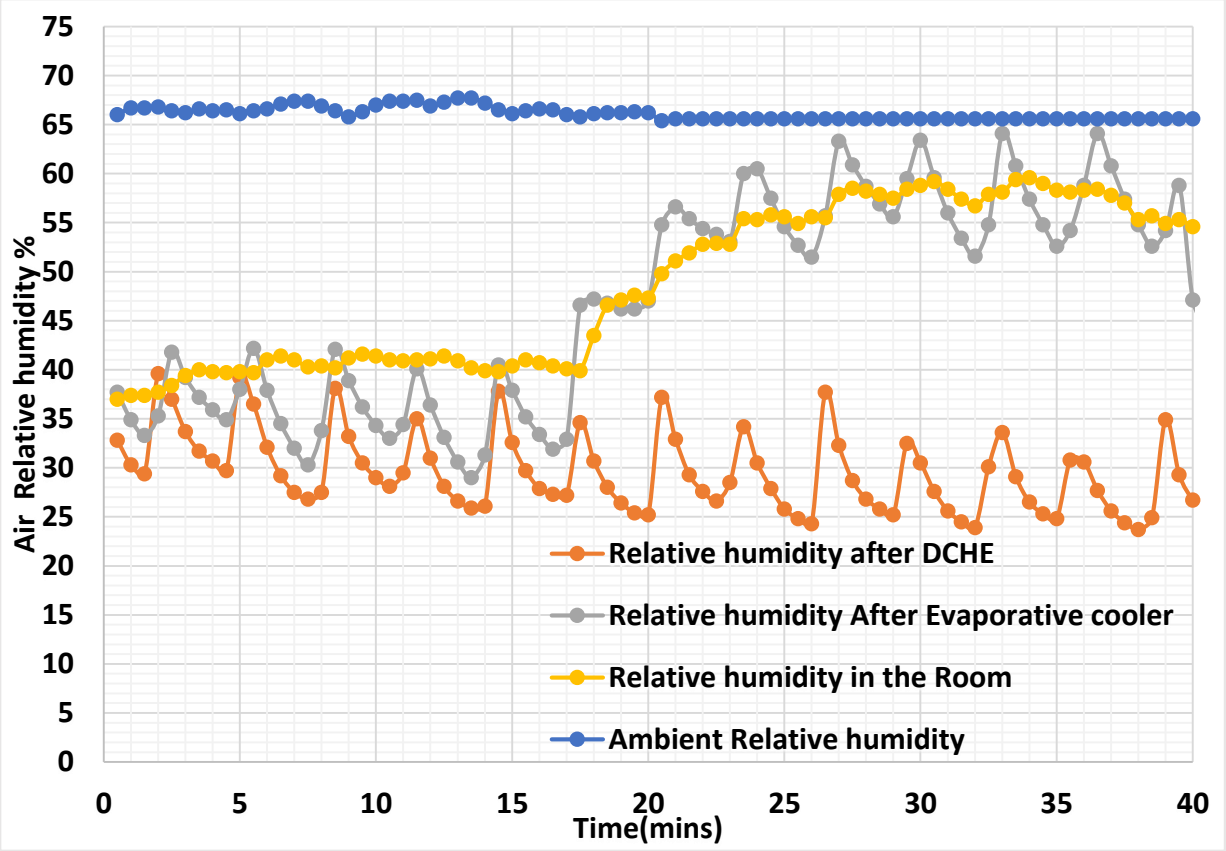



*Figure 7-23: Air relative humidity variation with time in the desiccant air-conditioning system for heating at a water flow rate of 5ml/s.*

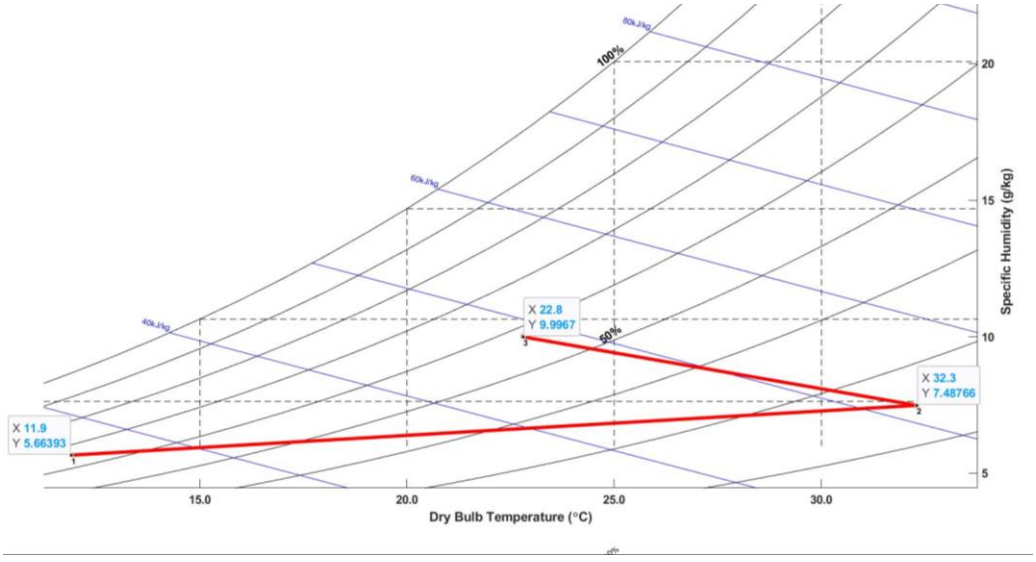



*Figure 7-24: Psychrometric chart of the process in the desiccant air-conditioning system for heating at a water flow rate of 5ml/s at minute 40.*

Figures 7-25 and 7-26 present the air temperature and relative humidity variation with time at various locations in the desiccant air conditioning system for heating application with a pump water flowrate of 10ml/s, an airspeed of 1.5m/s, and the half-cycle time of 2.5 mins over 40 mins. The ambient temperature and relative humidity are 12.7°C and 65%, respectively. In Figure 7-25, the orange line represents the temperature after DCHE varying from 32°C at the end of the adsorption process to 35°C at the end of the desorption process. The results show that the room increases to 25.9°C after 23 minutes. After the evaporative cooler is activated, the room temperature decreases to 23.3°C.

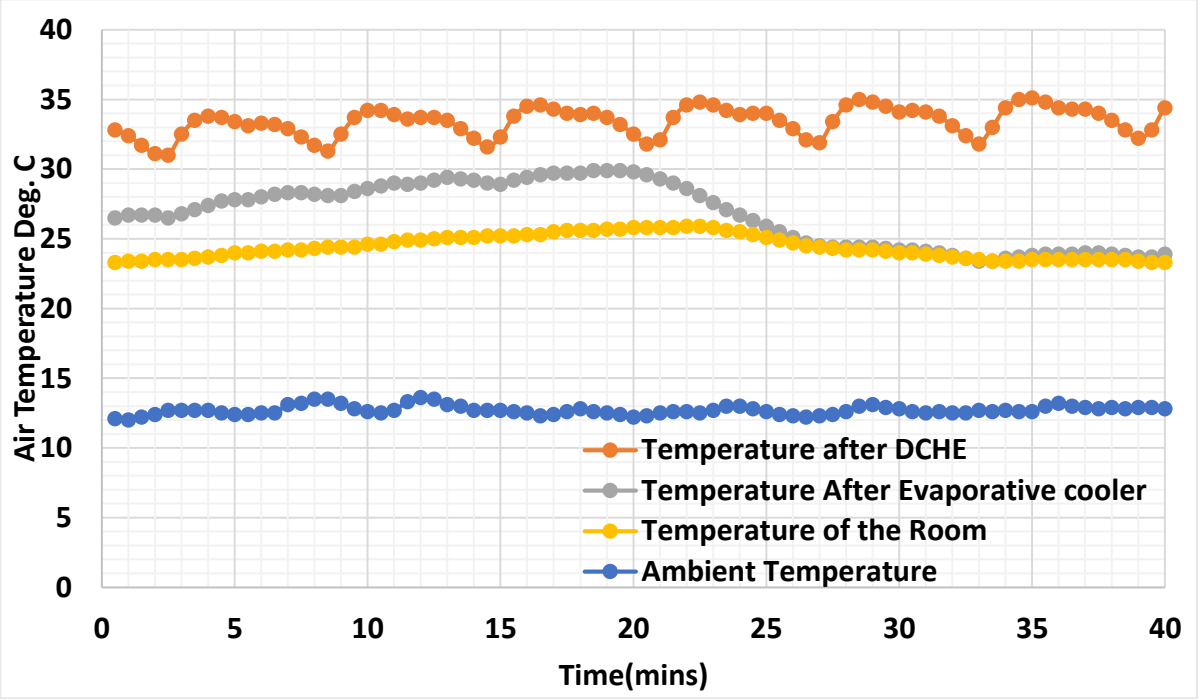



*Figure 7-25: Air temperature variation with time in the desiccant air-conditioning system for heating at a water flow rate of 10ml/s.*

Figure 7-26 shows the variation in the relative humidity where the humidity after the DCHE, as represented by the orange line, changes from 23% at the end of the adsorption process to 30% at the end of the desorption process. The grey line represents the humidity after the evaporative cooler. The room humidity reached 41% in the first 20 mins, but after the evaporative cooler pump is switched on, the room humidity starts to increase, reaching 55%, achieving the comfort condition for humidity. The process is presented on a Psychrometric chart in Figure 7-27. Processes 1-2 are the dehumidification and heating process as air passes through the DCHE, while processes 2-3 are the humidification and cooling process as the air passes through the evaporative cooler. The two processes resulted in heating the ambient air from 12.8°C to 24°C while reducing the air relative humidity from 65% to around 55%.

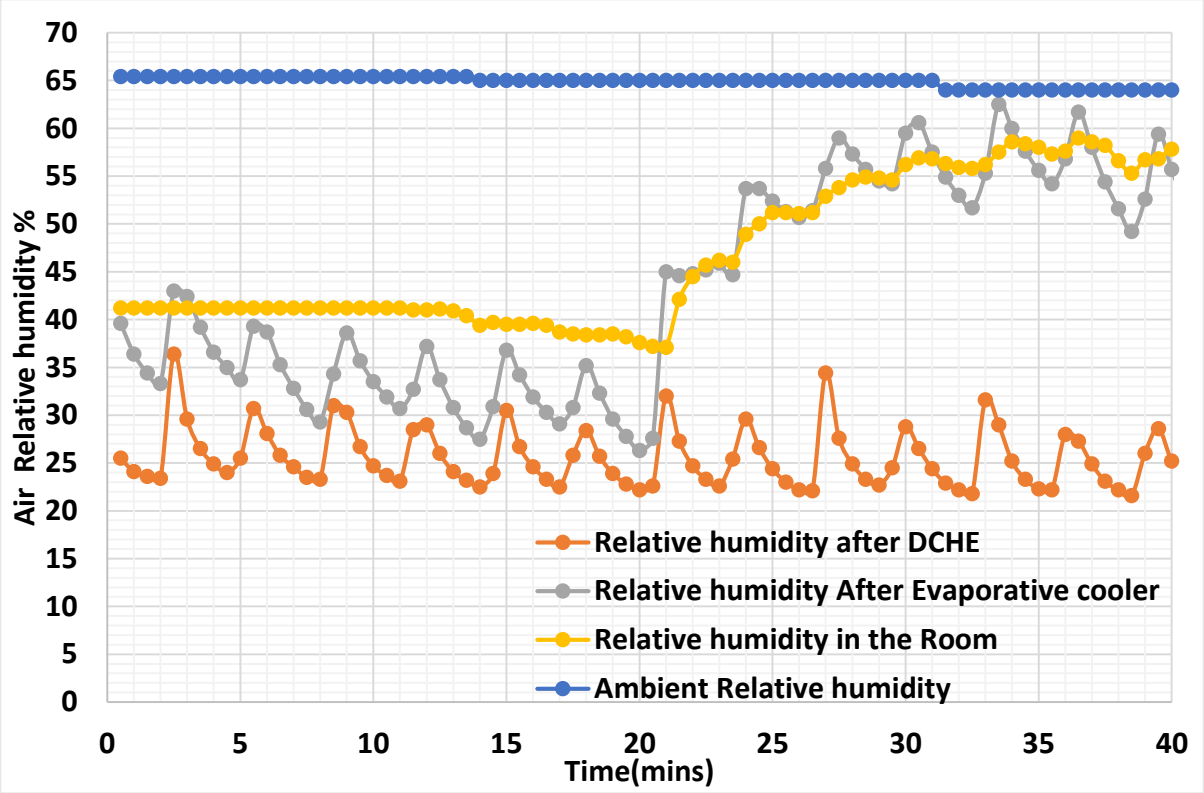



*Figure 7-26: Air relative humidity variation with time in the desiccant air-conditioning system for heating at a water flow rate of 10ml/s.*

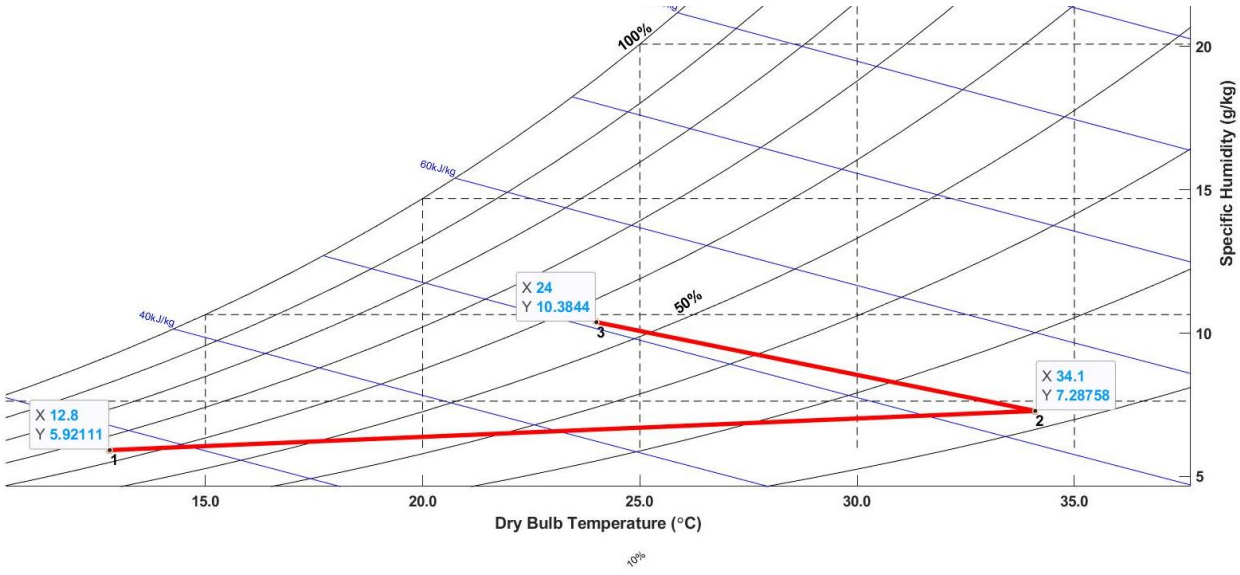



*Figure 7-27: Psychrometric chart of the process in the desiccant air-conditioning system for heating at a water flow rate of 10ml/s at minute 40.*

Figures 7-28 and 7-29 present the air temperature and relative humidity variation with time at various locations in the desiccant air conditioning system for heating application with a pump water flowrate of 15ml/s, an airspeed of 1.5m/s, and the cyclic half-cycle time of 2.5 mins over 40 mins. The ambient air temperature and relative humidity are 13.3°C and 62%, respectively. In Figure 7-28, the orange line represents the temperature after DCHE varying from 32°C at the end of the adsorption process to 36°C at the end of the desorption process. The results show that the room increases to 25.9°C after 18 minutes. After the evaporative cooler is activated, the room temperature decreased to 23.7°C.

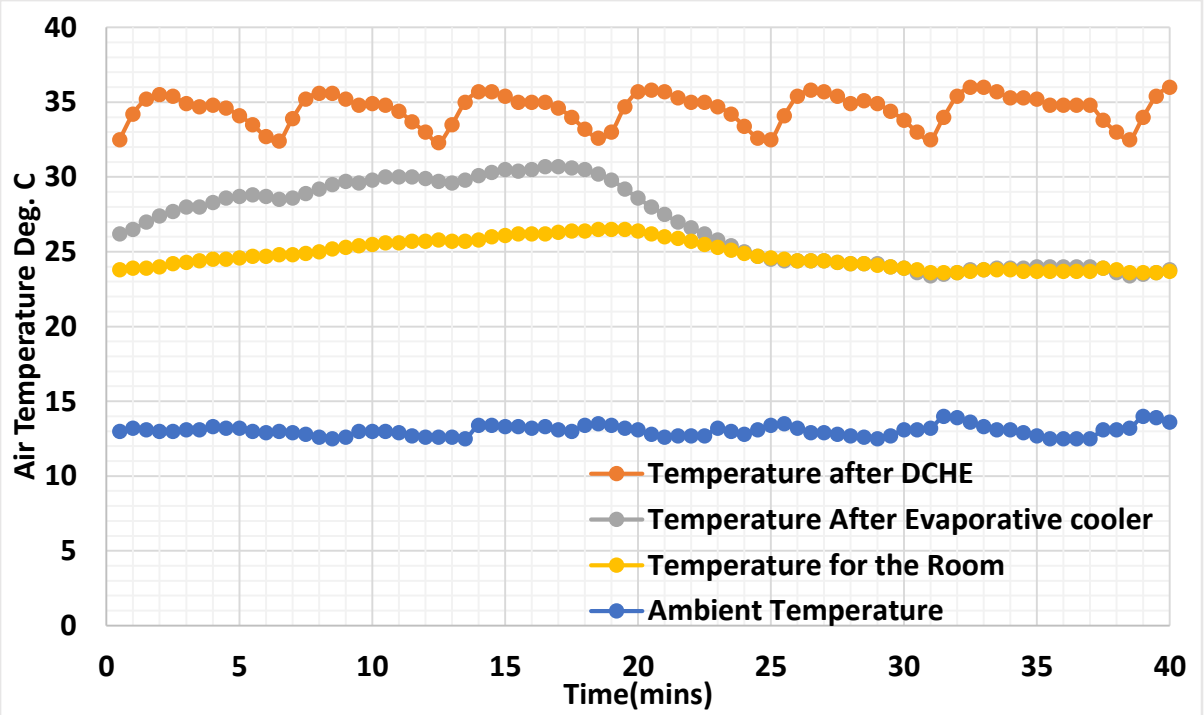



*Figure 7-28: Air temperature variation with time in the desiccant air-conditioning system for heating at a water flow rate of 15ml/s.*

Figure 7-29 shows the variation in the relative humidity where the humidity after the DCHE, as represented by the orange line, changes from 20.8% at the end of the adsorption process to 28% at the end of the desorption process. The grey line represents the humidity after the evaporative cooler. The room humidity reached 37% in the first 20 mins, but after the evaporative cooler pump is switched on, the room humidity starts to increase, reaching 57%, achieving the comfort condition for humidity. The process is presented on a Psychrometric chart in Figure 7-30. Processes 1-2 are the dehumidification and heating process as air passes through the DCHE, while processes 2-3 are the humidification and cooling process as the air

passes through the evaporative cooler. The two processes resulted in heating the ambient air from 13.1°C to 23.9°C while reducing the air relative humidity from 62% to around 57%.

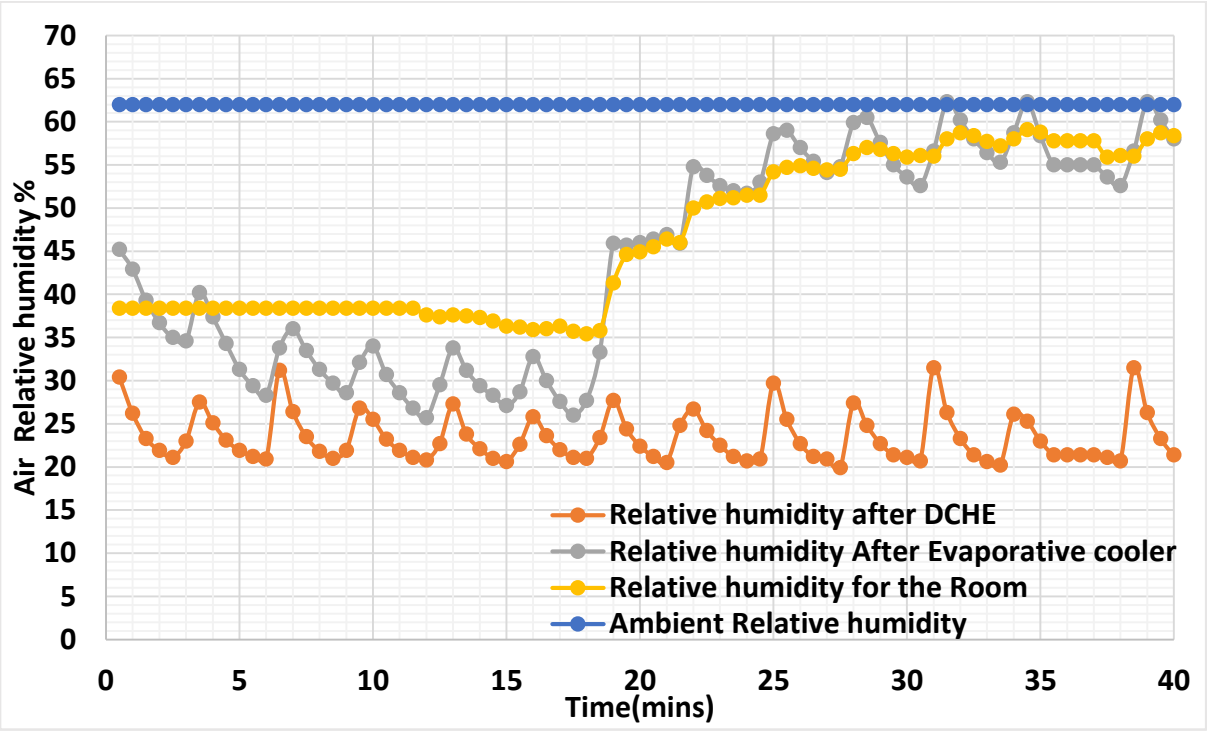



*Figure 7-29: Air relative humidity variation with time in the desiccant air-conditioning system for heating at a water flow rate of 15ml/s.*

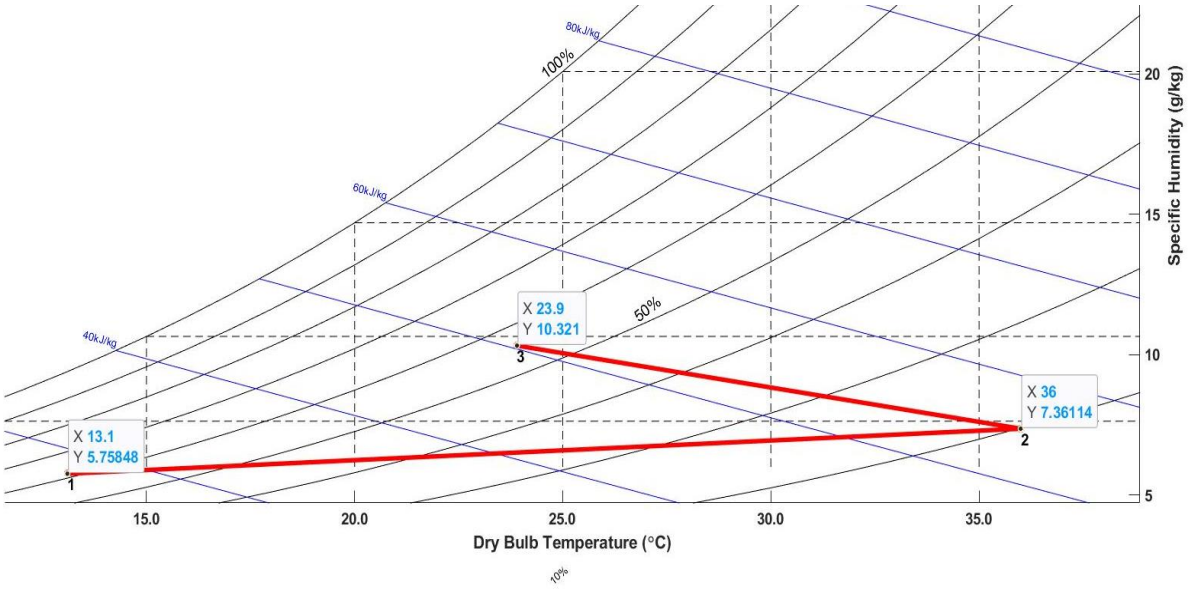



*Figure 7-30: Psychrometric chart of the process in the desiccant air-conditioning system for heating at a water flow rate of 15ml/s at minute 40.*

Figure 7-31 represents the COP of the system at different water flow rates in the evaporative cooler, and it is seen that 10ml/s produced the highest COP of 0.9781, which outperforms the 5 and 15 ml/s.

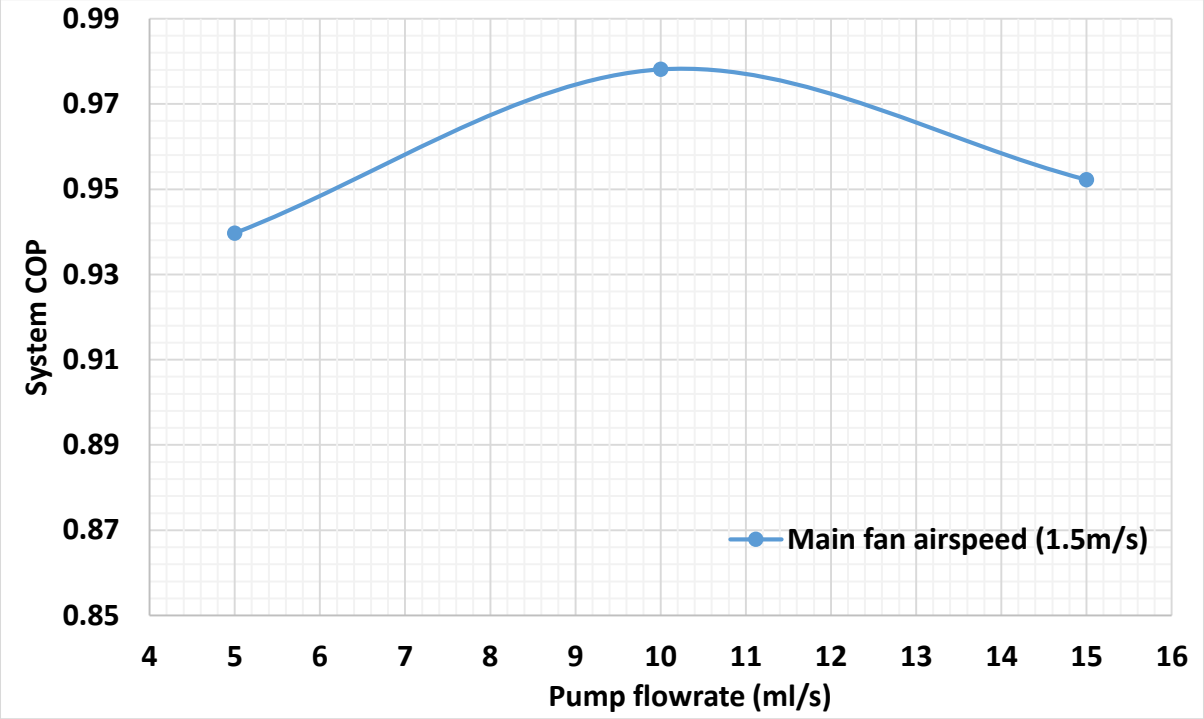



*Figure 7-31: Coefficient of Performance (COP) versus water flow rate for 5, 10, and 15ml/s.*

Figures 7-32 and 7-33 present the air temperature and relative humidity variation with time at various locations in the desiccant air conditioning system for heating application with a pump water flowrate of 5ml/s, an airspeed of 3.5m/s, and the cyclic half-cycle time of 2.5 mins over 40 mins. The ambient air temperature and relative humidity are 14°C and 55.5%, respectively. In Figure 7-32, the orange line represents the temperature after DCHE varying from 25°C at the end of the adsorption process to 29°C at the end of the desorption process. The results show that the room increases to 25.6°C after 20 minutes. After the evaporative cooler is activated, the room temperature decreased to 23.7°C lower than the previous case, as shown in Figure7-29 by 1.2°C.

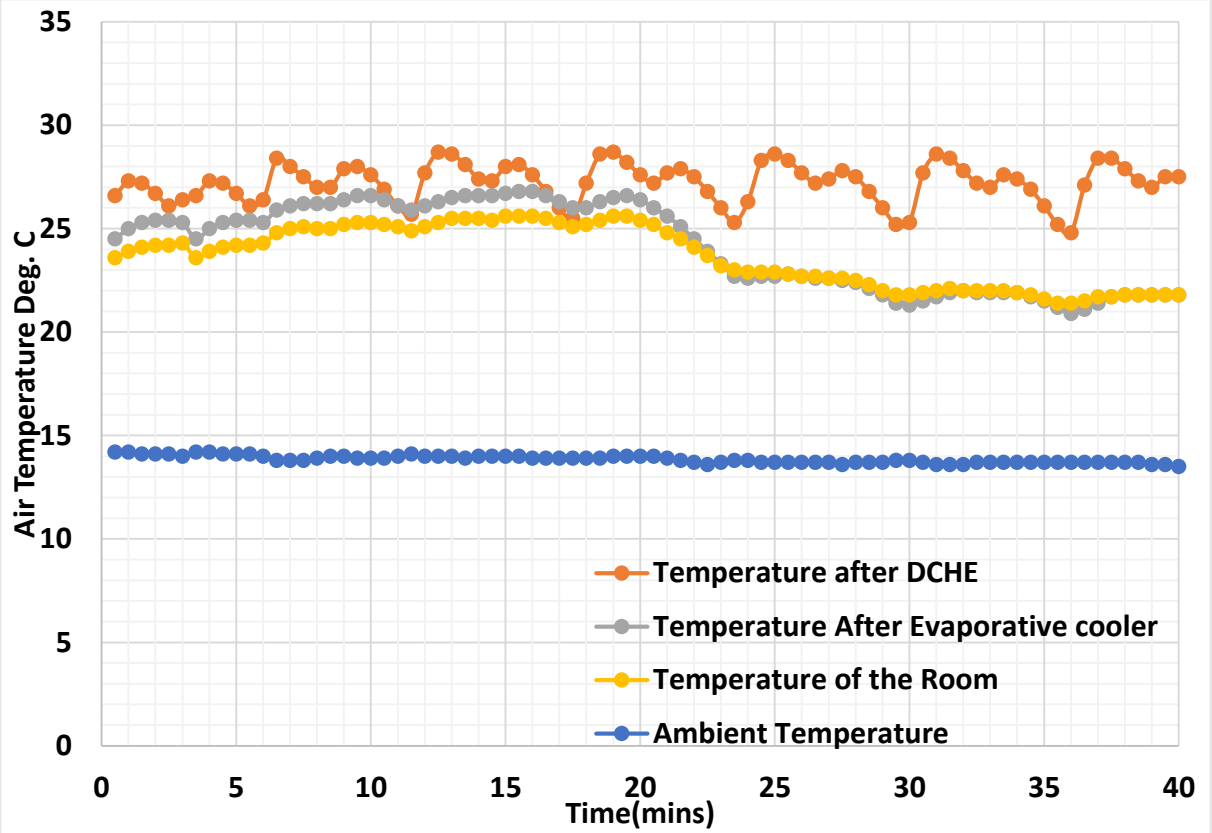



*Figure 7-32: Air temperature variation with time in the desiccant air-conditioning system for heating at a water flow rate of 5ml/s.*

Figure 7-33 shows the variation in the relative humidity where the humidity after the DCHE, as represented by the orange line, changes from 25.9% at the end of the adsorption process to 33% at the end of the desorption process. The grey line represents the humidity after the evaporative cooler. The room humidity reached 29% in the first 20 mins, but after the evaporative cooler pump is switched on, the room humidity increases, reaching 52%, achieving the comfort condition for humidity. The process is presented on a Psychrometric chart in Figure 7-34. Processes 1-2 are the dehumidification and heating process as air passes through the DCHE, while processes 2-3 are the humidification and cooling process as the air passes through the evaporative cooler. The two processes resulted in heating the ambient air from 14°C to 21.9°C while reducing the air relative humidity from 55% to around 52%.

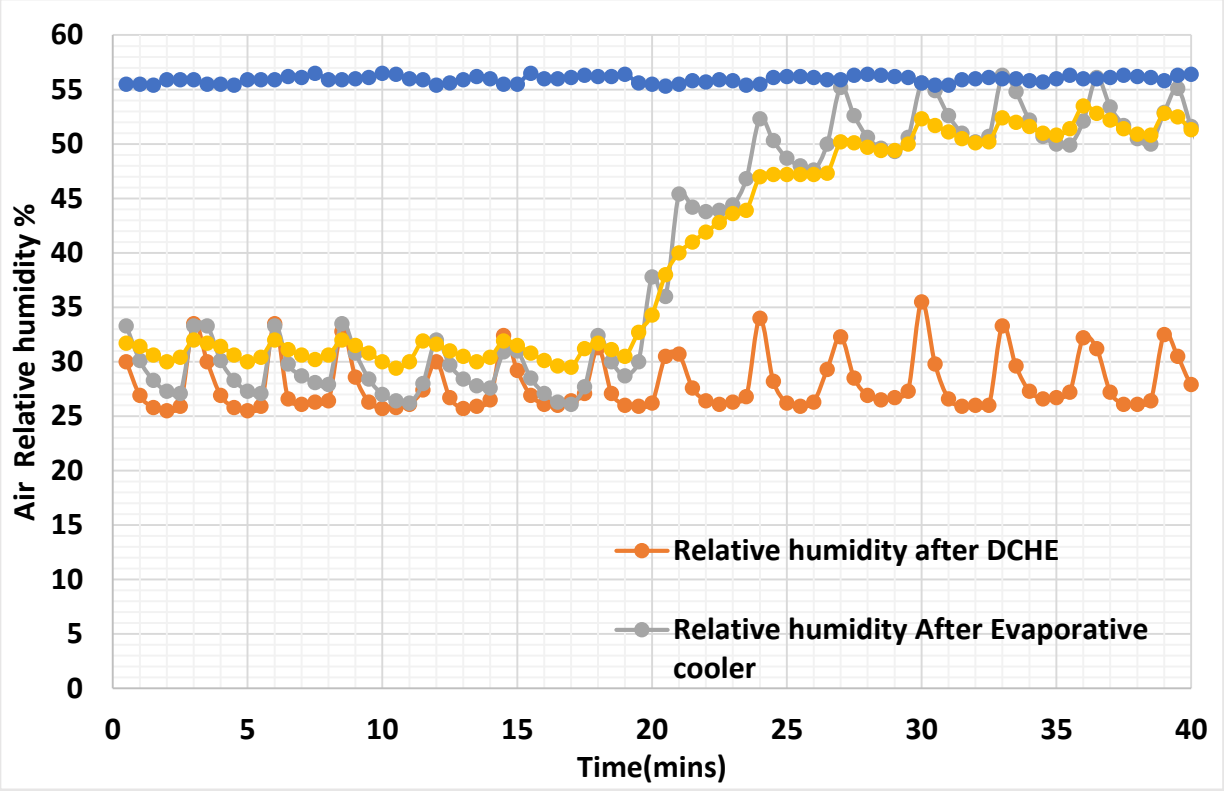



*Figure 7-33: Air relative humidity variation with time in the desiccant air-conditioning system for heating at a water flow rate of 5ml/s.*

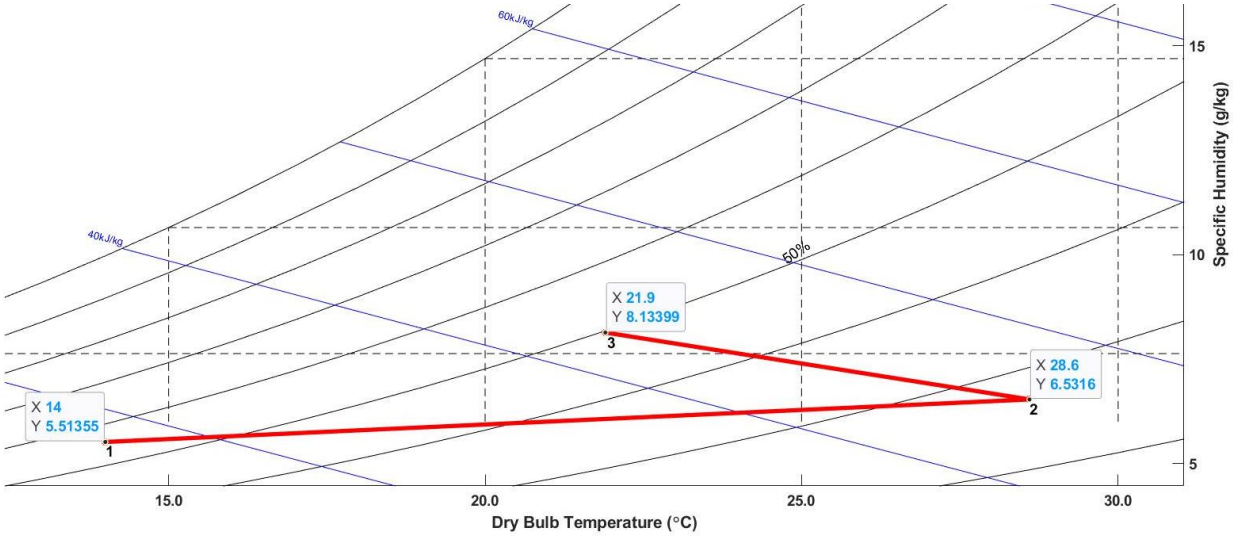



*Figure 7-34: Psychrometric chart of the process in the desiccant air-conditioning system for heating at a water flow rate of 5ml/s at minute 40.*

Figures 7-35 and 7-36 present the air temperature and relative humidity variation with time at various locations in the desiccant air conditioning system for heating application with a pump water flowrate of 10ml/s, an airspeed of 3.5m/s, and the cyclic half-cycle time of 2.5

mins over 40 mins. The ambient air temperature and relative humidity are 13.7°C and 56.3%, respectively. In Figure 7-35, the orange line represents the temperature after DCHE varying from 24°C at the end of the adsorption process to 28.2°C at the end of the desorption process. The results show that the room temperature increases to 24.6°C after 20 minutes. After the evaporative cooler is activated, the room temperature decreased to 20.6°C.

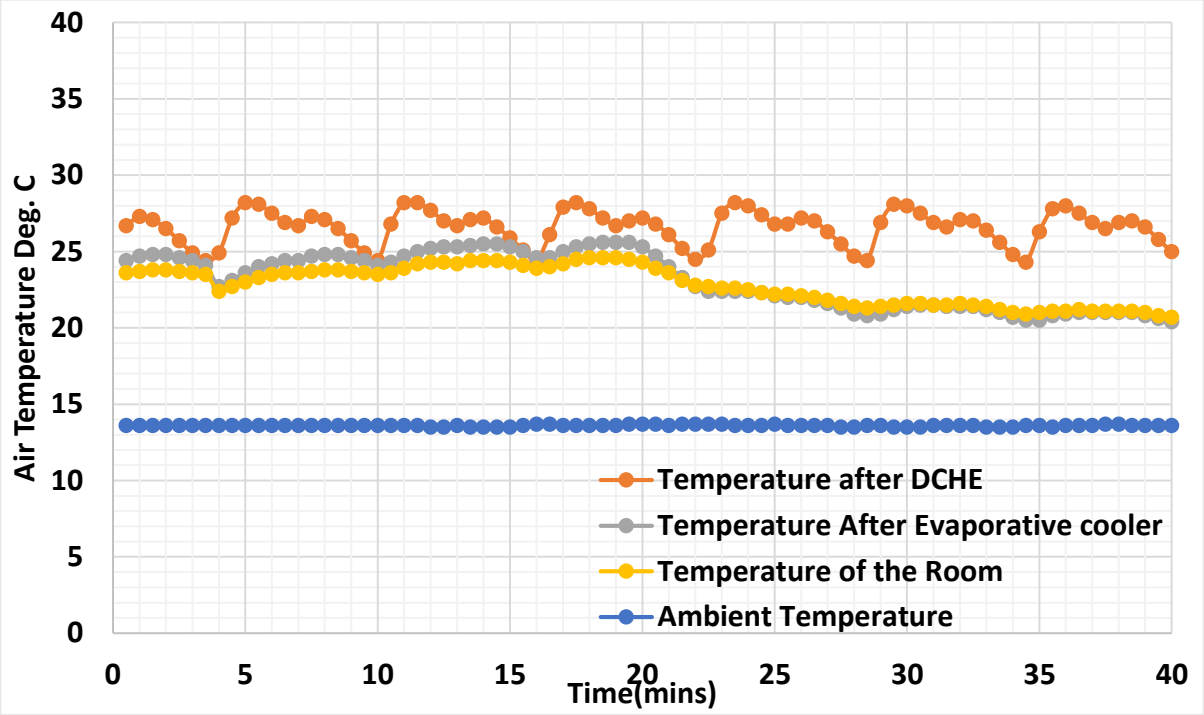



*Figure 7-35: Air temperature variation with time in the desiccant air-conditioning system for heating at a water flow rate of 10ml/s.*

Figure 7-36 shows the variation in the relative humidity where the humidity after the DCHE, as represented by the orange line, changes from 26.4% at the end of the adsorption process to 33.8% at the end of the desorption process. The grey line represents the humidity after the evaporative cooler. The room humidity reached 37% after the 20 mins, but after the evaporative cooler pump is switched on, the room humidity starts to increase, reaching 53.1%, achieving the comfort condition for humidity. The process is presented on a Psychrometric chart in Figure 7-37. Processes 1-2 are the dehumidification and heating process as air passes through the DCHE, while processes 2-3 are the humidification and cooling process as the air passes through the evaporative cooler. The two processes resulted in heating the ambient air from 13.6°C to 21.9°C while reducing the air relative humidity from 55% to around 53.1%.

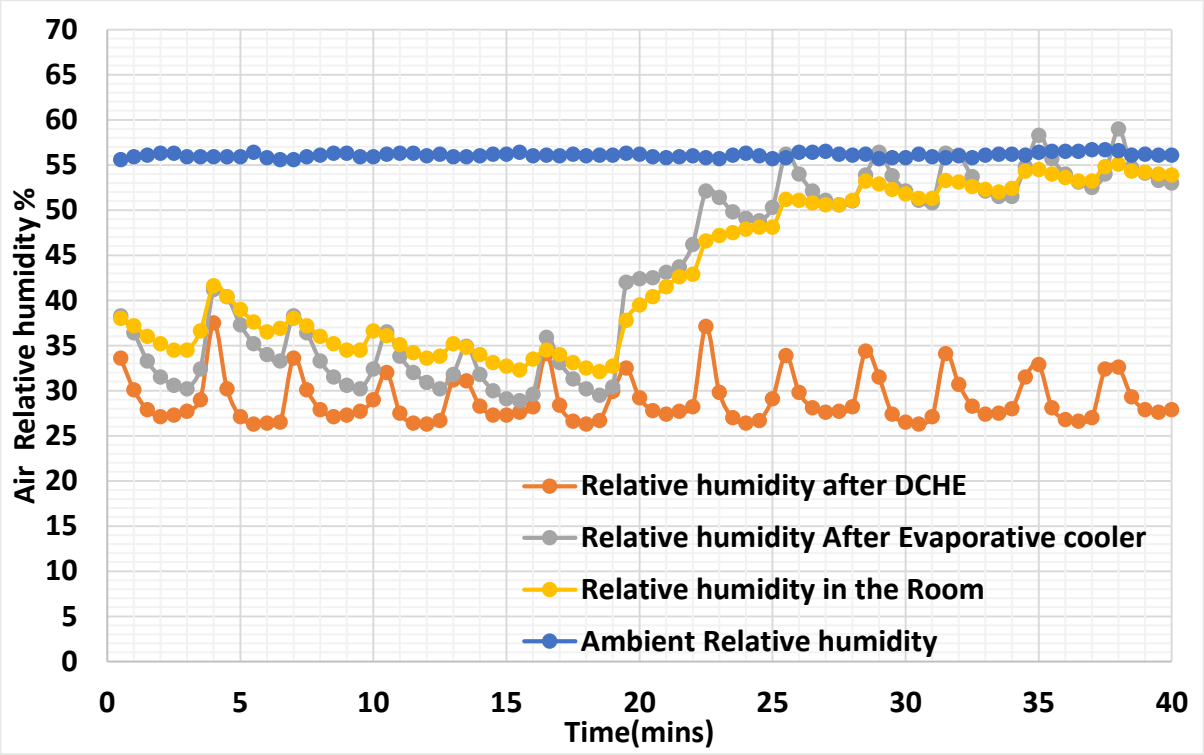



*Figure 7-36: Air relative humidity variation with time in the desiccant air-conditioning system for heating at a water flow rate of 10ml/s.*

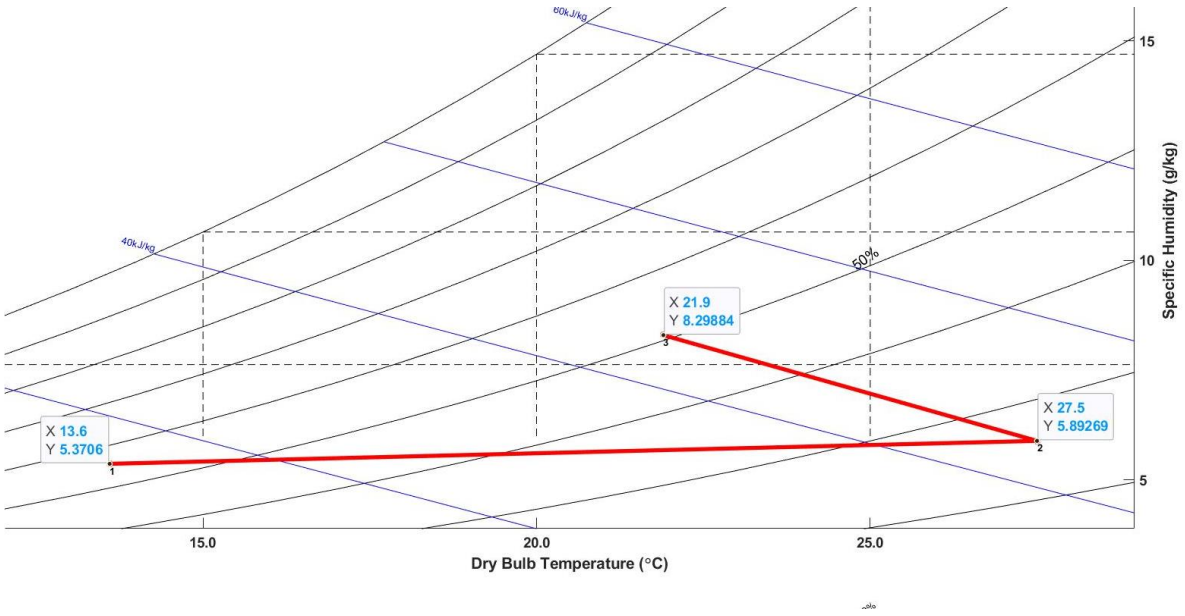



*Figure 7-37: Psychrometric chart of the process in the desiccant air-conditioning system for heating at a water flow rate of 10ml/s at minute 40.*

Figures 7-38 and 7-39 present the air temperature and relative humidity variation with time at various locations in the desiccant air conditioning system for heating application with a pump water flowrate of 15ml/s, an airspeed of 3.5m/s, and the cyclic half-cycle time of 2.5

mins over 40 mins. The ambient air temperature and relative humidity are 13.7°C and 62%, respectively. In Figure 7-38, the orange line represents the temperature after DCHE varying from 24°C at the end of the adsorption process to 28.2°C at the end of the desorption process. The results show that the room increases to 24.1°C after 20 minutes. After the evaporative cooler is activated, the room temperature decreased to 20.4°C.

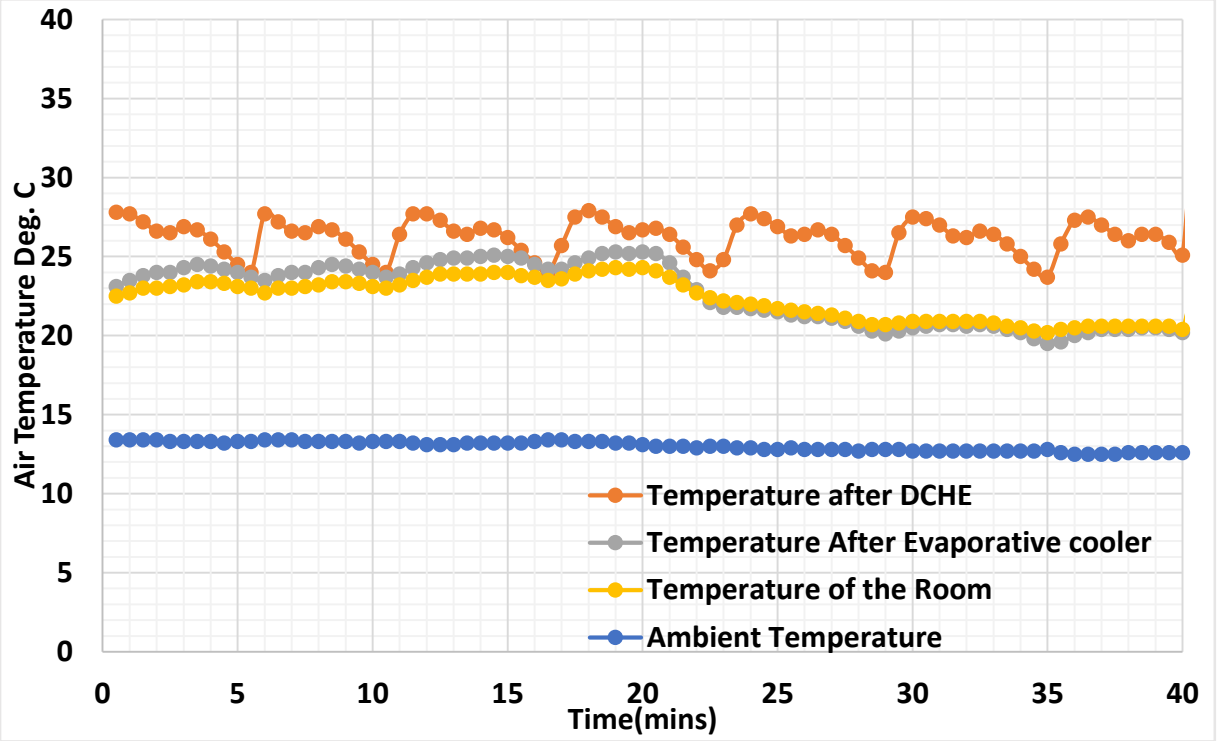



*Figure 7-38: Air temperature variation with time in the desiccant air-conditioning system for heating at a water flow rate of 15ml/s.*

Figure 7-39 shows the change in the relative humidity. The humidity after the DCHE is 27.7%, represented by the orange line, consistent throughout the process. The grey line represents the humidity after the evaporative cooler. The room humidity is settled in the first 20 mins at 35.8%; after the evaporative cooler pump is switched on, the room humidity starts to increase, reaching 56.1%, achieving the comfort condition for humidity after 5 mins of operation. The process is presented on a Psychrometric chart in Figure 7-40. Processes 1-2 are the dehumidification and heating process as air passes through the DCHE, while processes 2-3 are the humidification and cooling process as the air passes through the evaporative cooler. The two processes resulted in heating the ambient air from 12.7°C to 21°C while reducing the air relative humidity from 63.9% to around 56.1%.

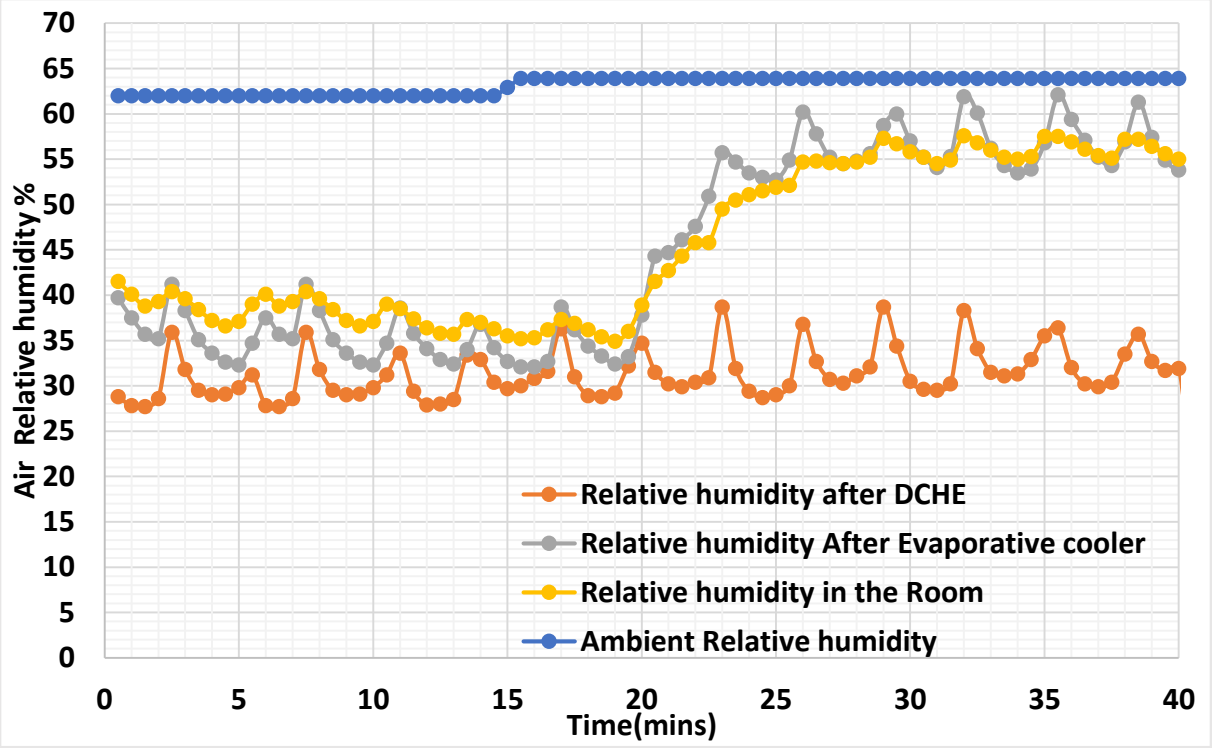



*Figure 7-39: Air relative humidity variation with time in the desiccant air-conditioning system for heating at a water flow rate of 15ml/s.*

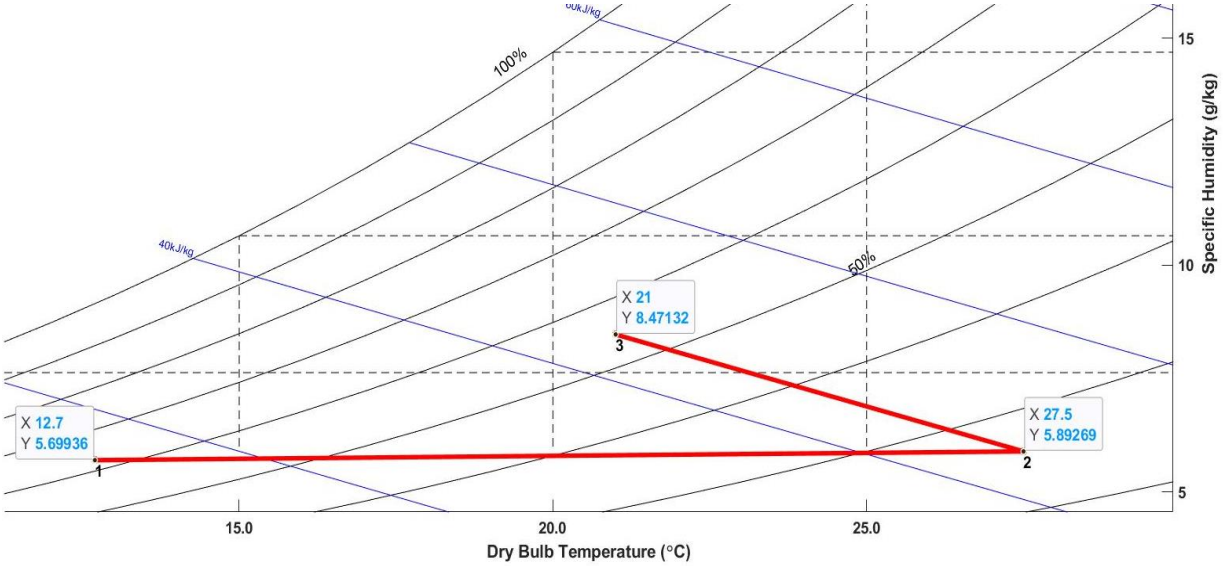



*Figure 7-40: Psychrometric chart of the process in the desiccant air-conditioning system for heating at a water flow rate of 15ml/s at minute 40.*

Figure 7-41 represents the COP of the system after applying different flow rates for the evaporative cooler, and it is seen that 5ml/s produces the highest COP, achieving 0.873, which outperformed the 10 and 15 ml/s.

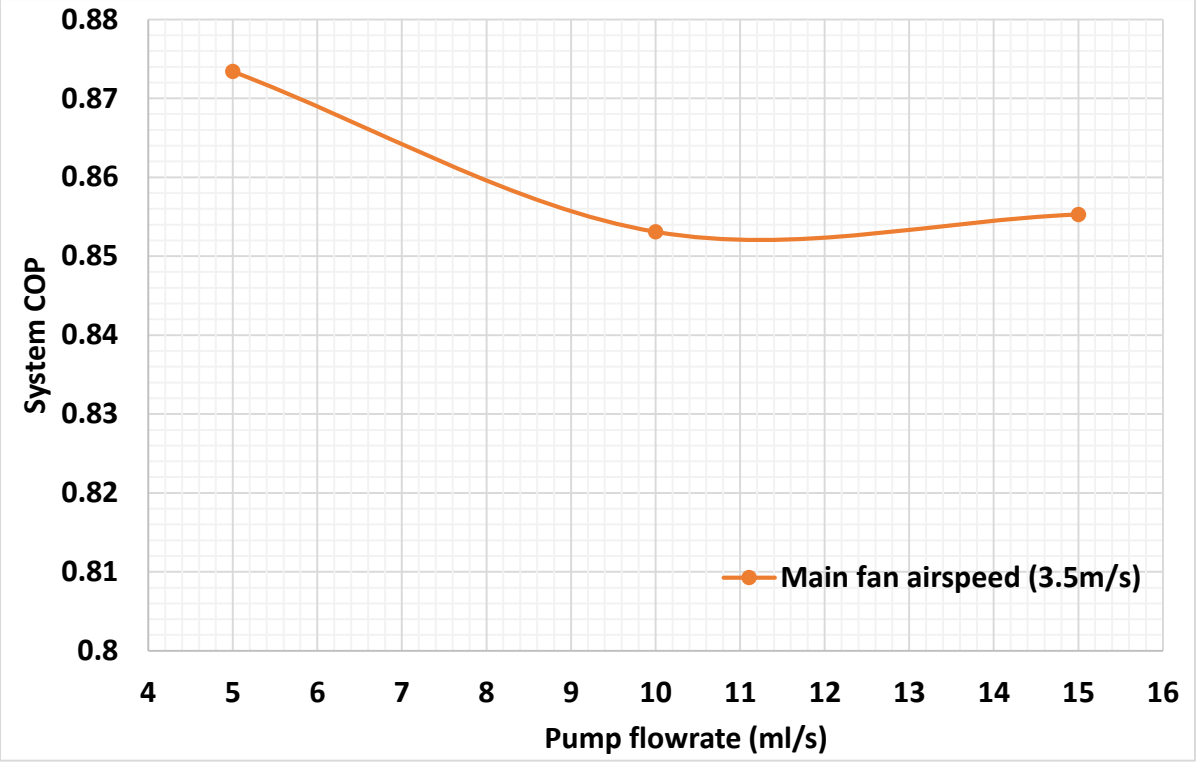



*Figure 7-41: Coefficient of Performance (COP) versus water flow rate for 5, 10, and 15ml/s.*

In conclusion, the results showed that the evaporative cooler combined with the desiccant-coated heat exchanger could heat the incoming air temperature and control the humidity level independently.

## 7.3. Desiccant air conditioning system for cooling

Figure 7-42 illustrates a system for conditioning humid air from a room using a combination of two desiccant-coated heat exchangers, an air-to-water heat exchanger, and a direct evaporative cooler. Humid air enters the system and is switched between two desiccant-coated heat exchangers, DCH1 and DCH2, where it is dehumidified, resulting in low humidity and high-temperature air. This air then passes through an air-to-water heat exchanger, where it transfers the heat to the water and cools down. The cooled air subsequently flows through a direct evaporative cooler, further reducing its temperature while maintaining low humidity if needed. Finally, the conditioned air, characterized by low temperature and low humidity, is recirculated back into the room controlled by a variable speed fan to ensure optimal room conditions. The system operates in an environment with conditions of 30 °C and 90% relative humidity.

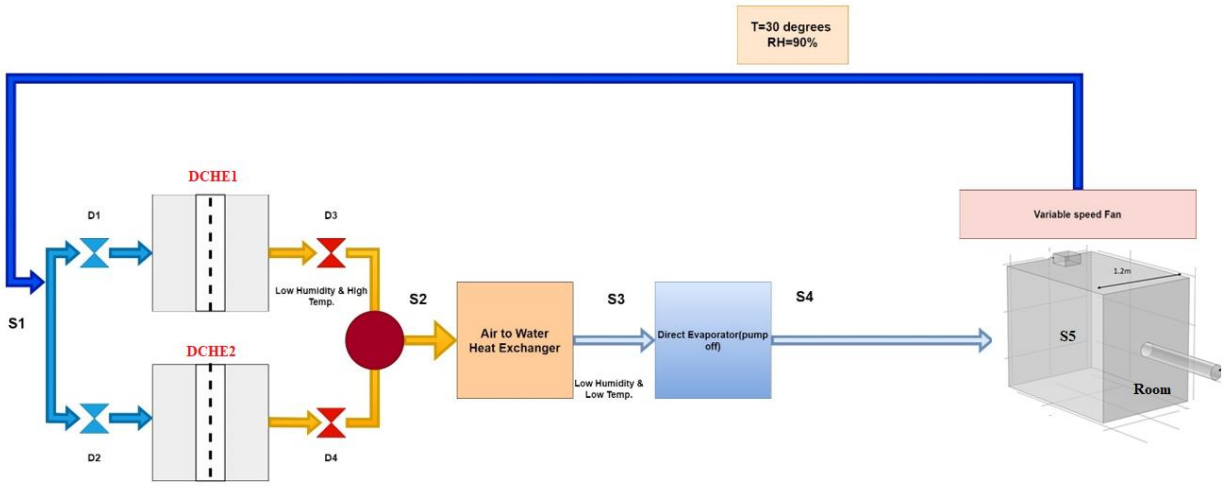



*Figure 7-42: Desiccant cooling system with temperature and humidity Sensors positions.*

### 7.3.1. Effect of air to water HE inlet water temperature on controlling the air relative humidity and the temperature level

Figure 7-43 illustrates the temperature variation with time at different positions in the desiccant air conditioning system for cooling applications over 20 mins, including the temperatures before the DCHE, after the DCHE, inside the room, and after the air-to-water heat exchanger. Initially, the temperature before the DCHE starts at around 31°C, indicating the condition of the incoming air from the room. The air temperature after the DCHE starts at 36.6°C and increases to approximately 40°C, peaking around 2.5 mins before gradually decreasing as the system stabilizes. Inside the room, the temperature starts at the peak of around 37°C, representing the artificial initial condition before any cooling effects from the system components start. This peak temperature decreases as the system operates, influenced by the circulated conditioned air. After passing through the air-to-water heat exchanger, the air temperature starts to cool down at around 20°C and continues cooling slightly, indicating the efficiency of the heat exchange process. The room temperature is settled at 23°C. Notably, the system undergoes a half-cycle time at the 10-mins mark, potentially for desiccant regeneration or operational adjustments. The tap water feeding the air-to-water heat exchanger is maintained at 18°C, providing a cooling effect that helps maintain a controlled room environment. The evaporative cooler pump is switched off because the level of humidity in this case is high due to the sensible cooling.

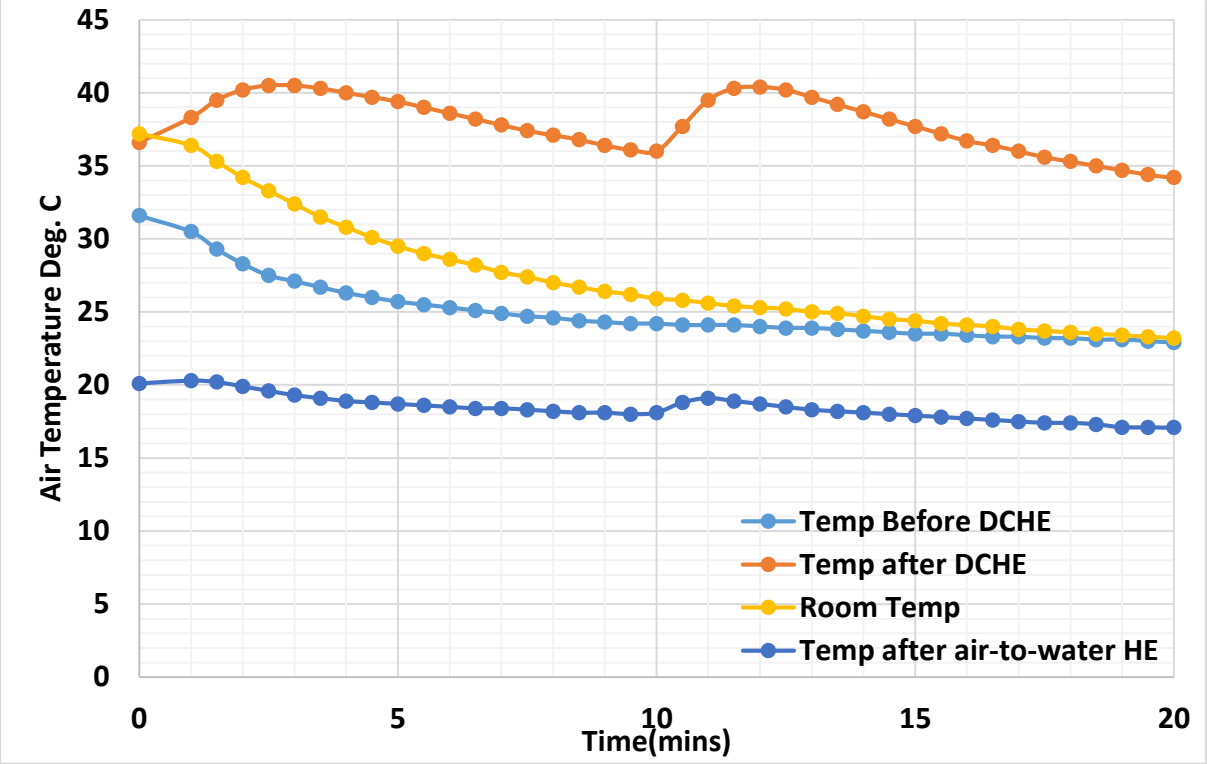



*Figure 7-43: Air temperature variation with time in the desiccant air-conditioning system for cooling at water inlet temperature of 18°C and half-cycle time 10mins.*

Figure 7-44 shows the variation of air relative humidity (RH) with time at different positions in the desiccant air conditioning system for a cooling system over 20 mins, including the humidity measurements before the DCHE, after the DCHE, inside the room, and after the air-to-water heat exchanger. The initial relative humidity before the DCHE is high, of around 95%, indicating the humid condition of the incoming air. This value drops sharply to around 80% within the first few minutes, stabilizing around 66.5% for the remainder of the period, demonstrating the effectiveness of the DCHE in moisture removal. After the DCHE, the relative humidity drops significantly to around 30%, indicating a substantial reduction in moisture content due to the desiccant's adsorption capacity. A notable spike to around 50% at the 10-mins mark, which corresponds with the system's half-cycle time, suggests a temporary increase in humidity, possibly due to the switching moment. This is followed by a reduction to approximately 35%. The room's relative humidity starts around 80%, representing the initial condition before the system's intervention. First, the room air's relative humidity increased artificially to 90%; as the system operates, the RH gradually decreases to around 60%, showing the impact of the conditioned air in maintaining a more controlled and less humid environment. Finally, the specific humidity after the water heat

exchanger remains stable, slightly above 12.325g/kg(d.a), indicating consistent performance in maintaining the desired humidity level.

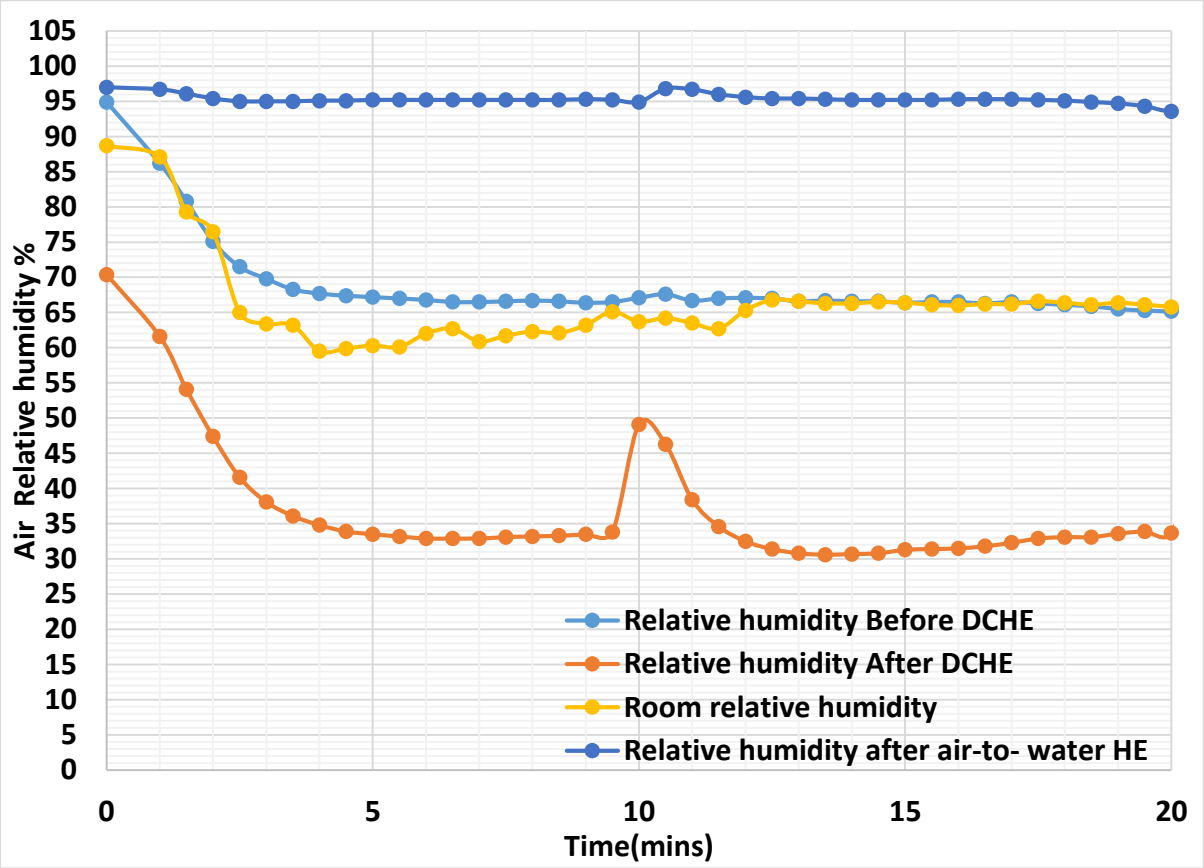



*Figure 7-44: Air humidity variation with time in the desiccant air-conditioning system for cooling at water inlet temperature of 18°C and half-cycle time 10mins.*

Figure 7-45 illustrates the temperature variation with time at different positions in the desiccant air conditioning system for cooling applications over 20 mins, including the temperatures before the DCHE, after the DCHE, inside the room, and after the air-to-water heat exchanger. Initially, the temperature before the DCHE starts at around 27.6°C, indicating the condition of the incoming air from the room. The air temperature after the DCHE starts at 40.8°C, increases to approximately 41.5°C, peaking around 2.5 mins before gradually decreasing as the system stabilizes. Inside the room, the temperature starts at the peak of around 34.1°C, representing the artificial initial condition before any cooling effects from the system components. This peak temperature decreases as the system operates, influenced by the circulated conditioned air. After passing through the air-to-water heat exchanger, the air temperature starts to cool down at around 18.5°C and continues cooling slightly, indicating the efficiency of the heat exchange process. The room temperature is settled at 22.8°C. Notably, the system undergoes a half-cycle time at the 5-mins mark, potentially for desiccant

regeneration or operational adjustments. The tap water feeding the air-to-water heat exchanger is maintained at 18°C, providing a cooling effect that helps maintain a controlled room environment. The evaporative cooler pump is switched off because the level of humidity in this case is high due to the sensible cooling.

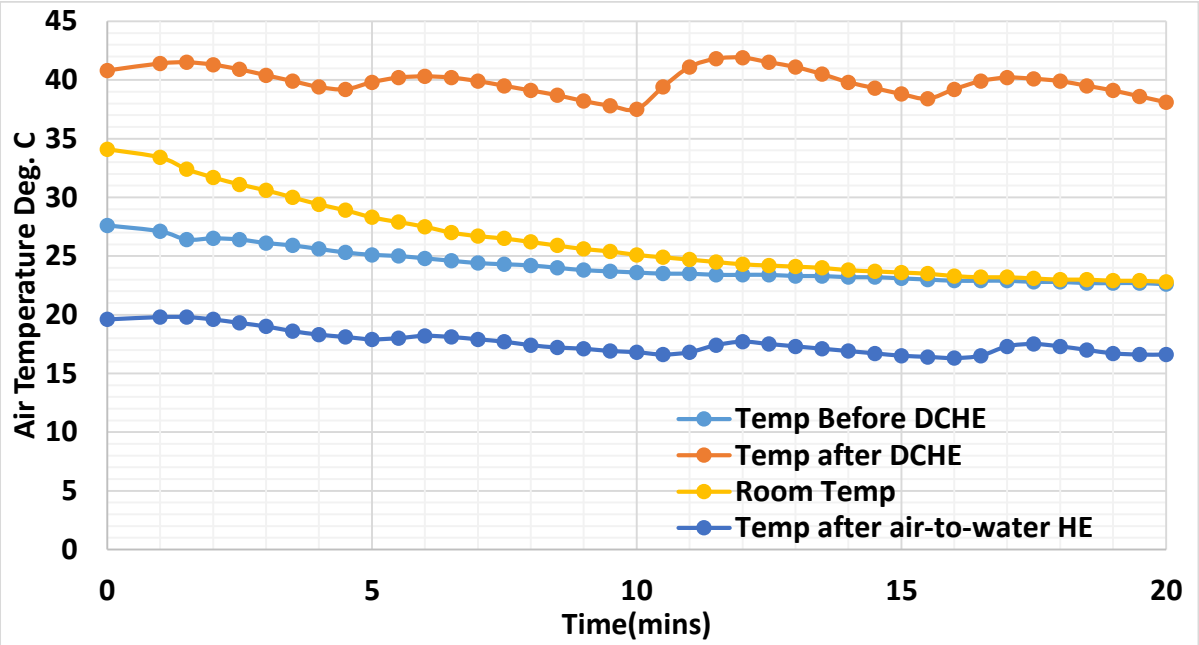



*Figure 7-45: Air temperature variation with time in the desiccant air-conditioning system for cooling at water inlet temperature of 18°C and half-cycle time 5mins.*

Figure 7-46 shows the variation of air relative humidity (RH) with time at different positions in the desiccant air conditioning system for a cooling system over 20 mins, including the humidity measurements before the DCHE, after the DCHE, inside the room, and after the air-to-water heat exchanger. The initial relative humidity before the DCHE is high, of around 95%, indicating the humid condition of the incoming air. This value drops sharply to around 80% within the first few minutes, stabilizing around 65% for the remainder of the period, demonstrating the effectiveness of the DCHE in moisture removal. After the DCHE, the relative humidity drops significantly to around 30%, indicating a substantial reduction in moisture content due to the desiccant's adsorption capacity. A notable spike to around 50% at the 5-mins mark, which corresponds with the system's half-cycle time, suggests a temporary increase in humidity, possibly due to the switching moment. This is followed by a reduction to approximately 35%. The room air's initial relative humidity is 95%; as the system operates, the RH gradually decreases to around 63%, showing the impact of the conditioned air in maintaining a more controlled and less humid environment.

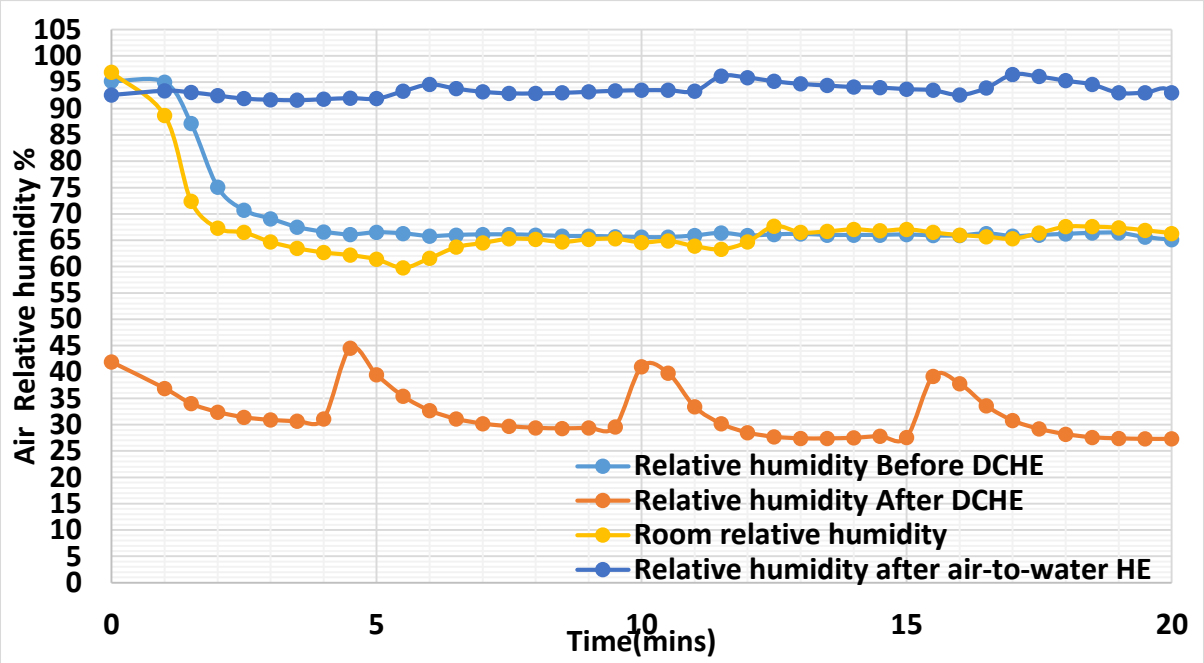



*Figure 7-46: Air humidity variation with time in the desiccant air-conditioning system for cooling at water inlet temperature of 18°C and half-cycle time 5mins.*

Figure 7-47 illustrates the temperature variation with time at different positions in the desiccant air conditioning system for cooling applications over 20 mins, including the temperatures before the DCHE, after the DCHE, inside the room, and after the air-to-water heat exchanger. Initially, the temperature before the DCHE starts at around 33.5°C, indicating the condition of the incoming air from the room. The air temperature after the DCHE starts at 44.3°C, and increases to approximately 45.8°C, peaking around 2.5 mins before gradually decreasing as the system stabilizes. Inside the room, the temperature starts at the peak of around 34.1°C, representing the artificial initial condition before any cooling effects from the system component starts. This peak temperature decreases as the system operates, influenced by the circulated conditioned air. After passing through the air-to-water heat exchanger, the air temperature starts to cool down to around 18.5°C and continues cooling slightly, indicating the efficiency of the heat exchange process. The room temperature is settled at 23.3°C. Notably, the system undergoes a half-cycle time at the 2.5-mins mark, potentially for desiccant regeneration or operational adjustments. The tap water feeding the air-to-water heat exchanger is maintained at 18°C, providing a cooling effect that helps maintain a controlled room environment. The evaporative cooler pump is switched off because the level of humidity in this case is high due to the sensible cooling.

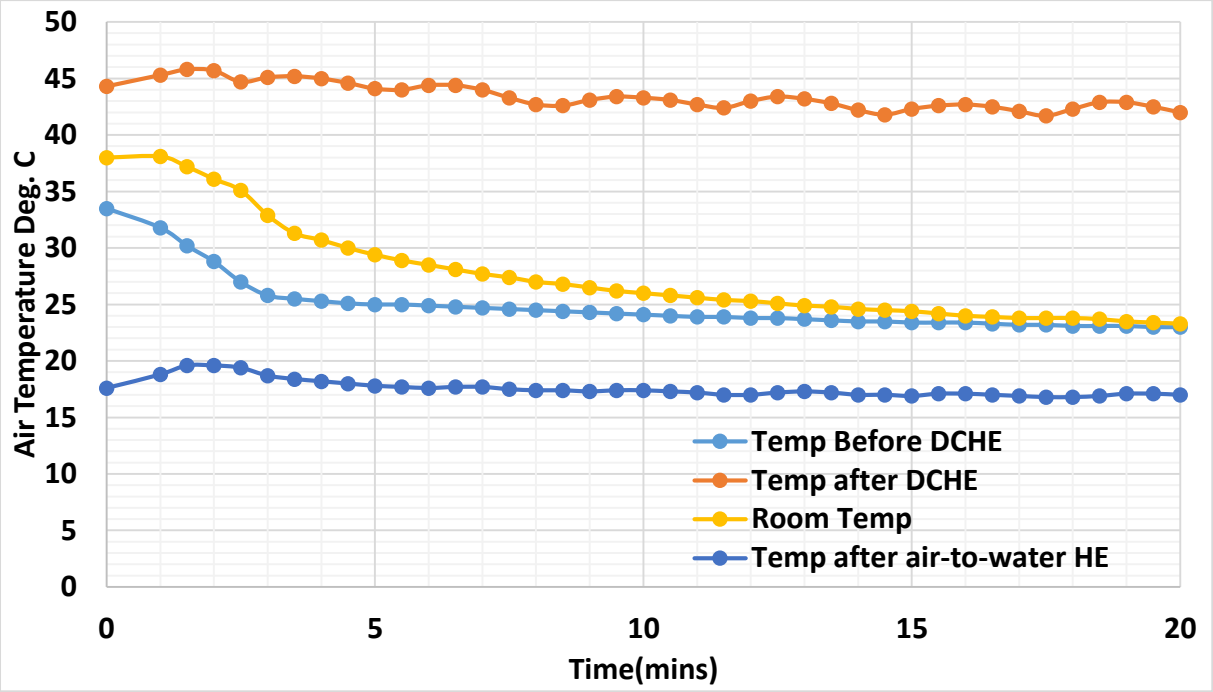



*Figure 7-47: Air temperature variation with time in the desiccant air-conditioning system for cooling at water inlet temperature of 18°C and half-cycle time 2.5mins.*

Figure 7-48 shows the variation of air relative humidity (RH) with time at different positions in the desiccant air conditioning system for a cooling system over 20 mins, including the humidity measurements before the DCHE, after the DCHE, inside the room, and after the air-to-water heat exchanger. The initial relative humidity before the DCHE is high, of around 95%, indicating the humid condition of the incoming air. This value drops sharply to around 80% within the first few minutes, stabilizing around 70% for the remainder of the period, demonstrating the effectiveness of the DCHE in moisture removal. After the DCHE, the relative humidity drops significantly to around 30%, indicating a substantial reduction in moisture content due to the desiccant's adsorption capacity. A notable spike to around 37.9% at the 2.5-mins mark, which corresponds with the system's half-cycle time, suggests a temporary increase in humidity, possibly due to the switching moment. This is followed by a reduction to approximately 35%. The room air's relative humidity increased artificially to 95%; as the system operates, the RH gradually decreases to around 68.7%, showing the impact of the conditioned air in maintaining a more controlled and less humid environment.

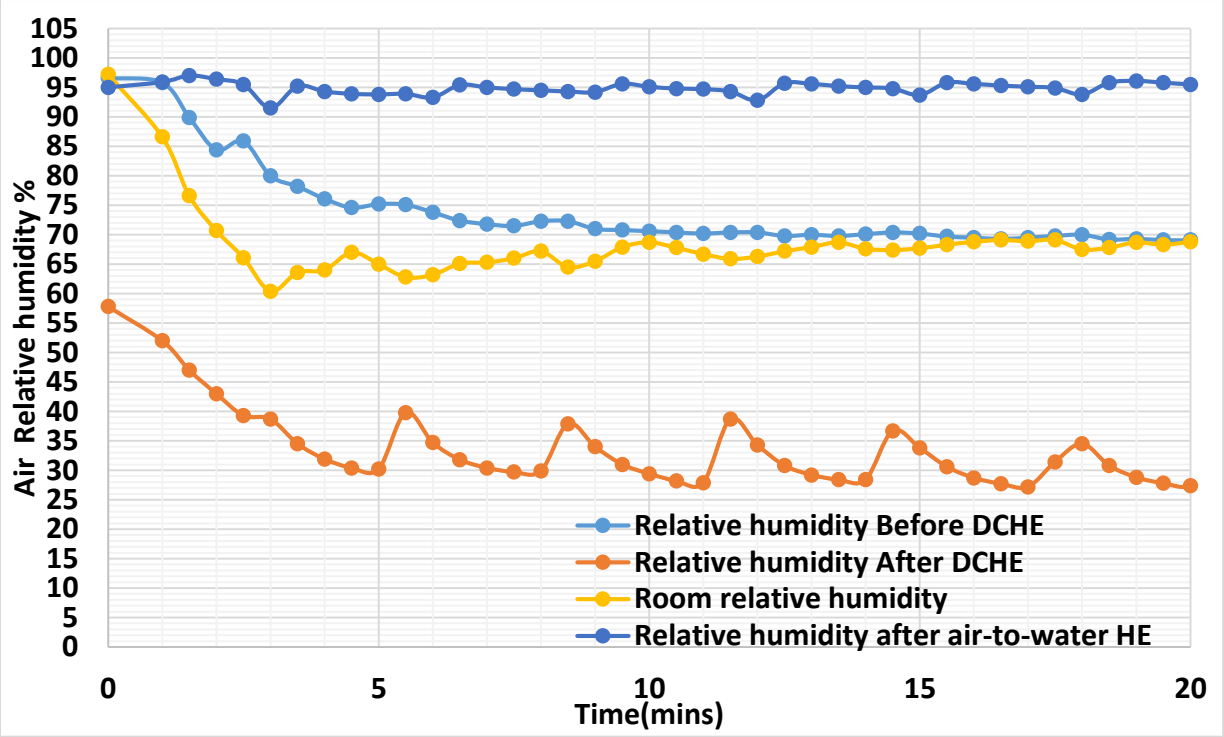



*Figure 7-48: Air humidity variation with time in the desiccant air-conditioning system for cooling at water inlet temperature of 18°C and half-cycle time 2.5mins.*

Figure 7-49 presents the change in the room condition on a psychrometric chart at various half-cycle times of 10mins, 5mins and 2.5mins and water inlet temperature to the water-to-air heat exchanger of 18°C.

For 10 mins half-cycle time, the system effectively reduces the initial high humidity levels with a specific humidity of 32.864g/kg(d.a), stabilizing the indoor environment to a specific humidity of 10.832g/kg(d.a), a more comfortable and controlled state.

For 5 mins half-cycle time, the specific humidity after the water heat exchanger remains stable, slightly above 12.351g/kg(d.a), indicating consistent performance in maintaining the desired humidity level. The system effectively reduces initial high humidity levels, stabilizing the indoor environment to a more comfortable and controlled state with a specific humidity of 11.465 g/kg(d.a).

For 2.5 mins half-cycle time, The specific humidity after the water heat exchanger remains stable, slightly above 12.351g/kg(d.a), indicating consistent performance; the humidity level is higher than the desired level. The system effectively reduces initial high humidity levels, stabilizing the indoor environment with a specific humidity of 12.743 g/kg(d.a). Figure 7-49 shows the room air temperature decreases from 36.8°C to 23°C, and the room air relative

humidity decreases from 95% to 60-65%, highlighting the developed desiccant air conditioning system's ability to achieve the required comfort conditions.

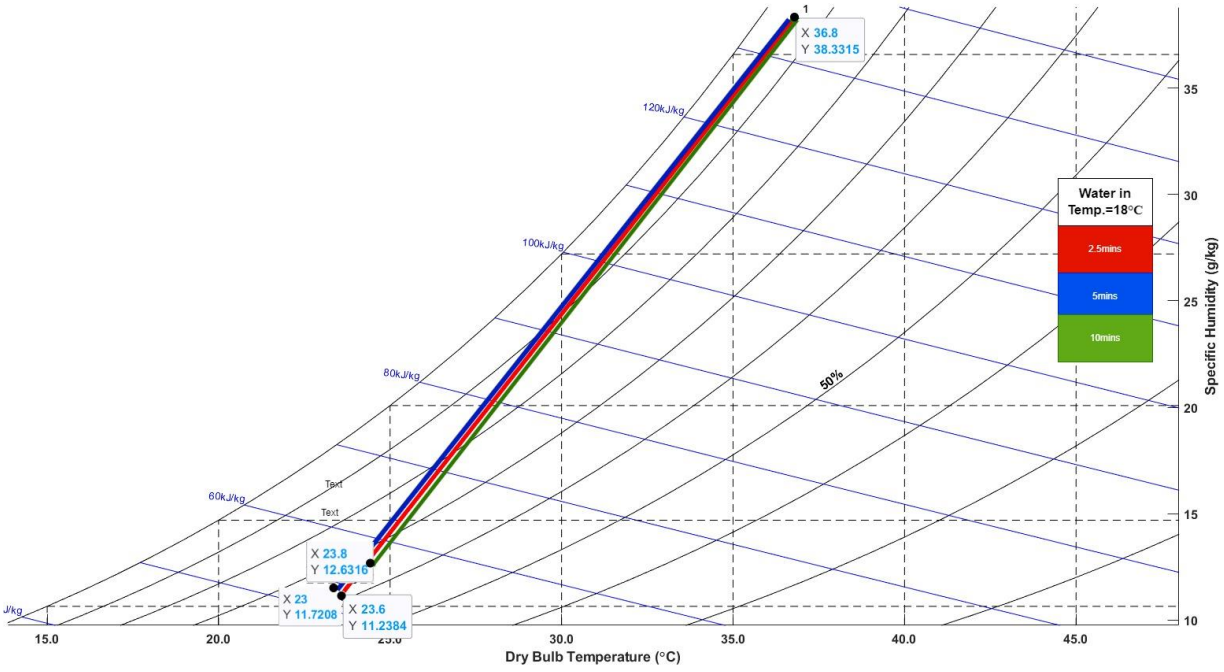



*Figure 7-49*: *Psychrometric chart for the room conditions change at a water inlet temperature for the heat exchanger of 18°C and different half-cycle time .*

Figure 7-50 to 7-57, present the experimental results when the temperature of the tap water is increased to 21°C and different half-cycle times: 10mins, 5mins, and 2.5mins. Figure 7-50 illustrates the temperature variation with time at different positions in the desiccant air conditioning system for cooling applications over 20 mins, including the temperatures before the DCHE, after the DCHE, inside the room, and after the air-to-water heat exchanger. Initially, the temperature before the DCHE starts at around 30°C, indicating the condition of the incoming air from the room. The air temperature after the DCHE starts at 36.7°C, and increases to approximately 40°C, peaking around 2.5 mins before gradually decreasing as the system stabilizes. Inside the room, the temperature starts at the peak of around 36.8°C, representing the artificial initial condition before any cooling effects from the system components. This peak temperature decreases as the system operates, influenced by the circulated conditioned air. After passing through the air-to-water heat exchanger, the air temperature starts to cool down to around 21.8°C and continues cooling slightly, indicating

the efficiency of the heat exchange process. The room temperature is settled at 24.9°C. Notably, the system undergoes a half-cycle time at the 10-mins mark, potentially for desiccant regeneration or operational adjustments. The tap water feeding the air-to-water heat exchanger is maintained at 21°C, providing a cooling effect that helps maintain a controlled room environment. The evaporative cooler pump is switched off because the level of humidity in this case is high due to the sensible cooling.

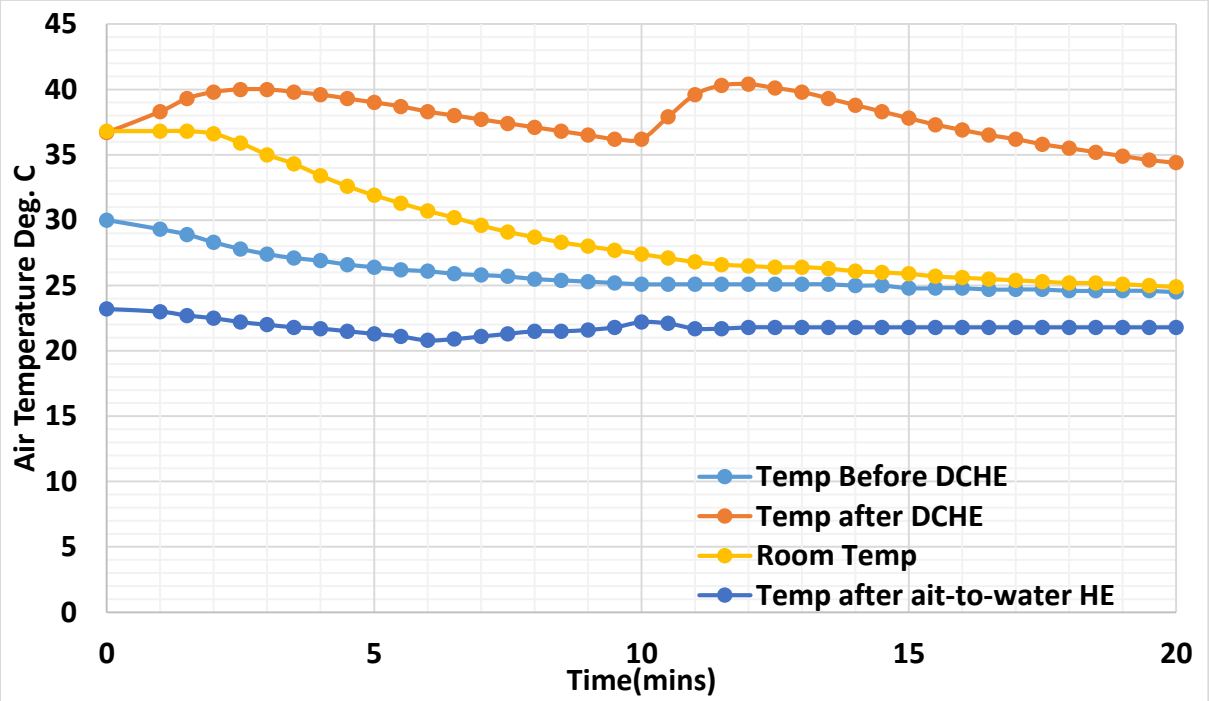



*Figure 7-50: Air temperature variation with time in the desiccant air-conditioning system for cooling at water inlet temperature of 21°C and half-cycle time 10mins.*

Figure 7-51 shows the variation of air relative humidity (RH) with time at different positions in the desiccant air conditioning system for a cooling system over 20 mins, including the humidity measurements before the DCHE, after the DCHE, inside the room, and after the air-to-water heat exchanger. The initial relative humidity before the DCHE is high, of around 96%, indicating the humid condition of the incoming air. This value drops sharply to around 80% within the first few minutes, stabilizing around 65% for the remainder of the period, demonstrating the effectiveness of the DCHE in moisture removal. After the DCHE, the relative humidity drops significantly to around 35%, indicating a substantial reduction in moisture content due to the desiccant's absorption capacity. A notable spike to around 52% at the 2.5-mins mark, which corresponds with the system's half-cycle time, suggests a temporary increase in humidity, possibly due to the switching moment. This is followed by a

reduction to approximately 35%. The room air's relative humidity increased artificially to 96%; as the system operates, the RH gradually decreases to around 57.2%, showing the impact of the conditioned air in maintaining a more controlled and less humid environment.

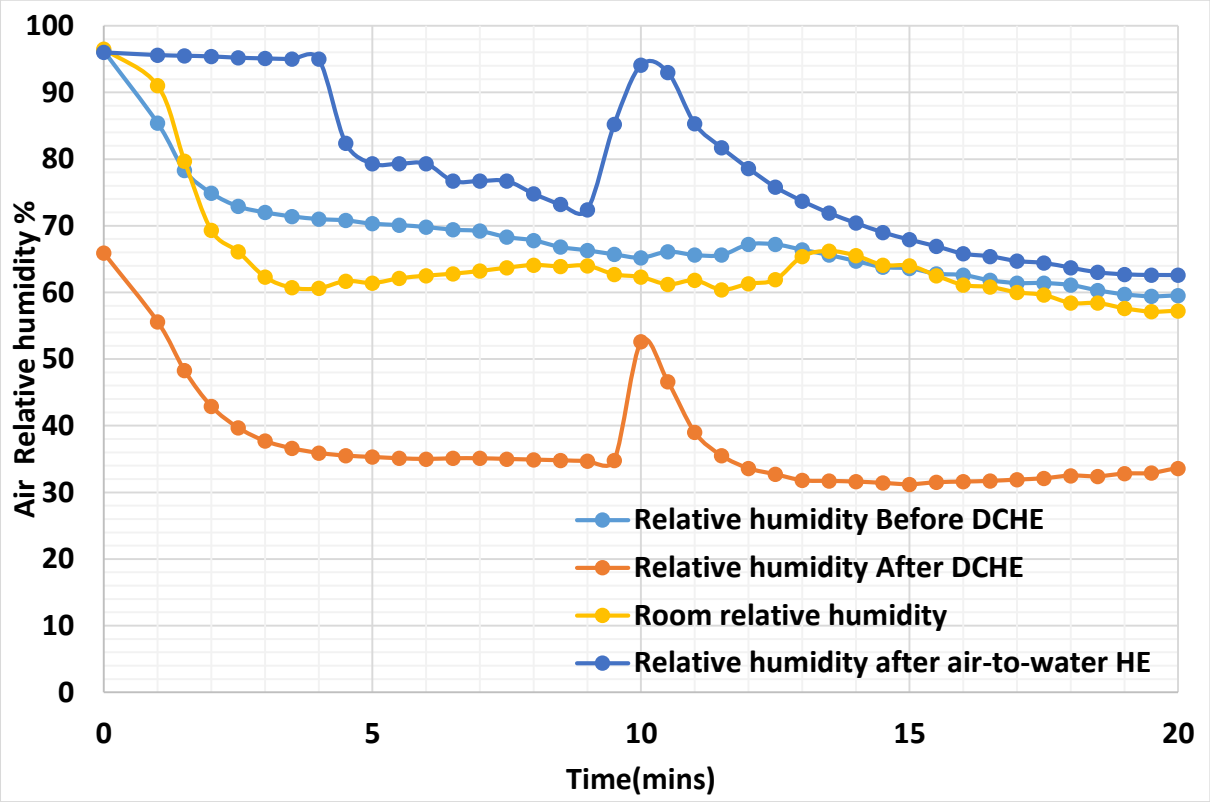



*Figure 7-51: Air humidity variation with time in the desiccant air-conditioning system for cooling at water inlet temperature of 21°C and half-cycle time 10mins.*

Figure 7-52 illustrates the temperature variation with time at different positions in the desiccant air conditioning system for cooling applications over 20 mins, including the temperatures before the DCHE, after the DCHE, inside the room, and after the air-to-water heat exchanger. Initially, the temperature before the DCHE starts at around 31.2°C, indicating the condition of the incoming air from the room. The air temperature after the DCHE starts at 31.2°C, increasing to approximately 42.5°C, peaking around 2.5 mins before gradually decreasing as the system stabilizes. Inside the room, the temperature starts at the peak of around 35.2°C, representing the artificial initial condition before any cooling effects from the system components start. This peak temperature decreases as the system operates, influenced by the circulated conditioned air. After passing through the air-to-water heat exchanger, the air temperature starts to cool down at around 21.8°C and continues cooling slightly, indicating the efficiency of the heat exchange process. The room temperature is settled at 25.3°C. Notably, the system undergoes a half-cycle time at the 5-mins mark,

potentially for desiccant regeneration or operational adjustments. The tap water feeding the air-to-water heat exchanger is maintained at 21°C, providing a cooling effect that helps maintain a controlled room environment. The evaporative cooler pump is switched off because the level of humidity in this case is high due to the sensible cooling.

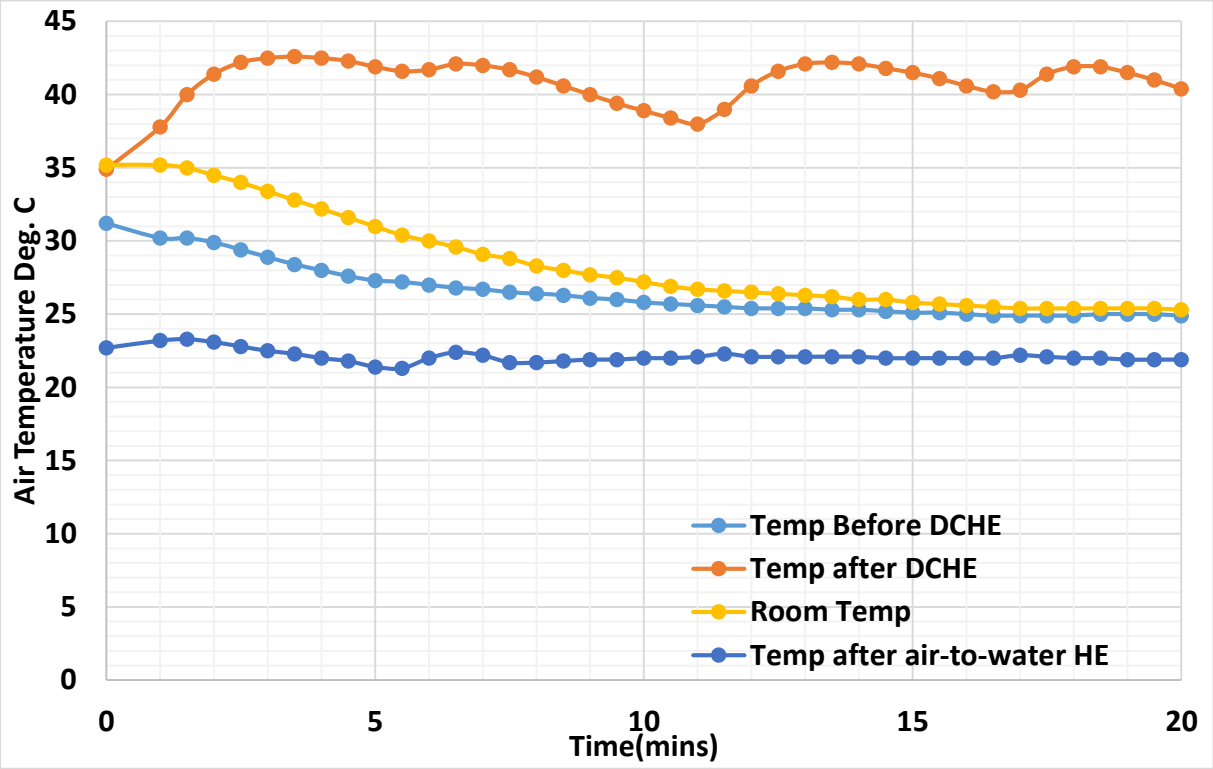



*Figure 7-52: Air temperature variation with time in the desiccant air-conditioning system for cooling at water inlet temperature of 21°C and half-cycle time 5mins.*

Figure 7-53 shows the variation of air relative humidity (RH) with time at different positions in the desiccant air conditioning system for a cooling system over 20 mins, including the humidity measurements before the DCHE, after the DCHE, inside the room, and after the air-to-water heat exchanger. The initial relative humidity before the DCHE is high, of around 97.1%, indicating the humid condition of the incoming air. This value drops sharply to around 80% within the first few minutes, stabilizing around 63% for the remainder of the period, demonstrating the effectiveness of the DCHE in moisture removal. After the DCHE, the relative humidity drops significantly to around 30%, indicating a substantial reduction in moisture content due to the desiccant's adsorption capacity. A notable spike to around 43.9% at the 5-mins mark, which corresponds with the system's half-cycle time, suggests a temporary increase in humidity, possibly due to the switching moment. This is followed by a reduction to approximately 35%. The room air's relative humidity increased artificially to 97%;

as the system operates, the RH gradually decreases to around 56%, showing the impact of the conditioned air in maintaining a more controlled and less humid environment.

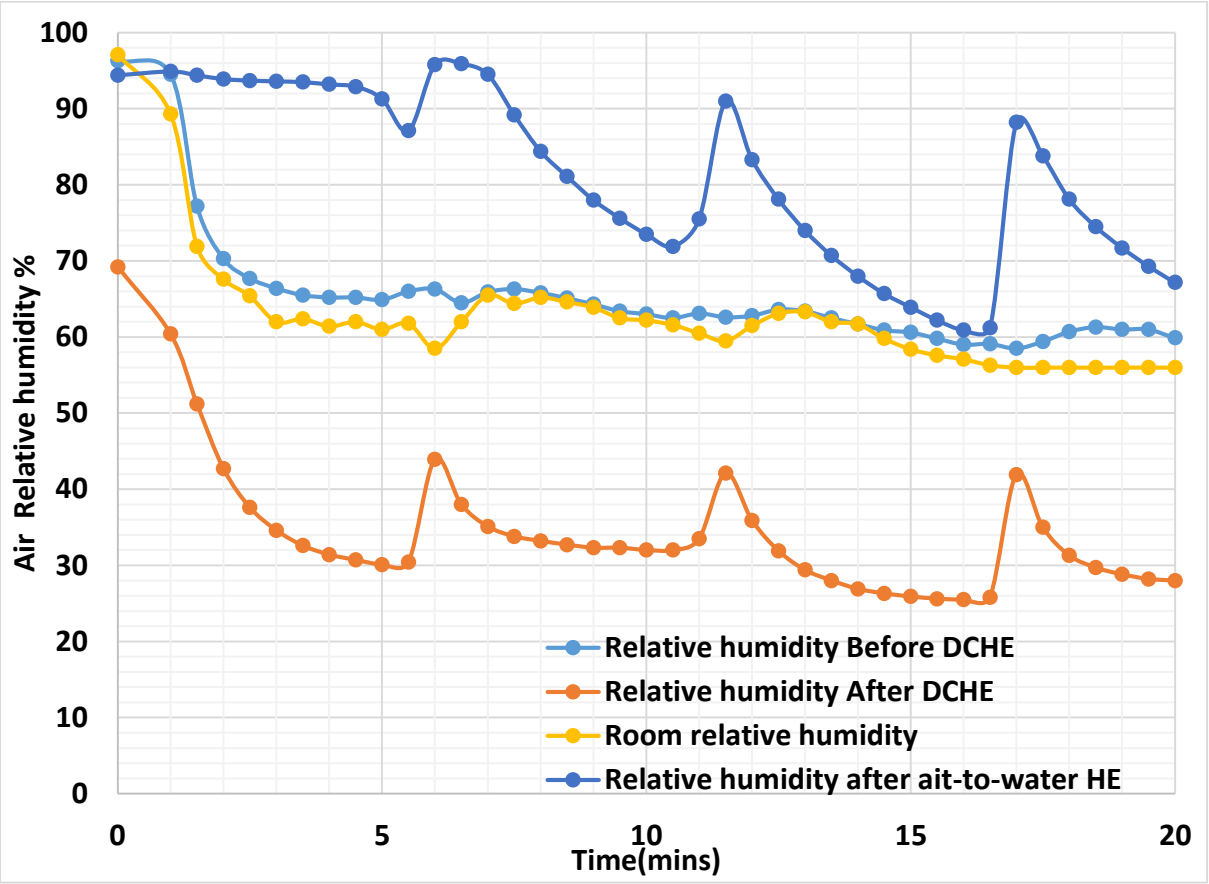



*Figure 7-53: Air humidity variation with time in the desiccant air-conditioning system for cooling at water inlet temperature of 21°C and half-cycle time 5mins.*

Figure 7-54 illustrates the temperature variation with time at different positions in the desiccant air conditioning system for cooling applications over 20 mins, including the temperatures before the DCHE, after the DCHE, inside the room, and after the air-to-water heat exchanger. Initially, the temperature before the DCHE starts at around 29.1°C, indicating the condition of the incoming air from the room. The air temperature after the DCHE starts at 39.3°C, increases to approximately 43.1°C, peaking around 2.5 mins before gradually decreasing as the system stabilizes. Inside the room, the temperature starts at the peak of around 32.6°C, representing the artificial initial condition before any cooling effects from the system components. This peak temperature decreases as the system operates, influenced by the circulated conditioned air. After passing through the air-to-water heat exchanger, the air temperature starts to cool down at around 21.4°C and continues cooling slightly, indicating the efficiency of the heat exchange process. The room temperature is settled at 25.2°C.

Notably, the system undergoes a half-cycle time at the 2.5-mins mark, potentially for desiccant regeneration or operational adjustments. The tap water feeding the air-to-water heat exchanger is maintained at 21°C, providing a cooling effect that helps maintain a controlled room environment. The evaporative cooler pump is switched off because the level of humidity in this case is high due to the sensible cooling.

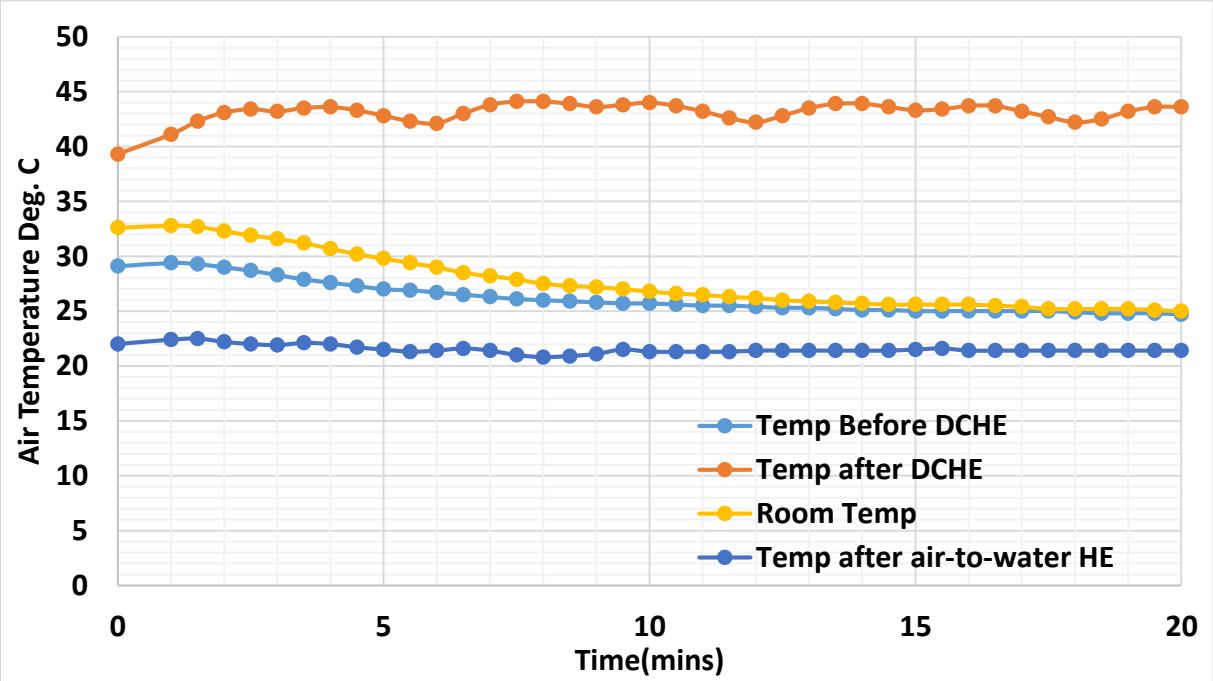



*Figure 7-54: Air temperature variation with time in the desiccant air-conditioning system for cooling at water inlet temperature of 21°C and half-cycle time 2.5mins.*

Figure 7-55 shows the variation of air relative humidity (RH) with time at different positions in the desiccant air conditioning system for a cooling system over 20 mins, including the humidity measurements before the DCHE, after the DCHE, inside the room, and after the air-to-water heat exchanger. The initial relative humidity before the DCHE is high, of around 95%, indicating the humid condition of the incoming air. This value drops sharply to around 80% within the first few minutes, stabilizing around 62% for the remainder of the period, demonstrating the effectiveness of the DCHE in moisture removal. After the DCHE, the relative humidity drops significantly to around 26.5%, indicating a substantial reduction in moisture content due to the desiccant's adsorption capacity. A notable spike to around 34.4% at the 5-mins mark, which corresponds with the system's half-cycle time, suggests a temporary increase in humidity, possibly due to the switching moment. This is followed by a reduction to approximately 24.9%. The room air's relative humidity increased artificially to

97%; as the system operates, the RH gradually decreases to around 59%, showing the impact of the conditioned air in maintaining a more controlled and less humid environment.

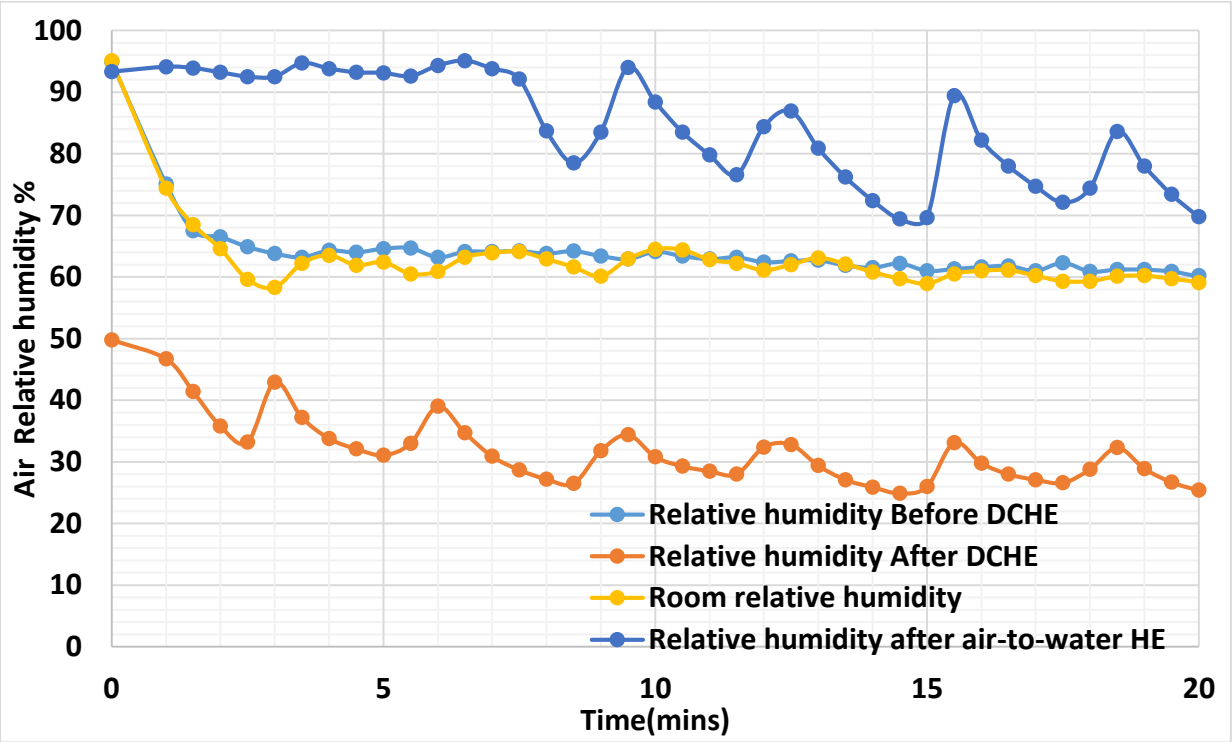



*Figure 7-55: Air humidity variation with time in the desiccant air-conditioning system for cooling at water inlet temperature of 21°C and half-cycle time 2.5mins.*

Figure 7-56 illustrates the variation of the Coefficient of Performance (COP) of the desiccant air conditioning with the half-cycle time at two inlet water temperatures to the air-to-water heat exchanger, namely 18°C and 21°C. The graphs demonstrate that the coefficient of performance (COP) drops as the half-cycle time increases, indicating a decrease in the system's efficiency over a longer half-cycle time. At the beginning, the graph for water at 18°C exhibits a greater coefficient of performance (COP) of 0.705 than that for water at 21°C of 0.605. Lower water temperatures initially improve efficiency, but this benefit diminishes with a longer half-cycle time. The best COP is achieved at 2.5 mins as a half-cycle time.

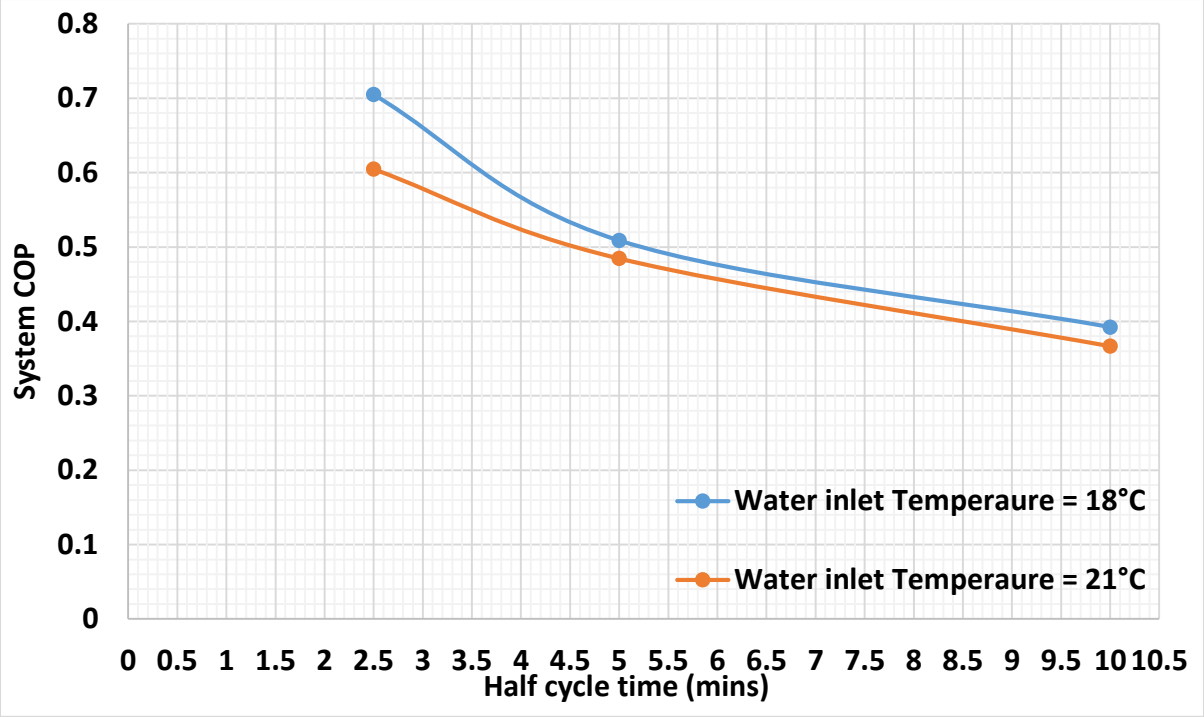



*Figure 7-56: COP for the desiccant air-conditioning system for cooling at a water inlet temperature of 21°C and 18°C at different half-cycle time s 2.5, 5, and 10mins.*

Figure 7-57 presents the change in the room condition on a psychrometric chart at various half-cycle times of 10mins, 5mins and 2.5mins and water inlet temperature to the water-to-air heat exchanger of 21°C.

For 10 mins half-cycle time, the specific humidity after the water heat exchanger starts with a high value of 15.389 g/kg(d.a) and settles slightly above 11.660g/kg(d.a), indicating consistent performance; the humidity level is within the desired level. The system effectively reduces initial high humidity levels, stabilizing the indoor environment at a reasonable, comfortable condition with a specific humidity of 11.437g/kg(d.a).

For 5 mins half-cycle time, after the water heat exchanger, the specific humidity starts with a high value of 16.588g/kg(d.a) for 7 minutes and settles slightly above 11.796g/kg(d.a), indicating consistent performance; the humidity level is within the wanted level. The system effectively reduces initial high humidity levels, stabilizing the indoor environment at a reasonable, comfortable condition with a specific humidity of 11.133g/kg(d.a).

For 2.5 mins half-cycle time, after the water heat exchanger, the specific humidity starts with a high value of 15.382g/kg(d.a) for the first 9 mins and settles slightly above 11.796g/kg(d.a), indicating consistent performance; the humidity level is within the wanted level. The system effectively reduces initial high humidity levels, stabilizing the indoor environment at a

reasonable, comfortable condition with a specific humidity of 9.818g/kg(d.a). Figure 7-56 shows the room air temperature decreases from 36.8°C to 25°C, and the room air relative humidity decreases from 95% to 53-60%, highlighting the developed desiccant air conditioning system's ability to achieve the required comfort conditions.

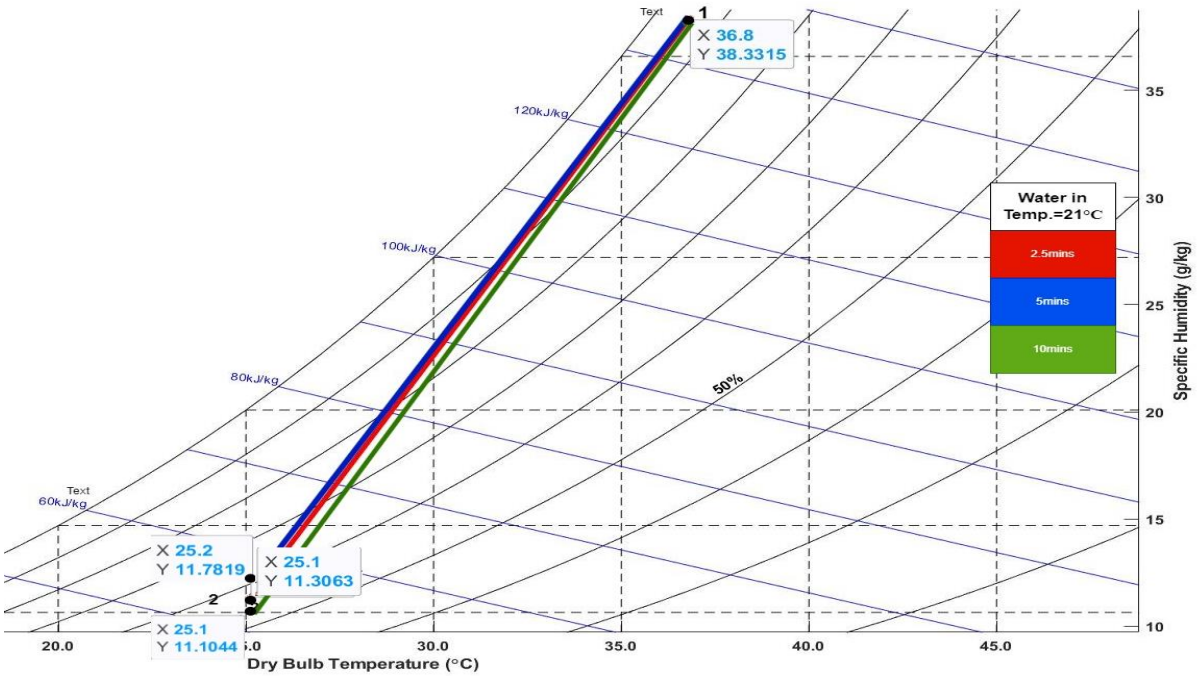



*Figure 7-57*: *Psychrometric chart of the room conditions at a water inlet temperature to the heat exchanger of 21°C at different half-cycle times.*

The above-described results proved that we can control the humidity and the temperature by controlling the tap inlet water for the air-to-water heat exchanger, and the desiccant air conditioning system can achieve the comfort conditions for the room.

### 7.3.2. Cooling/Heating Power Consumption:

Calculating the system's power consumption is crucial. The equations for calculating the percentage reduction in power consumption is calculated as follows:

Reduction percentage (cooling) $\% = \frac{Y-685.8}{Y} \times 100$ (7-4)

Reduction percentage (heating) $\% = \frac{X-525}{X} \times 100$ (7-5)

Where X is the power consumption for heating and Y is the power consumption for cooling by conventional portable air conditioners.

**Desiccant system for cooling**: $P * N + P_fan$ +*Q_cooling*= 685.8 watts

**Desiccant system for heating**: $P * N + P_fan +$ P_pump =525 watts

Where N is the Number of tubes, P is the power of one single tube, $P_fan$ is the fan power, and P_pump is the power for the evaporative cooler pump.

*Q_cooling*= $\dot{m}_w \times (T_{w,out} - T_{w,in})$ (7-6)

*Q_cooling is the cooling effect of the Air-to-water heat exchanger,* $\dot{m}_w$ *is the inlet water mass flow rate, and* $\Delta\ (T_{w,out} - T_{w,in}) = 1.5$℃

**Conventional system power consumption for cooling and heating (X and Y)**: 2000 watts

The desiccant air conditioning system consumes 66% less energy than the conventional air conditioner for cooling. The desiccant air conditioning system for heating consumes **74% less energy** than the conventional air conditioner. This significant reduction in power consumption further demonstrates the energy efficiency of the desiccant system in heating and cooling applications.

## 7.4.Summary

The experiments presented in this chapter using desiccant air conditioning systems for heating and cooling applications highlighted the importance of independent humidity and temperature control. These systems effectively remove moisture from the air before cooling or heating, maintaining consistent temperature and humidity levels. This independent control improved indoor comfort and reduced energy consumption of achieving the comfort condition, minimizing the need for repeated cooling or heating. The results demonstrated the efficiency and effectiveness of desiccant air conditioning in environments requiring precise climate control, particularly in high-humidity settings.

Results showed that:

1. The humidity and the temperature can be controlled separately.
2. The temperature and the humidity level are consistent after the DCHE. The evaporative cooler is used in the heating phase to tune up the humidity level and cool down the temperature inside the room.
3. The best half-cycle time is 2.5mins, the primary fan airspeed is 1.5m/s, and the COP is 1.06 for heating the room; the pump flow rate for the evaporative cooler is 10ml/s, and the comfort conditions are achieved with the temperature and humidity of 25°C and 55% respectively.

4. The cooling can be achieved by controlling the tap water temperature for the air-to-water heat exchanger with the same airspeed of 1.5m/s, setting the temperature of the air-to-water heat exchanger to 21°C, and switching the pump of the evaporative cooler leading to achieve sensible cooling for the airflow after the DCHE. The comfort conditions are achieved with temperature and humidity of 25°C and 59%, respectively, over 20 mins of operation.
5. The total power consumption for the system for heating is 525 W and cooling is 685.8 W compared with the conventional system, achieving a reduction of 66% less energy than the conventional air conditioner and 74% less energy for heating compared to the conventional air conditioner.

# Chapter 8 Conclusions and Future Work

The increasing global temperatures and extreme weather events have led to a growing need for sustainable cooling and heating solutions. Metal-organic framework (MOF) materials, when integrated into desiccant cooling systems, offer a promising solution for urban centres, providing high water adsorption capabilities and energy-efficient climate regulation. These systems can reduce energy consumption by 20-50% and decrease the carbon footprint by 30-60% when paired with renewable energy sources. Evaporative cooling technology, which cools the air by spraying water and absorbing heat through evaporation, is more energy-efficient than traditional vapour compression refrigeration systems. Combining MOF-based desiccant systems with evaporative cooling and air-to-water heat exchangers can improve performance and energy efficiency. MOF-based desiccant systems can reduce power consumption by up to around 66% and heating by 74% compared to conventional split unit air conditioners. These systems also meet ASHRAE comfort standards, maintaining an indoor environment of 25°C and 55-60% relative humidity. The development and deployment of MOF-based desiccant systems combined with evaporative cooling offer a significant advancement in sustainable climate control technologies, contributing to global efforts to mitigate climate change and promote environmental sustainability. Therefore, this thesis experimentally and numerically assesses the performance of the desiccant air condition system using advanced MOF material (MOF-303/G) to achieve comfort conditions.

## 8.1.Conclusions

This PhD work aims to exploit the superior water adsorption capability of Metal Organic Framework (MOF) materials to develop an energy-efficient desiccant air conditioning system capable of independently controlling indoor temperature and relative humidity for cooling and heating applications. The study investigated ways of enhancing the performance of desiccant air conditioning systems by testing different advanced adsorbent materials and assessing their performance when combined with an evaporative cooler and air-to-water heat exchanger at different operating conditions. Numerical modelling and experimental testing were used to evaluate the performance of MOF desiccant air conditioning system and the following conclusions are made.

- A one-dimensional dynamic model was created utilising MATLAB software to predict the performance of MOFs in terms of moisture removal rate and coefficient of

performance (COP). The findings indicated that Aluminium fumarate achieved the highest Coefficient of Performance (COP) of 0.65, accompanied by a water removal rate of 12.65 g/kg(d.a). MIL-101(Cr) achieved the highest moisture removal rate of 15.99 g/kg of dry air, although it exhibited a coefficient of performance (COP) of 0.44. MIL-100(Fe) exhibited a coefficient of performance (COP) of 0.43 and achieved a moisture removal rate of 7.91 g/kg. CPO-27(Ni) exhibited a coefficient of performance (COP) of 0.4, with a moisture removal capacity of 6.55 g/kg, compared to silica gel. This study highlights the importance of MOF materials in moisture removal processes within desiccant cooling applications.

- Six MOF materials coated on wire-finned tubes were used for water vapour removal from ambient air. The results showed that MOF-303/G achieved the highest water uptake of 22%, outperforming the other materials like MOF-801/G 17.5% and MOF-100(Fe)/G 16%. This material was then used to develop a novel electrically heated wire-finned multi-tube heat exchanger. The heat exchanger was tested at different power input values, achieving MOF surface temperatures of 45°C, 60°C, and 70°C. Increasing the MOF-303/G surface temperature during regeneration increased water uptake from 6.3% at 45°C to 17.15% at 70°C. The Coefficient of Performance (COP) of the MOF-303/G DCHE was determined and compared to other desiccant-coated heat exchangers in the literature. The wire-finned tube heat exchanger coated with MOF-303/G demonstrates substantial potential compared to conventional designs, making it suitable for desiccant air conditioning applications. This design has shown great potential for desiccant air conditioning applications, and its superior performance has made it a candidate for further real-world testing.
- In the context of greenhouse climate control, a novel system was developed that integrates MOF-based desiccant-coated heat exchangers (DCHEs) with air-to-air heat exchangers and evaporative coolers. Computational fluid dynamics (CFD) modelling of MOF-303/G-coated heat exchangers demonstrated the system's ability to recover water from reducing greenhouse relative humidity, which can be repurposed for irrigation and produces the highest water removal rate per unit power consumption of 2.69g/kgMOF/W.hr., thus addressing food security challenges in arid regions achieving the target return air relative humidity of 50-60%.

- Additionally, experiments using desiccant air conditioning systems for heating and cooling highlighted the importance of independently controlling humidity and temperature. These systems effectively maintained consistent climate conditions, enhanced indoor comfort, and reduced energy consumption. The research showed that humidity and temperature could be controlled separately, with optimal results achieved through specific system settings—such as a half-cycle time of 2.5 minutes, an airspeed of 1.5 m/s, and target temperature settings for heating and cooling phases. The desiccant air conditioning system achieved the ASHRAE comfort conditions with a 66% reduction in energy consumption in cooling application and a 74% reduction in energy consumption in heating application compared to conventional air conditioning systems.

This PhD work highlights the developed system's potential for energy savings and independent control of indoor temperature and humidity for climate control in residential, commercial, and agricultural environments.

## 8.2. Future work

- To optimise the efficiency of desiccant cooling systems and MOF-based climate control technologies, researchers might pursue various routes of research and development:
- Future research should prioritise optimising synthesis and coating techniques for MOF materials to improve their water adsorption capacity, thermal stability, and regeneration efficiency. Investigating novel composites or hybrid materials, such as integrating MOFs with other porous substances or graphene derivatives, can yield superior performance metrics.
- Investigate another advanced heat exchanger with micro-extended surfaces that increases the overall surface areas, such as microchannel heat exchangers or 3D-printed structures explicitly designed for MOF materials.
- Explore integrating the developed desiccant air conditioning system with renewable energy sources, such as solar thermal or geothermal energy. This integration can potentially decrease both the carbon footprint and operational costs significantly. Implementing intelligent control systems that maximise energy efficiency by utilising

up-to-date information from renewable sources and building conditions would be advantageous.

- Conducting field tests and implementing desiccant air conditioning systems in many climates and settings, including homes, businesses, and agricultural greenhouses, would yield helpful information about their effectiveness in diverse environments. This would aid in enhancing system designs and pinpointing particular scenarios when these technologies provide the most substantial advantages.
- Performing thorough life cycle assessments (LCA) and cost-benefit studies of desiccant cooling systems compared to conventional HVAC systems will yield a more precise comprehension of their environmental consequences and economic feasibility. Potential future research could investigate methods to decrease production expenses and enhance the scalability of systems based on MOFs.
- Advanced Control Strategies: Developing sophisticated control strategies, such as machine learning algorithms, can significantly improve energy efficiency and comfort levels by optimising system performance in real time according to changing environmental circumstances and user preferences.
- Further investigation into water recovery strategies from desiccant air conditioning system, especially in arid places, can potentially enhance the value of these systems for agricultural and home purposes. Exploring techniques to cleanse and recycle the retrieved water within the system or for external uses could enhance the overall effectiveness of these systems.

# References


[1] Climate Change 2022, “Adaptation and Vulnerability. Contribution of Working Group II to the Sixth Assessment Report of the Intergovernmental Panel on Climate Change.,” Cambridge University Press, 2022. https://www.ipcc.ch/assessment-report/ar6/

[2] United Nations (2022), “World Population Prospects 2022.,” Revision 1, 2022. [Online]. Available:https://population.un.org/wpp/

[3] T. R. Oke, G. Mills, A. Christen, and J. A. Voogt, “Urban Climates,” in Urban Climates, Cambridge University Press, 2017, pp. i–i. [Online]. Available: https://www.cambridge.org/core/books/urban-climates/A02424592E1C7F9B9CD69DAD57A5B50B

[4] F. Schleussner, C. F., Lissner, T. K., Fischer, E. M., Wohltjen, J., & Lehner, “Weather extremes: A major challenge for society.,” Annu. Rev. Environ. Resour., vol. 48, pp. 1–30, 2023, [Online]. Available: https://www.annualreviews.org/journal/energy

[5] K. M. U. Ahmed, M. H. J. Bollen, and M. Alvarez, “A Review of Data Centers Energy Consumption and Reliability Modeling,” IEEE Access, vol. 9, pp. 152536–152563, 2021, doi: 10.1109/ACCESS.2021.3125092.

[6] International Energy Agency (IEA), “The Future of Cooling: Opportunities for Energy-Efficient Air Conditioning. France: International Energy Agency,” p. 92, 2023.

[7] T. Guardian, “How Air Conditioning Is Changing the Planet,” 2023. https://www.theguardian.com/technology/2023/aug/27/staying-cool-without-air-con-warming-climate-crisis-planet

[8] M. J. Mendell, “Commentary: Air conditioning as a risk for increased use of health services,” Int. J. Epidemiol., vol. 33, no. 5, pp. 1123–1126, 2004, doi: 10.1093/ije/dyh264.

[9] M. A. Islam, A. Pal, K. Thu, and B. B. Saha, “Study on performance and environmental impact of supermarket refrigeration system in Japan,” Evergreen, vol. 6, no. 2, pp. 168–176, 2019, doi: 10.5109/2321014.

[10] A. Rezk, “Theoretical and Experimental Investigation of Silica gel / Water Adsorption Refrigeration Systems, Doctor of Philosophy ,” University of Birmingham, 2012.

[11] P. George, “Experimental and Numerical Investigation of a New MOF Based Adsorption Water Desalination System, Doctor of Philosophy,”University of Birmingham, 2018.

[12] L. W. Wang, R. Z. Wang, and R. G. Oliveira, “A review on adsorption working pairs for refrigeration,” Renewable and Sustainable Energy Reviews, vol. 13, no. 3. pp. 518–534, Apr. 2009. doi: 10.1016/j.rser.2007.12.002.

[13] Z. S. Lu et al., “Study of a novel solar adsorption cooling system and a solar absorption cooling system with new CPC collectors,” Renew. Energy, vol. 50, pp. 299–306, 2013, doi: 10.1016/j.renene.2012.07.001.

[14] S. Belguith, Z. Meddeb, and R. Ben Slama, “Performance analysis of desiccant cooling systems in a hot and dry climate,” Euro-Mediterranean J. Environ. Integr., vol. 6, no. 1, pp. 1–11, 2021, doi: 10.1007/s41207-020-00210-x.

[15] J. Luo and H. Yang, “A state-of-the-art review on the liquid properties regarding energy and environmental performance in liquid desiccant air-conditioning systems,” Appl. Energy, vol. 325, no. June, p. 119853, 2022, doi: 10.1016/j.apenergy.2022.119853.

[16] T. N.Borhani and M. Wang, “Role of solvents in CO2 capture processes: The review of selection and design methods,” Renew. Sustain. Energy Rev., vol. 114, no. July, p. 109299, 2019, doi: 10.1016/j.rser.2019.109299.

[17] R. H. Mohammed, M. Ahmadi, H. Ma, and S. Bigham, “Desiccants enabling energy-efficient buildings: A review,” Renew. Sustain. Energy Rev., vol. 183, no. February, p. 113418, 2023, doi: 10.1016/j.rser.2023.113418.

[18] Newair, “What Are Evaporative Coolers? Here’s Everything You Need to Know.,” 2023. https://www.newair.com/blogs/learn/what-are-evaporative-coolers

[19] R. AL-Dadah, S. Mahmoud, E. Elsayed, P. Youssef, and F. Al-Mousawi, “Metal-organic framework materials for adsorption heat pumps,” Energy, vol. 190, p. 116356, 2020, doi: 10.1016/j.energy.2019.116356.

[20] ASHRAE-55, “Thermal Environmental Conditions for Human Occupancy-2017,” ANSI/ASHRAE Stand. 55, vol. 7, p. 60, 2017.

[21] F. Nicol, “Adaptive thermal comfort standards in the hot-humid tropics,” Energy Build., vol. 36, no. 7, pp. 628–637, 2004, doi: 10.1016/j.enbuild.2004.01.016.

[22] M. Absar Alam, R. Kumar, A. S. Yadav, R. K. Arya, and V. P. Singh, “Recent developments trends in HVAC (heating, ventilation, and air-conditioning) systems: A comprehensive review,” Materials Today: Proceedings, 2023, doi: 10.1016/j.matpr.2023.01.357.

[23] D. La, Y. J. Dai, Y. Li, R. Z. Wang, and T. S. Ge, “Technical development of rotary desiccant dehumidification and air conditioning: A review,” Renew. Sustain. Energy Rev., vol. 14, no. 1, pp. 130–147, 2010, doi: 10.1016/j.rser.2009.07.016.

[24] R. Qi, L. Lu, and H. Yang, “Investigation on air-conditioning load profile and energy consumption of desiccant cooling system for commercial buildings in Hong Kong,” Energy Build., vol. 49, pp. 509–518, 2012, doi: 10.1016/j.enbuild.2012.02.051.

[25] A. M. Baniyounes, G. Liu, M. G. Rasul, and M. M. K. Khan, “Comparison study of solar cooling technologies for an institutional building in subtropical Queensland, Australia,” Renew. Sustain. Energy Rev., vol. 23, pp. 421–430, 2013, doi: 10.1016/j.rser.2013.02.044.

[26] A. Speerforck and G. Schmitz, “Experimental investigation of a ground-coupled desiccant assisted air conditioning system,” Appl. Energy, vol. 181, pp. 575–585, 2016, doi: 10.1016/j.apenergy.2016.08.036.

[27] H. X. Fu, L. Z. Zhang, J. C. Xu, and R. R. Cai, “A dual-scale analysis of a desiccant wheel with a novel organic-inorganic hybrid adsorbent for energy recovery,” Appl. Energy, vol. 163, pp. 167–179, 2016, doi: 10.1016/j.apenergy.2015.10.175.

[28] J. A. Shamim, W. L. Hsu, S. Paul, L. Yu, and H. Daiguji, “A review of solid desiccant dehumidifiers: Current status and near-term development goals in the context of net zero energy buildings,” Renew. Sustain. Energy Rev., vol. 137, no. September 2020, p. 110456, 2021, doi: 10.1016/j.rser.2020.110456.

[29] E. Robens and S. Jayaweera, “Early history of adsorption measurements,” Adsorpt. Sci. Technol., vol. 32, no. 6, pp. 425–442, 2014, doi: 10.1260/0263-6174.32.6.425.

[30] R. D. Noble and P. A. Terry, Eds., “Adsorption,” in Principles of Chemical Separations with Environmental Applications, Cambridge: Cambridge University Press, 2004, pp. 182–213. doi: DOI: 10.1017/CBO9780511616594.008.

[31] E. M. Elsayed and A. Hussein, “Numerical and Experimental Evaluation of Advanced Metal-Organic F Ramework Materials for Adsorption Heat Pumps, Doctor of Philosophy,” University of Birmingham, 2018.

[32] K. Ariga, A. Vinu, Y. Yamauchi, Q. Ji, and J. P. Hill, “Nanoarchitectonics for mesoporous materials,” Bull. Chem. Soc. Jpn., vol. 85, no. 1, pp. 1–32, 2012, doi: 10.1246/bcsj.20110162.

[33] J. Rouquerol, P. Llewellyn, and K. Sing, Adsorption by Clays, Pillared Clays, Zeolites and Aluminophosphates, 2nd ed. Elsevier Ltd., 2013. doi: 10.1016/B978-0-08-097035-6.00012-7.

[34] K. Kinashi, Y. Kambe, M. Misaki, Y. Koshiba, K. Ishida, and Y. Ueda, "Reporting physisorption data for gas/solid systems — with special reference to the determination of surface area and porosity," J. Polym. Sci. Part A Polym. Chem., vol. 50, no. 24, pp. 5107–5114, 2012, doi: 10.1002/pola.26338.

[35] "Masthead," Berichte der Bunsengesellschaft für Phys. Chemie, vol. 86, no. 10, p. fmi-fmi, 1982, doi: https://doi.org/10.1002/bbpc.19820861001.

[36] V.-C. Niculescu, M. Constantinescu, F. Bucura, D. Ion-Ebrasu, and A. Soare, "SBA-16 Mesoporous Nanosilica: Synthesis, Characterization and Sorption Properties," Smart Energy Sustain. Environ., vol. 23, p. 69+, Feb. 2020, [Online]. Available: https://link.gale.com/apps/doc/A645943952/AONE?u=anon~1ad039a4&sid=googleScholar&xid=1cf88215

[37] J. Rouquerol, F. Rouquerol, and K. Sing, Adsorption by Powders and Porous Solids: Principles, Methodology and Applications. Elsevier Science, 1998. [Online]. Available: https://books.google.co.uk/books?id=hNCREhZ7Wt8C

[38] M. M. Rahman, A. Z. Shafiullah, A. Pal, M. A. Islam, I. Jahan, and B. B. Saha, "Study on optimum iupac adsorption isotherm models employing sensitivity of parameters for rigorous adsorption system performance evaluation," Energies, vol. 14, no. 22, 2021, doi: 10.3390/en14227478.

[39] M. Abdelgaied, M. A. Saber, M. M. Bassuoni, and A. M. Khaira, "Adsorption air conditioning: a comprehensive review in desiccant materials, system progress, and recent studies on different configurations of hybrid solid desiccant air conditioning systems," Environ. Sci. Pollut. Res., vol. 30, no. 11, pp. 28344–28372, 2023, doi: 10.1007/s11356-023-25209-z.

[40] K. Thu, A. Chakraborty, B. B. Saha, and K. C. Ng, "Thermo-physical properties of silica gel for adsorption desalination cycle," Appl. Therm. Eng., vol. 50, no. 2, pp. 1596–1602, 2013, doi: 10.1016/j.applthermaleng.2011.09.038.

[41] D. Wang, J. Zhang, Q. Yang, N. Li, and K. Sumathy, "Study of adsorption characteristics in silica gel-water adsorption refrigeration," Appl. Energy, vol. 113, pp. 734–741, 2014, doi: 10.1016/j.apenergy.2013.08.011.

[42] N. C. Srivastava and I. W. Eames, “A review of adsorbents and adsorbates in solid-vapour adsorption heat pump systems,” Appl. Therm. Eng., vol. 18, no. 9–10, pp. 707–714, 1998, doi: 10.1016/S1359-4311(97)00106-3.

[43] M. Sultan, I. I. El-Sharkawy, T. Miyazaki, B. B. Saha, and S. Koyama, “An overview of solid desiccant dehumidification and air conditioning systems,” Renew. Sustain. Energy Rev., vol. 46, pp. 16–29, 2015, doi: 10.1016/j.rser.2015.02.038.

[44] M. Olivares-Marín, C. Fernández-González, A. Macías-García, and V. Gómez-Serrano, “Preparation of activated carbon from cherry stones by chemical activation with ZnCl 2,” Appl. Surf. Sci., vol. 252, no. 17, pp. 5967–5971, 2006, doi: 10.1016/j.apsusc.2005.11.008.

[45] P. C. Wankat, Adsorption engineering, vol. 14, no. 3. 1991. doi: 10.1016/0923-1137(91)90043-n.

[46] Y. I. Matatov-Meytal, M. Sheintuch, G. E. Shter, and G. S. Grader, “Optimal temperatures for catalytic regeneration of activated carbon,” Carbon N. Y., vol. 35, no. 10–11, pp. 1527–1531, 1997, doi: 10.1016/S0008-6223(97)00103-6.

[47] S. Shimooka et al., “Development of hydrophilic active carbon for high performance adsorption heat pump,” Kagaku Kogaku Ronbunshu, vol. 32, no. 6, pp. 528–534, 2006.

[48] X. Mou and Z. Chen, “Experimental and predictive study on the performance and energy consumption characteristics for the regeneration of activated alumina assisted by ultrasound,” Ultrason. Sonochem., vol. 70, no. July 2020, p. 105314, 2021, doi: 10.1016/j.ultsonch.2020.105314.

[49] T. Venegas, M. Qu, K. Nawaz, and L. Wang, “Critical review and future prospects for desiccant coated heat exchangers: Materials, design, and manufacturing,” Renew. Sustain. Energy Rev., vol. 151, no. July 2020, p. 111531, 2021, doi: 10.1016/j.rser.2021.111531.

[50] H. Leiming, G. Tianshu, J. Yu, and W. Ruzhu, “Hygroscopic property of metal matrix composite desiccant,” J. Refrig, vol. 2, p. 12, 2014.

[51] Y. D. Tu, R. Z. Wang, and T. S. Ge, “Moisture uptake dynamics on desiccant-coated, water-sorbing heat exchanger,” Int. J. Therm. Sci., vol. 126, no. December 2017, pp. 13–22, 2018, doi: 10.1016/j.ijthermalsci.2017.12.015.

[52] C. X. Jia, Y. J. Dai, J. Y. Wu, and R. Z. Wang, “Use of compound desiccant to develop high performance desiccant cooling system,” Int. J. Refrig., vol. 30, no. 2, pp. 345–353, 2007, doi: 10.1016/j.ijrefrig.2006.04.001.

[53] X. H. Liu, X. Q. Yi, and Y. Jiang, “Mass transfer performance comparison of two commonly used liquid desiccants: LiBr and LiCl aqueous solutions,” Energy Convers. Manag., vol. 52, no. 1, pp. 180–190, 2011, doi: 10.1016/j.enconman.2010.06.057.

[54] A. Karmakar, V. Prabakaran, D. Zhao, and K. J. Chua, “A review of metal-organic frameworks (MOFs) as energy-efficient desiccants for adsorption driven heat-transformation applications,” Appl. Energy, vol. 269, no. December 2019, p. 115070, 2020, doi: 10.1016/j.apenergy.2020.115070.

[55] P. G. Youssef, H. Dakkama, S. M. Mahmoud, and R. K. AL-Dadah, “Experimental investigation of adsorption water desalination/cooling system using CPO-27Ni MOF,” Desalination, vol. 404, pp. 192–199, 2017, doi: 10.1016/j.desal.2016.11.008.

[56] A. Rezk, R. Al-Dadah, S. Mahmoud, and A. Elsayed, “Characterisation of metal organic frameworks for adsorption cooling,” Int. J. Heat Mass Transf., vol. 55, no. 25–26, pp. 7366–7374, 2012, doi: 10.1016/j.ijheatmasstransfer.2012.07.068.

[57] K. Zu, S. Cui, and M. Qin, “Performance comparison between metal-organic framework (MOFs) and conventional desiccants (silica gel, zeolite) for a novel high temperature cooling system,” IOP Conf. Ser. Mater. Sci. Eng., vol. 609, no. 5, 2019, doi: 10.1088/1757-899X/609/5/052013.

[58] B. Bozbiyik, T. Van Assche, J. Lannoeye, and D. E. De Vos, “Stepped water isotherm and breakthrough curves on aluminium fumarate metal – organic framework : experimental and modelling study,” Adsorption, vol. 0, no. 0, p. 0, 2016, doi: 10.1007/s10450-016-9847-0.

[59] X. Liu, X. Wang, and F. Kapteijn, “Water and Metal-Organic Frameworks: From Interaction toward Utilization,” Chem. Rev., vol. 120, no. 16, pp. 8303–8377, 2020, doi: 10.1021/acs.chemrev.9b00746.

[60] S. Z. Shahvari, V. A. Kalkhorani, C. R. Wade, and J. D. Clark, “Benefits of metal–organic frameworks sorbents for sorbent wheels used in air conditioning systems,” Appl. Therm. Eng., vol. 210, no. December 2021, p. 118407, 2022, doi: 10.1016/j.applthermaleng.2022.118407.

[61] X. Zheng, T. S. Ge, and R. Z. Wang, “Recent progress on desiccant materials for solid desiccant cooling systems,” Energy, vol. 74, no. 1. Elsevier Ltd, pp. 280–294, 2014. doi: 10.1016/j.energy.2014.07.027.

[62] AgriTechTomorrow, “Greenhouse Cooling: Everything You Need to Know to Beat the Heat," AgriTechTomorrow, 2023,” 2023. [Online]. Available:

https://www.agritechtomorrow.com/article/2023/07/cooling-a-greenhouse-everything-you-need-to-know-to-beat-the-heat/14676.

[63] M. V. Solovyeva, L. G. Gordeeva, T. A. Krieger, and Y. I. Aristov, “MOF-801 as a promising material for adsorption cooling: Equilibrium and dynamics of water adsorption,” Energy Convers. Manag., vol. 174, no. August, pp. 356–363, 2018, doi: 10.1016/j.enconman.2018.08.032.

[64] T. Hu, S. Chang, H. Wu, L. Li, and W. Yuan, “Construction of high thermal conductivity MOFs composite phase change materials with reinforced light-to-thermal conversion,” Sol. Energy Mater. Sol. Cells, vol. 232, no. August, 2021, doi: 10.1016/j.solmat.2021.111339.

[65] J. Wang, X. Huang, H. Gao, A. Li, and C. Wang, “Construction of CNT@Cr-MIL-101-NH2 hybrid composite for shape-stabilized phase change materials with enhanced thermal conductivity,” Chem. Eng. J., vol. 350, no. May, pp. 164–172, 2018, doi: 10.1016/j.cej.2018.05.190.

[66] K. Diab et al., “Enhancing the Water Sorption Kinetics and Thermophysical Properties of Zirconium Metal-Organic Frameworks for More Efficient Sorption-Driven Applications,” SSRN Electron. J., 2022, doi: 10.2139/ssrn.4185990.

[67] I. P. Koronaki, E. Papoutsis, V. Papaefthimiou, and E. Rogdakis, “Numerical and experimental analysis of a solid desiccant wheel,” Therm. Sci., vol. 20, no. 2, pp. 613–621, 2016, doi: 10.2298/TSCI141118041K.

[68] R. Narayanan, Heat-driven cooling technologies. Elsevier Inc., 2017. doi: 10.1016/B978-0-12-805423-9.00007-7.

[69] A. M. Hamed, W. R. Abd-Elrahman, S. H. El-Emam, and M. M. Awad, “Theoretical and experimental investigation on the transient coupled heat and mass transfer in a radial flow desiccant packed bed,” Energy Convers. Manag., vol. 65, pp. 262–271, 2013, doi: 10.1016/j.enconman.2012.07.025.

[70] W. L. Hsu, S. Paul, J. A. Shamim, K. Kitaoka, and H. Daiguji, “Design and performance evaluation of a multilayer fixed-bed binder-free desiccant dehumidifier for hybrid air-conditioning systems: Part II – Theoretical analysis,” Int. J. Heat Mass Transf., vol. 116, pp. 1370–1378, 2018, doi: 10.1016/j.ijheatmasstransfer.2017.09.080.

[71] M. Mikhaeil, M. Gaderer, and B. Dawoud, “On the application of adsorber plate heat exchangers in thermally driven chillers; An experimental and analytical study,” Appl. Therm. Eng., vol. 220, no. November 2022, p. 119713, 2023, doi: 10.1016/j.applthermaleng.2022.119713.

[72] T. Venegas, M. Qu, K. Nawaz, and L. Wang, “Critical review and future prospects for desiccant coated heat exchangers: Materials, design, and manufacturing,” Renew. Sustain. Energy Rev., vol. 151, 2021, doi: 10.1016/j.rser.2021.111531.

[73] S. Stefański, Ł. Mika, K. Sztekler, W. Kalawa, Ł. Lis, and W. Nowak, “Adsorption bed configurations for adsorption cooling application,” E3S Web Conf., vol. 108, 2019, doi: 10.1051/e3sconf/201910801010.

[74] M. M. Saleh, R. Al-Dadah, S. Mahmoud, E. Elsayed, and O. El-Samni, “Wire fin heat exchanger using aluminium fumarate for adsorption heat pumps,” Appl. Therm. Eng., vol. 164, no. April 2019, p. 114426, 2020, doi: 10.1016/j.applthermaleng.2019.114426.

[75] P. Vivekh, M. Kumja, D. T. Bui, and K. J. Chua, “Recent developments in solid desiccant coated heat exchangers – A review,” Appl. Energy, vol. 229, no. August, pp. 778–803, 2018, doi: 10.1016/j.apenergy.2018.08.041.

[76] T. Zakirov, A. Galeev, and M. Khramchenkov, “Drainage and impregnation capillary pressure curves calculated by the X-ray CT model of Berea sandstone using Lattice Boltzmann’s method,” IOP Conf. Ser. Earth Environ. Sci., vol. 155, no. 1, pp. 0–9, 2018, doi: 10.1088/1755-1315/155/1/012012.

[77] M. Rivera-Torrente et al., “Understanding the Effects of Binders in Gas Sorption and Acidity of Aluminium Fumarate Extrudates,” Chem. - A Eur. J., vol. 28, no. 5, pp. 1–11, 2022, doi: 10.1002/chem.202103420.

[78] T. Venegas, M. Qu, K. Nawaz, and L. Wang, “Critical review and future prospects for desiccant coated heat exchangers: Materials, design, and manufacturing,” Renewable and Sustainable Energy Reviews, vol. 151. Elsevier Ltd, Nov. 01, 2021. doi: 10.1016/j.rser.2021.111531.

[79] V. Prabakaran and K. J. Chua, “Current State-of-the-Art in Desiccant Dehumidifiers BT - Advances in Desiccant Dehumidification: From Fundamentals to Applications,” V. Prabakaran and K. J. Chua, Eds. Cham: Springer International Publishing, 2021, pp. 23–48. doi: 10.1007/978-3-030-80843-3_2.

[80] H. Yanagi, “Silica Gel / Water Adsorption — Cooling System,” pp. 1–7, 2015.

[81] J. J. Guilleminot, A. Choisier, J. B. Chalfen, S. Nicolas, and J. L. Reymoney, “Heat transfer intensification in fixed bed adsorbers,” Heat Recover. Syst. CHP, vol. 13, no. 4, pp. 297–300, 1993, doi: 10.1016/0890-4332(93)90052-W.

[82] H. Demir, M. Mobedi, and S. Ülkü, “A review on adsorption heat pump: Problems and solutions,” Renew. Sustain. Energy Rev., vol. 12, no. 9, pp. 2381–2403, 2008, doi: 10.1016/j.rser.2007.06.005.

[83] I. Albaik, K. Diab, R. Al-Dadah, S. Mahmoud, and M. A. Ismail, “Coating Thickness Effect on the Cyclic Performance of Aluminum and Zirconium Metal-Organic Frameworks for Heat Pump Application,” 2021, vol. 22. doi: https://doi.org/10.46855/energy-proceedings-9428.

[84] A. Fattah-alhosseini, M. Karbasi, and H. Bahramian, “A thorough investigation of the utilization of metal-organic framework (MOF) coated titanium dioxide in photocatalytic applications: A review,” Appl. Surf. Sci. Adv., vol. 18, no. October, p. 100504, 2023, doi: 10.1016/j.apsadv.2023.100504.

[85] I. Albaik et al., “A comparison between the packed and coated finned tube for adsorption system using aluminium fumarate: Numerical study,” Therm. Sci. Eng. Prog., vol. 22, no. January, p. 100859, 2021, doi: 10.1016/j.tsep.2021.100859.

[86] J. A. Shamim, W. L. Hsu, S. Paul, L. Yu, and H. Daiguji, “A review of solid desiccant dehumidifiers: Current status and near-term development goals in the context of net zero energy buildings,” Renew. Sustain. Energy Rev., vol. 137, no. March 2020, p. 110456, 2021, doi: 10.1016/j.rser.2020.110456.

[87] A. S. Valarezo, X. Y. Sun, T. S. Ge, Y. J. Dai, and R. Z. Wang, “Experimental investigation on performance of a novel composite desiccant coated heat exchanger in summer and winter seasons,” Energy, vol. 166, pp. 506–518, 2019, doi: 10.1016/j.energy.2018.10.092.

[88] A. Kumar and R. Pratap, “Regeneration of Solid Desiccant Materials by Parabolic Dish Collector : A Review,” vol. 6, no. 2, pp. 1552–1556, 2018.

[89] H. Demir, “Comparison of Microwave and Conventional Driven Adsorption Heat Pump Cycle Duration,” Int. J. Eng. Technol. IJET, vol. 1, no. 1, p. 8, 2015, doi: 10.19072/ijet.49991.

[90] S. M. Lu and W. J. Yan, “Development and experimental validation of a full-scale solar desiccant enhanced radiative cooling system,” Renew. Energy, vol. 6, no. 7, pp. 821–827, 1995, doi: 10.1016/0960-1481(95)00069-V.

[91] I. Albaik, M. Badawy Elsheniti, R. Al-Dadah, S. Mahmoud, and İ. Solmaz, “Numerical and experimental investigation of multiple heat exchanger modules in cooling and desalination adsorption system using metal organic framework,” Energy Convers. Manag., vol. 251, no. November 2021, 2022, doi: 10.1016/j.enconman.2021.114934.

[92] Y. Yao, W. Zhang, and B. He, “Investigation on the kinetic models for the regeneration of silica gel by hot air combined with power ultrasonic,” Energy Convers. Manag., vol. 52, no. 11, pp. 3319–3326, 2011, doi: 10.1016/j.enconman.2011.06.002.

[93] C. Ellison, J. Hoffman, and D. Shekhawat, “Comparison of microwave and conventional heating for CO2 desorption from zeolite 13X,” Int. J. Greenh. Gas Control, vol. 107, no. March, p. 103311, 2021, doi: 10.1016/j.ijggc.2021.103311.

[94] W. Yang, W. Wang, Z. Ding, Z. Wang, X. Zhao, and S. He, “Performance study of a novel solar solid dehumidification/regeneration bed for use in buildings air conditioning systems,” Energies, vol. 10, no. 9, 2017, doi: 10.3390/en10091335.

[95] B. Li, L. Hua, Y. Tu, and R. Wang, “A Full-Solid-State Humidity Pump for Localized Humidity Control,” Joule, vol. 3, no. 6, pp. 1427–1436, 2019, doi: 10.1016/j.joule.2019.03.018.

[96] M. Kubota, N. Hanaoka, H. Matsuda, and A. Kodama, “Dehumidification behavior of cross-flow heat exchanger type adsorber coated with aluminophosphate zeolite for desiccant humidity control system,” Appl. Therm. Eng., vol. 122, pp. 618–625, 2017, doi: 10.1016/j.applthermaleng.2017.05.047.

[97] Y. Zhao, Y. J. Dai, T. S. Ge, H. H. Wang, and R. Z. Wang, “A high performance desiccant dehumidification unit using solid desiccant coated heat exchanger with heat recovery,” Energy Build., vol. 116, pp. 583–592, 2016, doi: 10.1016/j.enbuild.2016.01.021.

[98] H. H. Wang, T. S. Ge, X. L. Zhang, and Y. Zhao, “Experimental investigation on solar powered self-cooled cooling system based on solid desiccant coated heat exchanger,” Energy, vol. 96, pp. 176–186, 2016, doi: 10.1016/j.energy.2015.12.067.

[99] L. H. Zhao, R. Z. Wang, and T. S. Ge, “Desiccant coated heat exchanger and its applications,” International Journal of Refrigeration, vol. 130. Elsevier Ltd, pp. 217–232, Oct. 01, 2021. doi: 10.1016/j.ijrefrig.2021.06.008.

[100] Y. D. Tu, R. Z. Wang, T. S. Ge, and X. Zheng, “Comfortable, high-efficiency heat pump with desiccant-coated, water-sorbing heat exchangers,” Sci. Rep., vol. 7, Jan. 2017, doi: 10.1038/srep40437.

[101] Y. Jiang, T. S. Ge, R. Z. Wang, and L. M. Hu, “Experimental investigation and analysis of composite silica-gel coated fin-tube heat exchangers,” Int. J. Refrig., vol. 51, pp. 169–179, 2015, doi: 10.1016/j.ijrefrig.2014.11.012.

[102] A. Kumar and A. Yadav, “Experimental investigation of solar driven desiccant air conditioning system based on silica gel coated heat exchanger,” Int. J. Refrig., vol. 69, pp. 51–63, 2016, doi: 10.1016/j.ijrefrig.2016.05.008.

[103] K. Y. Li, W. J. Luo, B. Y. Tsai, and Y. Der Kuan, “Performance analysis of two-stage solid desiccant densely coated heat exchangers,” Sustain., vol. 12, no. 18, Sep. 2020, doi: 10.3390/SU12187357.

[104] T. S. Ge, Y. J. Dai, and R. Z. Wang, “Performance study of silica gel coated fin-tube heat exchanger cooling system based on a developed mathematical model,” Energy Convers. Manag., vol. 52, no. 6, pp. 2329–2338, 2011, doi: 10.1016/j.enconman.2010.12.047.

[105] T. S. Ge, W. Cao, X. Pan, Y. J. Dai, and R. Z. Wang, “Experimental investigation on performance of desiccant coated heat exchanger and sensible heat exchanger operating in series,” Int. J. Refrig., vol. 83, pp. 88–98, 2017, doi: 10.1016/j.ijrefrig.2017.07.005.

[106] L. M. Hu, T. S. Ge, Y. Jiang, and R. Z. Wang, “Performance study on composite desiccant material coated fin-tube heat exchangers,” Int. J. Heat Mass Transf., vol. 90, pp. 109–120, 2015, doi: 10.1016/j.ijheatmasstransfer.2015.06.033.

[107] S. J. Oh et al., “Studying the performance of a dehumidifier with adsorbent coated heat exchangers for tropical climate operations,” Sci. Technol. Built Environ., vol. 23, no. 1, pp. 127–135, 2017, doi: 10.1080/23744731.2016.1218234.

[108] X. Y. Sun, Y. J. Dai, T. S. Ge, Y. Zhao, and R. Z. Wang, “Comparison of performance characteristics of desiccant coated air-water heat exchanger with conventional air-water heat exchanger – Experimental and analytical investigation,” Energy, vol. 137, pp. 399–411, 2017, doi: 10.1016/j.energy.2017.03.078.

[109] X. Y. Sun, Y. J. Dai, T. S. Ge, Y. Zhao, and R. Z. Wang, “Experimental and comparison study on heat and moisture transfer characteristics of desiccant coated heat exchanger with variable structure sizes,” Appl. Therm. Eng., vol. 137, pp. 32–46, Jun. 2018, doi: 10.1016/j.applthermaleng.2018.03.071.

[110] X. Y. Sun, Y. J. Dai, T. S. Ge, Y. Zhao, and R. Z. Wang, “Heat and mass transfer comparisons of desiccant coated microchannel and fin-and-tube heat exchangers,” Appl. Therm. Eng., vol. 150, pp. 1159–1167, Mar. 2019, doi: 10.1016/j.applthermaleng.2019.01.071.

[111] P. Lertboonkankit and S. Chirarattananon, “Experimental investigation on a desiccant air dehumidifier constructed from a water-to-air heat exchanger,” Energy Procedia, vol. 138, pp. 628–634, 2017, doi: 10.1016/j.egypro.2017.10.174.

[112] P. Vivekh, D. T. Bui, Y. Wong, M. Kumja, and K. J. Chua, “Performance evaluation of PVA-LiCl coated heat exchangers for next-generation of energy-efficient dehumidification,” Appl. Energy, vol. 237, no. January, pp. 733–750, 2019, doi: 10.1016/j.apenergy.2019.01.018.

[113] T. S. Ge, Y. J. Dai, R. Z. Wang, and Z. Z. Peng, “Experimental comparison and analysis on silica gel and polymer coated fin-tube heat exchangers,” Energy, vol. 35, no. 7, pp. 2893–2900, 2010, doi: 10.1016/j.energy.2010.03.020.

[114] Y. Zhao, T. S. Ge, Y. J. Dai, and R. Z. Wang, “Experimental investigation on a desiccant dehumidification unit using fin-tube heat exchanger with silica gel coating,” Appl. Therm. Eng., vol. 63, no. 1, pp. 52–58, 2014, doi: 10.1016/j.applthermaleng.2013.10.018.

[115] X. Y. Sun, Y. J. Dai, T. S. Ge, Y. Zhao, and R. Z. Wang, “Comparison of performance characteristics of desiccant coated air- water heat exchanger with conventional air-water heat exchanger e Experimental and analytical investigation,” Energy, vol. 137, pp. 399–411, 2017, doi: 10.1016/j.energy.2017.03.078.

[116] P. Hou, K. Zu, M. Qin, and S. Cui, “A novel metal-organic frameworks based humidity pump for indoor moisture control,” Build. Environ., vol. 187, no. June 2020, p. 107396, 2021, doi: 10.1016/j.buildenv.2020.107396.

[117] A. Bhatia, “Principles of Evaporative Cooling System,” PDH Online | PDH Cent., vol. 231, pp. 1–55, 2012, [Online]. Available: http://www.pdhonline.org/courses/m231/m231.htm

[118] M. Ryhl, W. Brix, L. Ove, D. Version, and L. Ove, “Analysis of a solid desiccant cooling system with indirect evaporative cooling Bellemo,” 2017.

[119] N. Kapilan, A. M. Isloor, and S. Karinka, “A comprehensive review on evaporative cooling systems,” Results Eng., vol. 18, no. March, p. 101059, 2023, doi: 10.1016/j.rineng.2023.101059.

[120] R. Poku, T. W. Oyinki, and E. A. Ogbonnaya, “The Effects of Evaporative Cooling in Tropical Climate,” Am. J. Mech. Eng., vol. 5, no. 4, pp. 145–150, 2017, doi: 10.12691/ajme-5-4-5.

[121] G. Heidarinejad and H. Pasdarshahri, “Potential of a desiccant-evaporative cooling system performance in a multi-climate country,” Int. J. Refrig., vol. 34, no. 5, pp. 1251–1261, 2011, doi: 10.1016/j.ijrefrig.2011.03.008.

[122] O. Amer, R. Boukhanouf, and H. G. Ibrahim, “A Review of Evaporative Cooling Technologies,” Int. J. Environ. Sci. Dev., vol. 6, no. 2, pp. 111–117, 2015, doi: 10.7763/ijesd.2015.v6.571.

[123] Y. Zhou, Z. Yan, Q. Dai, and Y. Yu, “Experimental study on the performance of a novel hybrid indirect evaporative cooling/thermoelectric cooling system,” Build. Environ., vol. 207, no. PA, p. 108539, 2022, doi: 10.1016/j.buildenv.2021.108539.

[124] J. K. Jain and D. A. Hindoliya, “Energy saving potential of indirect evaporative cooler under Indian climates,” Int. J. Low-Carbon Technol., vol. 11, no. 2, pp. 193–198, 2016, doi: 10.1093/ijlct/ctt076.

[125] A. Zouaoui, L. Zili-Ghedira, and S. Ben Nasrallah, “Open solid desiccant cooling air systems: A review and comparative study,” Renew. Sustain. Energy Rev., vol. 54, pp. 889–917, 2016, doi: 10.1016/j.rser.2015.10.055.

[126] M. M. Rafique, P. Gandhidasan, A. Shafiqur Rehman, and L. M. Alhems, “Performance Analysis of a Desiccant Evaporative Cooling System Under Hot and Humid Conditions,” Environ. Prog. Sustain. Energy, vol. 33, no. 3, pp. 676–680, 2014, doi: 10.1002/ep.

[127] M. M. S. Dezfouli, S. Mat, G. Pirasteh, K. S. M. Sahari, K. Sopian, and M. H. Ruslan, “Simulation analysis of the four configurations of solar desiccant cooling system using evaporative cooling in tropical weather in Malaysia,” Int. J. Photoenergy, vol. 2014, 2014, doi: 10.1155/2014/843617.

[128] L. Merabti, M. Merzouk, N. Kasbadji Merzouk, and W. Taane, “Performance study of solar driven solid desiccant cooling system under Algerian coastal climate,” Int. J. Hydrogen Energy, vol. 42, no. 48, pp. 28997–29005, 2017, doi: 10.1016/j.ijhydene.2017.08.067.

[129] T. S. Ge, Y. Li, R. Z. Wang, and Y. J. Dai, “Experimental study on a two-stage rotary desiccant cooling system,” Int. J. Refrig., vol. 32, no. 3, pp. 498–508, 2009, doi: 10.1016/j.ijrefrig.2008.07.001.

[130] J. D. Chung, D. Y. Lee, and S. M. Yoon, “Optimization of desiccant wheel speed and area ratio of regeneration to dehumidification as a function of regeneration temperature,” Sol. Energy, vol. 83, no. 5, pp. 625–635, May 2009, doi: 10.1016/j.solener.2008.10.011.

[131] G. Angrisani, F. Minichiello, C. Roselli, and M. Sasso, “Experimental analysis on the dehumidification and thermal performance of a desiccant wheel,” Appl. Energy, vol. 92, pp. 563–572, 2012, doi: 10.1016/j.apenergy.2011.11.071.

[132] E. A. Tiwari, “Design and Fabrication of Desiccant Wheel Dehumidifier,” Int. J. Adv. Res. Mech. Eng. Technol., vol. 1, no. 1, pp. 7–16, 2015.

[133] S. De Antonellis, M. Intini, C. M. Joppolo, L. Molinaroli, and F. Romano, “Desiccant wheels for air humidification: An experimental and numerical analysis,” Energy Convers. Manag., vol. 106, pp. 355–364, 2015, doi: 10.1016/j.enconman.2015.09.034.

[134] A. Alahmer, S. Alsaqoor, and G. Borowski, “Effect of parameters on moisture removal capacity in the desiccant cooling systems,” Case Stud. Therm. Eng., vol. 13, no. November 2018, p. 100364, 2019, doi: 10.1016/j.csite.2018.11.015.

[135] C. Wang, L. Hua, H. Yan, B. Li, Y. Tu, and R. Wang, “A Thermal Management Strategy for Electronic Devices Based on Moisture Sorption-Desorption Processes,” Joule, vol. 4, no. 2, pp. 435–447, 2020, doi: 10.1016/j.joule.2019.12.005.

[136] T. S. Ge, F. Ziegler, and R. Z. Wang, “A mathematical model for predicting the performance of a compound desiccant wheel (A model of compound desiccant wheel),” Appl. Therm. Eng., vol. 30, no. 8–9, pp. 1005–1015, 2010, doi: 10.1016/j.applthermaleng.2010.01.012.

[137] P. Majumdar and W. M. Worek, “Combined heat and mass transfer in a porous adsorbent,” Energy, vol. 14, no. 3, pp. 161–175, 1989, doi: 10.1016/0360-5442(89)90059-5.

[138] R. Narayanan, “Solid and gas-side resistance of a silica-gel disccant wheel,” in Energy Procedia, 2019, vol. 160, pp. 139–146. doi: 10.1016/j.egypro.2019.02.129.

[139] M. Beccali, F. Butera, R. Guanella, and R. S. Adhikari, “Simplified models for the performance evaluation of desiccant wheel dehumidification,” Int. J. Energy Res., vol. 27, no. 1, pp. 17–29, 2003, doi: 10.1002/er.856.

[140] X. J. Zhang, Y. J. Dai, and R. Z. Wang, “A simulation study of heat and mass transfer in a honeycombed rotary desiccant dehumidifier,” Appl. Therm. Eng., vol. 23, no. 8, pp. 989–1003, 2003, doi: 10.1016/S1359-4311(03)00047-4.

[141] Y. Weixing, Z. Yi, L. Xiaoru, and Y. Xiugan, “Study of a new modified cross-cooled compact solid desiccant dehumidifier,” Appl. Therm. Eng., vol. 28, no. 17–18, pp. 2257–2266, 2008, doi: 10.1016/j.applthermaleng.2008.01.006.

[142] T. S. Ge, Y. J. Dai, Y. Li, and R. Z. Wang, “Simulation investigation on solar powered desiccant coated heat exchanger cooling system,” Appl. Energy, vol. 93, pp. 532–540, 2012, doi: 10.1016/j.apenergy.2011.11.089.

[143] M. Jagirdar and P. S. Lee, “Mathematical modeling and performance evaluation of a desiccant coated fin-tube heat exchanger,” Appl. Energy, vol. 212, no. September 2017, pp. 401–415, 2018, doi: 10.1016/j.apenergy.2017.12.038.

[144] A. Rahnama, M. Amani, and M. Bahrami, “Analytical solution for heat and mass transfer in desiccant coated heat exchangers,” Appl. Therm. Eng., vol. 219, no. PA, p. 119467, 2023, doi: 10.1016/j.applthermaleng.2022.119467.

[145] L. Liu et al., “Numerical modelling and parametric study of an air-cooled desiccant coated cross-flow heat exchanger,” Appl. Therm. Eng., vol. 169, no. December 2019, p. 114901, 2020, doi: 10.1016/j.applthermaleng.2020.114901.

[146] L. Yadav and A. Yadav, “Mathematical investigation of purge sector angle for clockwise and anticlockwise rotation of desiccant wheel,” Appl. Therm. Eng., vol. 93, pp. 839–848, 2016, doi: 10.1016/j.applthermaleng.2015.10.062.

[147] T. S. Ge, Y. Li, R. Z. Wang, and Y. J. Dai, “A review of the mathematical models for predicting rotary desiccant wheel,” Renew. Sustain. Energy Rev., vol. 12, no. 6, pp. 1485–1528, 2008, doi: 10.1016/j.rser.2007.01.012.

[148] A. Yadav and L. Yadav, “Comparative performance of desiccant wheel with effective and ordinary regeneration sector using mathematical model,” Heat Mass Transf. und Stoffuebertragung, vol. 50, no. 10, pp. 1465–1478, 2014, doi: 10.1007/s00231-014-1349-6.

[149] J. Y. San and S. C. Hsiau, “Effect of axial solid heat conduction and mass diffusion in a rotary heat and mass regenerator,” Int. J. Heat Mass Transf., vol. 36, no. 8, pp. 2051–2059, 1993, doi: 10.1016/S0017-9310(05)80136-X.

[150] A. YADAV, “Evaluation and Optimization of Desiccant Wheel Performance,” Master of Technology, N.LT KURUKSHETRA, 2011.

[151] R. H. Mohammed, O. Mesalhy, M. L. Elsayed, and L. C. Chow, “Novel compact bed design for adsorption cooling systems: parametric numerical study,” Int. J. Refrig., 2017, doi: 10.1016/j.ijrefrig.2017.04.028.

[152] J. G. Lee, K. J. Bae, and O. K. Kwon, “Performance investigation of a two-bed type adsorption chiller with various adsorbents,” Energies, vol. 13, no. 10, May 2020, doi: 10.3390/en13102553.

[153] T. Splith et al., “Molecular Dynamics Phenomena of Water in the Metalorganic Framework MIL-100(Al), as Revealed by Pulsed Field Gradient NMR and Atomistic Simulation,” vol. 100, 2017, doi: 10.1021/acs.jpcc.7b06240.

[154] Z. Yu, J. Deschamps, L. Hamon, P. Karikkethu Prabhakaran, and P. Pré, “Modeling hydrogen diffusion in hybrid activated carbon-MIL-101(Cr) considering temperature variations and surface loading changes,” Microporous Mesoporous Mater., vol. 248, pp. 72–83, 2017, doi: 10.1016/j.micromeso.2017.03.059.

[155] M. Davarpanah, Z. Hashisho, D. Crompton, and J. E. Anderson, “Modeling the performance of a metal-organic framework (MIL-101) for the adsorption of toluene in an industrial fluidized bed adsorber and comparison to other adsorbent materials,” Sep. Purif. Technol., vol. 288, no. February, p. 120685, 2022, doi: 10.1016/j.seppur.2022.120685.

[156] S. Krishnamurthy, R. Blom, M. C. Ferrari, and S. Brandani, “Edinburgh Research Explorer Adsorption and diffusion of CO2 in CPO-27 – Ni beads,” Adsorption, 2019, doi: 10.1007/s10450-019-00162-x.

[157] D. B. Jani, M. Mishra, and P. K. Sahoo, “Experimental investigations on hybrid solid desiccant - Vapor compression air-conditioning system for Indian climate,” Refrig. Sci. Technol., no. September, pp. 3041–3049, 2015, doi: 10.18462/iir.icr.2015.0229.

[158] J. D. Chung and D. Y. Lee, “Effect of desiccant isotherm on the performance of desiccant wheel,” Int. J. Refrig., vol. 32, no. 4, pp. 720–726, 2009, doi: 10.1016/j.ijrefrig.2009.01.003.

[159] O. O. Rabhy, I. G. Adam, M. Elsayed Youssef, A. B. Rashad, and G. E. Hassan, “Numerical and experimental analyses of a transparent solar distiller for an agricultural greenhouse,” Appl. Energy, 2019, doi: 10.1016/j.apenergy.2019.113564.

[160] J. Lim, W. Han, L. T. H. Thang, Y. W. Lee, and J. H. Shin, “Customizable Nichrome Wire Heaters for Molecular Diagnostic Applications,” Biosensors, vol. 14, no. 3, 2024, doi: 10.3390/bios14030152.

[161] I. Albaik, K. E. Diab, R. Al-Dadah, and S. Mahmoud, “Zirconium Metal Organic Framework / Graphene Nanoplatelets Composite for More Efficient Cooling and Desalination Adsorption System.”

[162] A. N. Aziz et al., “MOF-801/Graphene Adsorbent Material for Greenhouse Climate Control System—Numerical Investigation,” Energies, vol. 16, no. 9, 2023, doi: 10.3390/en16093864.

[163] K. Diab, “Novel Composite Metal-Organic Frameworks Materials For Efficient Atmospheric Water Harvesting, Master of Research”, University of Birmingham, 2023.

[164] C. C. Chang, W. J. Luo, C. W. Lu, Y. S. Cheng, B. Y. Tsai, and Z. H. Lin, “Effects of process air conditions and switching cycle period on dehumidification performance of desiccant-coated heat exchangers,” Science and Technology for the Built Environment, vol. 23, no. 1, pp. 81–90, 2017, doi: 10.1080/23744731.2016.1210971.

[165] C. Multiphysics, “Heat Transfer Module,” © 1998–2018 Comsol, pp. 1–222, 2015, [Online].Available:https://doc.comsol.com/5.4/doc/com.comsol.help.heat/HeatTransferModuleUsersGuide.pdf

[166] COMSOL Multiphysics, “AC / DC Module User ’ s Guide,” © 1998–2019 Comsol, p. 300, 2019.[Online]. Available: https://doc.comsol.com/5.4/doc/com.comsol.help.acdc/ACDCModuleUsersGuide.pdf

[167] H. Tun and C. C. Chen, “Isosteric heat of adsorption from thermodynamic Langmuir isotherm,” Adsorption, vol. 27, no. 6, pp. 979–989, 2021, doi: 10.1007/s10450-020-00296-3.

[168] I. Solmuş, C. Yamali, C. Yildirim, and K. Bilen, “Transient behavior of a cylindrical adsorbent bed during the adsorption process,” Appl. Energy, vol. 142, pp. 115–124, 2015, doi: 10.1016/j.apenergy.2014.12.080.

[169] M. J. Lampinen, “Thermodynamics of humid air,” Dep. Energy Technol. Ene-39.4027-Mass Transf. P, p. 39, 2015.

[170] I. Albaik, “Numerical and experimental development of an efficient adsorption desalination and cooling system”, Doctor of Philosophy,” University of Birmingham 2022.

[171] A. N. Aziz, S. Mahmoud, R. Al-Dadah, M. A. Ismail, and M. K. Al Mesfer, “Numerical and experimental investigation of desiccant cooling system using metal organic framework materials,” Appl. Therm. Eng., vol. 215, no. July, p. 118940, 2022, doi: 10.1016/j.applthermaleng.2022.118940.

[172] Dr. R. S. Bindu, Akshay Naik, Neeraj Kumar, Nirmal Choudhary, and Prakhar Gupta, “Design of Indirect Evaporative Cooler,” Int. J. Eng. Res., vol. V6, no. 06, pp. 253–260, 2017, doi: 10.17577/ijertv6is060118.

[173] I. Kovačević and M. Sourbron, “The numerical model for direct evaporative cooler,” Appl. Therm. Eng., vol. 113, pp. 8–19, 2017, doi: 10.1016/j.applthermaleng.2016.11.025.

[174] I. H. Bell, J. Wronski, S. Quoilin, and V. Lemort, “Pure and pseudo-pure fluid thermophysical property evaluation and the open-source thermophysical property library coolprop,” Ind. Eng. Chem. Res., vol. 53, no. 6, pp. 2498–2508, 2014, doi: 10.1021/ie4033999.

## AppendixI: Matlab Greenhouse Code

```
clc
clear all

% Greenhouse feeding heat exchanger

 Tp = 45;  %% from desiccant wheel point 3

 Tw = 30 ; %% from greenhouse

 phi_in=.75;

  w1=py.CoolProp.CoolProp.HAPropsSI('W','T',Tw+273,'P',101325,'R',phi_in);

%% input prameters for in direct heat exchanger
 t = 0.4 % Thickness of plates

 L = 0.6 % Length of plates,

 a = 0.4 %Width of plates,

 segma= 4e-3; %Channel width,

 n = 70; %No of plates,

 At = 16.8; %Total heat exchange area

 V = 2.5; %Velocity of primary air

Vs = 2.5; %Velocity of secondary air




% V = input (' Velocity of primary air at inlet (m/s) = ');

% n = input ('No. of plates = ');
% t = input (Thickness of plates (mm) = ');
% a = input (Width of plates (m) = ');
% L = input (Length of plates (m) = ');
% segma = input (Channel width (m) = ');
Cp = 1005;
Pr = 0.711;
k = 0.027;
neu = 16.97*10^-6;
roh_air = 1.127;
Re = (V*L)/ neu;
```

```
hp = (0.664*(Re^0.5)) * (Pr^(1/3) *k)/L;
CA = ( segma /2) * a* n;
mp = (roh_air *CA*V)*3600;
Vp = mp/ roh_air;
At = n*a*L;
Uz = hp;
A = (-Uz * a * n * 3600) / ( mp * Cp) ;
x=0 ;
for i =1:60
 x = x + 0.01;
 T = ( Tp - Tw ) *exp( A * x ) + Tw ;
if i==1
fprintf(' T(0.000000)=%f\n ', Tp);
end
fprintf(' T(%f)=%f\n ',x,T);
end
fprintf(' T(0.000000) = %f °C\n ', Tp);
fprintf(' T(%f) = %f °C\n ', x , T );
fprintf(' Volume flow rate = %f m3/hr\n ', Vp ) ;
fprintf(' Mass flow rate = %f kg/hr\n ', mp ) ;
fprintf(' Total heat exchange Area = %f\n ', At ) ;
x = [ 0.0:0.01:0.6 ] ;
y = ( Tp- Tw ) * exp(A * x) + Tw ;
plot (x,y) ;
Yap=5/1000;

%%%
```

```
To=273+20;

Do=((1-epth)*5.47e-12)/1.163;       %Molecular difftisivity

%V=2423;            %Latent heat of Condensation


Sh=2.5;            %Sher wood number

Cpa=1005;          %Specific heat of air

Ka=0.16;          %Thermal conductivity

Nu=2.45;           %Nusselt number

h=(Nu*Ka*C)/(4*Af);%Convective heat transfer coefficient

Cpv=1864;          %specific heat of water vapours

Cpd=715;           %Specific heat of desiccant

Kd=140;          %Thermal conductivity

Mdot=9.1/60; %Kg/s


AreaDuct=0.17*.17;

Mdotchannel=Af*0.000049*u; %Kg/s

CHnumber=1;


%%%%%%%%%%%%%% %
%Initialize Time
%%%%%%%%%%%%%% %
t(1)=0; %InitialisingTimestep

Dt=0.175;%Local distance between adjacent time steps

numt=8; %Total Time Steps
%%%%%%%%%%%%%% %
%TimeStepsandnumberofdivisions
%%%%%%%%%%%%%% %
Lw=0.33 ;         %Length of the Channels along the channel

ndivs=8;

numx=ndivs+1;

Dx=Lw/ndivs;      %Local distance between adjacent points in space

z=0:Dx:Lw;
```

```
%%%%%%%%%%%%%% %
%Defining Air and Desiccant Initial conditions
%%%%%%%%%%%%%% %
Wpro_initial=91/1000; %Moisture content in Desiccant

Tdpro_initial=76+273; %Temperature of air >>>>>>>> 31 degree &1

Ydpro_initial=4.1e-003; %Humidity ratio of Air in equilibrium with
Desiccant

 Tapro_initial=273+(Tp-y(1,61)+Tw); %Temperature of Air(Process)


%
Yapro_initial=py.CoolProp.CoolProp.HAPropsSI('W','T',Tapro_initial,'P',1013
25,'R',phi_in); %%%%%Moisturecontent in Air from greenhouse

 Yapro_initial=w1;
% Tapro_initial=273+38.52; %Temperature of Air(Process)

% Yapro_initial=35/1000;


Tareg_initial=76+293; %Temperature of Air(Regeneration)



% Hfg=(2504.4-2.4425*(Tdpro_initial-273));  %Latent heat of Condensation
Hfg=2400;
total_mass_needed=CHnumber*Pe*Lw*Thegma*roh_d;   % MOF Mass gramms


Cycle=0; %Initialising Process
Cyclenum=7; %Total process length
for n=1:Cyclenum
Cycle = Cycle+1;
%%%%%%%%%%%%%%%
%Section2
%%%%%%%%%%%%%% %
%Process Region
%Process Phase constants
%%%%%%%%%%%%%% %
Tpro=Tapro_initial;     %Temperature as sociated with mass transfer
coefficient
Dpro=(2.302e-5)*(Po/Patm)*((Tpro/To)^1.81);
Kypro=(roh_a*Sh*Dpro*C)/(4*Af); %Coefficient of massconvection
Tdpro(1)=Tdpro_initial;
Wpro(1)= Wpro_initial;
Qstpro=Hfg*(1+(0.2843*exp(-10.28*Wpro(1))));%Heat of sorption
Depro=(Do*exp((-0.974e-3)*(Qstpro/Tdpro(1)))); %Desiccant effective
diffusivity
%%%%%%%%%%%%%%%
%Defining initial air and desiccant parameters in a selected domain
%under process section
%Initial Conditions left and wright colmns
%%%%%%%%%%%%%%%
  for i=1:numx
  Yapro(i,1)= Yapro_initial;
```

```
  Wpro(i,1)=  Wpro_initial;
  Tapro(i,1)= Tapro_initial;
  Tdpro(i,1)= Tdpro_initial;
  Ydpro(i,1)= Ydpro_initial;
  end
for i=1:numx
  for j=numt+1 %final cell of the diagonal B.C.
  Yapro(i,j)= Yapro_initial;
  Wpro(i,j)=  Wpro_initial;
  Tapro(i,j)= Tapro_initial;
  Tdpro(i,j)= Tdpro_initial;
  Ydpro(i,j)= Ydpro_initial;
  RHpro=zeros(numx,numt+1);
  end
end
%%%%%%%%%%%%%% %
%Initial Conditions for Process Air Top and bottom
%%%%%%%%%%%%%% %
for j=1:numt+1
    Yapro(1,j)=Yapro_initial;
    Tapro(1,j)=Tapro_initial;
end

for j=1:numt%Starting of Process time step
t(j+1)=t(1)+Dt;
%%%%%%%%%%%%%% %
%Finite difference equation representation for moisture conservation in air
%%%%%%%%%%%%%% %
for i=2:numx
Ka=((Kypro*(Ydpro(i,j)))+((Dh*roh_a*Yapro(i,j))/Dt));
Aa=(((Dh*roh_a)/Dt)+((Dh*roh_a*u)/Dx)+Kypro);
Ba=(((Dh*roh_a*u)/Dx));
Yapro(i,j+1)=((Ka+(Ba*Yapro(i-1,j)))/Aa) ;
%%%%%%%%%%%%%% %
%Finite difference equation representation for energy conservation in air
%%%%%%%%%%%%%%%
Rb=(h*Tdpro(i,j))+(Cpv*Kypro*(Ydpro(i,j)-Yapro(i,j))*Tdpro(i,j));
Sb=(Dh*Cpa*roh_a)/Dt;
Ab=(((Dh*Cpa*roh_a)/Dt)+((Dh*Cpa*roh_a*u)/(Dx))+h+(Cpv*Kypro*(Ydpro(i,j)-
Yapro(i,j))));
Bb=(((Dh*Cpa*roh_a*u)/(Dx)));
Cb=(((Ka*Dh)/(Dx*Dx)));
Kb=Rb+(Sb*Tapro(i,j));
Tapro(i,j+1)=((Kb+(Bb*(Tapro(i-1,j))))/Ab);
end
%%%%%%%%%%%%%% %
%Finite difference equation representation for moisture conservation in
desiccant
%%%%%%%%%%%%%%%
for i=2:numx-1
Rc=Kypro*(Yapro(i,j+1)-Ydpro(i,j+1));
Sc=(roh_d*Thegma)/Dt;
Ac=(((roh_d*Thegma)/Dt)+((2*Depro*roh_d*Thegma)/(Dx*Dx)));
Bc=(((Depro*roh_d*Thegma)/(Dx*Dx)));
Cc=(((Depro*roh_d*Thegma)/(Dx*Dx)));
Kc=Rc+(Sc*Wpro(i,j));
Wpro(1,j+1)=((Kc+((Cc+Bc)*(Wpro(i+1,j+1))))/Ac);
Wpro(i,j+1)=((Kc+(Cc*(Wpro(i-1,j+1)))+(Bc*(Wpro(i+1,j+1))))/Ac);
%%%%%%%%%%%%%% %
%Finite difference equation representation for energy conservation in
desiccant
```

```
%%%%%%%%%%%%%% %
Rd=((h*Tapro(i,j+1))+(Kypro*(Yapro(i,j+1)-
Ydpro(i,j+1))*Qstpro)+(Cpv*Kypro*(Yapro(i,j+1)-
Ydpro(i,j+1))*Tapro(i,j+1)));
Sd=(Cpd*roh_d*Thegma)/Dt;
Ad=(((Cpd*roh_d*Thegma)/Dt)+((2*Kd*Thegma)/(Dx*Dx))+h+(Cpv*Kypro*(Yapro(i,j
+1)-Ydpro(i,j+1))));
Bd=(((Kd*Thegma)/(Dx*Dx)));
Cd=(((Kd*Thegma)/(Dx*Dx)));
Kdd=Rd+(Sd*Tdpro(i,j));
Tdpro(1,j+1)=((Kdd+((Cd+Bd)*(Tdpro(i+1,j+1))))/Ad);
Tdpro(i,j+1)=((Kdd+(Cd*(Tdpro(i-1,j+1)))+(Bd*(Tdpro(i+1,j+1))))/Ad);
%%%%%%%%%%%%%% %
%Relation for Humidity ratio of Air in equilibrium with Desiccant
%%%%%%%%%%%%%% %
RHpro(i,j)= 302.92*((Wpro(i,j+1))^4) - 182.23*(Wpro(i,j+1))^3 +
29.271*((Wpro(i,j+1))^2) - 0.3267*Wpro(i,j+1) - 0.0006;
Pvspro=exp(23.196-(3816.44/(Tdpro(i,j+1)-46.13))) ;
Ydpro(i,j+1)=((0.62188*RHpro(i,j))/((Patm/Pvspro)-RHpro(i,j)));
end
%%%%%%%%%%%%%% %
%Boundary conditions for moisture and energy balance in desiccant
%%%%%%%%%%%%%% %
Tdpro(numx,j+1)=((Kdd+((Cd+Bd)*(Tdpro(numx-1,j+1))))/Ad);

Wpro(numx,j+1)=((Kc+((Cc+Bc)*(Wpro(numx-1,j+1))))/Ac);

RHpro(i,j)=302.92*((Wpro(i,j+1))^4) - 182.23*(Wpro(i,j+1))^3 +
29.271*((Wpro(i,j+1))^2) - 0.3267*Wpro(i,j+1) - 0.0006;
Pvspro=exp(23.196-(3816.44/(Tdpro(numx-1,j+1)-46.13)));

Ydpro(numx,j+1)=((0.62188*RHpro(i,j))/((Patm/Pvspro)-RHpro(i,j)));
end
%%%%%%%%%%%%%%%
%Section3
%%%%%%%%%%%%%% %
%Regeneration Phase constants
%%%%%%%%%%%%%% %
Treg=Tareg_initial;%Temperature as sociated with mass transfer coefficient
Dreg=(2.302e-5)*(Po/Patm)*((Treg/To)^1.81);
Kyreg=(roh_a*Sh*Dreg*C)/(4*Af);%Coefficient of mass convection
Tdreg(1)=Tdpro(numx,numt+1);%Temp of desiccant
Wreg(1)=Wpro(numx,numt+1);
Qstreg=Hfg*(1+(0.2843*exp(-10.28*Wreg(1))));%Heatofsorption
Dereg=(Do*exp((-0.974e-
3)*(Qstreg/Tdreg(1))));%Desiccanteffectivediffiisivity
u1=u;%Velocity of regeneration air
%%%%%%%%%%%%%% %
%Defining initial air and desiccant parameters in a selected domain
%underprocesssection
%%%%%%%%%%%%%% %
for i=1:numx
Yareg(i,1)=0.017;
Wreg(i,1)=Wpro(numx,numt+1);
Tareg(i,1)=343;
Tdreg(i,1)=Tdpro(numx,numt+1);
Ydreg(i,1)=Ydpro(numx,numt+1);
end
for i=1:numx
for j=numt+1
Yareg(i,j)=0.017;
```

```
Wreg(i,j)=Wpro(numx,numt+1);
Tareg(i,j)=343;
Tdreg(i,j)=Tdpro(numx,numt+1);
Ydreg(i,j)=Ydpro(numx,numt+1);

end
end
%%%%%%%%%%%%%% %
%Initial Conditions for Regeneration Air
%%%%%%%%%%%%%% %
for j= 1:numt+1 %Starting of Regeneration time step
Yareg(1,j)=0.024;
Tareg(1,j)=343;
end

for j=1:numt
 t(j+1)= t(j)+Dt;
%%%%%%%%%%%%%% %
%Finite difference equation representation for moisture conservation in air
%%%%%%%%%%%%%%%
for i=2:numx
Ka=((Kyreg*(Ydreg(i,j)))+((Dh*roh_a*Yareg(i,j))/Dt));
Aa=(((Dh*roh_a)/Dt)-((Dh*roh_a*u1)/Dx)+Kyreg);
Ba=((-(Dh*roh_a*u1)/Dx));
Yareg(i,j+1)=((Ka+(Ba*Yareg(i-1,j)))/Aa);
%%%%%%%%%%%%%% %
%Finite difference equation representation for energy conservation in air
%%%%%%%%%%%%%%%
Rb=(h*Tdreg(i,j))+(Cpv*Kyreg*(Ydreg(i,j)-Yareg(i,j))*Tdreg(i,j));
Sb=(Dh*Cpa*roh_a)/Dt;
Ab=(((Dh*Cpa*roh_a)/Dt)+((Dh*Cpa*roh_a*u1)/(Dx))+h+(Cpv*Kyreg*(Ydreg(i,j)-
Yareg(i,j))));
Bb=(((Dh*Cpa*roh_a*u1)/(Dx)));
Cb=(((Ka*Dh)/(Dx*Dx)));
Kb=Rb+(Sb*Tareg(i,j));
Tareg(i,j+1)=((Kb+(Bb*(Tareg(i-1,j))))/Ab);
end
%%%%%%%%%%%%%% %
%Finitedifferenceequationrepresentationfo rmoistureconservation
%indesiccant
%%%%%%%%%%%%%%%
for i=2:numx-1
Rc=Kyreg*(Ydreg(i,j+1)-Yareg(i,j+1));
Sc=(roh_d*Thegma)/Dt;
Ac=(((roh_d*Thegma)/Dt)+((2*Dereg*roh_d*Thegma)/(Dx*Dx)));
Bc=(((Dereg*roh_d*Thegma)/(Dx*Dx)));
Cc=(((Dereg*roh_d*Thegma)/(Dx*Dx)));
Kc=Rc+(Sc*Wreg(i,j));
Wreg(1,j+1)=((Kc+((Cc+Bc)*(Wreg(i+1,j+1))))/Ac);
Wreg(i,j+1)=((Kc+(Cc*(Wreg(i-1,j+1)))+(Bc*(Wreg(i+1,j+1))))/Ac);
%%%%%%%%%%%%%% %
%Finite difference equation representation for energy conservation
%indesiccant
%%%%%%%%%%%%%% %
Rd=((h*Tareg(i,j+1))+(Kyreg*(Yareg(i,j+1)-
Ydreg(i,j+1))*Qstreg)+(Cpv*Kyreg*(Yareg(i,j+1)-
Ydreg(i,j+1))*Tareg(i,j+1)));
Sd=(Cpd*roh_d*Thegma)/Dt;
Ad=(((Cpd*roh_d*Thegma)/Dt)+((2*Kd*Thegma)/(Dx*Dx))+h+(Cpv*Kyreg*(Yareg(i,j
+1)-Ydreg(i,j+1))));
Bd=(((Kd*Thegma)/(Dx*Dx)));
```

```
Cd=(((Kd*Thegma)/(Dx*Dx)));
Kdd=Rd+(Sd*Tdreg(i,j));
Tdreg(1,j+1)=((Kdd+((Cd+Bd)*(Tdreg(i+1,j+1))))/Ad);
Tdreg(i,j+1)=((Kdd+(Cd*(Tdreg(i-1,j+1)))+(Bd*(Tdreg(i+1,j+1))))/Ad);
%%%%%%%%%%%%%% %
%Relation for Humidity ratio of Air in equilibrium with Desiccant
%%%%%%%%%%%%%% %
%Isotherm for 801
% RHpro(i,j)=52825*((Wpro(i,j+1))^4) - 35461*(Wpro(i,j+1))^3 +
8035*((Wpro(i,j+1))^2) - 609.64*Wpro(i,j+1) + 15.743;
RHpro(i,j)=302.92*((Wpro(i,j+1))^4) - 182.23*(Wpro(i,j+1))^3 +
29.271*((Wpro(i,j+1))^2) - 0.3267*Wpro(i,j+1) - 0.0006;
% RHpro(i,j)=1271*((Wpro(i,j+1))^6) - 2036*((Wpro(i,j+1))^5) +
1182.5*((Wpro(i,j+1))^4) - 289.39*(Wpro(i,j+1))^3 +
21.643*((Wpro(i,j+1))^2)+ 2.1688*Wpro(i,j+1) - 0.0119;
% RHpro(i,j)=(0.0078)-(0.05759*Wpro(i,j+1))+(24.16554*((Wpro(i,j+1))^2))-
(124.478*((Wpro(i,j+1))^3))+(204.226*((Wpro(i,j+1))^4));%RelativeHumidity
ofsilicagel
Pvspro=exp(23.196-(3816.44/(Tdpro(i,j+1)-46.13)));
Ydpro(i,j+1)=((0.62188*RHpro(i,j))/((Patm/Pvspro)-RHpro(i,j)));
end
%%%%%%%%%%%%%% %
%Boundary conditions for moisture and energy balance in desiccant
%%%%%%%%%%%%%% %
Tdreg(numx,j+1)=((Kdd+((Cd+Bd)*(Tdreg(numx-1,j+1))))/Ad);
Wreg(numx,j+1)=((Kc+((Cc+Bc)*(Wreg(numx-1,j+1))))/Ac);
RHreg=302.92*((Wreg(numx-1,j+1))^4) - 182.23*(Wreg(numx-1,j+1))^3 +
29.271*(Wreg(numx-1,j+1))^2 - 0.3267*Wreg(numx-1,j+1) - 0.0006;
Pvsreg=exp(23.196-(3816.44/(Tdreg(numx-1,j+1)-46.13)));
Ydreg(numx,j+1)=((0.62188*RHreg)/((Patm/Pvsreg)-RHreg));

end  %Ending of Process time step
%%%%%%%%%%%%%%
%Section4
%%%%%%%%%%%%%% %
%Assigning final values of desiccantas initial values for next cycle
%%%%%%%%%%%%%% %
Wpro_initial=Wreg(numx,numt+1);
Tdpro_initial=Tdreg(numx,numt+1);
Ydpro_initial=Ydreg(numx,numt+1);
%%%%%%%%%%%%%% %
%ResultGeneration
%Intheformofmatrixdefiningtheparticularcalculatedvariablesbothintimeandspac
e
%coordinates
%%%%%%%%%%%%%% %
%ForProcessSection
%%%%%%%%%%%%%% %
Yapro(:,:);%Process air moisturecontent
Tapro(:,:);%Process air temperature
Wpro(:,:);%Process side desiccant moisture content
Tdpro(:,:);%Process side desiccanttemperature
%%%%%%%%%%%%%% %
%ForRegenerationSection
%%%%%%%%%%%%%% %
Yareg(:,:);%Regeneration air moisture content
Tareg(:,:);%Regeneration air temperature
Wreg(:,:);%Regeneration side desiccant moisture content
Tdreg(:,:);%Regeneration side desiccant temperature
%%%%%%%%%%%%%% %
%Cofficiento fperformanc e(I nterm so flaten tcoolin gcapacity )
```

```
%%%%%%%%%%%%%%%%
COP=((Yapro_initial-Yapro(numx,numt+1))*Hfg)/(Tareg_initial-Tapro_initial)
end %Ending of Cycle

%%%%%%%%%%%%%%%%
```

```
fprintf(' Total heat exchange Area = %f\n ', At ) ;
x = [ 0.0:0.01:0.6 ] ;
y2 = ( Tp- Tw2 ) * exp(A * x) + Tw2 ;
plot (x,y2) ;
Yap=5/1000;
```

```
%%%%%%%%%%%%%%%%%%%%%%%%%%%%%%%%%%%%%%%%%%%%%%%%%%%%%%%%%%%%%%%%%%%%%%%%

Cpa=py.CoolProp.CoolProp.PropsSI("C",'P',101325,'Q',0,'air');
Cpv=py.CoolProp.CoolProp.PropsSI("C",'P',101325,'Q',0,'Water');
roh_a= py.CoolProp.CoolProp.PropsSI("D",'T',298.15,'P',101325,'air');

%%%%%
T_in=y2(1,61);
 W=Yapro(numt-1,numx-1);
%
phi_inv=py.CoolProp.CoolProp.HAPropsSI('R','T',(T_in+273),'P',101325,'W',W)
;
%
Tww=25+273;
Ws=py.CoolProp.CoolProp.HAPropsSI('W','T',Tww,'P',101325,'R',0.6);

%%%%%%%%%%%%%%%
D=1.7;  %distance between plates
Dva=1.87e-10*T_in^2.072;  %The diffusion coefficient of vapour in air

Nu=2.54;
Sh=2.54;
Dh=3.40e-3;

Ka=40;    %% air thermal conductivity
HT=Ka*Nu/Dh; % heat transfer coeffecient

HM=Dva*Sh/Dh; %mass transfer coeffecient
B=849;
Af=8.32e-3;
P=B*Af;
V=3;
Q=Af*V;
m_o=roh_a*Q;

%descritization
n=5;
t=0.5;
dt=0.01;
runs=t/dt + 1;
Deltax=1/n;
 tic;
 %%%%%%%%%%%%%%%%%%%%%%%%%%%%
zz=(Cpa+W*Cpv)/Deltax;
z=(P*HT+Cpv*P*HM*roh_a*(Ws-W))/m_o;
o= (P*HM*roh_a*Deltax)/m_o;
```

```
for i=1:1:n+1
    L(i)=(i-1)*Deltax;
end
TT = zeros(runs,n+1);
Ww = zeros(runs,n+1);
%Set initial conditions
TT(1,:)= T_in+273;
Ww(1,:)=W;
for i=1:1:runs  %% boundary conditions left and right
             TT(i,1) = T_in+273 ;
             TT(i,5) = T_in+273 ;

             Ww(i,1)=W;
             Ww(i,5)=W;
end
for j=2:1:n     %% boundary condions top and bottom
     TT(1,j)= T_in+273 ;
     Ww(1,j)= W ;
end
for j=1:1:runs-1 %%spatial domain
    for i=2:1:n %% time domain

        TT(j+1,i)=(zz/(zz-z))*TT(j,i)-(z/(zz-z))*Tww;
        Ww(j+1,i)=o*Ws+Ww(j,i)*(1-o);

    end


end
toc

%% psychromitric chart connection
axhandle=psychplotting(20,93,0,100); %TDB 10-40C and SH 6-30 g/kg

processdata=[  Tw            w1
%
%              y(1,61)   w1

            (Tapro_initial-273)    Yapro_initial

            (Tapro(numt-1,numx-1)-273)    Yapro(numt-1,numx-1)

             y2(1,61)                      Yapro(numt-1,numx-1)

             (TT(51,2)-273)                  Ww(51,2)
       ];

plot(axhandle,processdata(:,1),processdata(:,2)*1000,'-r+') %plot process
data on psychrometrics plot
for i=1:length(processdata) %plot process data numbers
htext =
text(processdata(i,1),processdata(i,2)*1000,num2str(i),'color','k','horizon
talalignment','left','verticalalignment','top','fontweight','bold');
end
```

## AppendixII: Arduino Code for Switching Scenarios and Controlling DCHEs

```
 unsigned char POWER_LEVEL;
int x;
void setup()
{
  pinMode(3,OUTPUT);  //  suction fan
pinMode(2,OUTPUT);  //  Evaporative fan
  ////////////////////
  pinMode(8,OUTPUT); // D1
  pinMode(9,OUTPUT); // D2
  pinMode(11,OUTPUT);// D3
  pinMode(12,OUTPUT); // D4
///////DCHE2
pinMode(4,OUTPUT);
pinMode(5,OUTPUT);
pinMode(6,OUTPUT);
pinMode(7,OUTPUT);
pinMode(10,OUTPUT);
///////DCHE1
pinMode(14,OUTPUT);
pinMode(15,OUTPUT);
pinMode(16,OUTPUT);
pinMode(17,OUTPUT);
pinMode(18,OUTPUT);
//// D5 & D6
pinMode(19,OUTPUT);
pinMode(20,OUTPUT);
//////////////////////////////
////////////////////////////////////////////////////// activate two beds 30
mins
POWER_LEVEL = 30;
 analogWrite(3, POWER_LEVEL*2.55);
 analogWrite(2, POWER_LEVEL*2.55);
 delay(2000);
digitalWrite(8,HIGH); //D1
digitalWrite(9, HIGH);// D2
digitalWrite(20, HIGH);// D6
digitalWrite(19, HIGH); //D5 exit of
/// DCHE 2 off
/// DCHE 1 on desorption for 30 mins
digitalWrite(4, HIGH);
delay(1000);
digitalWrite(5, HIGH);
delay(1000);
digitalWrite(6, HIGH);
```

```
delay(1000);
digitalWrite(7, HIGH);
delay(1000);
digitalWrite(10, HIGH);
delay(1000);

/// DCHE 1 on desorption for 30 mins
digitalWrite(14, HIGH);
delay(1000);
digitalWrite(15, HIGH);
delay(1000);
digitalWrite(16, HIGH);
delay(1000);
digitalWrite(17, HIGH);
delay(1000);
digitalWrite(18, HIGH);
delay(1000);

delay(900000); ////// wait 15 mins
//////////////////////////////////////////// adsorption two beds

digitalWrite(8,HIGH); //D1
delay(1000);
digitalWrite(9, HIGH);// D2
delay(1000);
digitalWrite(20, LOW);// D6
delay(1000);
digitalWrite(19, LOW); //D5
delay(1000);
digitalWrite(11,HIGH);// D3
delay(1000);
digitalWrite(12, HIGH); //D4
delay(1000);

/// DCHE 1 off first cycle
digitalWrite(4, LOW);
delay(1000);
digitalWrite(5, LOW);
delay(1000);
digitalWrite(6, LOW);
delay(1000);
digitalWrite(7, LOW);
delay(1000);
digitalWrite(10, LOW);
delay(1000);

/// DCHE 1 off first cycle
digitalWrite(14, LOW);
```

```
delay(1000);
digitalWrite(15, LOW);
delay(1000);
digitalWrite(16, LOW);
delay(1000);
digitalWrite(17, LOW);
delay(1000);
digitalWrite(18, LOW);
delay(1000);
delay(900000); ////// wait 15 mins
//////////////////////////
 delay(10000);
               digitalWrite(8,LOW ); //D1 exit off
               digitalWrite(9, LOW); //D2 supply onm p
               digitalWrite(11, LOW); //D3 exit off
               digitalWrite(12, LOW); //D4 exit off
               digitalWrite(19, LOW); //D5 exit off
               digitalWrite(20, LOW); //D6 exit off
}

void loop()
{
  POWER_LEVEL = 5;

              if (POWER_LEVEL>100) {POWER_LEVEL=100;}

              analogWrite(3, POWER_LEVEL*2.55);
            analogWrite(2, POWER_LEVEL*2.55);


//////////////////////////////////////////////////
delay(5000);
////// All DCHE Off

digitalWrite(12, HIGH);// D4
delay(1000);
digitalWrite(19, HIGH); //D5 exit of
delay(1000);
 digitalWrite(20, LOW); //D6 exit off
 delay(1000);
/// DCHE 2 off
/// DCHE 2 on desorption for 30 mins
digitalWrite(4, LOW);
delay(1000);
digitalWrite(5, LOW);
delay(1000);
digitalWrite(6, LOW);
delay(1000);
```

```
digitalWrite(7, LOW);
delay(1000);
digitalWrite(10, LOW);
delay(1000);

/// DCHE 1 on desorption for 30 mins
digitalWrite(14, HIGH);
delay(1000);
digitalWrite(15, HIGH);
delay(1000);
digitalWrite(16, HIGH);
delay(1000);
digitalWrite(17, HIGH);
delay(1000);
digitalWrite(18, HIGH);
delay(1000);


//////////
digitalWrite(8,HIGH); //D1
delay(1000);
digitalWrite(9, HIGH);// D2
delay(5000);

POWER_LEVEL = 30;
 analogWrite(3, POWER_LEVEL*2.55);

delay(600000); //delay 10mins
////////////////////////////////////////
POWER_LEVEL = 5;
 analogWrite(3, POWER_LEVEL*2.55);
delay(1000);

digitalWrite(8,LOW); //D1
delay(1000);
digitalWrite(9, LOW);// D2
delay(5000);                  // wait 5sec through swithching


 ////////////////////////////////////////////////////////////////////////////
////
/// switching
digitalWrite(11,HIGH ); //D3
delay(1000);
digitalWrite(12, LOW);// D4
delay(1000);
digitalWrite(19, LOW); //D5
delay(1000);
digitalWrite(20, HIGH); //D6
```

```
delay(10000);
digitalWrite(8,HIGH); //D1
delay(1000);
digitalWrite(9, HIGH);// D2
delay(5000);

POWER_LEVEL = 30;
 analogWrite(3, POWER_LEVEL*2.55);
 delay(1000);

////// All DCHE 1 Off   finsh desorption
digitalWrite(14, LOW);
delay(1000);
digitalWrite(15, LOW);
delay(1000);
digitalWrite(16, LOW);
delay(1000);
digitalWrite(17, LOW);
delay(1000);
digitalWrite(18, LOW);
delay(1000);


////////// All DCHE 2 on
digitalWrite(4, HIGH);
delay(1000);
digitalWrite(5, HIGH);
delay(1000);
digitalWrite(6, HIGH);
delay(1000);
digitalWrite(7, HIGH);
delay(1000);
digitalWrite(10, HIGH);
delay(1000);

  delay(600000);       //10 mins adsorption

    POWER_LEVEL = 5;
    analogWrite(3, POWER_LEVEL*2.55);
    delay(1000);
    digitalWrite(8,LOW); //D1
delay(1000);
digitalWrite(9, LOW);// D2
delay(5000);                  // wait 5sec through swithching

}
```

## Appendix III: Arduino Code for controlling Evaporative cooler

```
//Libraries
#include <DHT.h>
#define DHTPIN1 2
#define DHTPIN2 4
#define PWM 3

#define DHTTYPE1 DHT22 // DHT 22 (AM2302)
#define DHTTYPE2 DHT22 // DHT 22 (AM2302)


DHT dht1(DHTPIN1, DHTTYPE1);
DHT dht2(DHTPIN2, DHTTYPE1);


int pot;
int out;

//Variables
int chk;
float hum1;  //Stores humidity value
float temp1; //Stores temperature value
float hum2;  //Stores humidity value
float temp2; //Stores temperature value
void setup()
{
  pinMode(PWM,OUTPUT);
Serial.begin(9600);
dht1.begin();
dht2.begin();
}


void loop()
{
    delay(1000);
//Read data and store it to variables hum and temp
hum1 = dht1.readHumidity();
temp1= dht1.readTemperature();
hum2 = dht2.readHumidity();
temp2= dht2.readTemperature();
//Print temp and humidity values to serial monitor
Serial.print("Humidity1_Room: ");
Serial.print(hum1);
Serial.print(" %, Temp1: ");
Serial.print(temp1);
Serial.println(" Celsius");
//Serial.print("Humidity2_After DCHE: ");
```

```
//Serial.print(hum2);
//Serial.print(" %, Temp2: ");
//Serial.print(temp2);
//Serial.println(" Celsius");
delay(1000); //Delay 2 sec.

//////////////////////////////////////

if( hum1 <= 36)
  {
    pot=700;
  out=map(pot,0,1023,0,255);
  analogWrite(PWM,out);
delay(700);
return;

  }

if( hum1 <= 50.5)
  {
    pot=700;
  out=map(pot,0,1023,0,255);
  analogWrite(PWM,out);
delay(700);
return;

  }
else if (hum1 > 50.2) {

    pot=0;
  out=map(pot,0,1023,0,255);
  analogWrite(PWM,out);

  return;
}}
```